Exciting and steering propagating spin waves using a graded magnonic index

by

Carl Simon Davies

Submitted to the University of Exeter

as a thesis for the degree of

Doctor of Philosophy in Physics

In September 2016

I certify that all material in this thesis which is not my own work has been identified and that no material has previously been submitted and approved for the award of a degree by this or any other University.

(Signature) 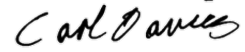

ABSTRACT

In this thesis, the results of time-resolved magneto-optical imaging experiments, micromagnetic simulations and analytical theory will be presented. These three approaches were used in order to understand how spin waves can be both excited and steered using magnetic non-uniformities (which gives rise to the graded magnonic index). The latter quantity refers to the smooth spatial variation of both the effective magnetic field and magnetization, and is naturally associated with any non-uniform magnetic configuration. The samples (continuous or geometrically patterned) studied in this thesis are composed of either Permalloy (a nickel-iron alloy) or Yttrium-Iron-Garnet (YIG). The Permalloy films are studied using one of two pump-probe techniques, which are distinguished by the character of the pump. The first technique – time-resolved scanning Kerr microscopy (TRSKM) - uses a fast magnetic field delivered by a coplanar waveguide, in order to pump magnetization dynamics, whereas the second technique – time-resolved optically-pumped scanning optical microscopy (TROPSOM) - instead uses an ultrashort optical pulse. In both systems, an optical probe is used to image the excited dynamics via the magneto-optical polar Kerr effect. The experimental realization of both systems will be extensively discussed, and the results acquired using these two techniques underpin the work discussed in two distinct chapters. The YIG samples, in contrast, were studied using Brillouin light scattering microscopy. In order to complement and understand the experimentally-acquired results, and furthermore to circumvent the diffraction-limited resolution associated with optical experiments, the magnetization dynamics in both the Permalloy and YIG samples were extensively modelled using micromagnetic calculations. In all these studied samples, a non-uniform magnetic configuration - giving rise to the graded magnonic index - was generated through either geometrical patterning or thermal modification of the magnetization. There are four key findings that are discussed in this thesis. The first involves the fact that the graded magnonic index gives rise to a spatially-varying frequency of resonance. By therefore exciting the entire sample with a spatially-uniform temporally-harmonic microwave magnetic field (as delivered, for example, by a wide current-carrying strip), one can efficiently excite resonance within a targeted region of magnetization. The resonantly-excited magnetization consequently, via the magnonic dispersion mismatch, emits propagating spin waves into the adjacent regions of the sample. Depending on the spatial character of the graded magnonic

index, the generated spin waves either take on the form of tightly-focused beams, or more traditional plane waves. Importantly, it is shown that this scheme of excitation can be used to excite spin waves with nanometric wavelengths, despite the exciting field having very large / infinite spatial extent. Alongside the proof-of-principle experimental and numerical measurements, a hybrid numerical/analytical model is constructed, allowing the distribution of local resonances to be mapped across any arbitrary (but stable) micromagnetic configuration. The second key finding discussed in this thesis relates to the capability of the graded magnonic index to continuously steer propagating spin waves. In order to understand the results obtained from both experiment and micromagnetic simulations, the propagation of spin waves across magnetic landscapes is interpreted as a result of adiabatic adjustment of the spin-wave group velocity, arising from the continual need for the spin-wave dispersion to adapt with the variation of both the effective magnetic field and the magnetization. Again, this finding is general indeed, allowing the path of spin waves to be predicted and explained across any landscapes with continuous variation of magnetic parameters. The third key finding involves the lateral confinement, and dispersive conversion, of propagating spin waves. If a spin wave propagates along a stripe (i.e. a waveguide), the magnonic dispersion shifts, such that there is overlap between the dispersive spectra characterizing the spin waves that are propagating parallel and orthogonal to the magnetization. By therefore joining two orthogonal waveguides so as to form a T-junction, one can realize a magnonic beam splitter – this is the building block of parallel magnonic circuitry. The fourth and final set of results discussed in this thesis concerns the magnetization dynamics that are excited within a Permalloy film by a tightly-focused optical pulse. The interpretation of the presented data is not yet complete, at the time of writing, but it is clearly observed that the optical stimulus gives rise to both a non-propagating quadrupolar pattern and propagating quasi-circular ripples in the measured magneto-optical Kerr response. These results, in particular, are relevant to the design of spin-wave devices involving optical stimuli. Overarching these four findings is the theme of "graded-index magnonics", which involves the study of spin waves hosted by continuously-varying magnetic landscapes. The results presented in this thesis, as a whole, reveal that the graded magnonic index not only can be exploited either to excite or steer propagating spin waves in a deliberate manner, but is in fact a ubiquitous feature that needs to be taken into account when considering any dynamical phenomena in nano- and micro-magnetism.

CONTENTS

ACKNOWLEDGEMENTS

A lifetime consists of many chapters, and I am happy to say that I have enjoyed this chapter – the process of studying for a PhD – very much. I have studied in-depth some complicated (but beautiful!) physics, travelled all around the world to discuss my results, and had the privilege to work with an amazing bunch of people. I do believe, however, that a PhD is impossible to achieve without a strong network of friends and family, and so I know I owe a large number of people a tremendous debt – these people have not only helped me professionally, in terms of my research, but they have also helped me to laugh and enjoy things along the way. Without all this help, I never would have made it this far.

I would first like to thank my friends and course mates who were with me in Exeter during my undergraduate studies – in particular (and strictly in alphabetical order) Jeff Chan, Nathan Cobourne, Alun Daley, Neil Horton, Christy Moen, Vikesh Patel, and Gareth Ward. As well as helping one another with studying / revision, we had a lot of fun, and I've really enjoyed our meet-ups since the autumn of 2013 (even the Spartan races!) I would also like to thank Adrian Lewis (my maths teacher at Glan Afan comprehensive school) and Jayne Morgan (my physics teacher at Neath Port Talbot College), who made me interested in pursuing physics at university.

A big thank you goes to my friends and peers in Exeter – in particular (again in strict alphabetical order) Tom Constant, Joe Dockrey, Tom Graham, Jen Lewis, Ian Hooper, Peter Karlsen, Rhiannon Mitchell-Thomas, Fedor Mushenok, Laura Parke, Sam Shelley, Alexandre Teulle, Ben Tremain, Gareth Ward and Matt Wilson. The Wednesday football sessions, house parties and pub outings were frequently a lifeline during my PhD, letting me get away from all the work. I also have very fond memories of our (consistently disastrous, but equally amazing) karaoke sessions in the Ship Inn!

In the magnetism group at Exeter, I would like to thank Rob Hicken, Paul Keatley and Leigh Shelford, who always had useful insight (and a good "outsider's perspective") when discussing my results during group meetings. Outside of the magnetism group, I'm very grateful to Chris Forrest, who was always more than happy to help fix our multiple workstations. I would also like to separately thank Fedor Mushenok, Volodymyr Kruglyak,

Natalie Whiteheard, Euan Hendry and Del Atkinson for their critical reading of this thesis, and suggestions for how to improve it.

I have been fortunate during my PhD research to have met, and sometimes work with, a number of talented researchers from all around the world. Alexandr Sadovnikov and Sergey Grishin, you performed many BLS experiments to corroborate our ideas, and obtained many beautiful results. We have had a very fruitful collaboration so far (resulting in 4 joint publications to date!) and I hope our collaborations can keep going strong. Sergei Chertapolov, you have been very kind towards me, and helped me greatly with improving things in the lab, and producing excellent samples. Vlad Poimanov, you helped me understand a lot about the complicated derivations and interpretation of magnetostatic spin-wave theory. Dan Allwood, you have been very supportive and generous towards me. Paweł Gruszecki and Maciej Krawczyk, you guys have pursued (by coincidence, almost simultaneously) the ideas of "graded-index magnonics", and we have had many stimulating conversations when we have met. Andriy Kuchko and the Gorobets family, you were excellent hosts when I visited Kiev for a month. So, thank you to you all.

Paul Keatley, you have been (and still am) a great friend, and you have provided me with a lot of useful and insightful advice over the course of my PhD and beyond, about physics and life in general. I've thoroughly enjoyed our time spent together during conference trips (Beijing, San Diego and Glasgow were tremendous fun), and I look forward to seeing you around in the future. I wish you, Kelly, Noah and Thea all the best!

Fedor Mushenok, thank you for all your advice and encouragement during the year and a half we have worked together – I think I have become a little more Russian as a result! It's been great (and often a relief) having someone alongside me "in the trenches", happy to share the many and regular battles I faced with lab equipment, data analysis, and physics questions. Spasibo tebe za vse!

Gareth Ward, I cannot thank you enough. Over the seven years we have both been living in Exeter, we have lived together for about two and a half years – it's been fantastic! As well as being a really fun guy to be around, you've offered a lot of tips and advice during my PhD, frequently lent a sympathetic ear when things weren't going so well, and have been an inspiration with your discipline and progress (both in and outside of physics). We have had a lot of good times, and I know I am very lucky to count on you as a good friend. Good luck with finishing your own thesis - I know you will find it straightforward!

Volodymyr, you have been very kind and generous towards me during our five years (so far) working together, and I consider myself lucky to have had you as a supervisor and mentor. Your sense of humour always put a smile on my face, and your indefatigable spirit has pushed me to try to achieve the same - as a result, I think we have achieved a lot together. Thank you for all your help, and I look forward to continuing our work together in the coming future.

Thank you Vicky, for sticking by me while I pursue these seemingly esoteric ideas. It's been a long journey so far, especially in terms of travelling between Essex, Exeter, and everywhere in between (we both know long-distance relationships aren't fun). However, in spite of the geographical distance, we have shared many laughs, and it has been a real comfort knowing that, at the end of the day, we can chat about more light-hearted matters / forget about everything else. We have grown together so much already, and I really look forward to seeing what the future has in store for us. I love you lots.

Last but by no means least, I would like to thank my mother (Meryl), grandparents (Arwel and Jean), my brother and sister (Paul and Lucy), and my aunt, uncle and cousin (Fiona, Mark and Luke), for all their encouragement, support and help, outside the world of physics. Diolch yn fawr.

LIST OF PUBLICATIONS

1) A. V. Sadovnikov, **C. S. Davies**, S. V. Grishin, V. V. Kruglyak, D. V. Romanenko, Yu. P. Sharaevskii and S. A. Nikitov, "Magnonic beam splitter: The building block of parallel magnonic circuitry" *Appl. Phys. Lett.* **106**, 192406 (2015).

2) **C. S. Davies**, A. Francis, A. V. Sadovnikov, S. V. Chertopalov, M. T. Bryan, S. V. Grishin, D. A. Allwood, Yu. P. Sharaevskii, S. A. Nikitov and V. V. Kruglyak, "Towards graded-index magnonics: Steering spin waves in magnonic networks" *Phys. Rev. B* **92**, 020408(R) (2015).

3) **C. S. Davies** and V. V. Kruglyak, "Graded-index magnonics" *Low Temp. Phys.* **41**, 976 (2015).

4) **C. S. Davies**, A. V. Sadovnikov, S. V. Grishin, Yu. P. Sharaevskii, S. A. Nikitov and V. V. Kruglyak, "Generation of propagating spin waves from regions of increased dynamic demagnetizing field near magnetic antidots" *Appl. Phys. Lett.* **107**, 162401 (2015).

5) **C. S. Davies**, A. V. Sadovnikov, S. V. Grishin, Yu. P. Sharaevskii, S. A. Nikitov and V. V. Kruglyak, "Field-controlled phase-rectified magnonic multiplexer" *IEEE Trans. Magn.* **51**, 3401904 (2015).

6) **C. S. Davies**, Y. Au and V. V. Kruglyak, "Prototype magnonic device development" *Magnetics Technology International*, pp.54-57 (2016).

7) **C. S. Davies** and V. V. Kruglyak, "Generation of propagating spin waves from edges of magnetic nanostructures pumped by uniform microwave magnetic field" *IEEE Trans. Magn.* **52**, 2300504 (2016).

8) V. V Kruglyak, Y. Au, O. Kazak, **C. S. Davies**, F. B. Mushenok and A. N. Kuchko, "Symmetry of Spin Waves Excited in Thin Magnetic Films by Femtosecond Optical Pulses" *Proceedings of Ultrafast Magnetism Conference 2015* ***in press*** (2017).

9) V. V. Kruglyak, **C. S. Davies**, V. S. Tkachenko, O. Yu. Gorobets, Yu. I. Gorobets and A. N. Kuchko, "Formation of the band spectrum of spin waves in one-dimensional magnonic crystals with different types of interfacial boundary conditions" *J. Phys. D: Appl. Phys.* ***in press*** (2017).

10) F. B. Mushenok, R. Dost, **C. S. Davies**, D. A. Allwood, B. Inkson and V. V. Kruglyak, "Broadband conversion of microwaves into propagating spin waves in patterned magnetic structures" ***submitted*** (2017).

LIST OF FIGURES

LIST OF TABLES

DECLARATION

A significant number of students and researchers have contributed to the work presented and discussed in this thesis. Here, I outline the general contributions from other individuals to the results shown in each chapter. In addition, specific important contributions will be acknowledged in each chapter. It is an impossible task, however, to note the specific contributions by Prof. Volodymyr Kruglyak (my Ph.D. supervisor), as his contributions permeate throughout the entirety of this thesis.

Chapter 1: ***Introduction***

The introduction to this thesis, discussing the advance of technology and the possibility for magnonics to contribute to this in the coming future, is my own work. Extensive references to primary and secondary sources are provided throughout.

Chapter 2: ***Background concepts of ferromagnetism and spin-wave dynamics***

The description of the background concepts, underpinning the results presented in this thesis, was compiled by myself. All the concepts and ideas in this chapter were drawn from the scientific literature, and so extensive references are provided throughout, in order to give credit where it is due. This review is non-exhaustive, and so the references also act as a resource for readers who wish to understand further the discussed material.

Chapter 3: ***Experimental and numerical techniques***

The background principles of the magneto-optical techniques (both the magneto-optical Kerr effect and Brillouin light scattering) used to image the excitation and propagation of spin waves, and also the brief discussion of how light interacts with matter, were compiled by myself, using the credited scientific literature.

The time-resolved scanning Kerr microscope (TRSKM) system, discussed in Section 3.2, is a result of continuous development in Exeter since 2002, with major contributions from Prof. Rob Hicken, Prof. Anjan Barman, Prof. Volodymyr Kruglyak, Dr. Paul Keatley, and Dr. Yat-Yin Au. Only minor modifications to the experimental setup were implemented by myself.

The time-resolved optically-pumped scanning optical microscope (TROPSOM) system was first assembled by Dr. Toby Davison, Dr. Yat-Yin Au, and Prof. Volodymyr Kruglyak in 2011. Substantial modifications of the experimental setup, from its first design, were made by myself.

In Section 3.6, I discuss the principles underpinning the micromagnetic package Object-Oriented Micro-Magnetic Framework (OOMMF). This was compiled by myself, drawing wholly from the scientific literature (which is credited throughout).

Chapter 4: ***Exciting spin waves using a graded magnonic index***

The experimental measurements that are discussed in Section 4.2 were wholly performed by Dr. Alexandr Sadovnikov and Dr. Sergey Grishin at the University of Saratov in Russia, and are included for the sake of completeness. All the micromagnetic simulations discussed in this chapter were performed and post-processed by myself. The hybrid analytical / numerical model discussed in Section 4.4 was developed by myself, with contributions from Dr. Vladyslav Poimanov (who works at Donetsk National University in Ukraine), and implemented numerically by myself. The majority of the results discussed in Sections 4.2 and 4.3 has already been published in two articles.[1-2]

Chapter 5: ***Steering spin waves using a graded magnonic index***

The results presented in this chapter were collected as part of a large collaboration. Initially, preliminary TRSKM measurements were performed by myself and Mr. Andrew Francis, using a Permalloy sample fabricated by Dr. Matthew Bryan and Prof. Dan Allwood (both of whom worked at the University of Sheffield). All the TRSKM measurements presented in this chapter were acquired solely by myself, using a Permalloy sample fabricated by Dr. Sergei Chertopalov (who worked at Donetsk National University in Ukraine). The LabView software used to control the experimental equipment was written by Dr. Yat-Yin Au, at the University of Exeter. The micromagnetic calculations were wholly performed and post-processed by myself. The interpretation of the experimental and micromagnetic results was developed by myself, Dr. Alexandr Sadovnikov, and Dr. Sergey Grishin. The majority of the results / ideas discussed in this chapter has already been published in two articles[3-4].

Chapter 6: ***Lateral confinement and dispersive-conversion of propagating spin waves***

The experimental measurements that are discussed in this chapter were wholly performed by Dr. Alexandr Sadovnikov, Dr. Dmitrii Romanenko and Dr. Sergey Grishin (all of whom worked at Saratov State University), and are included for the sake of completeness. All the micromagnetic simulations discussed were performed and post-processed by myself. The majority of the results presented in this chapter has already been published in one article.[5]

Chapter 7: ***Spatiotemporal imaging of the laser-induced dynamics across magnetic films***

The Permalloy films discussed in this chapter were grown by Dr. Ehsan Ahmad (who worked at the University of Exeter). I was responsible for measuring all the experimental results that are discussed in Chapter 7, using LabView programs written wholly by Dr. Fedor Mushenok. The post-processing MatLab scripts were written separately by either myself or Dr. Fedor Mushenok. The interpretation of the acquired data has (to date) been primarily developed by myself.

CHAPTER 1

INTRODUCTION

In 1965 and 1975, Gordon Moore forecasted that the density of transistors within integrated circuits would double annually[6] and biennially[7] respectively. In the five decades that have followed these predictions, electrical engineers, condensed-matter physicists and semiconductor manufacturers have consistently sought to achieve "more Moore", and this pursuit has been largely responsible for the rapid and dramatic development and miniaturization of technology. It is now becoming increasingly evident, however, that the seemingly inexorable improvement of conventional semiconductor-based computational architecture is unsustainable. Indeed, indications of the plateauing of Moore's exponential law are already beginning to emerge,[8] with the clock rate of modern processors having not improved since 2004. More recently, Intel have formally announced[9] that their biennial "tick-tock" strategy[10] of chip development is being revised to a triennial "process-architecture-optimization" model, due to the difficulties associated with manufacturing integrated circuits boasting feature sizes below 22 nm.

As part of the drive to fulfil Moore's law, a global consortium of integrated device manufacturers established in 1998 the International Technology Roadmap for Semiconductors.[11] This is a set of documents published biennially, which identifies potential bottlenecks in the upcoming manufacture of integrated circuitry, and advises where efforts in research should be devoted. In particular, since 2015, the Roadmap concentrates on seven topics - one of these topics is devoted to the discussion of "beyond-CMOS" technologies,[12] which could compliment and / or supersede conventional integrated circuits. Potential candidates currently being studied include spintronics,[13] graphene nanoribbons,[14] tunnel junction devices,[15] memristors,[16] and molecular electronics.[17] Another area of research, which has recently begun to garner significant attention, involves the development of magnonic technology,[18] which uses spin waves (and their quanta, magnons) to both transmit and process data.

Magnonic technology boasts several properties that give it a distinct advantage over its electronic counterpart.[19] Electronics is restricted in the sense that information is transmitted using only one scalar variable (charge). In contrast, wave-based signal carriers allow computational operations to be performed with vector variables (amplitude and phase). This second degree of freedom enables computing architecture to be reduced both in size and complexity. Specifically with regard to spin waves, magnetization is an inherently non-volatile quantity, and so no power is drawn by the magnonic circuit during standby. Moreover, since spin waves do not necessitate the translational transfer of particles, the energy required to drive magnonic technology is dramatically reduced. This causes spin waves to be free of the Joule heating associated with electronics, and could therefore enable the circumvention of the heating problem, which has stalled the growth of electronic clock rates since 2004.[8] This increased clock rate is further augmented by the quadratic dispersion of exchange spin waves, whereby the miniaturization of magnonic wavelengths causes the operating frequency to increase by a power of two. To illustrate this comparison between electronic and magnonic technology more quantitatively, one can consider the example of a full adder circuit.[20] Using CMOS-based technology, with a 32 nm node, such a device has a footprint of 6.4 μm^2, requires 28 transistors, and draws 10 fJ of energy. In contrast, the magnonic counterpart, using a wavelength of 32 nm, has a spatial footprint of 0.026 μm^2, and just requires three majority gates and 24 aJ to function. Magnonic technology, in light of these numerous technical advantages, therefore possibly offers a viable pathway through which Moore's law can be prolonged.

In addition to the aforementioned advantages of magnonic technologies, the properties of spin waves and magnons can be substantially engineered using a wide variety of tuning parameters. This offers a broad toolbox, using which all kinds of magnonic devices can be fashioned. For example, by periodically modulating a spin-wave waveguide, one can construct a reprogrammable magnonic crystal,[21] which supports and forbids the propagation of spin waves with certain frequencies. Alternatively, by driving the precession of magnetization with a stronger excitation, one can enter the non-linear regime, giving rise to the excitation of solitons[22] and the possibility of high harmonic generation.[23] In keeping with the current exploration of the rich playground of magnonics, this thesis is devoted to investigating how propagating spin waves can be excited and steered using non-uniformities in magnetic bodies.

The ubiquity of non-uniformity complicates our understanding of the world around us in an immeasurable number of ways. If however the influence of non-uniformity is properly understood, it can be exploited to realize more sophisticated applications. In transformation optics, for example, a spatially-varying refractive index is used to steer rays of light in particular directions. In magnonic systems, the potential landscape across which spin waves propagate is given by both the smoothly-varying distribution of the magnetization and the effective field. These two ingredients, combined, give rise to a magnonic index (the spin-wave analogue of the refractive index). By designing a system in which there is a graded magnonic index, it is straightforward to envisage the steering of propagating spin waves.

The optical refractive index is limited in the sense that it is only capable of guiding beams of light. In a magnonic system, in contrast, the magnetization is capable of precessing at a resonant frequency, dictated by the length and orientation of the magnetization and effective field vectors. In a system with a graded magnonic index, therefore, there is also a spatially-varying frequency of resonance. By exciting the entire magnonic system at a particular frequency, the exciting field is only able to couple most efficiently with particular regions of magnetization. This local but resonant excitation therefore serves as a spin-wave source, capable of injecting propagating spin waves into the adjacent regions of magnetization.[24] The graded magnonic index therefore not only enables the path of propagating spin waves to be altered, but it also allows the very generation of said propagating spin waves.

In this thesis, a combination of experimental measurements, micromagnetic calculations and analytical theory is used to explore how the graded magnonic index can be exploited to excite and steer propagating spin waves. In a similar vein to the electromagnetic applications that are already being developed using transformation optics, it is hoped that the field of graded-index magnonics will similarly prove useful in the design and construction of magnonic devices. Indeed, as the magnonic technology continues to miniaturize, non-uniformity – and by association the principals of graded-index magnonics - will become increasingly important.

In Chapter 2, the concepts underpinning magnetism and spin-wave dynamics are reviewed. All the results and measurements discussed in this thesis concern ferromagnetic / ferrimagnetic materials, and so the background concepts pertaining to these substances are focused on. The phenomena of ferromagnetism can be partially understood using a

phenomenological mean field theory. However, in order to fully understand ferromagnetic / ferrimagnetic behavior, it is necessary to discuss the results of quantum mechanics, and in particular the exchange / super exchange interaction. The interactions that govern the static distribution of magnetic configurations – specifically, the Zeeman, demagnetizing, exchange and magneto-crystalline interactions – are then reviewed in turn. Together, these interactions give rise to an effective field, which is associated with any magnetic system. Once the principles relating to the static behavior of magnetization has been outlined, the dynamics are discussed. Magnetization dynamics, in general, are governed by the Landau-Lifshitz equation, which describes the precession of magnetization about the effective field. Using the Landau-Lifshitz equation, the dynamics can be discussed in two distinct regimes. When the magnetization oscillations are free, the Kittel equation characterizing the fundamental mode of resonance can be derived. If instead the magnetization is driven by an exciting magnetic field, the dispersion of dipolar spin waves (in the magnetostatic limit) is obtained. This dispersion is characterized by a peculiar anisotropy, drastically depending on the relative orientation of the magnetization and the direction of spin-wave propagation. To include the influence of the isotropic exchange interaction, one can use the dipole-exchange dispersion relation. Using these dispersion relations, it is possible to construct isofrequency curves, which correspond to the distribution of the wave vector solutions that satisfy the spin-wave dispersion at a certain frequency. These curves are used extensively throughout this thesis in order to characterize and explain the behavior of the propagating spin waves. This chapter concludes with a brief review of spin-wave width-modes, which are supported by magnonic waveguides.

In Chapter 3, the experimental and numerical techniques used to acquire the results presented in this thesis are intensively discussed. The chapter begins with a brief description of the magneto-optical Kerr effect, which was used throughout to experimentally image magnetization dynamics within Permalloy samples. Once this background has been established, the experimental details of the two magneto-optical microscopes used by myself at the University of Exeter are extensively detailed. Both microscopes are based on a pump-probe technique, but differ significantly in the character of the pump. The first microscope – the time-resolved scanning Kerr microscope (TRSKM) – uses a magnetic field delivered by a coplanar waveguide to stimulate magnetization dynamics, whereas the second microscope – the time-resolved optically-pumped scanning optical microscope (TROPSOM) – uses ultrashort optical pulses as the pump. The implementation of both techniques is discussed in

turn. Some measurements presented in this thesis were acquired by collaborators using Brillouin light scattering (BLS) microscopy – the third section of this chapter, therefore, is devoted to a brief description of the concepts underpinning BLS microscopy. In the fourth and final section of this chapter, the principles of micromagnetic simulations are discussed. The micromagnetic package Object-Oriented Micro-Magnetic Framework (OOMMF) was extensively used throughout this thesis to complement and understand the experimental measurements, and furthermore as a stand-alone tool to study systems which could not be directly studied using experiment. This section therefore discusses the principles underpinning the operation of OOMMF, and details how the magnetic interactions are integrated within the micromagnetic package.

In Chapter 4, the graded magnonic index is exploited in order to excite propagating spin waves. In the introduction of this chapter, I discuss the Schlömann mechanism of spin-wave excitation, which was first outlined in 1964. This mechanism involves the efficient coupling of a spatially-uniform exciting magnetic field with targeted regions of magnetization, which consequently launches spin waves of finite wave vector into the neighboring regions of magnetization. In the first section of this chapter, a patterned Yttrium-Iron-Garnet (YIG) film was studied using both BLS microscopy and micromagnetic simulations. Specifically, the YIG film contains an embedded isolated antidot, but is otherwise continuous. Due to the static demagnetizing field generated by the magnetized antidot, the internal field immediately adjacent to the antidot is raised, compared to the internal field far from the antidot. This therefore enables the graded magnonic index to be used to excite spin-wave caustic beams, originating from the resonantly-excited magnetization immediately adjacent to the antidot. In the second section of this chapter, a miniaturized antidot system was studied using the same methodology. Due to the increasing dominance of the exchange interaction, the excited spin waves are instead observed to be more isotropic. The dynamic demagnetizing field has hitherto been neglected entirely from the discussion. A wide longitudinally-biased stripe (modelling a semi-infinite film) was therefore investigated, and it is shown that the dynamic demagnetizing field can similarly be used to excite plane propagating spin waves from the edges of a patterned film. In the third and final section of this chapter, a hybrid numerical / analytical model was developed in order to evaluate the local frequency of resonance across a magnetic ground-state, offering to therefore explain all the results discussed in this chapter.

In Chapter 5, the graded magnonic index is used to steer propagating spin waves across a network of Permalloy waveguides. Specifically, a T-junction of waveguides was transversely biased using a spatially-uniform magnetic field. The non-uniform distribution of the demagnetizing field across the structure caused there to be two dominant modes of resonance, separated in frequency, and moreover each spatially confined to either the leg or the arms of the junction. Upon exciting the structure with a spatially-uniform exciting field, resonance was excited within the leg of the T-junction, exciting spin-wave caustic beams propagating across the arms via the Schlömann mechanism. Extensive TRSKM measurements and OOMMF simulations were used to image and understand the character of the excited spin waves. When the bias field was applied symmetrically across the structure, two spin-wave beams were symmetrically excited, both propagating along the left and right arms of the junction. If instead the external bias field was rotated by just 15°, only one spin-wave beam was observed propagating across one arm. This observed spin-wave beam was identified as undergoing continuous refraction and distributed scattering, due to the graded magnonic index. A hybrid numerical / analytical model was constructed in order to understand both the propagation path of the observed spin wave, and the absence of the other spin wave. Using this model, it was identified that a second spin-wave beam was in fact generated via the Schlömann mechanism, but the graded magnonic index caused the beam to undergo "anomalous reflection". Hence, it was not observed propagating across the other arm of the T-junction.

In Chapter 6, the graded magnonic index was used to transform the modes of propagating magnetostatic width-modes from one dispersive type to another, across a T-junction of YIG waveguides. This system was extensively studied using BLS microscopy and OOMMF calculations. In a wholly continuous thin film, the dispersion of spin waves propagating in the plane of the film, but at a direction either parallel or orthogonal to the magnetization, do not overlap at all. In a waveguide, in contrast, it is possible to excite width-modes, corresponding to laterally-confined propagating spin waves. Across these waveguides, one can identify significant overlap between the two spin-wave bands, arising from effects introduced solely by the finite width of the film. This overlap, therefore, was exploited to efficiently convert spin-wave width-modes across the T-junction of YIG waveguides.

In Chapter 7, the magnetization dynamics induced by the optical excitation of Permalloy films are studied. The graded magnonic index, in the context of this chapter, refers to the spatially varying magnetization induced by the thermal load delivered by the optical pulse, but no clear graded-index effects were definitively observed in this chapter. In the TROPSOM setup, two laser beams (of different wavelength) were focused to form tightly-focused spots on the surface of a Permalloy film. One of the beams acts as a pump for magnetization dynamics, and the other serves as a probe. Measurements of both the transient reflectivity and magneto-optical Kerr signal were acquired. In the first section, the measured spatiotemporal dynamics across a 20 nm thick Permalloy film are discussed. Here, a monopolar signal was detected in the transient reflectivity channel, which was assumed to correspond to the nominally-Gaussian spatial profile of the pump spot. In the Kerr channel, in contrast, a quadrupolar signal was consistently observed: the origin of this signal's symmetry is currently unknown. In the second section, similar dynamics excited within a 50 nm thick Permalloy film are studied. The Kerr signal was similar to that observed in the 20 nm thick film, but here the reflectivity signal was frequently dipolar. Again, the dipolar signal is not understood in its physical origin. In addition to the aforementioned non-propagating signals, propagating ripples were detected in the Kerr channel. In the third and final section of this chapter, the results acquired using TROPSOM are generally and speculatively discussed. Finally, the results of the research presented in this thesis are summarized in Chapter 8, alongside some speculative discussion of future research directions in the field of "graded-index magnonics".

CHAPTER 2

BACKGROUND CONCEPTS OF MAGNETISM AND SPIN-WAVE DYNAMICS

2.1 Introduction

In this chapter, my aim is to introduce the background concepts essential for the understanding of the further material presented in this thesis. I begin this chapter by briefly discussing the classifications of magnetic phenomena – namely, diamagnetism, paramagnetism and ferromagnetism. Since the experimental measurements, numerical results and theoretical descriptions discussed in this thesis all concern ferromagnetic and ferrimagnetic materials, I then discuss the key results arising from the semi-classical Weiss model of ferromagnetism. Despite this model being wholly phenomenological, it can be used to explain the temperature-dependence of ferromagnetic substances with substantial success. I will then introduce and extensively discuss the quantum mechanical exchange interaction, which underpins the modern understanding of ferromagnetism. Extending from this, I will then outline the concept of superexchange, which gives rise to the phenomena of ferrimagnetism. Following this discussion of the origins of magnetism, some discussion is then given about the properties and character of the two magnetic materials – Permalloy and YIG – that are studied in this thesis.

Subsequently, I will then discuss the static and dynamic behavior of magnetization. The static magnetization of a substance is defined by the stable energetic equilibrium reached by a set of magnetic interactions, which all seek to minimize their individual energies. The magnetization dynamics of a magnetic body is governed by the Landau-Lifshitz equation, which is used in this chapter to derive the equations characterizing ferromagnetic resonance, the ferromagnetic Polder susceptibility, and the magnetostatic spin-wave dispersion. In addition to the lattermost dispersion, the dispersion relation characterizing dipole-exchange

spin waves is then briefly outlined, and the isofrequency curves characterizing the various spin-wave types are discussed. To conclude this chapter, I then briefly review the properties of spin-wave width-modes (propagating spin waves that are albeit laterally confined within waveguides). Note that, throughout this thesis, I consistently use the Gaussian unit system.

2.2 Semi-classical models of magnetism

In this section, I begin by discussing the models introduced by Langevin to explain the phenomena of diamagnetism and paramagnetism. Then, the mean field theory introduced by Weiss, to account for ferromagnetism, is discussed in more detail. This section then concludes with a brief description of the failings of the aforementioned semi-classical models.

2.2.1 Diamagnetism and paramagnetism

From the viewpoint of magnetism, all matter (including materials that are commonly considered to be "non-magnetic", such as wood, water, and hydrogen) can be ultimately classified as being either diamagnetic or paramagnetic. The difference in classification emerges when an external magnetic field is applied across the substance. In diamagnetic materials, the induced magnetization opposes the external magnetic field, whereas in paramagnetic materials, the induced magnetization rather aligns with the external magnetic field. Upon removal of the said magnetic field, the magnetization of both diamagnetic and paramagnetic materials is entirely lost.

The phenomena of diamagnetism and paramagnetism can be qualitatively understood using the semi-classical theory of orbital magnetic moments, first put forward by Paul Langevin in 1905.[25] The discussion given here follows those given by the textbooks written by Bates,[26] Morrish,[27] Aharoni[28] and Jiles.[29] An electron orbiting a nucleus in a closed loop, in the absence of any external magnetic field, will intrinsically have an orbital magnetic moment

$$\boldsymbol{\mu} = \frac{-|e| \cdot \pi r^2}{Tc} \hat{\boldsymbol{n}}, \tag{2.1}$$

where e is the electronic charge, r is the orbital radius, T is the orbital period, c is the speed of light, and $\hat{\boldsymbol{n}}$ is the unit vector normal to the plane across which the electron moves. The magnetic moment per unit volume V defines the magnetization $\boldsymbol{M}$ of a substance

$$\boldsymbol{M} = \frac{\boldsymbol{\mu}}{V}. \tag{2.2}$$

Upon applying an external magnetic field across a substance, the magnetization of a diamagnetic or paramagnetic substance will align parallel or antiparallel to the external bias respectively. The magnetization induced by a unit magnetic field is given by the magnetic susceptibility

$$\chi = \frac{\boldsymbol{M}}{\boldsymbol{H}_B}, \tag{2.3}$$

and so the diamagnetic and paramagnetic susceptibilities are negative and positive respectively. The magnitude of the diamagnetic susceptibility is typically on the order of 1×10^{-5}, whereas the paramagnetic susceptibility is about 1×10^{-3}. As already noted, all substances in existence are diamagnetic to some degree, but only some are paramagnetic – examples in the latter category include iron ions, or rare-earth ions.

While the magnetic susceptibility of a substance is independent of the external field, there is some dependence on the temperature *T*. For a diamagnetic substance, the temperature only indirectly enters the expression for the diamagnetic susceptibility χ_{dia} via the orbital radius. The orbital radius is only weakly dependent on *T*, and so the diamagnetic susceptibility is almost independent of the temperature. In contrast, the paramagnetic susceptibility χ_{par} varies inversely with the temperature according to the Curie (or Curie-Langevin) Law

$$\chi_{par} = \frac{C}{T}, \tag{2.4}$$

where *C* is the Curie constant. The material-specific Curie constant is given by

$$C = \frac{N\mu^2}{3k_B}, \tag{2.5}$$

where *N* is the number of particles within the paramagnetic substance, and k_{B} is the Boltzmann constant. When subjected to both a high magnetic field and a very low temperature, the magnetic moments within a paramagnetic substance align completely with the magnetic field, and so the substance can be magnetically saturated. If the temperature is then raised, the thermal energy of the magnetic moments increase, which reduces the

alignment of the moments. If the temperature is raised high enough, the thermal energy of the magnetic moments can dominate, destroying any and all net magnetization.

2.2.2 Ferromagnetism

The magnetic moment associated with paramagnetic materials aligns parallel to an externally-applied bias field, but upon removal of the external bias, the alignment of the ensemble of magnetic moments is entirely lost. This behavior implies there is no coupling between the magnetic moments. If instead it is supposed that the moments are strongly coupled, they can retain their collinearity upon removal of the bias field – this gives rise to the class of ferromagnetic media, which have a spontaneous magnetization in the absence of a bias field. To explain the origin of ferromagnetism, Pierre Weiss, in 1907, extended Langevin's model of paramagnetism to construct a mean field theory.[30] In his theory, Weiss postulated that, in addition to the externally-applied field $\boldsymbol{H}_{\mathrm{B}}$ acting to align the magnetic moments, there exists a phenomenological "Weiss molecular field" intrinsic to a ferromagnetic sample. This is given by $\boldsymbol{H}_{Weiss} = \lambda_{Weiss} \cdot \boldsymbol{M}$, where λ_{Weiss} is the molecular field constant (also referred to as the Weiss constant). Once the magnetic moments achieve some form of alignment, the magnetic moments generate a Weiss field, which further improves their alignment. This self-consistent ordering continues until thermal jitter impedes any further progress.

To describe the temperature dependence of a ferromagnetic substance at high temperature, the transformation $\boldsymbol{H}_B \rightarrow \boldsymbol{H}_B + \boldsymbol{H}_{Weiss}$ can be simply inserted within the Curie Law to yield the equation

$$M = C\frac{H_B + H_{Weiss}}{T}. \tag{2.6}$$

Solving this for the ferromagnetic susceptibility leads to the Curie-Weiss Law

$$\chi = \frac{C}{T - T_C}, \tag{2.7}$$

where $T_{\mathrm{c}} = C\lambda_{\mathrm{Weiss}}$ is the Curie temperature. This is the critical temperature above (below) which the substance exhibits paramagnetic (ferromagnetic) behavior. Note that the Curie-Weiss Law is only applicable in describing the magnetic susceptibility of a ferromagnet in the

paramagnetic regime (when $T > T_C$). In the ferromagnetic regime (when $T < T_C$), the magnetization is described by the transcendental equation[27]

$$M = N\mu\left[\coth\left(\frac{\mu\{H_B + \lambda_{Weiss}M\}}{k_BT}\right) - \frac{1}{(\mu\{H_B + \lambda_{Weiss}M\}/k_BT)}\right]. \tag{2.8}$$

The expression within the square bracket in Eq. 2.8 corresponds to the Langevin function, such that Eq. 2.8 is of the form

$$M = N\mu\left[\coth(a) - \frac{1}{a}\right] \equiv N\mu L(a), \tag{2.9}$$

where $a = \mu(H_B + \lambda_{Weiss}M)/k_BT$. Eq 2.9 cannot be solved analytically for M – rather, it must be numerically solved. To do this, two coupled equations for M, in the absence of an external bias field, can be obtained using Eq. 2.9 and the argument of the Langevin function

$$M = \frac{a \cdot k_BT}{\mu\lambda_{Weiss}}. \tag{2.10}$$

By plotting both M and L as functions of a (and therefore as functions of the inverse temperature), the points of intersection between the two curves correspond to the permitted magnetization. This graphical approach is outlined in Fig 2.1.

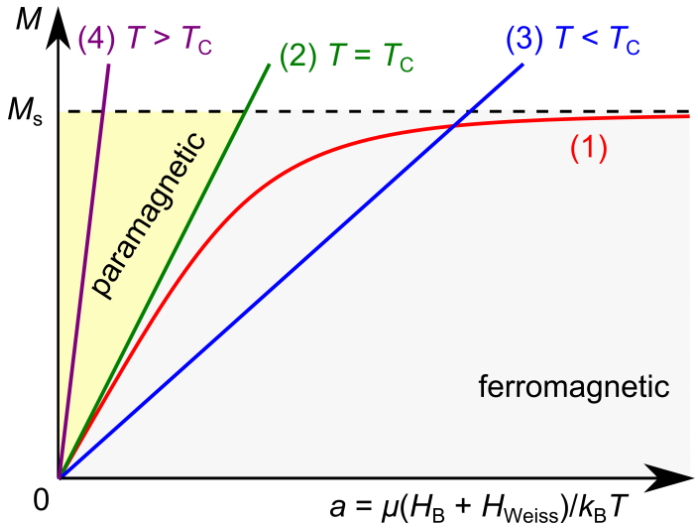

Fig. 2.1 Graphical solutions of Eq. 2.8. Curve (1) corresponds to Eq. 2.9, and the straight lines (2) - (4) correspond to Eq. 2.10 with different values of a (and, by extension, T).

Using the graphically-derived solutions shown in Fig. 2.1, one can draw several conclusions. Firstly, as a increases (T decreases), the Langevin function (curve (1) in Fig. 2.1) tends toward the asymptote $M = N\mu \equiv M_s$, where M_s is the saturation magnetization. Such temperature dependence is characteristic and expected of a ferromagnetic substance. Secondly, at the Curie temperature, the straight line (2) lies at a tangent to the Langevin function at $a = 0$, and so at and above this critical temperature there is zero spontaneous magnetization. In this regime, the previously-ferromagnetic substance is now paramagnetic. Through equating the gradient of the straight line (2) with the gradient of curve (1) as $a \to 0$, one can obtain a more exact expression for the Curie temperature

$$T_C = \frac{N\mu^2}{3k_B}\lambda_{Weiss}. \qquad (2.11)$$

This is the critical temperature which divides the paramagnetic and ferromagnetic regimes, as indicated in Fig. 2.1. At finite temperatures below the Curie temperature, there are two intersections between curve (1) and the straight line (3), at zero and finite magnetization. Only the latter represents a stable solution for the system, and so this is the spontaneous magnetization of the ferromagnetic substance.

2.2.3 Breakdown of the semi-classical models

The semi-classical models discussed in Sections 2.2.1 - 2.2.2 reasonably describe the phenomena of diamagnetism, paramagnetism and ferromagnetism. Broadly speaking, many experimental studies obtained results which agreed reasonably well with the classical models. However, there were two significant failings of the semi-classical theories, which indicated that a more complete model needed to be developed.

The first significant failing was pointed out by Niels Bohr in 1911, Hendrika Johanna van Leeuwen in 1919, and by John Hasbrouck Van Vleck in 1932.[31] In Langevin's description of both diamagnetism and paramagnetism, it was assumed that the magnetic substance could not rotate. At a finite temperature, there would be a distribution of electronic velocities, but the average velocity would be zero. Upon applying a magnetic field across the substance, the distribution of electronic velocities would be modified, but the average velocity (at thermal equilibrium) would still be zero, and so the applied magnetic field cannot generate any net magnetic moment.[32] Consequently, diamagnetism, paramagnetism and ferromagnetism cannot be explained using a classical / semi-classical approach.

The second failing of the classical models relates to the postulated Weiss field. By measuring the Curie point, one can directly deduce λ_{Weiss} via Eq. 2.11. For example, iron was measured as having a Curie temperature of about 1000 K, leading to a Weiss field of strength 10 MOe. A field of such strength cannot be explained at all using a classical approach – the dipole-dipole interaction (which will be discussed in detail in Section 2.4.3) generates a field on the order of 1 kOe, at distances comparable to the lattice constant. The origin of this gargantuan Weiss field therefore cannot be accounted for using a classical approach.

To address both these failings, it is necessary to introduce a quantum mechanical model of magnetism. This will be the subject of discussion in Section 2.3.

2.3 Quantum mechanical models of magnetism

In the previous section, the failings of the classical models of magnetism were pointed out. To resolve these problems, it is necessary to introduce a quantum-mechanical model of magnetism. The information given here was mostly obtained from the textbooks written by Morrish[27] and Jiles.[29]

2.3.1 The magnetic moment

In the classical atomic model, electrons were naively interpreted as orbiting the nucleus in a manner similar to how the earth orbits the sun, with the electronic radius being free to take on any value. The expression for the total energy *E* of a simple classical particle, with mass *m* and linear momentum ***p***, moving in a potential *V*, is given by the Hamiltonian

$$H = \frac{p^2}{2m} + V \,. \tag{2.12}$$

Quantum mechanically, however, particles are defined through their wave function $\psi(\boldsymbol{r})$. The observable properties of the wave function – eigenvalues - are obtained through applying suitable operators to ψ. The linear momentum of a wave function is obtained through applying the operator $\hat{p} = \frac{\hbar}{i}\nabla$, thus leading to the time-independent Schrodinger's equation (the quantum analogue of Eq. 2.12)

$$\left[-\frac{\hbar^2}{2m}\nabla^2 + V\right]\psi = E\psi \,. \tag{2.13}$$

The value of ψ for different values of E represents different states of the system. In general, electrons within an atom can be uniquely described using just four quantum numbers - the principal quantum number n (defined by Niels Bohr[33]), the orbital angular momentum quantum number l (defined by Arnold Sommerfeld[34]), the magnetic quantum number m_l, and the spin quantum number m_s. These respectively refer to the electronic energy level, the total angular momentum arising from the electron's orbital motion, the projection of the orbital angular momentum along a predefined axis, and the intrinsic angular momentum (also referred to as the spin or self-rotation) of the electron. These quantities, characterizing the fermionic electrons, are restricted to certain values, as outlined in Table 2.1.

Quantum number	**Range of values**
n	$1 \leq n$
l	$0 \leq l \leq n\text{-}1$
m_l	$-l \leq m_l \leq l$
m_s	$-s \leq m_s \leq s$

Table 2.1 The quantum numbers, and the discrete set of values they can take.

The energy E_n of an electron is given by

$$E_n = -\frac{Z^2 m_e e^4}{8h^2 {\varepsilon_0}^2} \cdot \frac{1}{n^2}\,, \tag{2.14}$$

where Z is the atomic number, m_e is the electronic mass, and ε_0 is the permittivity of free space. The total orbital angular momentum is given by

$$L = \hbar\sqrt{l(l+1)}\,, \tag{2.15}$$

therefore endowing the electron (via Eq. 2.1, in combination with the classical definition of the angular momentum) with an orbital magnetic moment

$$\mu_L = g_L \frac{e\hbar}{2m_e}\sqrt{l(l+1)}\,, \tag{2.16}$$

where g_L is the electron orbital g-factor ($g_L = 1$). The quantity $\frac{e\hbar}{2m_e}$ is often referred to as the Bohr magneton μ_B. The projection of the orbital magnetic moment onto the bias magnetic field $\boldsymbol{H}_B$ is given by

$$\mu_{Lz} = g_L \mu_B m_l . \tag{2.17}$$

The spin of the electron also imparts an additional magnetic moment

$$\mu_{Sz} = g_s \mu_B m_s , \tag{2.18}$$

where g_s is the electron spin g-factor ($g_s \approx 2.002$), and the spin s is always restricted to ±½ for a fermionic electron. The discrete character of these angular momentum-related quantum numbers is illustrated in Fig. 2.2 (a) - (c). If two or more electrons have the same energy, but different quantum numbers, the electron state is said to be degenerate. In the degenerate case when two electrons (subjected to a bias field) are both characterized by $l = 0$, and m_s is +½ and -½ for each electron respectively, the two electron states are energetically separated by

$$\Delta E = g_e |\mu_B| H_B . \tag{2.19}$$

This is referred to as the Zeeman Effect,[35] whereby a degenerate two-electron system can be split in energy (as shown in Fig. 2.2 (d)) through the application of a magnetic field.

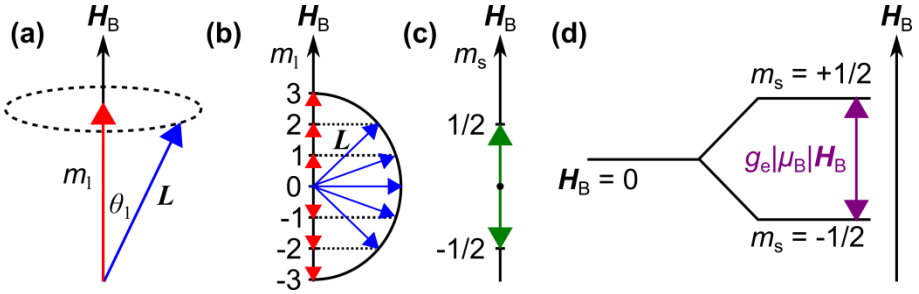

Fig. 2.2 **(a)** Precession of the orbital angular momentum $\boldsymbol{L}$ about the bias field $\boldsymbol{H}_B$. **(b)** Quantization of the magnetic quantum number m_l (the projection of the orbital angular momentum onto $\boldsymbol{H}_B$). **(c)** Quantization of the projection of the spin angular momentum m_s onto $\boldsymbol{H}_B$. **(d)** A schematic of the Zeeman effect.

The net angular momentum $\boldsymbol{J}$ of a light atom is obtained using the Russell-Saunders (L-S) coupling scheme. The orbital and spin angular momentum belonging to all the

electrons are separately summed, giving rise to $\boldsymbol{L} = \sum_i (\boldsymbol{m}_l)_i$ and $\boldsymbol{S} = \sum_i (\boldsymbol{m}_s)_i$, and then these quantities are then combined to yield the net angular momentum $\boldsymbol{J}_{LS} = \boldsymbol{L} + \boldsymbol{S}$. As a consequence, *J* is restricted to have a value within a group of levels

$$J = (L-S), (L-S+1), \ldots, (L+S-1), (L+S). \tag{2.20}$$

Such a group of levels is commonly referred to as a multiplet. The total magnetic moment belonging to an atom is

$$\mu = g_J \mu_B \sqrt{|J(J+1)|}, \tag{2.21}$$

where g_J is the Landé g-factor

$$g_J = 1 + g_s \frac{J(J+1) - L(L+1) + S(S+1)}{2J(J+1)}. \tag{2.22}$$

The projection of the magnetic moment onto the bias field is

$$\mu_z = g_J \mu_B m_J, \tag{2.23}$$

where m_J comprises the multiplet $m_J = -J, (-J+1), \ldots, (J-1), J$.

2.3.2 Quantum mechanical adaptation of the semi-classical models

The theory put forward by Langevin to explain the origin of diamagnetism suffered due to its assumption that the electronic radius was fixed, which cannot be justified on a classical basis. However, the spatial quantization of electronic orbits is a key axiom of quantum-mechanics, and it can be shown that the theory of quantum mechanics yields Eq. 2.8 exactly, for monatomic molecules.[27] The theory of diamagnetism therefore (within the context of this thesis) needs no further refinement.

Qualitatively, the classical theory of paramagnetism is also supported by the spatial quantization introduced by quantum mechanics. In contrast to the theories of diamagnetism and paramagnetism, however, the quantitative model of ferromagnetism requires significant refinement. Following the approach used in Sections 2.2.3 - 2.2.4, therefore, the Langevin theory of paramagnetism will first be refined, from which the Weiss theory of ferromagnetism will be extended.

When a paramagnetic gas is subjected to a magnetic field $\boldsymbol{H}_{\mathrm{B}}$, the net angular momentum vector $\boldsymbol{J}$ (rather than the orbital magnetic moment) precesses about $\boldsymbol{H}_{\mathrm{B}}$, where the projection of the magnetic moment on to $\boldsymbol{H}_{\mathrm{B}}$ is $m_{\mathrm{J}}g_{\mathrm{J}}\mu_{\mathrm{B}}$. The magnetic potential energy is then given by $m_{\mathrm{J}}g_{\mathrm{J}}\mu_{\mathrm{B}}H_{\mathrm{B}}$, and the number of atoms with a particular orientation of the magnetic moment is therefore determined by the Boltzmann factor $\exp\left(m_J g_J \mu_B H_B / k_B T\right)$. The magnetization of the ensemble of atoms is then given by[26]

$$M = N g_J J \mu_B B_J(x), \tag{2.24}$$

where $x = \frac{J g_J \mu_B H_B}{k_B T}$, and $B_J(x)$ is the Brillouin function

$$B_J(x) = \frac{2J+1}{2J}\coth\left(\frac{2J+1}{2J}x\right) - \frac{1}{2J}\coth\left(\frac{x}{2J}\right). \tag{2.25}$$

If all the magnetic moments of the paramagnetic gas align with the bias magnetic field, the total angular momentum quantum number J can assume all values, and so $J \to \infty$. With this condition, the Brillouin function tends towards the Langevin function, and so Langevin's semi-classical model of paramagnetism naturally emerges as a limiting-case of the quantum mechanical model.

The quantum mechanical analogue of the Weiss model of ferromagnetism can then be obtained through applying the transformation $\boldsymbol{H}_B \to \boldsymbol{H}_B + \boldsymbol{H}_{Weiss}$ within the argument of the Brillouin function, such that

$$x = \frac{J g_J \mu_B}{k_B T}\left(H_B + \lambda_{Weiss} \cdot M\right). \tag{2.26}$$

To focus on the regime in which the spontaneous magnetization ($M_s = N J g_J \mu_B$) is present, the bias field $\boldsymbol{H}_{\mathrm{B}}$ is set to zero, therefore allowing Eq. 2.24 and Eq. 2.26 to be written in the forms

$$M = M_s B_J(x), \tag{2.27}$$

and

$$\frac{M}{M_s} = \frac{k_B T}{N \lambda_{Weiss} J^2 {g_J}^2 {\mu_B}^2} x, \tag{2.28}$$

respectively, where

$$x = \frac{Jg_J \mu_B}{k_B T} \lambda_{Weiss} M \,. \tag{2.29}$$

By Taylor expanding the Brillouin function, it can be shown that $B_J(x)\big|_{x\to 0} = \frac{J+1}{3J} x$. The same approach as was used to obtain Eq. 2.11 can then be applied to obtain the quantum mechanical analogue of the Curie temperature T_f

$$T_f = \frac{N\lambda_{Weiss}\mu^2 {g_J}^2}{3k_B} J(J+1). \tag{2.30}$$

Eliminating λ_{Weiss} from Eq. 2.29 and Eq. 2.30 reveals the general equation

$$\frac{M}{M_s} = \frac{J+1}{3J}\left(\frac{T}{T_f}\right) x \,. \tag{2.31}$$

The behaviour of Eq. 2.31 (for finite values of *J*) is shown in Fig. 2.3, alongside typical results acquired from experiment.[36] As can be seen, the curves calculated using $J = ½$ and $J = 1$ agree well with the experimental data, but the best fit of the experimental data is empirically of the form

$$M = M_s\left(1 - \beta T^{3/2}\right), \tag{2.32}$$

where β is a fitting parameter. Eq. 2.32 – commonly referred to as the Bloch Law - will be derived more rigorously in the next section, using the exchange interaction and the theory of magnons.

2.3.3 Exchange interaction

So far, ferromagnetism has been understood in terms of a mean field theory, which extended the Langevin theory of paramagnetism via the introduction of the fictitious Weiss field. Whilst Weiss' theory was adapted in Section 2.3.2 to incorporate quantum mechanical theory, further refinement is required to understand the origin of Eq. 2.32. In addition, the quantum mechanical theory hitherto used has given no insight in to the physical origin of the exceedingly large Weiss field. To therefore account for this field, it is necessary to invoke the exchange interaction.

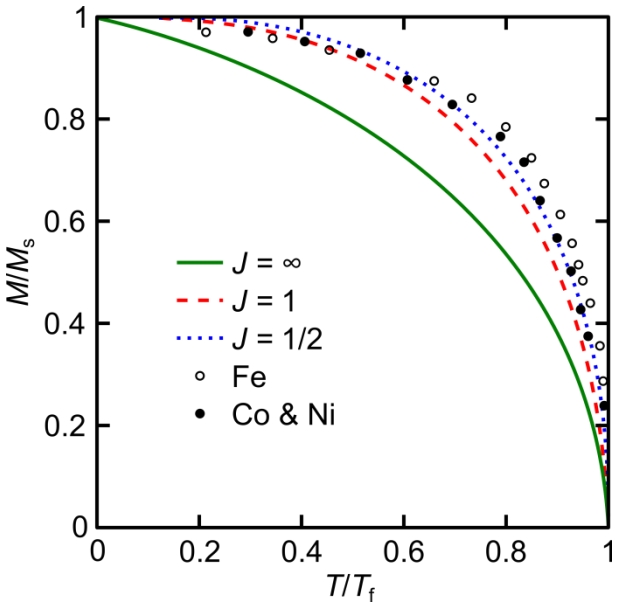

Fig. 2.3 The magnetization of a ferromagnetic substance as a function of temperature, where the curves were calculated using Eq. 2.32 with J as indicated, and the points represent experimental data.[27]

The exchange interaction was first introduced by Heitler and London in 1927, in order to model the binding energy of a hydrogen molecule.[37] In the following year, Werner Heisenberg adapted the Heitler-London model to develop a theory of ferromagnetism,[38] by incorporating spin within the total wave function characterizing a two-electron system. The region of overlap between the two electrons is governed by the Pauli Exclusion Principle, which states that no two electrons with identical quantum numbers can occupy the same quantum state. As a result, the spins belonging to the two electrons must be correlated, giving rise to magnetic order and thus the exchange energy.

The exchange energy can be intuitively understood through considering a non-interacting pair of electrons, each experiencing a known external potential $V(r_1)$ and $V(r_2)$ which is independent of the position of the other. Assuming (naively) that the electrons are distinguishable, the Schrödinger equation characterizing the system of electrons is of the form

$$\left[-\frac{\hbar^2}{2m_e}\left(\nabla_1{}^2+\nabla_2{}^2\right)+V(r_1)+V(r_2)\right]\psi = E\psi\,, \tag{2.33}$$

where the subscripts 1 and 2 refer to either the first or second electron respectively. The solutions of the Schrodinger equation are then given by

$$\psi_a(1)\psi_b(2) \text{and } \psi_a(2)\psi_b(1), \tag{2.34}$$

where, for example, $\psi_a(1)$ is the one-electron wave function describing the situation when electron 1 is in the state *a*. However, in reality, the electrons are indistinguishable, and so the interchanging of the electrons at positions r_1 and r_2 cannot be detected. Thus one can immediately deduce

$$|\psi(1,2)|^2 dr_1 dr_2 = |\psi(2,1)|^2 dr_1 dr_2, \tag{2.35}$$

where $\psi(1,2)$ is the wave function characterizing the pair of elections. This therefore implies that the wave function can be either symmetric

$$\psi(1,2) = +\psi(2,1), \tag{2.36}$$

or antisymmetric

$$\psi(1,2) = -\psi(2,1). \tag{2.37}$$

In order to satisfy Eq. 2.35, the wave function characterizing the two-electron system must be a linear combination of the single-electron wave functions

$$\psi_{symm}(1,2) = \frac{1}{\sqrt{2}}[\psi_a(1)\psi_b(2) + \psi_a(2)\psi_b(1)], \tag{2.38}$$

or

$$\psi_{anti}(1,2) = \frac{1}{\sqrt{2}}[\psi_a(1)\psi_b(2) - \psi_a(2)\psi_b(1)], \tag{2.39}$$

where all the single-electron wave functions have been individually normalized, and the subscripts “symm” and “anti” refer to the net wavefunction being symmetric or antisymmetric respectively.

So far, the electronic wave function has been treated as a function of space only. However, the spin angular momentum also contributes to the wave function. The wave function should therefore be written in the form

$$\psi = \Phi_{space}\chi_{spin}, \tag{2.40}$$

where Φ_{space} is the space-dependent solution to the Schrodinger equation for an electron devoid of spin (therefore described by the quantum numbers n, l and m_l), and the spinor χ_{spin} is a function of the electronic spin (m_s) only. Since $m_s = \pm 1/2$ for an electron, the single-electron spinor can only be $\chi_{\pm 1/2}$. The combination of spinors belonging to the pair of electrons can therefore be understood as being symmetric χ_{spin}^{symm} or antisymmetric χ_{spin}^{anti}, in a similar manner as the spatial wave functions. Now, the Pauli Exclusion Principle directly states that the two-electron wave function must be antisymmetric (the two electrons cannot have identical quantum numbers), and therefore be given by Eq. 2.39. To satisfy this condition, the two-electron wave function must have spatial and spinor parts with opposite symmetry, which can be achieved through the combinations

$$\psi_I = \Phi_{space}^{symm}\chi_{spin}^{anti}, \tag{2.41}$$

or

$$\psi_{II} = \Phi_{space}^{anti}\chi_{spin}^{symm}, \tag{2.42}$$

where the two-electron spinors are given by the linear combination of the single-electron spinors

$$\chi_{spin}^{symm} = \frac{1}{\sqrt{2}}\left[\chi(1)\chi(2) + \chi(2)\chi(1)\right], \tag{2.43}$$

and

$$\chi_{spin}^{anti} = \frac{1}{\sqrt{2}}\left[\chi(1)\chi(2) - \chi(2)\chi(1)\right]. \tag{2.44}$$

When the two electronic spins are antiparallel, the two-electron wave function is in the so-called singlet state

$$\psi_{singlet}(1,2) = A\left[\Phi_a(1)\Phi_b(2) + \Phi_a(2)\Phi_b(1)\right]\cdot\left[\chi_{+1/2}(1)\chi_{-1/2}(2) - \chi_{+1/2}(2)\chi_{-1/2}(1)\right], \tag{2.45}$$

where A is a normalizing constant. Alternatively, the two electronic spins can be parallel, leading to the triplet state, whereby the two-electron wave function can take one of three forms

$$\psi_{triplet}(1,2) = B[\Phi_a(1)\Phi_b(2) - \Phi_a(2)\Phi_b(1)] \cdot \begin{bmatrix} \chi_{+\frac{1}{2}}(1)\chi_{+\frac{1}{2}}(2) \\ \chi_{+\frac{1}{2}}(1)\chi_{-\frac{1}{2}}(2) + \chi_{+\frac{1}{2}}(2)\chi_{-\frac{1}{2}}(1) \\ \chi_{-\frac{1}{2}}(1)\chi_{-\frac{1}{2}}(2) \end{bmatrix}, \tag{2.46}$$

where B is a normalizing constant.

The two-electron system is now extended so as to comprise two hydrogen atoms, constituting a H_2 molecule. The Hamiltonian of the H_2 molecule is defined electrostatically by

$$\hat{H} = \frac{e^2}{|\boldsymbol{r}_{n_2} - \boldsymbol{r}_{n_1}|} + \frac{e^2}{|\boldsymbol{r}_{e_2} - \boldsymbol{r}_{e_1}|} - \frac{e^2}{|\boldsymbol{r}_{n_1} - \boldsymbol{r}_{e_1}|} - \frac{e^2}{|\boldsymbol{r}_{n_2} - \boldsymbol{r}_{e_2}|}, \tag{2.47}$$

where $\boldsymbol{r}_{n_1}$, $\boldsymbol{r}_{n_2}$, $\boldsymbol{r}_{e_1}$ and $\boldsymbol{r}_{e_2}$ is the position of the first and second nuclei, and the position of the electron orbiting the first and second nuclei respectively. By then considering $\hat{H}$ as an electrostatic perturbation of the two-electron system, the energy of the singlet E_{singlet} and triplet E_{triplet} states are given by

$$E_{singlet} = A^2(K + J_{ex}), \tag{2.48}$$

and

$$E_{triplet} = B^2(K - J_{ex}), \tag{2.49}$$

where K is the average Coulombic energy

$$K = \int \Phi_a(1)^* \Phi_b(2)^* H \Phi_a(1)\Phi_b(2) dr_1 dr_2, \tag{2.50}$$

and J_{ex} is the exchange integral

$$J_{ex} = \int \Phi_a(1)^* \Phi_b(2)^* H \Phi_a(2)\Phi_b(1) dr_1 dr_2. \tag{2.51}$$

The exchange interaction is therefore a direct consequence of the indistinguishability of the two electrons. This gives rise to a corresponding exchange energy, equal to the difference in energy between the two-electron systems with parallel and antiparallel spins. This energy, and its associated field, directly accounts for the postulated Weiss field invoked in the semi-classical description of ferromagnetism

For the hydrogen molecule, J_{ex} is negative, and so the spins of the molecule in its ground state are antiparallel. Hydrogen is therefore classified as antiferromagnetic, by which the net magnetization is formed of two sublattices of magnetization, both equal in magnitude but antiparallel in orientation.[39] In contrast, a ferromagnetic material requires that J_{ex} be positive.* This property can be qualitatively understood by considering the spatial wave functions Φ_a and Φ_b to be wholly positive in the region of appreciable electronic overlap. Consequently, J_{ex} is positive if

$$\frac{e^2}{\left|\boldsymbol{r}_{n_2}-\boldsymbol{r}_{n_1}\right|}+\frac{e^2}{\left|\boldsymbol{r}_{e_2}-\boldsymbol{r}_{e_1}\right|}>\frac{e^2}{\left|\boldsymbol{r}_{n_1}-\boldsymbol{r}_{e_1}\right|}+\frac{e^2}{\left|\boldsymbol{r}_{n_2}-\boldsymbol{r}_{e_2}\right|}, \tag{2.52}$$

which physically states that the repulsion between the nuclei and between the electrons is stronger than the attraction between the nuclei and their associated uncompensated electrons. Such a circumstance occurs when the distance between neighbouring atoms in the crystal is less than the distance between the nuclei and the uncompensated electrons. This is characteristic of iron, cobalt and nickel, and also rare-earth elements, as shown in Fig. 2.4.

Importantly, the exchange interaction indicates that ferromagnetism originates not from atomic properties, but rather from electronic structures. This therefore possibly explains, through the modification of interatomic distances, how some substances (including, for example, Chromium-based compounds[40] and the class of Heusler alloys[41-42]) can be ferromagnetic, despite all the constituent elements of the substance not being ferromagnetic.

* It is important to note that the description of the exchange interaction given here corresponds to the simplest system possible (a hydrogen molecule). For more complicated multi-electronic system, the above approach of calculating the spin coupling (based on the Heitler-London model) is fundamentally inadequate.[27] The question of deriving from first principles more general values of J_{ex} is still unresolved.

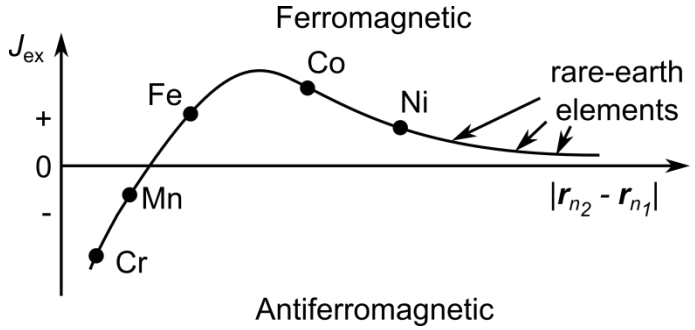

Fig. 2.4 The variation of the exchange integral as a function of the interatomic distance $\left|\boldsymbol{r}_{n_2} - \boldsymbol{r}_{n_1}\right|$, corresponding to the Bethe-Slater curve.[43] The exchange integrals belonging to several magnetic elements are indicated.

2.3.4 Magnons and exchange spin waves

The concept of a quantum mechanical spin wave was first introduced by Felix Bloch in 1930.[44] This primitive excitation of magnetization can be understood by considering a ferromagnetic substance at absolute zero as a one-dimensional chain of spins, extending to infinity. As there is no thermal agitation, the spins are all aligned parallel to the axis of quantization (for the sake of argument here, pointing upwards), therefore defining the ground state of the system with an energy given by the Heisenberg Hamiltonian

$$H_{Heisenberg} = -2\sum_{i,j}\left(J_{ex}\right)_{i,j}\boldsymbol{S}_i \cdot \boldsymbol{S}_j \,. \tag{2.53}$$

where $\boldsymbol{S}_{i,j}$ are adjacent spins. Now, the temperature is raised very slightly, so as one spin is flipped. The exchange interaction will seek to parallelize all the spins, and so the flipped spin will revert back to pointing upwards, but at the cost of flipping its neighbouring spin. This spin-flipping will then propagate across the chain of spins, giving rise to a propagating spin wave. Using Eq. 2.53, and assuming that the exchange integral J_{ex} is spatially uniform, it is possible to derive a dispersion relation for exchange spin waves[27]

$$\omega = J_{ex}a^2 \cdot k^2 \,, \tag{2.54}$$

whereby the exchange spin wave (of frequency ω and wave vector k) propagates across a simple cubic lattice (of lattice constant a). Because spin waves, on a quantum level, are propagating packets of flipped spins, they are referred to as magnons, analogous to photons and phonons. As with all particles, magnons have an associated energy E_k and momentum p_k.

Since the chain of spins is symmetric in energy with regard to the interchanging of two reversed spins, magnons are classified as bosons, and therefore are described by Bose-Einstein statistics. Furthermore, since there is no limit on the total number of spin waves that can propagate across the chain of spins, magnons are wholly degenerate. Their energy is quantized in terms of the discrete vibrational quantum number n_k

$$E = n_k \cdot \hbar\omega_k , \tag{2.55}$$

and the average value of the vibrational quantum number ($\bar{n}_k$) at a particular temperature is given by the Bose-Einstein distribution

$$\bar{n}_k = \frac{1}{e^{E_k/k_B T} - 1} . \tag{2.56}$$

The magnons can also be understood semi-classically, whereby the chain of N spins are classical vectors S, each capable of precessing about the upward-pointing axis of quantization. In the ground state, all the spin vectors (of length $M(T=0)$, where M is a function of temperature) are pointing upwards. Now, upon introducing slight thermal agitation, the spin, instead of being flipped, is instead slightly canted from the axis of quantization. This spin vector will then precess, inducing (via exchange coupling) the neighbouring spin to also cant and precess, albeit with a lag in phase. In this fashion, the spin wave consists of a phase-coherent collective precession of spin vectors, with a dispersion given by[27]

$$\omega = 2J_{ex}\left[1 - \cos(ka)\right]. \tag{2.57}$$

By Taylor expanding Eq. 2.57 for small k, one can obtain Eq. 2.54, indicating that both the quantum and semi-classical descriptions of exchange spin waves are consistent, and can be used interchangeably.

2.3.5 Quantum model of ferromagnetism

At the end of Section 2.3.2, it was highlighted that Weiss's theory of ferromagnetism, with quantum mechanical refinement, was unable to account for the Bloch Law, which best described the results presented in Fig. 2.3. In order to reveal the origin of Eq. 2.32, it is necessary to invoke the theory of magnons. The total number of magnons $n_{magnons}$ across a

chain of spins is found by summing $\bar{n}_k$ across all the *k*-states supported by the system. Now, the number of states within an infinitesimally small wave vector range *dk* is given by

$$D(k)dk = \frac{dV_k}{V_k}, \tag{2.58}$$

where $D(k)$ is the density of states, $dV_k = 4\pi k^2 dk$ is the volume of a spherical shell in reciprocal space, and $V_k = (2\pi/L)^3$ is the volume of a single state (of side-length *L*). Using the magnonic dispersion relation (Eq. 2.54), Eq. 2.58 can be reformulated in terms of energy

$$D(E)dE = \frac{V_k}{4a^3\pi^2 J_{ex}^{3/2}} E^{1/2} dE, \tag{2.59}$$

where *D*(*E*) is the density of states in terms of energy. Integrating both sides of Eq. 2.59 leads to the equation

$$n_{magnons} = \frac{V_k}{4a^3\pi^2 J_{ex}^{3/2}} \int_0^\infty \frac{E^{1/2}}{e^{E/k_B T} - 1} dE, \tag{2.60}$$

and by making the substitution $x = E/k_B T$, Eq. 2.60 can be solved through a series expansion to reveal[27]

$$n_{magnons} = 0.1174 V_k \left(\frac{k_B T}{a^2 J_{ex}} \right)^{\frac{3}{2}}. \tag{2.61}$$

Now, the excitation of spin-flipping magnons corresponds to a change in the net magnetization, given by

$$\frac{\Delta M}{M(0)} = \frac{M(0) - M(T)}{M(0)} = \frac{n_{magnons}}{N}, \tag{2.62}$$

and so it is possible to show[27]

$$M = M_s \left(1 - 0.1174 V_k \left(\frac{k_B T}{N a^2 J_{ex}} \right)^{\frac{3}{2}} \right). \tag{2.63}$$

This is the more complete form of the Bloch Law,[45] and successfully describes the experimentally-observed thermal dependence of magnetization. This therefore indicates that the quantum-mechanical description of exchange energy and exchange spin waves successfully describes the temperature-dependent behaviour of ferromagnetic substances.

2.3.6 Superexchange interaction, and ferrimagnetism

While the exchange interaction is able to explain the phenomena of ferromagnetism and antiferromagnetism (J_{ex} being positive and negative respectively), there are further exchange-related interactions that need to be used in order to explain the magnetic behavior of more complex crystalline structures. Manganese Oxide, for example, is observed to possess antiferromagnetic order, despite the fact that the antiferromagnetically-coupled Mn^{2+} ions are separated by a diamagnetic O^{2-} ion. To explain this behavior, Hendrik Kramers proposed in 1934 the superexchange interaction,[46] which was refined by Phillip Anderson in 1950.[47]

The superexchange interaction is most commonly explained through the interaction of the four free electrons within Mn_2O. The ground state of this molecule consists of two Mn^{2+} and one O^{2-} ions arranged adjacently. The electron in the leftmost Manganese ion has a particular spin (for the sake of argument, up). This compels, via the exchange interaction, the overlapping electron belonging to the neighbouring Oxygen ion to have antiparallel spin (down). The second electron in Oxygen then aligns up, inducing (again via the exchange interaction) the neighbouring electron belonging to the Manganese ion to have downward spin. The Oxygen, in short, serves as an intermediary for the exchange interaction, allowing the said interaction to act across larger distance (hence the term "superexchange").

The superexchange interaction, in Manganese Oxide, gives rise to antiferromagnetic order. However, if the two antiferromgnetically-coupled ions bridged by the intermediary have different spin, net magnetic order can be generated. This leads to the class of magnetic materials termed ferrimagnets. A ferrimagnetic substance consists of two sublattices of magnetization, where both sublattices have a difference in strength, and are oriented antiparallel to each other (as dictated by the superexchange interaction). One example of this material, which is discussed frequently throughout this thesis, is YIG (Ytrrium Iron Garnet). The properties and character of this material will be discussed in more depth in Section 2.5.2.

2.4 Energetics of a ferromagnetic system

The static and dynamic behavior of a ferromagnetic system is governed by a variety of competing interactions, all seeking to contribute towards the minimization of the total free energy density w of the magnetized system. In equilibrium, the static magnetization $\boldsymbol{M}_0$ of a ferromagnetic system is given by Brown's differential equation[48]

$$\boldsymbol{M}_0 \times \boldsymbol{H}_{eff,0} = 0\,, \tag{2.64}$$

where $\boldsymbol{H}_{eff,0}$ is the static effective magnetic field, defined as the functional derivative of the free energy density with respect to the magnetization[28]

$$\boldsymbol{H}_{eff,0} = -\frac{\delta w}{\delta \boldsymbol{M}}\,. \tag{2.65}$$

The free energy density is composed of the energy densities associated with all the magnetic interactions existing within the magnetic system. By therefore considering the free energy associated with each magnetic interaction, the total free energy can be split into its constituent parts

$$U = U_{Zee} + U_{ex} + U_{demag} + U_{ani} + U_{other}, \tag{2.66}$$

where U_{Zee}, U_{ex}, U_{demag} and U_{ani} are the energies of the Zeeman, exchange, demagnetizing and magneto-crystalline anisotropic contributions respectively. The final term U_{other} represents the contribution from all other magnetic interactions, originating from (for example) magnetoelasticity[49] or Dzyaloshinskii-Moriya coupling.[50] In the following sections, the Zeeman, exchange, magneto-dipole and crystalline anisotropy energies will be discussed in turn.

2.4.1 Zeeman energy

Upon application of an external magnetic field, the magnetization of paramagnetic and ferromagnetic media will tend to align parallel to the external bias, in order to minimize the potential energy of the permanent magnetic moments – this potential energy is referred to as the Zeeman energy. The Zeeman energy is given by

$$U_{Zee} = -\boldsymbol{M}(\boldsymbol{r},t)\cdot \boldsymbol{H}_B(\boldsymbol{r},t). \tag{2.67}$$

2.4.2 Exchange energy

As was discussed in Section 2.3.3, ferromagnetic substances possess spontaneous magnetization due to the quantum mechanical exchange interaction, which originates from the difference in energy between the parallel and antiparallel alignment of two coupled spins. By considering the j^{th} spin to be misaligned from the immediately-adjacent i^{th} spin by an angle θ_{ij}, the exchange energy (defined in Eq. 2.53) is given by

$$U_{ex} = -2J_{ex}M_s{}^2\sum_j \cos\theta_{ij} \ . \tag{2.68}$$

By assuming the neighboring spins are only slightly canted relative to each other, Eq. 2.68 can be expanded as a series, hence revealing[27]

$$U_{ex} = 2J_{ex}M_s{}^2a^2\left[(\nabla M_x)^2 + (\nabla M_y)^2 + (\nabla M_z)^2\right], \tag{2.69}$$

across a cube of side-length a. Using the vector identity

$$\left[(\nabla u_x)^2 + (\nabla u_y)^2 + (\nabla u_z)^2\right] + \left(\boldsymbol{u}\cdot\nabla^2\boldsymbol{u}\right) = 0, \tag{2.70}$$

Eq. 2.69 can be rewritten as

$$U_{ex} = \frac{-2J_{ex}a^2}{M_s{}^2}\boldsymbol{M}\cdot\nabla^2\boldsymbol{M}\,, \tag{2.71}$$

giving rise to the exchange energy density

$$w_{ex} = -\frac{2J_{ex}}{aM_s{}^2}\boldsymbol{M}\cdot\nabla^2\boldsymbol{M}\,. \tag{2.72}$$

This then leads to the convenient definition[51] of the exchange field

$$\boldsymbol{H}_{ex} = \frac{D}{M_s}\nabla^2\boldsymbol{M}\,, \tag{2.73}$$

where $D = 2A_{ex}/M_s$ is the exchange stiffness, and $A_{ex} = J_{ex}/a$ is the exchange constant.

An important point concerning the exchange field relates to its range of influence. As indicated in Fig. 2.4, the term J_{ex} rapidly shrinks for increasing interatomic distances. The exchange interaction therefore acts predominantly across length scales on the order of several nanometres. To quantify the spatial extent across which the exchange interaction dominates, the exchange length is given by[52]

$$l_{ex} = \sqrt{\frac{A_{ex}}{2\pi M_s{}^2}} \,. \tag{2.74}$$

The exchange length is invariably on the nanometric scale. For example, the material parameters of Permalloy (A_{ex} = 1.3 μerg / cm, M_s = 800 G) and YIG (A_{ex} = 0.3 μerg / cm, M_s = 140 G) lead to an exchange length of 5.7 nm and 15.6 nm respectively.[52]

2.4.3 Dipolar energy

The interaction between the magnetic dipoles of atoms is described by the magnetodipole (or dipolar) interaction. The magnetic field $\boldsymbol{H}_{\text{dipole,i}}$ generated by an isolated dipole moment $\boldsymbol{\mu}_i$, measured at a point $\boldsymbol{r}$ relative to the moment's position $\boldsymbol{r}_i$, is of the form[28]

$$\boldsymbol{H}_{dipole,i}(\boldsymbol{r}) = \frac{1}{r^3}\left[-\boldsymbol{\mu}_i + \frac{3}{r^2}\boldsymbol{r}(\boldsymbol{\mu}_i \cdot \boldsymbol{r})\right]. \tag{2.75}$$

If a second dipole moment $\boldsymbol{\mu}_j$ is positioned at a second point $\boldsymbol{r}_j$, and $\boldsymbol{r}$ is now the distance between the two moments $\boldsymbol{r} = \boldsymbol{r}_j - \boldsymbol{r}_i$, the dipolar energy E_{dipole} between the two dipoles is given by

$$E_{dipole}(\boldsymbol{\mu}_i, \boldsymbol{\mu}_j, \boldsymbol{r}) = \frac{1}{r^3}\left[-\boldsymbol{\mu}_i \cdot \boldsymbol{\mu}_j + \frac{3}{r^2}(\boldsymbol{\mu}_i \cdot \boldsymbol{r})(\boldsymbol{\mu}_j \cdot \boldsymbol{r})\right]. \tag{2.76}$$

To obtain the dipolar energy between more than two magnetic moments, Eq. 2.76 merely needs to be summed across all dipole-dipole pairs.

Across a uniformly-magnetized sample, spatially extending to infinity in all three dimensions, the dipolar fields created by all the moments compensate and therefore annul each other. However, upon introducing discontinuity across the magnetic system (through, for example, finite volume or magnetic inhomogeneities), such compensation is lost, and net dipolar fields are induced. Inside and outside the magnetic body, this dipolar field is referred to as either the demagnetizing field or the stray field respectively. To describe further the influence of the static demagnetizing field $\boldsymbol{H}_{\text{demag}}$, the Maxwell equations[53] need to be considered

$$\nabla \cdot \boldsymbol{E} = 4\pi\rho\,, \tag{2.77}$$

$$\nabla \cdot \boldsymbol{B} = 0\,, \tag{2.78}$$

$$\nabla \times \boldsymbol{E} = -\frac{1}{c}\frac{\partial \boldsymbol{B}}{\partial t}\,, \tag{2.79}$$

$$\nabla \times \boldsymbol{B} = \frac{4\pi}{c}\boldsymbol{J} + \frac{1}{c}\frac{\partial \boldsymbol{E}}{\partial t}\,, \tag{2.80}$$

where $\boldsymbol{E}$ and $\boldsymbol{B}$ are the electric and magnetic fields respectively, ρ is the electric charge density, and $\boldsymbol{J}$ is the electric current density. Since dipolar spin waves have a much smaller frequency compared to light (for the same wave vector), one can employ the magnetostatic approximation, leading to the magnetostatic Maxwell equations (in the absence of a current density)

$$\nabla \cdot \boldsymbol{B} = \nabla \cdot \left(\boldsymbol{H}_{demag} + 4\pi\boldsymbol{M}\right) = 0\,, \tag{2.81}$$

$$\nabla \times \boldsymbol{H}_{demag} = 0\,. \tag{2.82}$$

From Eq. 2.82, the rotationless demagnetizing field can be defined as the gradient of a magnetostatic scalar potential Ψ, via $\boldsymbol{H}_{demag} = -\nabla\Psi$. This gives rise to the magnetostatic Poisson equation

$$\nabla^2\Psi = \nabla \cdot \left(4\pi\boldsymbol{M}\right) \equiv -\beta\,, \tag{2.83}$$

where β is a "fictitious" magnetic charge density. It is important to note that Eq. 2.78 implies that no magnetic monopoles can exist – hence magnetic charges are "fictitious" - but the concept of magnetic charges frequently lends itself well to the qualitative description of magnetic phenomena.

The magnetic charge density can be separated into its volumetric contributions $\beta_v = -\nabla \cdot \boldsymbol{M}$ (arising from nonuniformities in the magnetization strength or orientation) and surface contributions $\beta_s = \boldsymbol{M} \cdot \hat{\boldsymbol{n}}$ (originating from the magnetization having non-zero projection onto the outward-pointing vector $\hat{\boldsymbol{n}}$ normal to the sample surface). For a magnetic body of finite volume, therefore, Eq. 2.83 can be solved to obtain[28]

$$\Psi(\boldsymbol{r}) = -\int \frac{\beta_v}{|\boldsymbol{r}' - \boldsymbol{r}|}\, d^3r' + \int \frac{\beta_s}{|\boldsymbol{r}' - \boldsymbol{r}|}\, d^2r'\,. \tag{2.84}$$

Across the volume of a sample, the demagnetizing field generally attempts to align antiparallel to the magnetization. At the edges of the sample, the magnetization will seek to minimise the strength of energetically-expensive stray fields, and so will attempt to align parallel to the edges. The latter contribution leads to a tendency for magnetization to align parallel to the long axis of a magnetic stripe - this is commonly referred to as shape anisotropy.

In general, the space-dependent demagnetizing field is difficult to calculate. However, for the special case of a uniformly-magnetized ellipsoid, the distributions of the magnetization and demagnetizing field are both uniform. The latter has no volumetric contribution, leading to the expression

$$\boldsymbol{H}_{demag} = -\nabla\left(\int \frac{\boldsymbol{M}\cdot\hat{\boldsymbol{n}}}{|\boldsymbol{r}'-\boldsymbol{r}|}\,d^2r'\right). \tag{2.85}$$

Since the demagnetizing field depends linearly on the magnetization, one can therefore define

$$\boldsymbol{H}_{demag} = -\vec{\vec{N}}\boldsymbol{M}\,, \tag{2.86}$$

where $\vec{\vec{N}}$ is the demagnetizing tensor. The demagnetizing tensor is defined entirely by the shape of the magnetic body, and has a trace of 4π. When the principal axes of $\vec{\vec{N}}$ coincide with the principal axes of the ellipsoid, the off-diagonal elements of $\vec{\vec{N}}$ are zero. By extending the ellipsoid to construct certain geometries, one can analytically calculate the diagonal elements of $\vec{\vec{N}}$ - typical examples of special ellipsoidal shapes, and their corresponding demagnetizing tensor elements, are shown in Table 2.2.

Geometry	N_{xx}	N_{yy}	N_{zz}
Sphere	1/3	1/3	1/3
Cylinder extending along *z*-axis	1/2	1/2	0
Film extending across *x*-*y* plane	0	0	1

Table 2.2 The diagonal elements of the demagnetizing tensor characterizing well-defined ellipsoidal geometries (magnetized uniformly along the *z*-axis). Note all elements shown here have been normalized by 4π.

In addition to the demagnetizing tensor elements shown in Table 2.2, the elements of the demagnetizing tensor associated with uniformly-magnetized ellipsoidal bodies - with

semi-principal axes of general length - have been numerically calculated.[54] In the general case, however, for non-ellipsoidal samples, the demagnetizing tensor is impossible to analytically determine, and micromagnetic simulations offer the only way for the strength and distribution of real demagnetizing fields to be reasonably estimated. Due to the demagnetizing field, the magnetization within a sample is not exposed to solely the bias magnetic field - a useful measure of the net field generated within a patterned magnetic sample is therefore given by the internal field $\boldsymbol{H}_{\mathrm{i}}$

$$\boldsymbol{H}_i = \boldsymbol{H}_B + \boldsymbol{H}_{demag}. \tag{2.87}$$

2.4.4 Magneto-crystalline anisotropic energy

Across an infinitely-large magnetic body, the magnetization is free to align along any nominated direction, as dictated by the orientation of the bias field and / or the magnetic history of the sample. By confining the body in some way, it is possible to introduce shape anisotropy. In addition to this, the spin-orbit interaction directly links the lattice of magnetization to the sample's crystalline lattice, and so it is possible for the magnetization to tend to align parallel or orthogonal to certain crystallographic axes, regardless of the sample's shape. If the magnetization tends to align parallel (orthogonal) to a certain axis, this is referred to as an easy (hard) axis. This effect is known as magneto-crystalline anisotropy, and can be detected and measured by applying a bias field along a certain direction of a magnetic body, and measuring the magnetization that is projected onto the bias field.[27] The energy that is associated with magneto-crystalline anisotropy can be phenomenologically expressed as a power series of the magnetization, which must be even due to symmetry considerations. For example, a crystal boasting uniaxial magneto-crystalline anisotropy (of strength K_1 and orientation $\hat{\boldsymbol{n}}$) has an energy term

$$U_{ani} = K_1 \sin^2 \theta, \tag{2.88}$$

where θ is the angle extended between the magnetization and $\hat{\boldsymbol{n}}$.

2.5 Material properties and character of Permalloy and YIG

In this thesis, the studied samples are composed of either Permalloy or YIG. In the following two sections, therefore, I will discuss the properties of these materials.

2.5.1 Permalloy

Permalloy consists of a Nickel-Iron alloy, both constituent elements of which have cubic structure. The properties of this metallic material vary considerably, depending on the relative concentrations of the two elements. If the Nickel content is below 30%, Permalloy has body-centred cubic crystalline structure, whereas if it is above, Permalloy has instead face-centred cubic (fcc) crystalline structure.

While the Permalloy discussed throughout this thesis has fcc crystalline structure, the magnetic properties of the alloy still depends heavily on the ratio of the elements. Pure Nickel (Iron) has a saturation magnetization of 488 G (1713 G) at room temperature,[55] and so $Ni_{80}Fe_{20}$ – the alloy that was nominally studied in this thesis – has a weighted average saturation magnetization of 733 G. The large gap between $M_{s,Ni}$ and $M_{s,Fe}$ makes $M_{s,Py}$ sensitive to the ratio of the Nickel and Iron elements. $Ni_{75}Fe_{25}$, for example, has a weighted average saturation magnetization of 795 G. For this reason, the saturation magnetization of Permalloy (the generic alloy) quoted in the scientific literature varies between 700 G and 860 G.[56-57] The ratio of the Nickel and Iron elements also influences significantly the magnetostriction and magnetocrystalline anisotropy of Permalloy.[58] Magnetostriction refers to the phenomenon where a stress / strain applied to a magnetic material gives rise to a magnetostrictive anisotropy. For a cubic material, the magnetostrictive constant is given by λ_{100} and λ_{111}, which defines the response to stress applied along the [100] and [111] crystal axes respectively.[†] In Nickel, $\lambda_{100} = -46\times10^{-6}$ and $\lambda_{111} = -25\times10^{-6}$, and for Iron, $\lambda_{100} = 21\times10^{-6}$ and $\lambda_{111} = -22\times10^{-6}$. In Permalloy where the Nickel content ranges from 30% to 100%, the magnetostriction coefficients range between $+40\times10^{-6}$ and -60×10^{-6}. In the special case of $Ni_{80}Fe_{20}$, both magnetostriction coefficients become close to zero. As for the cubic magnetocrystalline anisotropy of Permalloy, the leading anisotropy constant K_1 ranges between $+20\times10^{-6}$ ergs/ cm and -60×10^{-6} ergs / cm, when the percentage of Ni varies between 30% and 100%. Again, K_1 passes through zero for the special case of $Ni_{80}Fe_{20}$.

Permalloy is typically characterized as having an exchange constant of 1.3 μerg / cm, and a gyromagnetic ratio of 2.92 MHz / Oe.[59] An important property of Permalloy, relevant to investigations of magnetization dynamics, concerns its damping. In Permalloy, the Gilbert damping parameter is about 0.008, causing spin waves to propagate across distances on the

[†] If $\lambda > 0$, the induced magnetization aligns parallel to the applied strain, whereas if $\lambda < 0$, the induced magnetization aligns orthogonally to the applied strain.

order of 10 μm. While Permalloy is metallic, making it suitable for integration within convential CMOS-based computational architecture, the damping certainly needs to be reduced further, in order to make magnonic technology more viable. Very recently, progress has been reported in further reducing this parameter in the metallic alloy $Fe_{75}Co_{25}$,[60-61] and so it could be anticipated, perhaps, that future research in the field of magnonics may shift towards using $Fe_{75}Co_{25}$ instead as the material of choice, rather than Permalloy.

2.5.2 YIG

YIG – Yttrium Iron garnet ($Y_3Fe_5O_{12}$) – posseses a wide range of magnetic properties which render it extremely useful for investigations of magnetization dynamics.[62] It is a ferrimagnetic monocrystalline material, which entirely owes its magnetization to the Fe^{3+} ions, since Y^{3+} and Oxygen are both diamagnetic.[63] Per unit cell, of lattice constant 12.376 Å, there are 80 atoms, twenty of which are Fe^{3+} ions. The Fe^{3+} ions form two distinct sub-lattices (octahedral and tetrahedral structures), with different configurations of neighbouring O^{2+} ions - these Oxygen ions are responsible for the superexchange interaction that exists in YIG. The octahedral (tetrahedral) sublattice hosts eight (twelve) Fe^{3+} ions. The two sublattices of Iron have magnetization oriented antiparallel to one other, and so are partially compensated, giving rise to a net magnetic moment.

Electrically. YIG has a rather large band gap (about 2.9 eV), making it a dielectric. This, unfortunately, has the disadvantage of making it incompatible with current semiconductor-based CMOS technology. Due to it being ferrimagnetic, YIG has a substantially smaller saturation magnetization compared to Permalloy. At room temperature, $M_{s,YIG}$ = 140 G. The exchange constant[64] of YIG is about 0.3 μerg / cm, giving rise to an exchange length of about 16 nm. It has a gyromagnetic ratio of 2.810 MHz / Oe, and and no significant crystalline anisotropy. Arguably the most important property of YIG lies in its low damping of spin waves. The Gilbert damping parameter (linewidth) of YIG is on the order of 1×10^{-4} (0.5 Oe), allowing spin waves to propagate along distances on the order of centimeters, and to have a lifetime of 100s of nanoseconds.

2.6 Magnetization dynamics

In the following sections, I will discuss the equations that characterize the dynamic behavior of a magnetic system. The information given here lends heavily from the textbook written by Gurevich and Melkov[65] and the review article written by Lock.[66]

2.6.1 Equations of motion

The dynamical behavior of magnetization within a ferromagnetic material is described by the Landau-Lifshitz (LL) equation[67]

$$\frac{\partial \boldsymbol{M}(\boldsymbol{r},t)}{\partial t} = -\gamma \boldsymbol{M}(\boldsymbol{r},t) \times \boldsymbol{H}_{eff} + \boldsymbol{R}\,, \tag{2.89}$$

where $\boldsymbol{R}$ corresponds to a damping term. This equation of motion was first proposed by Lev Landau and Evgeny Lifshitz in 1935. Further terms can be added to the right-hand side of Eq. 2.89, to describe (for example) thermal fluctuations[68-72] and spin-transfer torque,[73-74] but in this thesis no such additions are considered. Moreover, the effective field, defined in Eq. 2.65, can also be understood as the vector sum of all the fields interacting with the magnetization. This therefore leads to the alternative definition of the effective field

$$\boldsymbol{H}_{eff} = \boldsymbol{H}_{Zee} + \boldsymbol{H}_{exc} + \boldsymbol{H}_{demag} + \boldsymbol{H}_{anisotropy} + \boldsymbol{H}_{other}\,. \tag{2.90}$$

For simplicity, considering the case where damping is absent (so $\boldsymbol{R}$ = 0 in Eq. 2.89), the magnetization will precess indefinitely about the effective field. This situation is shown in Fig. 2.5 (a), where the tangential velocity as defined by Eq. 2.89 is indicated.

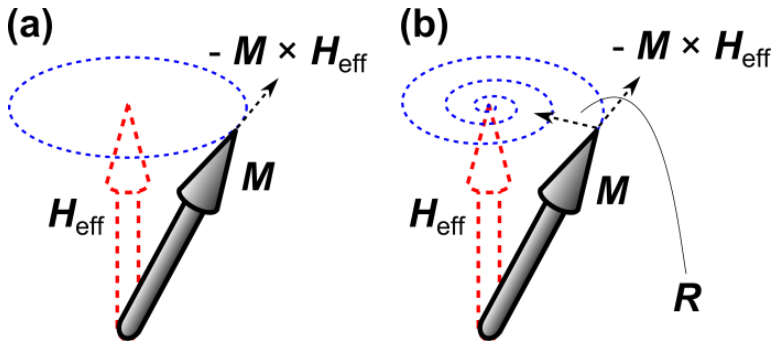

Fig. 2.5 Graphical representations of the magnetization trajectory as dictated by the Landau-Lifshitz equation **(a)** with no damping, and **(b)** with a phenomenological damping term $\boldsymbol{R}$ included.

In real systems, the magnetization will be unable to precess indefinitely, due to damping. In general, the damping of magnetization precession involves the transfer of energy from the spin bath to the phononic and electronic baths.[75] This can be mediated, for example, by magneto-elastic coupling,[76-77] scattering of spin waves from electrons,[78] and the generation

of eddy currents.[79] In lieu of a microscopic understanding of such dissipation mechanisms, Landau and Lifshitz introduced in 1935 the damping term

$$\boldsymbol{R}_{LL} = -\frac{\lambda}{{M_S}^2}\left(\boldsymbol{M}(\boldsymbol{r},t)\times\left[\boldsymbol{M}(\boldsymbol{r},t)\times\boldsymbol{H}_{eff}\right]\right), \tag{2.91}$$

where λ is a phenomenological coefficient. This vector triple product directs the magnetization towards the axis defined by the effective field, causing the magnetization to spiral inwards towards the effective field (as shown in Fig. 2.5 (b)) until eventually the magnetization is both static and parallel to the effective field.

The damping term introduced by Landau and Lifshitz, however, suggested that the frequency of precession scaled positively as λ increased, which is unphysical.[80] So, in 1955, Thomas Gilbert[81] derived the Landau-Lifshitz equation using Lagrangian mechanics, and obtained the damping term

$$\boldsymbol{R}_{LLG} = \frac{\alpha}{M_S}\boldsymbol{M}(\boldsymbol{r},t)\times\frac{\partial\boldsymbol{M}(\boldsymbol{r},t)}{\partial t}, \tag{2.92}$$

where α is the Gilbert damping coefficient. It is straightforward to show that the two damping terms R_{LL} and R_{LLG} are equivalent, as $\alpha \to 0$.[75] However, more importantly, the Gilbert damping term results in the physically more plausible scenario where the precessional frequency tends towards zero as $\alpha \to \infty$.

2.6.2 Free magnetization oscillations

The Landau-Lifshitz-Gilbert equation is generally non-linear, due to the dependence of the demagnetizing, anisotropy and exchange fields on the magnetization.[82] This gives rise to a wide variety of non-linear phenomena (including, for example, the formation of spin-wave solitons[83] and spin-wave bullets,[84] and high harmonic generation[23]), all of which are united by the cone angle of the precessing magnetization being relatively large. The majority of the work presented in this thesis stays within the linear regime, however, where the cone angle of the dynamic magnetization is small, and so this section is restricted to the discussion of linear spin dynamics. To describe such dynamics, the Landau-Lifshitz-Gilbert equation is linearized, by considering only the influence of small time-varying perturbations to the static magnetization and effective magnetic field. This allows one to separate the magnetization and effective magnetic field into their static and dynamic parts

$$\boldsymbol{M} = \boldsymbol{M}_0(\boldsymbol{r}) + \boldsymbol{m}(\boldsymbol{r},t), \tag{2.93}$$

$$\boldsymbol{H}_{eff} = \boldsymbol{H}_{eff,0}(\boldsymbol{r}) + \boldsymbol{h}_{eff}(\boldsymbol{r},t), \tag{2.94}$$

where $h_{eff} << H_{eff,0}$ and $m << M_0$. Note that the co-ordinate system to be used henceforth is transformed such that $\boldsymbol{H}_{eff,0} = H_{eff,0}\hat{\boldsymbol{z}}$ and $\boldsymbol{M}_0 = M_0\hat{\boldsymbol{z}}$.

The dynamic terms within Eqs. 2.93 - 2.94 are assumed to have components only in the *x*-*y* plane. It is of course possible to consider dynamics along the *z*-axis, parallel to the static magnetization: physically, this corresponds to the variation in the modulus of the magnetization (which can be achieved through heating[85-86] of the magnetic body, for example), and can be characterized by the Landau-Lifshitz-Baryakhtar[87] or Bloch-Bloembergen[88] equations, among others. In this section, however, it will be assumed that there is no variation in the magnetization along the *z*-axis, and so $\boldsymbol{M}_0 = M_s\hat{\boldsymbol{z}}$. Furthermore, it will be assumed that the system is dissipationless, which will simplify the following treatment. The influence of non-zero damping will be discussed later on.

Substituting Eqs. 2.93 - 2.94 into the LL equation yields

$$\frac{\partial(\boldsymbol{M}_0 + \boldsymbol{m})}{\partial t} = -\gamma\left[\boldsymbol{M}_0 \times \boldsymbol{H}_{eff,0} + \boldsymbol{M}_0 \times \boldsymbol{h}_{eff} + \boldsymbol{m} \times \boldsymbol{H}_{eff,0} + \boldsymbol{m} \times \boldsymbol{h}_{eff}\right]. \tag{2.95}$$

In the zeroth approximation, where only zero-order (static) terms are retained, Eq. 2.95 reduces to $\boldsymbol{M}_0 \times \boldsymbol{H}_{eff,0} = 0$. This merely reiterates that the static magnetization is parallel to the static effective field, when the system is in its ground equilibrium state. In the first approximation, the first-order dynamic components of Eq. 2.95 are retained, which leads to the equation

$$\frac{\partial \boldsymbol{m}}{\partial t} = -\gamma \boldsymbol{M}_0 \times \boldsymbol{h}_{eff} - \gamma \boldsymbol{m} \times \boldsymbol{H}_{eff,0}. \tag{2.96}$$

The dynamic components of the magnetization and effective field are now assumed to have temporal plane-wave solutions, such that $\boldsymbol{m}(\boldsymbol{r},t) = \boldsymbol{m}(\boldsymbol{r})\exp(i\omega t)$ and $\boldsymbol{h}(\boldsymbol{r},t) = \boldsymbol{h}(\boldsymbol{r})\exp(i\omega t)$. This leads to

$$i\omega \boldsymbol{m} = -\gamma \boldsymbol{M}_0 \times \boldsymbol{h}_{eff} - \gamma \boldsymbol{m} \times \boldsymbol{H}_{eff,0}. \tag{2.97}$$

The effective field can also be separated further in terms of the Zeeman field and the demagnetizing field, using the demagnetizing tensor described in Section 2.4.3 to define the latter (note that $\overleftrightarrow{N}$ is pre-multiplied by a factor of 4π, so now the trace of $\overleftrightarrow{N}$ is unity)

$$\boldsymbol{H}_{eff,0} = \boldsymbol{H}_B - 4\pi\overleftrightarrow{N}\boldsymbol{M}_0, \tag{2.98}$$

$$\boldsymbol{h}_{eff} = \boldsymbol{h}_B - 4\pi\overleftrightarrow{N}\boldsymbol{m}. \tag{2.99}$$

Substitution of Eqs. 2.98 - 2.99 into the linearized LL equation (Eq. 2.97) therefore leads to the equation

$$i\omega\boldsymbol{m} = -\gamma\boldsymbol{M}_0 \times \boldsymbol{h}_B + 4\pi\gamma M_0 \times \overleftrightarrow{N}\boldsymbol{m} - \gamma\boldsymbol{m} \times \boldsymbol{H}_B + 4\pi\gamma\boldsymbol{m} \times \overleftrightarrow{N}\boldsymbol{M}_0. \tag{2.100}$$

It is the purpose of this section to consider free (undriven) oscillations of the magnetization, and so $\boldsymbol{h}_B = 0$. Eq. 2.100 then corresponds to a pair of homogeneous equations, and thus can be solved for the eigenfrequency $\omega = \omega_{FMR}$ such that

$$\omega_{FMR} = \gamma\sqrt{\left(H_B - 4\pi M_S\left[N_{zz} - N_{xx}\right]\right)\left(H_B - 4\pi M_S\left[N_{zz} - N_{yy}\right]\right) - \left(4\pi M_S\right)^2 N_{xy}N_{yx}}. \tag{2.101}$$

For the case of a uniformly-magnetized ellipsoid, in which $\boldsymbol{H}_B$ (and $\boldsymbol{M}_0$) is directed along one of the symmetry axes of the ellipsoid (which is itself parallel to the *z*-axis), the demagnetizing tensor is diagonal, reducing Eq. 2.101 to the Kittel equation[89]

$$\omega_{FMR} = \gamma\sqrt{\left(H_B + 4\pi M_S\left[N_{xx} - N_{zz}\right]\right)\left(H_B + 4\pi M_S\left[N_{yy} - N_{zz}\right]\right)}. \tag{2.102}$$

For a continuous thin film magnetized in-plane, and transformed such that the *x*-axis corresponds to the normal of the film, it can be deduced that $N_{xx} = 1$ and $N_{yy} = N_{zz} = 0$. Thus

$$\omega_{FMR} = \gamma\sqrt{H_B\left(H_B + 4\pi M_S\right)}. \tag{2.103}$$

The solutions shown in Eqs. 2.102 - 2.103 all correspond to the frequency of ferromagnetic resonance (FMR). Physically, FMR is defined as the collective phase-coherent precession of magnetization in a single-domain state - the uniform mode of magnetization precession - and therefore corresponds to a spin wave of infinite wavelength.

2.6.3 Driven magnetization oscillations

In Section 2.5.2, the discussion was restricted to the study of free oscillations within magnetic samples, by fixing $\boldsymbol{h}_B = 0$ after obtaining Eq. 2.100. This enabled the frequency of

FMR – characterizing a spin wave of infinite wavelength – to be determined. In order to excite harmonic spin waves with finite wave vector across a uniform magnetic system, it is necessary to drive the magnetic system using a dynamic field, such that $\boldsymbol{h}_B \neq 0$. This leads to an inhomogeneous system of equations being defined by Eq. 2.97

$$\begin{pmatrix} i\omega & \gamma H_B \\ -\gamma H_B & i\omega \end{pmatrix}\begin{pmatrix} m_x \\ m_y \end{pmatrix} = \begin{pmatrix} \gamma M_S h_{B,y} \\ -\gamma M_S h_{B,x} \end{pmatrix}. \tag{2.104}$$

Solving Eq. 2.104 for the dynamic magnetization reveals the Polder susceptibility tensor $\bar{\bar{\chi}}$

$$\begin{pmatrix} m_x \\ m_y \end{pmatrix} = \begin{pmatrix} \chi_{xx} & \chi_{xy} \\ \chi_{yx} & \chi_{yy} \end{pmatrix}\begin{pmatrix} h_{B,x} \\ h_{B,y} \end{pmatrix}, \tag{2.105}$$

where

$$\chi_{xx,yy} = \frac{\omega_M \omega_H}{{\omega_H}^2 - \omega^2}, \tag{2.106}$$

$$\chi_{xy,yx} = \pm i \cdot \frac{\omega_M \omega}{{\omega_H}^2 - \omega^2}, \tag{2.107}$$

and

$$\omega_M = \gamma M_S, \tag{2.108}$$

$$\omega_H = \gamma H_B. \tag{2.109}$$

Physically, the Polder susceptibility tensor characterises the response of a ferromagnetic material to a dynamic magnetic field.

If the frequency of excitation ω is equal to ω_{H}, the denominators of Eqs. 2.106 - 2.107 tends to zero, and the Polder susceptibility becomes ill-defined. This is a consequence of assuming the system was dissipationless. By introducing a non-zero Gilbert damping coefficient in Eq. 2.95, the corresponding equations characterizing the frequency of FMR and the Polder susceptibility can be obtained via the transformation

$$\omega_H \rightarrow \omega_H + i\alpha\omega. \tag{2.110}$$

As a result, the frequency of FMR in an entirely unbounded ferromagnet is given by

$$\omega_{FMR} = \frac{\omega_H}{1+\alpha^2}, \tag{2.111}$$

and the elements of the Polder susceptibility tensor (in the presence of damping, and to first order) are given by[65]

$$\chi_{xx,yy} = \frac{\omega_M \omega_H \left[\omega_H{}^2 - \omega^2\right]}{\left[\omega_H{}^2 - \omega^2\right]^2 + \left(2\alpha\omega\omega_H\right)^2} - i \cdot \frac{\alpha\omega_M \omega \left[\omega_H{}^2 + \omega^2\right]}{\left[\omega_H{}^2 - \omega^2\right]^2 + \left(2\alpha\omega\omega_H\right)^2}, \tag{2.112}$$

$$\chi_{xy,yx} = \frac{\omega_M \omega \left[\omega_H{}^2 - \omega^2\right]}{\left[\omega_H{}^2 - \omega^2\right]^2 + \left(2\alpha\omega\omega_H\right)^2} - i \cdot \frac{2\alpha\omega_M \omega_H \omega^2}{\left[\omega_H{}^2 - \omega^2\right]^2 + \left(2\alpha\omega\omega_H\right)^2}. \tag{2.113}$$

The typical variation of the real and imaginary parts of the modified Polder susceptibility elements $\chi_{xy,yx}$ as a function of the frequency is presented in Fig. 2.6. Note that the real and imaginary profiles of $\chi_{xx,yy}$ are broadly similar to those shown in Fig. 2.6, but there are modest quantitative differences (as evident in Eqs. 2.112 – 2.113).

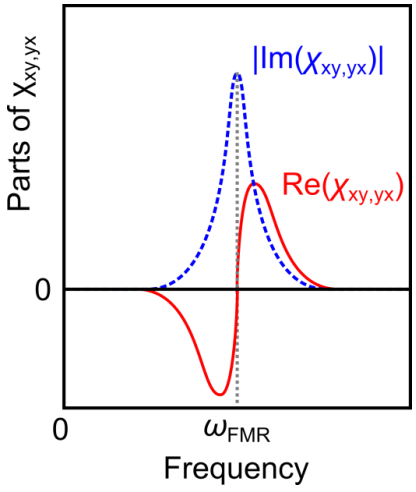

Fig. 2.6 The typical variation[65] of the real and imaginary parts of the Polder susceptibility tensor elements $\chi_{xy,yx}$ on the electromagnetic frequency, with non-zero damping.

By substituting Eq. 2.111 into Eqs. 2.112 - 2.113, one can identify certain resonance conditions. Specifically, when the system is driven at resonance, the real parts of $\chi_{xx,xy,yx,yy}$ pass a zero-crossing, and the absolute imaginary parts of $\chi_{xx,xy,yx,yy}$ maximize. These conditions underpin the interpretation of results acquired using vector-network-analyser ferromagnetic resonance experiments.[90]

2.6.4 Magnetostatic spin waves

Using the Polder susceptibility tensor in the absence of damping, one can define the complex amplitude of ac magnetic induction

$$\begin{aligned} \boldsymbol{b} &= \boldsymbol{h} + 4\pi\boldsymbol{m} \\ &= \boldsymbol{h} + 4\pi(\vec{\chi}\boldsymbol{h}) \\ &= \vec{\mu}\boldsymbol{h} \end{aligned} \tag{2.114}$$

where the magnetic permeability tensor is defined as $\vec{\mu} = (\vec{I} + 4\pi\vec{\chi})$. Upon substituting Eqs. 2.106 - 2.107 into Eq. 2.114, one obtains a more complete solution for the magnetic permeability tensor

$$\vec{\mu} = \begin{pmatrix} \mu & i\nu & 0 \\ -i\nu & \mu & 0 \\ 0 & 0 & 1 \end{pmatrix}, \tag{2.115}$$

where

$$\mu = 1 + \frac{\omega_M \omega_H}{{\omega_H}^2 - \omega^2}, \tag{2.116}$$

$$\nu = \frac{\omega_M \omega}{{\omega_H}^2 - \omega^2}, \tag{2.117}$$

and $\omega_M = 4\pi \cdot \gamma M_S$. Using Eq. 2.114, one can also define a scalar potential ψ via

$$\boldsymbol{h} = -\nabla\psi\,. \tag{2.118}$$

Eqs. 2.114 and 2.118 can then be combined with Eq. 2.78 to derive the Walker equation[91]

$$\mu\left(\frac{\partial^2\psi}{\partial x^2} + \frac{\partial^2\psi}{\partial y^2}\right) + \frac{\partial^2\psi}{\partial z^2} = 0\,. \tag{2.119}$$

To solve Eq. 2.119, it is necessary to introduce some boundary conditions. These are obtained, for example, by restricting the ferromagnetic system so as to form a film, extending to infinity in the *y*-*z* plane, and having a finite thickness *s* across the *x*-direction. This configuration is shown in the inset of Fig. 2.7 (a). Now, when $\mu = 0$, the Walker equation can be solved for an arbitrary potential, independent of *z*, yielding the frequency of FMR as

defined in Eq. 2.103. If, instead, $\mu \neq 0$, the Walker equation describes spin-waves of finite wave-vector.

The two interfaces introduced by the finite thickness of the film leads to the potential taking the form of ψ_i or ψ_e inside and outside the film respectively. The Walker equation therefore becomes

$$\mu\left(\frac{\partial^2\psi_i}{\partial x^2}+\frac{\partial^2\psi_i}{\partial y^2}\right)+\frac{\partial^2\psi_i}{\partial z^2}=0, \tag{2.120}$$

$$\frac{\partial^2\psi_e}{\partial x^2}+\frac{\partial^2\psi_e}{\partial y^2}+\frac{\partial^2\psi_e}{\partial z^2}=0. \tag{2.121}$$

Also, the continuity of the magnetic induction normal to the surfaces, and the continuity of the magnetic field parallel to the surfaces, must be maintained. These two statements lead to the boundary conditions

$$\mu\frac{\partial\psi_i}{\partial x}+i\nu\frac{\partial\psi_i}{\partial y}=\frac{\partial\psi_e}{\partial x}, \tag{2.122}$$

$$\psi_i=\psi_e, \tag{2.123}$$

at $x = 0$ and $x = s$. Inside the film, the potential must satisfy the Walker equation, whereas the potential outside of the film must obey Laplace's equation (Eq. 2.83, but with $\boldsymbol{M} = 0$). The magnetic potentials can be assumed to have plane wave solutions

$$\psi_i=\left[A\sin(k_{xi}x)+B\cos(k_{xi}x)\right]\exp\left(-ik_y y-ik_z z\right), \tag{2.124}$$

$$\psi_{1e}=C\exp\left(-k_{xe}x-ik_y y-ik_z z\right), \tag{2.125}$$

$$\psi_{2e}=D\exp\left(k_{xe}x-ik_y y-ik_z z\right), \tag{2.126}$$

where k_{xe}, k_{xi}, k_y and k_z are the wave-vector components along the respective co-ordinate axes, and A, B, C and D are arbitrary coefficients. Substitution of Eqs. 2.124 - 2.126 into Eqs. 2.120 - 2.121 leads to the system of equations

$$\begin{cases} -k_{xe}C\exp(-k_{xe}s) = \mu_{xx}k_{xi}\left[A\cos(k_{xi}s) - B\sin(k_{xi}s)\right] + \nu_{xy}k_y\left[A\sin(k_{xi}s) + B\cos(k_{xi}s)\right] \\ k_{xe}D = A\mu_{xx}k_{xi} + B\nu_{xy}k_y \\ C\exp(-k_{xe}s) = A\sin(k_{xi}s) + B\cos(k_{xi}s) \\ B = D \end{cases} . \quad (2.127)$$

Solving these equations reveals the dispersion equation for magnetostatic spin waves

$$-k_{xe}{}^2 - 2\mu_{xx}k_{xi}k_{xe}\cot(k_{xi}s) + \mu_{xx}{}^2k_{xi}{}^2 - \nu_{xy}{}^2k_y{}^2 = 0 . \quad (2.128)$$

By substituting Eqs. 2.124 - 2.126 into Eqs. 2.122 – 2.123, one can obtain expressions for k_{xi} and k_{xe} in terms of k_y and k_z

$$k_{xi} = \sqrt{\frac{-k_z{}^2 - k_y{}^2\mu}{\mu}} , \quad (2.129)$$

$$k_{xe} = \sqrt{k_z{}^2 + k_y{}^2} , \quad (2.130)$$

thus allowing the implicit dispersion relation to be written more clearly in terms of k_y and k_z

$$(\mu+1)k_z{}^2 + (\mu^2 - \nu^2 + 1)k_y{}^2 + 2\mu\sqrt{\left(-\frac{k_z{}^2}{\mu} - k_y{}^2\right)\left(k_z{}^2 + k_y{}^2\right)}\cot\left(s\sqrt{\frac{-k_z{}^2}{\mu} - k_y{}^2}\right) = 0 . \quad (2.131)$$

Since Eq. 2.131 is an implicit function, it must - in the general case - be solved numerically. By solving this in such a fashion, one can obtain the dispersion of magnetostatic spin waves as a function of k_y and k_z - presented in Fig. 2.7 (a) is a sketch of the allowed solutions (which was first published[92] by Richard Damon and John Eshbach in 1961).

The most striking feature apparent in Fig. 2.7 (a) is the anisotropy of the magnetostatic dispersion. Depending on the frequency of excitation, one can excite certain spin-wave types, propagating at a particular direction relative to the magnetization. If the frequency of excitation is above that of the frequency of FMR, magnetostatic surface spin waves (MSSWs) propagate. These spin waves have positive dispersion, and are only capable of propagating at and above a certain angle $\varphi_c = \tan^{-1}\left(\sqrt{\omega_H}\right)$ relative to the magnetization, as indicated in Fig. 2.7 (a). Moreover, it is possible to derive analytically the magnetostatic spin-wave dispersion in the limit of $k_z \to 0$, whereby the spin-wave propagation is wholly orthogonal to the magnetization (in this configuration, the spin waves can have maximum frequency). By

setting $k_z = 0$, one can reformulate the Walker equation with the assumption of plane wave solutions $\psi \propto \exp(i\boldsymbol{k}\cdot\boldsymbol{r})$ in space to obtain

$$\mu\left(k_x^{\,2} + k_y^{\,2}\right) = 0. \tag{2.132}$$

The solutions of Eq. 2.132 are either $\mu = 0$ or $k_y^{\,2} = -k_x^{\,2}$. Since the former solution does not permit finite wave-vector solutions, one can deduce that, because k_y needs to be real, k_x must be imaginary. Thus, the out-of-plane component of such a spin wave is a decaying exponential, where the spin-wave amplitude is maximised at one surface of the film, and attenuates according to $1/|k_y|$ as the depth increases (as shown in the inset of Fig. 2.7 (b)).[93] After extensive rearrangement of Eq. 2.131, the analytical dispersion for spin waves propagating transversely wholly orthogonally to the magnetization has the form[92]

$$\omega = \sqrt{\omega_H^{\,2} + \omega_H\omega_M + \omega_M^{\,2}\left[2 + 2\coth\left(|k_y|s\right)\right]^{-1}}, \tag{2.133}$$

which simplifies to

$$\omega = \sqrt{\left(\omega_H + \frac{\omega_M}{2}\right)^2 - \left(\frac{\omega_M}{2}\right)^2 \exp\left(-2|k_y|s\right)}. \tag{2.134}$$

This dispersion relation is graphed in Fig. 2.7 (b), and is bound between the frequency limits ω_{FMR} and $\omega_H + \omega_M/2$. Notice that the dispersion becomes flat as the frequency tends towards the latter limit, indicating that the group velocity decreases with increasing frequency.

If instead the frequency of excitation is below that of the frequency of FMR, backward-volume magnetostatic spin waves (BVMSWs) are excited, capable of propagating at any non-orthogonal angle relative to the magnetization. These spin waves, in contrast to MSSWs, have negative dispersion and converge towards ω_H at high wave vector. The dispersion of BVMSWs propagating entirely parallel to the magnetization can be obtained by setting $k_y = 0$ within Eq. 2.131, yielding

$$\mu k_x^{\,2} + k_z^{\,2} = 0. \tag{2.135}$$

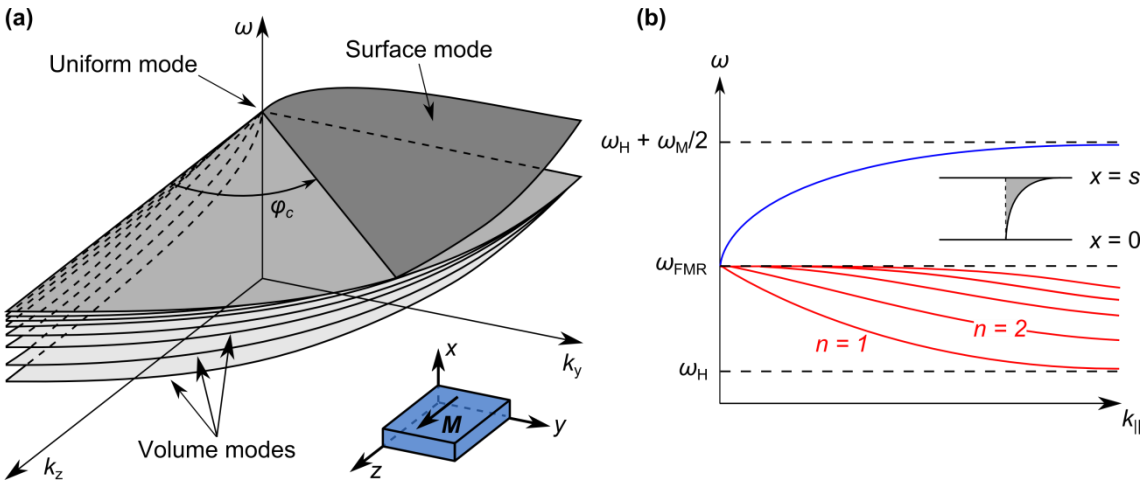

Fig. 2.7 **(a)** The mode spectrum of magnetostatic waves capable of propagating in a continuous film of finite thickness.[92] Inset: schematic of the co-ordinate system used. **(b)** The dispersion of the surface mode (blue line), where $k_{||} = k_y$ and $k_z = 0$, and the backward-volume modes (red line), where $k_{||} = k_z$ and $k_y = 0$. Inset: the characteristic profile of dynamic magnetization for MSSWs across the thickness of the film.

Due to the requirement that $\mu < 0$, plane waves are excited normal to the film. Note that, so far, no assumptions have been made so far about whether the magnetization is "pinned" or "unpinned" at the surfaces of the film – the profile of dynamic magnetization across the thickness of the film can therefore be rather complex, strongly depending on the wave vector, and the degree of magnetization-pinning at the film surfaces.[94-95] In the simplest case, the spin-wave dispersion (when the propagation is entirely parallel to the magnetization) can be reduced to the form[96]

$$\tan\left[\frac{|k_z|s}{2\sqrt{-\mu}} - \frac{(n-1)\pi}{2}\right] = \sqrt{-\mu}\,. \tag{2.136}$$

where n is the non-zero integer number of antinodes spanning the dynamic magnetization across the thickness of the film. This antinodal number defines the multiple volume modes shown in Fig. 2.7.

An important point related to spin waves concerns their reciprocal character. MSSWs are generally classified as non-reciprocal. By exciting MSSWs with an excitation uniform in profile across the thickness of a film, MSSWs will be observed propagating in both directions, but localized in amplitude to each surface of the film, and with opposite phase. The surface

across which the MSSWs localize can be switched by reversing the polarity of the magnetization - such behaviour was experimentally detected by Schneider *et al*.[97] This non-reciprocity can, in principle, be eliminated by exciting spin waves with longer wavelengths (so $|k_y|s \ll 1$). However, it was noted by Demidov *et al*[98] that counterpropagating MSSWs of differing amplitude can still be excited when $|k_z|s \ll 1$, when MSSWs are excited using a microstrip - the out-of-plane component of the exciting field has opposite phase on either side of the microstrip, and so the torque responsible for spin-wave generation on either side of the microstrip is either boosted or reduced.

In contrast to MSSWs, BVMSWs are classified as reciprocal when propagating wholly parallel to the magnetization. The local excitation of a magnetic film leads to the excitation of BVMSWs travelling both parallel and antiparallel to the magnetization, with no difference in amplitude or phase.[97] This classification becomes more nuanced however when the BVMSWs propagate at an angle relative to the magnetization. When $k_y \neq 0$ and $|k_z|s \leq 1$, there is consistently some degree of non-reciprocity.[94] Significantly, when the BVMSW travels at the critical angle φ_c with a wavelength such that $|k_z|s \ll 1$, the BVMSW mode has maximum amplitude on one side of the film, but zero amplitude on the other – such a backward-volume mode is hence wholly non-reciprocal.

It should be pointed out that it is also possible for spin waves to propagate across a film where the magnetization points normal to the film – these are classified as forward-volume magnetostatic spin waves.[96] No further detail will be given regarding these waves, however, as they do not feature in the results presented in this thesis.

2.6.5 Dipole-exchange spin waves

The dispersion relation characterizing exchange spin waves is isotropic, which contrasts starkly with the anisotropy associated with the magnetostatic spin waves propagating across thin films magnetized in-plane. Of course, these are both approximations: in real magnetic systems, both the exchange and demagnetizing terms coexist, and therefore a unifying dispersion, which puts both interactions on an equal footing, would be most ideal.

Such a unifying dispersion relation was derived using classical perturbation theory by Boris Kalinikos and Andrei Slavin in 1986.[99] The dispersion relation for dipole-exchange

spin waves (propagating wholly across the plane of the film, which is itself magnetized in-plane) is of the form

$$\omega(k,\theta,s)=\gamma\sqrt{\left(H_i+Dk^2\right)\left(H_i+Dk^2+4\pi M_s F_{pp}(k,\theta,s)\right)}, \tag{2.137}$$

where θ is the angle between the magnetization and spin-wave wave vector. The net wave vector is then given by

$$k^2=k_{\|}{}^2+k_p{}^2, \tag{2.138}$$

where $k_{\|}$ is the in-plane wave vector, and k_p is the quantized out-of-plane wave vector component (which has p antinodes)

$$k_p=\frac{p\pi}{s}. \tag{2.139}$$

where p can equal zero or any positive integer. F_{pp} is the dipole-dipole matrix element, which corresponds to the p-th quantized perpendicular standing spin-wave mode, and is defined by

$$F_{pp}=1-P_{pp}\cos^2\theta+4\pi M_s\frac{P_{pp}\left(1-P_{pp}\right)\sin^2\theta}{H_i+Dk^2}. \tag{2.140}$$

When the magnetization at the surfaces of the film is completely unpinned, P_{pp} is given by the explicit expression

$$P_{pp}=\frac{k_{\|}{}^2}{k^2}-\frac{2k_{\|}{}^3}{k^4 s}\cdot\frac{\left[1-(-1)^p\exp\left(-k_{\|}s\right)\right]}{\left(1+\delta_{0p}\right)}. \tag{2.141}$$

For the first perpendicular mode (p = 0), P_{00} reduces to

$$P_{00}=1-\frac{1-\exp\left(-k_{\|}s\right)}{k_{\|}s}. \tag{2.142}$$

Notice however that it was assumed that the dipole-exchange spin wave described by Eq. 2.142 had uniform profile across the thickness of the film (since p = 0). As such, the Kalinikos-Slavin dispersion relation (in the absence of exchange) reduces very accurately to the magnetostatic relation only when describing spin waves with a wavelength significantly larger than the film thickness.

Shown in Fig. 2.8 (a) is the typical dispersion given by Eq. 2.137 for dipole-exchange spin waves propagating across a 10 nm thick continuous film of Permalloy (in which M_s = 800 G and A_{ex} = 1.3 μerg / cm). For this calculation, the film was considered to be biased by a magnetic field of strength 500 Oe, applied along the *z*-axis. By examining the projections of the dispersion onto the k_y and k_z axes, as shown in Fig. 2.8 (b), the unifying character of the Kalinikos-Slavin dispersion relation is more obvious. At low wave vector, the dispersion resembles that of the anisotropic magnetostatic type, but at high wave vector, the two branches converge towards a function of k^2, reflecting the isotropy of the exchange interaction.

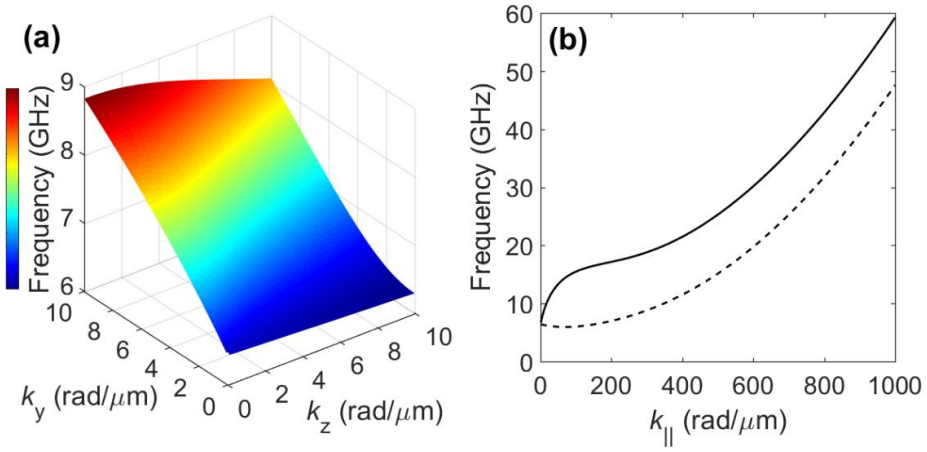

Fig. 2.8 **(a)** The dispersion of propagating dipole-exchange spin waves supported by a continuous film of Permalloy, of thickness 10 nm. The film was defined as having the material parameters M_s = 800 G and A_{ex} = 1.3 μerg / cm, and was assumed to possess an internal field H_i = 500 Oe directed parallel to the *z*-axis. **(b)** Projections of the dipole-exchange dispersion along k_y (solid line) and k_z (dashed line).

2.6.6 Isofrequency curves

The dispersion relations discussed in Sections 2.3.4 and 2.6.4 – 2.6.5 all describe the propagation of plane spin waves. Implicit in these sections was the assumption that the driving field ***h***, responsible for exciting the considered spin waves, was translationally invariant along one axis. However, it is sometimes more desirable to assume that the spin-wave frequency is fixed, and then identify the wave vector solutions that satisfy the dispersion relation. This approach can be understood merely by inspecting Fig. 2.8 (a), where the

identifiable bright yellow and cyan lines show positive wave vector solutions (k_y,k_z) corresponding to frequencies of 7.85 GHz and 7.23 GHz respectively. This is an example of an isofrequency curve (or surface in the three-dimensional case), which can be plotted for constant frequency in reciprocal space. In reciprocal space, the wave vector (k_y,k_z) is parallel to the phase velocity $\left(\boldsymbol{v}_{ph} = \hat{\boldsymbol{k}}\omega/k\right)$, whereas the group velocity is the gradient of the angular frequency with respect to the wave vector $\left(\boldsymbol{v}_g = \partial\omega/\partial\boldsymbol{k}\right)$. The group velocity is always orientated normal to the isofrequency curve.

The dispersion relations for magnetostatic and dipole-exchange spin waves cannot be reformulated such that $k_{y,z}\left(k_{z,y},\omega\right)$, and so the isofrequency curves must be calculated numerically. For magnetostatic spin waves, the separation of spin-wave manifolds above and below the frequency of FMR causes there to be two types of isofrequency curves. Shown in Fig. 2.9 (a) are exemplary isofrequency curves characterizing MSSWs propagating at frequencies of 5.4 GHz and 5.6 GHz within a 7.5 μm-thick film of Yttrium-Iron-Garnet (M_s = 140 G). The considered film was biased by a spatially-uniform magnetic field 1250 Oe directed along the *z*-axis, consequently leading to the film having the frequency of resonance f_{FMR} = 5.36 GHz. The isofrequency curves are composed of two open linear segments, connected by a smooth inflexion. The magnetization orientation dictates the axis of symmetry between the two curves (in this case, the line k_y = 0). Upon increasing the frequency of excitation (or instead reducing the internal field), the isofrequency curves are both deformed and pushed apart. Two example group and phase velocity vectors are shown in Fig. 2.9 (a). For MSSWs, the projection of the group velocity onto the wave vector is positive (reflecting the positive dispersion). Note the anisotropy of the magnetostatic dispersion generally causes the group and phase velocities to be non-collinear (except for the special case when k_z = 0).

For BVMSW modes, the isofrequency curves have significantly different character. Presented in Fig. 2.9 (b) are the isofrequency curves belonging to the same system as was studied in (a), but here the frequency of excitation is 5.33 GHz. Since the frequency of excitation is below that of the frequency of FMR, the two open curves are now arranged so as their axis of symmetry (the line k_z = 0) is orthogonal to the magnetization. Note there are also multiple pairs of isofrequency curves, corresponding to the different volume modes (only the first two modes are shown in Fig. 2.9 (b)). In contrast to the surface modes, increasing the

frequency of excitation (or reducing the internal field) moves the curves closer towards the line $k_z = 0$. The group and phase velocities are again generally non-collinear, but in this case, the projection of the group velocity onto the wave vector is negative. Also important to emphasize is that the curves become increasingly straight at higher values of $|k_y|$.

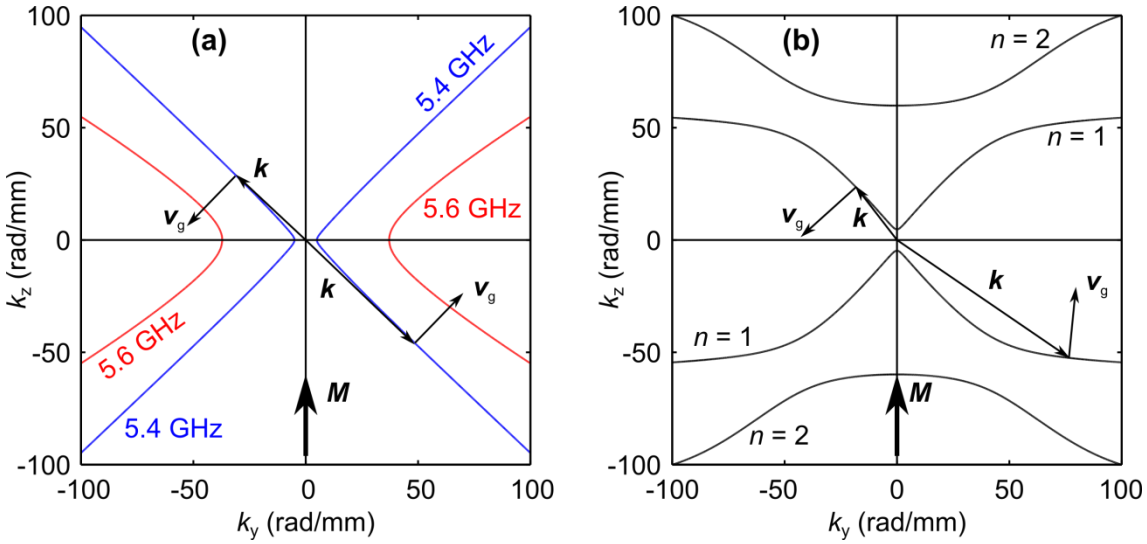

Fig. 2.9 Isofrequency curves, calculated using Eq. 2.131, characterizing the propagation of magnetostatic spin waves supported by a continuous film of YIG (7.7 μm thick). The YIG was assumed to have the material parameter M_s = 140 G, and to be biased by H_B = 1225 Oe (directed along the z-axis). Example unit vectors showing the directions of the wave vector and corresponding group velocity are indicated. **(a)** Surface spin waves are shown, with the frequencies of excitation 5.4 GHz (blue line) and 5.6 GHz (red line). **(b)** Volume spin waves with a frequency of 5.33 GHz are shown. The first two volume modes are shown, where n is the number of antinodes belonging to the dynamic magnetization across the thickness of the film.

The magnetostatic isofrequency curves are very similar to those derived by the Kalinikos-Slavin dispersion relation at low wave vector. However, the inclusion of the exchange interaction causes the formerly open curves to become closed. Shown in Fig. 2.10 (a) are the isofrequency curves characterizing the spin waves propagating across a 10 nm thick film of Permalloy, biased uniformly by a magnetic field H_B = 500 Oe along the z-axis. The spin-wave frequency is set to either 9 GHz (blue line) or 18 GHz (red line), and the FMR-mode supported by the film is of frequency f_{FMR} = 6.4 GHz. As the frequency of excitation increases, the anisotropy of the isofrequency curves reduces, and the isofrequency curve takes

on more elliptical shape. As the frequency increases further, they tend towards the curves described by the exchange dispersion.

In the limit of exchange only, the isofrequency curves are straightforward to describe. Shown in Fig. 2.10 (b) are the isofrequency curves characterizing spin waves of electromagnetic frequency 25 GHz and 50 GHz, propagating across a 3 nm-thick film of Permalloy, biased at 500 Oe (f_{FMR} = 6.4 GHz). The isofrequency curves are completely circular and isotropic, with a radius $k = \sqrt{\frac{[\omega/\gamma - H_B]}{D}}$. The group velocity in this case is always parallel to the phase velocity.

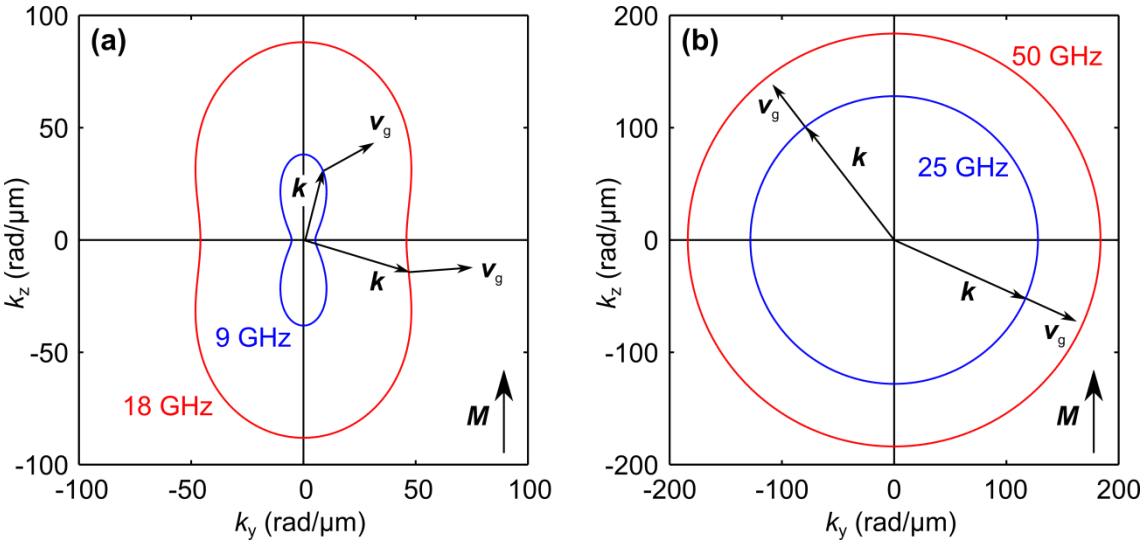

Fig. 2.10 Isofrequency curves, calculated using Eq. 2.135, characterizing the propagation of dipole-exchange and exchange spin waves within a continuous film of Permalloy (M_s = 800 G, A_{ex} = 1.3 μerg/cm) biased at H_B = 500 Oe applied along the *z*-axis. The magnetization is aligned parallel to the z-axis, and example directions of the wavevector and corresponding group velocity ($\boldsymbol{v}_g$) are indicated. **(a)** Dipole-exchange spin waves of frequency 9 GHz (blue line) and 18 GHz (red line), propagating in a film of thickness 20 nm, are shown. **(b)** Exchange spin waves of frequency 25 GHz (blue line) and 50 GHz (red line), propagating in a Permalloy film of thickness 3 nm, are shown.

2.6.7 Spin-wave width-modes

When deriving the dispersion of propagating magnetostatic spin waves, Damon and Eshbach assumed that the spin waves travelled across a film which was isolated, translationally invariant and uniformly magnetized. However, this is not an assumption one can normally make. The dispersion of propagating spin waves in an infinitely-extending thin film can be modified, for example, by the presence of a dielectric underlayer.[100] Moreover, thin films can be restricted (with symmetrical boundaries) in either one or two dimensions, giving rise to a stripe or square respectively. The boundary conditions associated with such patterned structures causes nodes of oscillation to exist at (or close to) the geometrical edges, causing square films to support confined spin-wave modes, for example.[82,101-102] Across stripes, in contrast, spin waves are capable of propagating along the long axis of the conduit, but will be confined across the short axis. This type of propagating spin wave is commonly referred to as a width-mode.

The behaviour of width-modes has already been extensively studied and reviewed.[82, 103-106] Magnetostatic width-modes are most commonly excited along a longitudinally-magnetized stripe through the application of a local exciting magnetic field (the exciting field is non-uniform in strength across the length and thickness of the stripe, but uniform across the width). Since the direction of propagation is parallel to the magnetization, reciprocal backward-volume width-modes would be excited. The precise position of the lateral nodes of oscillation are given by the boundary conditions of the magnetization at the edges of the waveguide.[107-108] The uniformity of the exciting field across the width of the stripe implies that the propagating width-modes must have sinusoidal spatial variation, and further there needs to be an odd number n of transverse antinodes.[82] At a given frequency of excitation, multiple odd modes can be simultaneously excited (albeit with different efficiencies).[109] The dispersion of width-modes can be obtained rather simply through the adaptation of the Kalinikos-Slavin dispersion relation[99] to include the transverse wave vector component

$$k_{\perp} = \frac{n\pi}{w_{eff}}, \tag{2.143}$$

where w_{eff} is the "effective width" of the stripe.[107] The effective width, rather than the geometrical width, is used in order to take into account the aforementioned boundary

conditions at the edges of the waveguide. As a consequence, the dispersion characterizing BVMSW width-modes (where $k_{\perp} > 0$) shifts towards higher frequencies, as *n* increases.

To excite laterally-confined propagating MSSWs, it is necessary for the waveguide to be magnetized transversely. The consequential non-zero static demagnetizing field leads to parabolic non-uniformity in the static internal field across the width of the waveguide. As a result, "potential wells" can be formed at the edges of the waveguide, supporting the propagation of localized edge-modes with reduced frequency.[51,104-110] If, instead, the frequency of excitation is higher than that required to support edge-modes, a MSSW width-mode will non-reciprocally propagate along the waveguide, spanning the reasonably uniform internal field across the central section of the waveguide's width. The dispersion of MSSW width-modes can be described using either the magnetostatic formulation presented by O'Keefe *et al*,[103] or the dipole-exchange formulation.[99] In contrast to BVMSW width-modes, the dispersion characterizing MSSW width-modes shifts towards lower frequencies as *n* increases.

2.7 Summary

In summary, the background concepts pertaining to the static and dynamic behavior of magnetism have been introduced. Special attention was devoted to the theoretical descriptions of the spin-wave dispersion, which is crucial for the understanding of the results presented in this thesis. In the next chapter, the experimental and numerical techniques used to study the excitation and propagation of spin waves will be discussed in detail.

CHAPTER 3

EXPERIMENTAL AND NUMERICAL TECHNIQUES

3.1 Introduction

In this chapter, I introduce and discuss the principles of operation and implementation of the experimental and numerical techniques used to obtain the results presented in this thesis. I begin this chapter by reviewing the magneto-optical Kerr effect, which was primarily used to experimentally image magnetization dynamics within Permalloy films. This is then followed by a brief outline of the two- and three-temperature models, which is often employed to describe how light interacts with matter (this model underpins the pumping aspect of the TROPSOM system). Following these theoretical descriptions, I will discuss in-depth the setup of the TRSKM and TROPSOM systems, which were used extensively to pump and probe ultrafast magnetization dynamics. Since some of the results discussed in this thesis were obtained using BLS microscopy, a brief description of the underlying principles of BLS will then be given. Note that, since I did not operate the BLS microscopy system, the discussion of the system will be brief. In the final section of this chapter, the principles of the open-source micromagnetic package Object-Oriented Micro-Magnetic Framework (OOMMF) will be discussed. This software was extensively used to complement and understand the experimentally-acquired results, and also as a standalone tool in order to study the static and dynamic behavior of magnetic systems.

3.2 Magneto-optical effects, and the interaction of light with matter

As far back as 1816, it was well-understood that light could be polarized (giving rise to some measureable interference effects[111]), and furthermore that the linear polarization of light influenced the degree of transmission through a substance.[112] Michael Faraday was the first to observe, in 1845, that the transmission of linearly-polarized light through heavy glass was affected by subjecting the glass to a magnetic field.[113] This discovery of the magneto-

optical Faraday effect was expanded upon by August Kundt in 1884,[114] who demonstrated that the polarization of linearly-polarized light was also rotated upon transmission through a ferromagnetic metal.

The Faraday effect occurs when linearly-polarized light transmits through a magnetized material. In 1877, John Kerr observed[115] that the plane of polarization of linearly-polarized light, incident on a polished pole of an electromagnet, underwent similar rotation upon reflection. This is known as the magneto-optical Kerr effect. The decision as to which of the two polarization-dependent magneto-optical effects should be used to image magnetization is dictated by the opacity of the material to be studied, and also the design of the measurement technique. The magneto-optical Kerr effect was used within all the TRSKM and TROPSOM measurements discussed in this thesis. To interpret the results acquired using TRSKM and TROPSOM, it is necessary to develop theoretical understanding of the Kerr effect: this will be provided in Section 3.2.1.

In addition to acting as a probe in both the TRSKM and TROPSOM systems, laser-generated light was also used to pump magnetization dynamics in the TROPSOM system. It is therefore also necessary to understand how light interacts with matter more generally, and how light can stimulate electron, phonon and magnetization dynamics. In 1956, the two-temperature model was introduced[116] to describe the non-equilibrium state between electrons and the lattice. This model was revised 40 years later by Eric Beaurepaire *et al.*,[117] in order to take into account the additional excitation of magnetization. This three-temperature model has been successfully used to account for a wide variety of experimental measurements, in which a magnetic substance is optically excited. In Section 3.2.2, both the two-temperature and three-temperature models are reviewed, in relevance to the operation of the TROPSOM system.

3.2.1 Theory of the magneto-optical Kerr effect

When light is incident on a plane surface, some of the light is transmitted / absorbed, and some of the light is reflected. Assuming that energy is conserved, it is immediately viable to state $T + R = 1$ where T and R denote the transmission and reflection coefficients of the boundary respectively. Both the transmission and reflection coefficients are highly dependent not only on the optical properties of the boundary, but also the wavelength and polarization of

the incident light. Phenomenologically, the response of a material (the electric displacement ***D***) to an electromagnetic field is given by

$$\boldsymbol{D} = \vec{\varepsilon}\boldsymbol{E} \tag{3.1}$$

where $\vec{\varepsilon}$ is the permittivity tensor. For symmetric isotropic systems, the permittivity tensor is merely a scalar quantity. Ferromagnetic materials however, by virtue of their magnetization, are intrinsically anisotropic. For a cubic ferromagnetic material, possessing magnetization ***m*** with a non-zero projection onto all three Cartesian axes, the permittivity tensor takes the form

$$\vec{\varepsilon} = \begin{pmatrix} 1 & im_z Q & -im_y Q \\ -im_z Q & 1 & im_x Q \\ im_y Q & -im_x Q & 1 \end{pmatrix}, \tag{3.2}$$

where Q is the Voigt constant.[118] With the magnetization aligned along the z-axis, the permittivity tensor simplifies to

$$\vec{\varepsilon} = \begin{pmatrix} \varepsilon_{xx} & \varepsilon_{xy} & 0 \\ -\varepsilon_{xy} & \varepsilon_{xx} & 0 \\ 0 & 0 & \varepsilon_{xx} \end{pmatrix}. \tag{3.3}$$

In accordance with Onsager's theorem[119-120] the magnetization-dependent elements of the permittivity tensor must obey certain symmetry constraints

$$\begin{aligned} \varepsilon_{\alpha\alpha}(\boldsymbol{m}) &= \varepsilon_{\alpha\alpha}(-\boldsymbol{m}) \\ \varepsilon_{\alpha\beta}(\boldsymbol{m}) &= -\varepsilon_{\beta\alpha}(-\boldsymbol{m}) \end{aligned} \tag{3.4}$$

These state that the diagonal and off-diagonal elements are even and odd functions of ***m*** respectively. To first-order, the diagonal elements are independent of ***m***, whereas the off-diagonal elements are linearly proportional to ***m***. The off-diagonal elements in Eq. 3.3 are therefore at the root of the polarization-dependent magneto-optical Kerr effect used to image magnetization dynamics in this thesis.

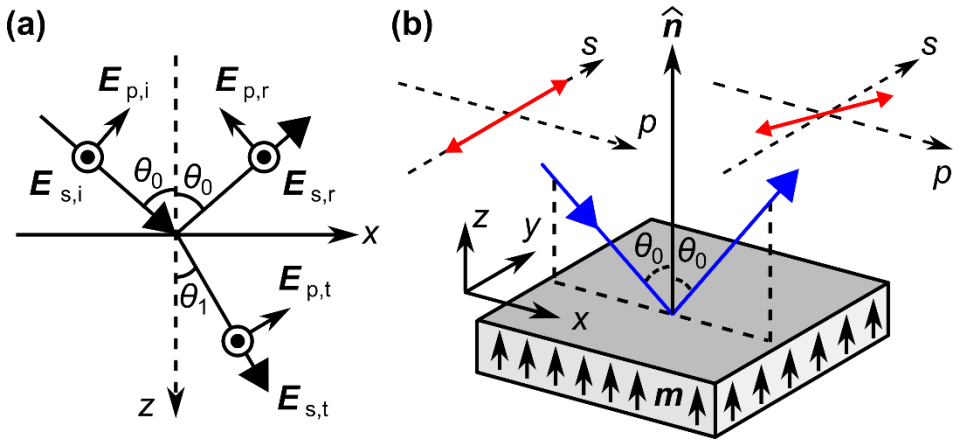

Fig. 3.1 **(a)** Geometry used to calculate the general form of the reflection coefficients.[121] **(b)** A sketch of how the polarization of *s*-polarized light is modified by the polar magneto-optical Kerr effect.

The problem of how light interacts with matter can be considered using the geometry presented in Fig. 3.1 (a), in which light incident on a surface (extending along the *x*-*y* plane) is both reflected and transmitted. The light is defined as being *p*- or *s*- polarized if the associated electric field ***E*** is parallel to, or orthogonal to, the plane of incidence respectively. Now, the electric field components prior to and after reflection are related through the Jones matrix formalism

$$\begin{pmatrix} E_{s,r} \\ E_{p,r} \end{pmatrix} = \begin{pmatrix} r_{ss} & r_{sp} \\ r_{ps} & r_{pp} \end{pmatrix} \begin{pmatrix} E_{s,i} \\ E_{p,i} \end{pmatrix}, \tag{3.5}$$

where r_{ij} are the reflection coefficients. By solving the Maxwell equations at the surface, with appropriate boundary conditions, the reflection coefficients can be derived

$$r_{ss} = \frac{n_0 \cos\theta_0 - n_1 \cos\theta_1}{n_0 \cos\theta_0 + n_1 \cos\theta_1}, \tag{3.6}$$

$$r_{pp} = \frac{n_1 \cos\theta_0 - n_0 \cos\theta_1}{n_1 \cos\theta_0 + n_0 \cos\theta_1} + \frac{2iQn_0 n_1 \cos\theta_0 \sin\theta_1 m_y}{(n_1 \cos\theta_0 + n_0 \cos\theta_1)^2 m}, \tag{3.7}$$

$$r_{ps} = -\frac{iQn_0 n_1 \cos\theta_0 (\sin\theta_1 m_x + \cos\theta_1 m_z)}{\cos\theta_1 (n_0 \cos\theta_0 + n_1 \cos\theta_1)(n_1 \cos\theta_0 + n_0 \cos\theta_1) m}, \tag{3.8}$$

$$r_{sp} = \frac{iQn_0 n_1 \cos\theta_0 (\sin\theta_1 m_x + \cos\theta_1 m_z)}{\cos\theta_1 (n_0 \cos\theta_0 + n_1 \cos\theta_1)(n_1 \cos\theta_0 + n_0 \cos\theta_1) m_s}, \tag{3.9}$$

where θ_0 and θ_1 are the angles of incidence and transmission (relative to the normal of the surface) respectively, and n_0 and n_1 are the refractive indices of the medium in which the light is incident and transmitted respectively. These coefficients then define the Kerr rotation Φ^K and ellipticity Ω^K via

$$\Phi_{s,p}^{K} = \pm \mathrm{Re}\left\{\frac{r_{sp,ps}}{r_{ss,pp}}\right\}, \tag{3.10}$$

and

$$\Omega_{s,p}^{K} = \pm \mathrm{Im}\left\{\frac{r_{sp,ps}}{r_{ss,pp}}\right\}, \tag{3.11}$$

for incident *s*- and *p*-polarized light respectively (as indicated by the subscript in Eqs. 3.10-3.11). For a ferromagnetic metal, the off-diagonal elements of $\vec{r}$ are non-zero and complex. As a result, *s*- or *p*-polarized light incident on a surface (magnetized out-of-plane) is reflected with some *p*- or *s*-polarization respectively, as is shown in Fig. 3.1 (b).

Using Eqs. 3.6 - 3.9, it is possible to differentiate between three MOKE geometries, depending on the relative orientation between the magnetization of the material and the plane of incidence of the incoming light. In both the polar and longitudinal Kerr effects, the magnetization lies parallel to the plane of incidence, but the magnetization is either normal to or parallel to the surface respectively. In both cases, the magneto-optical Kerr effect is observed with *s*- or *p*-polarized incident light, but in the former $r_{sp} = r_{ps}$, whereas in the latter $r_{sp} = -r_{ps}$. The polar and longitudinal Kerr effects can be selectively enhanced or diminished by adjusting the angle of incidence of the light: at normal incidence, the polar Kerr effect (induced when $m_z = 1$ and $m_x = m_y = 0$) is maximized but the longitudinal Kerr effect (present when $m_x = 1$ and $m_y = m_z = 0$) is zero, and at grazing incidence, vice versa. In contrast to the polar and longitudinal effects, the transverse Kerr effect – achieved when the magnetization lies in the plane of the surface, but normal to the light's plane of incidence (so $m_y = 1$ and $m_x = m_z = 0$) – does not influence the polarization of the incident light, but instead only alters the intensity of the reflected light. In the first approximation, all three effects are linearly proportional to the sample magnetization. In both the TRSKM and TROPSOM systems discussed in this thesis, the polar magneto-optical Kerr effect was exploited.

3.2.2 The two- and three-temperature models

Prior to the seminal study published by Beaurepaire *et al.* in 1996,[117] the evolution of the non-equilibrium state between electrons and the lattice was ubiquitously described using a two-temperature model.[116, 122-127] Upon local illumination of the surface of a metal, a significant fraction of the light's energy $\hbar\omega$ is deposited within the skin-depth of the metal's surface. This influx of energy leads to the excitation of "hot" transient electrons, with a corresponding electronic temperature T_e. The hot electrons then thermalize with the unexcited electrons through electron-electron scattering, causing the entire electronic system to reach a new thermal equilibrium compared to that prior to illumination. In Nickel, this process takes about 100 fs.[128] Across a time-scale of picoseconds, energy is then transferred from the electrons to the lattice via electron-phonon scattering. The lattice therefore also thermalizes, with a lattice temperature T_l. The causality implicit within this description – first the electrons are excited to form hot electrons, which then interact with the lattice - arises from the different relative masses of electrons and the lattice.‡ The process discussed above can be modelled using two coupled differential equations[129]

$$\begin{aligned} C_e(T_e)\frac{\partial T_e}{\partial t} &= \nabla\left[k_e(T_e)\nabla T_e\right] - G_{el}(T_e - T_l) + S(\mathrm{r},t) \\ C_l(T_l)\frac{\partial T_l}{\partial t} &= \nabla\left[k_l(T_l)\nabla T_l\right] - G_{el}(T_e - T_l) \end{aligned}, \qquad (3.12)$$

where S represents the laser source term, C_e and C_l are the heat capacities and k_e and k_l are the heat conductivities of the electron and lattice systems respectively, and G_{el} (proportional to the difference between the transient electron and lattice temperatures) accounts for the coupling between the electron and lattice systems. Since all the input terms aside from S depend on temperature, the system of equations given by Eq. 3.12 are non-linear, in general.

In 1996, Beaurepaire *et al.* published[117] the results of stroboscopic magneto-optical experiments, in which a continuous film of magnetized Nickel was optically excited by ultrashort laser pulses. The magnetization of the film was observed to drop rapidly within the first picosecond of illumination, and this was attributed to ultrafast demagnetization induced by the absorption of significant energy by the spin bath. Physically, this can be understood

‡ While the electron-electron / electron-phonon collision times are comparable, the transfer of energy from electrons to electrons is much faster compared to the rate of energy transfer from electrons to phonons.

using either the Bloch Law, or the Landau-Lifshitz-Baryakhtar equation,[87] whereby the thermal energy delivered to the magnetization results in a reduction in the length of the magnetization vector. Beaurepaire *et al.* phenomenologically explained their results by expanding on the two-temperature model, to include a third coupled equation describing the spins

$$\begin{aligned} C_e(T_e)\frac{\partial T_e}{\partial t} &= \nabla\left[k_e(T_e)\nabla T_e\right] - G_{el}(T_e - T_l) - G_{es}(T_e - T_s) + S \\ C_l(T_l)\frac{\partial T_l}{\partial t} &= \nabla\left[k_l(T_l)\nabla T_l\right] - G_{el}(T_l - T_e) - G_{sl}(T_s - T_l) \\ C_s(T_s)\frac{\partial T_s}{\partial t} &= -G_{es}(T_s - T_e) - G_{sl}(T_s - T_l) \end{aligned} \quad , \qquad (3.13)$$

where G_{es} and G_{sl} are the electron-spin and spin-lattice interaction constants respectively, and T_s is the temperature of the spin bath. This expanded model can be easily incorporated within the physical description given earlier, through considering the fact that hot electrons are capable not only of transferring energy to the lattice, but also to the spins.

3.3 Time-resolved scanning Kerr microscopy (TRSKM)

The description of the TRSKM system given here is divided into several sections. In the first section, the entire system will be outlined. In the subsequent sections, I will then discuss in-depth the design of the coplanar waveguide, and the character of the pumping field.

3.3.1 Time-resolved scanning Kerr microscopy system

The layout of the optical apparatus used within the TRSKM system is shown in Fig. 3.2. The laser source consisted of two parts: a diode-pumped continuous-wave (cw) Millenia Pro laser,[§] and a pulsed, mode-locked Tsunami oscillator.[**] The former was responsible for both the initial generation of an infra-red laser beam (of wavelength 1064 nm), and subsequent frequency doubling (using a lithium triborate crystal) of the said infra-red beam to output a visible green laser, of wavelength 532 nm. The Tsunami oscillator - composed of a folded resonant cavity and a titanium-sapphire (Ti:Sa) crystal - was then pumped by the 532 nm beam, outputting a pulsed mode-locked laser beam. The wavelength of this outputted laser could be adjusted between 650 nm and 1000 nm, but the output wavelength was tuned to

[§] Spectra Physics Millenia Pro 10S
[**] Spectra Physics Mode-locked 'Tsunami' Ti:Sapphire laser

800 nm for all the measurements presented in this thesis. The pulse duration was also fixed at 100 fs.

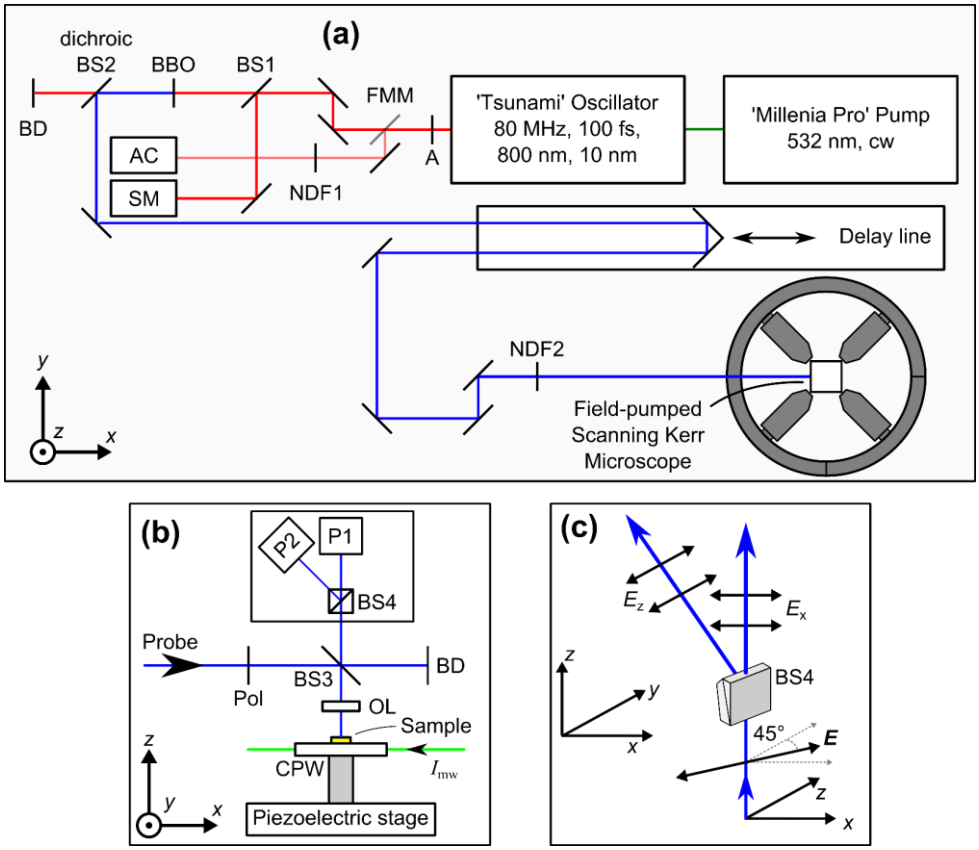

Fig. 3.2 **(a)** The layout of the optical components which comprise the TRSKM system. The abbreviations used correspond to the following: A = Aperture, FMM = Flip-mounted mirror, NDF = Neutral density filter, AC = Autocorrelator, SM = Spectrometer, BS = Beam splitter, BBO = Beta-barium-borate, and BD = Beam dump. **(b)** A side-on view of the field-pumped scanning Kerr microscope. The abbreviations used correspond to the following: Pol = Polarizer, BS = Beam splitter, BD = Beam dump, OL = Objective lens, CPW = Coplanar waveguide, P = Photodiode **(c)** A schematic of the polarizing beam splitter (BS).

For the measurements presented in this thesis, the laser's pulsing repetition rate was always set to 80 MHz. The temporal and wavelength profile of the laser beam was monitored using an APE autocorrelator (AC)[††] and OceanOptics spectrometer (SM),[‡‡] and the

[††] APE autocorrelator pulseCheck USB, Version 150
[‡‡] OceanOptics USB2000+ Spectrometer

cavity optics of the Tsunami oscillator were adjusted so as to achieve a laser beam with a full-duration-half-maximum (FDHM) of 100 fs, and a full-width-half-maximum (FWHM) of 10 nm. The output power of the laser beam (at 800 nm) was 2.7 W (leading to a single pulse having an energy of 33.75 nJ) and s-polarized (with an error less than 1:500). The spatial profile of the beam was TEM_{00}. Nominally, the noise, stability and beam divergence of the laser was lower than 0.2 %, 5 % and 0.18° respectively.

The laser beam, after leaving the Tsunami oscillator, navigated a series of optical elements, mounted and fixed on an optical bench. An aperture (A) was inserted immediately after the oscillator to enable correction of beam drift originating from within the oscillator. The first section of the optical bench was devoted to laser beam diagnostics. The spectrometer was positioned to allow the wavelength and FWHM of the scattered 800 nm laser beam to be checked at any time (the beam was split by a 50:50 beam-splitter BS1), and the autocorrelator was accessed by toggling a flip-mounted mirror (FMM). A neutral density filter (NDF1) was required to reduce the laser power incident on the autocorrelator to a reasonable strength (about 100 mW).

The 800 nm laser beam was then mildly focused by a plano-convex lens onto a crystal of beta-barium-borate (BBO). This is an optically non-linear crystal, which serves to double the frequency of the transmitted light, therefore outputting a visible blue laser beam of wavelength 400 nm. The blue beam was then collimated by a plano-concave lens. Both the lenses positioned before and after the BBO crystal were mounted on linear translation stages, to assist with the focusing and collimation of the incident and transmitted beams. Second harmonic generation can be an inefficient process, due to factors including the quality of focus, the crystalline quality / length of the doubling crystal, and its inherently non-linear aspect. For an input power of 1.35 W at 800 nm, the typical power of the output 400 nm beam was 150 mW, corresponding to a conversion efficiency of 11 %. The output beam from the BBO crystal was a mixture of 400 nm and 800 nm wavelengths, and so spectral separation was achieved through directing the mixed beam toward a longpass dichroic beam splitter (BS2) with a cutoff wavelength of 490 nm. Nominally, this mirror reflected (transmitted) more than 95 % (90 %) of light of wavelength 400 nm (800 nm). The transmitted 800 nm beam was dumped, and the reflected 400 nm beam was directed further across the optical bench. This beam now served as a probe. All mirrors beyond this dichroic beam splitter were

coated broadband dielectric mirrors suited for 350 nm – 400 nm wavelengths, with a nominal reflectivity of more than 99 % at angles of incidence between 0° and 45°.

Generally, to acquire time-resolution in a pump-probe measurement technique, it is necessary to vary the relative time delay between the pump and probe. To achieve this in the TRSKM system, the 400 nm probe beam was directed across a "delay line", which consisted of a retroreflector mounted on a single-axis motorized stage. The motorized stage was capable of linearly translating across a total distance of 60 cm, in nominally minimum steps of 500 nm. By therefore moving the retroreflector from one end of the delay line to the other, the path length of the laser was increased by 1.20 m, corresponding to a 4 ns delay in the time of arrival of the pulse on the sample. The minimum step size of the motorized stage led to a maximum time-resolution of 3.33 fs.

After traversing the delay line, but prior to entering the Kerr microscope, the power of the probe was reduced using a neutral density filter (NDF2), both to avoid burning the sample and damaging the detecting photodiodes (the latter devices had a damage threshold of about 20 mW). It is also necessary to note that, so far, the beam has been navigating the optical bench across a plane maintained 11 cm above the surface of the optical bench. The entrance to the Kerr microscope was about 29 cm above the optical bench, and so a periscope assembly was used to raise the height of the probe beam.

The probe was then directed into the Kerr microscope, the layout of which is presented in Fig. 3.2 (b). Note the viewpoint has been rotated here, compared to that used in panel (a). The incident beam was initially passed through a vertically-oriented polarizer, in order to eliminate any possible polarization rotation induced by the dielectric mirrors, and then split by a 50:50 non-polarizing beam splitter (BS3). The transmitted beam was dumped onto a white screen, and the reflected beam was directed toward an objective lens (OL), which was itself mounted on a piezo-electric stage, capable of moving 300 μm along all three Cartesian axes, in stable and reproducible steps of 10 nm. The objective lens[§§] used to focus the probe beam had a numerical aperture of 0.75, which nominally focused the probe into a diffraction-limited spot of diameter 340 nm onto the surface of the sample. Since the probe beam had a diameter larger than that of the entrance aperture of the objective lens, the profile of the focused beam was unaffected by the lateral translation of the piezo-electric stage.

[§§] Zeiss Objective LD Plan-Neofluar 63x / 0.75 Corr Ph2.

The sample was mounted on a coplanar waveguide (CPW), positioned underneath the objective lens. Further details regarding the CPW are discussed in Section 3.3.2. The CPW itself was mounted on a piezo-electric stage, capable of stepping by 300 nm in the *x*-*y* plane up to a maximum of 25 mm along both axes. The bias magnetic field across the sample was delivered by a quadrupole electromagnet, which was assembled by Dr. Yat-Yin Au. To construct this electromagnet, a copper wire was extensively wound about each cylindrical steel pole, and each wire was then connected to a 4-port junction box. Upon driving a dc current around the steel poles,[***] a net magnetic field was generated between the four poles. By switching the direction of the flow of current about the poles, the bias magnetic field could be directed along the positive and negative *x*- and *y*-axes as required. The strength and direction of the bias magnetic field was measured using a Hall effect sensor[†††] - by measuring the magnetic field generated by the electromagnet, as a function of current, the magnetic field was calibrated. The maximum bias magnetic field that could be delivered across the sample was measured to be 729 Oe.

Upon reflection from the sample surface, the probe beam was collected and collimated by the same objective lens, and directed again across the 50:50 beam splitter (BS3). The non-polarizing beam splitter dumped 50 % of the beam back out of the Kerr microscope, but the 50 % transmitted was directed towards an optical bridge detector. The optical bridge detector used in this setup was assembled by Dr. Yat-Yin Au.

An optical bridge detector contains a polarizing Glans-Thompson beam splitter (BS4) and two photodiodes (P1 and P2).[‡‡‡] The former optical element was itself composed of two cemented birefringent crystals of calcite, aligned so that their optical axes are parallel. Birefringent crystals are generally characterized by two distinct refractive indices $n_{\parallel}$ and $n_{\perp}$, depending on whether the incident light has an electric field parallel or orthogonal to the crystal's optical axis respectively. The crystal was cut in such a fashion so that $n_{\parallel} < n_{\perp}$ - hence the beam with an electric field parallel to the optical axis was unaffected in its path, whereas the beam with orthogonal polarization was deflected at 45°. This mechanism of polarization splitting is schematically shown in Fig. 3.2 (c). The two separated beams were then detected by two balanced silicon photodiodes of diameter 0.8 mm (which have a

[***] The current was delivered by a XHR 100-10 DC Power supply.
[†††] Lakeshore Model 421 Gaussmeter.
[‡‡‡] Strictly speaking, the silicon photodiodes were outside the bridge detector, and two fibre-optic cables were used to direct the collected light into the photodiodes.

responsivity of 0.14 A/W at 400 nm). Transimpedance amplifiers, with a gain of 10^6 Ω, were then used to convert the currents generated by the illuminated photodiodes into voltage signals.[§§§]

Prior to applying any excitation across the magnetic sample, the optical bridge detector was rotated such that the voltages recorded by the two photodiodes were equal. By monitoring the spatial distribution of the dc voltages in each photodiode, one can acquire images of the sample's surface, enabling the beam to be effectively focused. Now, upon exciting the magnetic sample, a small out-of-plane dynamic component of magnetization is generated, which rotates the plane of polarization of the incident light upon reflection by an angle Φ^K. The difference of the intensity of light detected by P1 and P2 is therefore

$$(I_{P1} - I_{P2}) \propto \left[\cos^2\left(\frac{\pi}{4} + \Phi^K\right) - \cos^2\left(\frac{\pi}{4} - \Phi^K\right) \right] \tag{3.14}$$

Using the trigonometric identity $\cos(\alpha + \beta) = \cos\alpha\cos\beta - \sin\alpha\sin\beta$, and the small angle approximation, Eq. 3.14 reduces to

$$(I_{P1} - I_{P2}) \propto \Phi^K \tag{3.15}$$

Since the Kerr angle is linearly proportional to the magnetization, the difference $(I_{P1} - I_{P2})$ represents the change in the out-of-plane component of magnetization.

The hierarchy of the electrical circuitry underpinning the TRSKM system is shown in Fig. 3.3 (a). A master clock[****] synchronized the repetition rate of the Tsunami oscillator (80 MHz) with the frequency of a microwave generator. The microwave generator outputted electrical signals of either pulsed[††††] or continuous-wave[‡‡‡‡] character (in the latter case, the frequency needed to be an integer multiple *n* of the Tsunami oscillator's repetition rate). The output from the microwave generator was further modulated by a function generator,[§§§§] which imparted a microwave current of frequency 3 kHz with periodic rectangular form. This modulation of the pump served to modulate the measured signal, enabling lock-in detection to be used. The electrical signal derived from the optical bridge detector was then measured

[§§§] The silicon photodiodes / transimpedance amplifier were integrated within a Thorlabs Balanced Amplified Photodetector, model PDB450A.
[****] AtlanTecRF Low Phase Noise Oscillator Instrument.
[††††] Picosecond Pulse Labs Impulse Generator, Model 3600.
[‡‡‡‡] Rohde & Schwarz SMF100A Microwave Signal Generator.
[§§§§] Agilent Technologies 33120A Function Generator (discontinued).

using a lock-in-amplifier[*****] at the reference frequency of 3 kHz (lock-in detection was required due to the small size of the signal, which was on the order of microvolts). The relative timings of the electronic devices are shown in Fig. 3.3 (b) – (f).

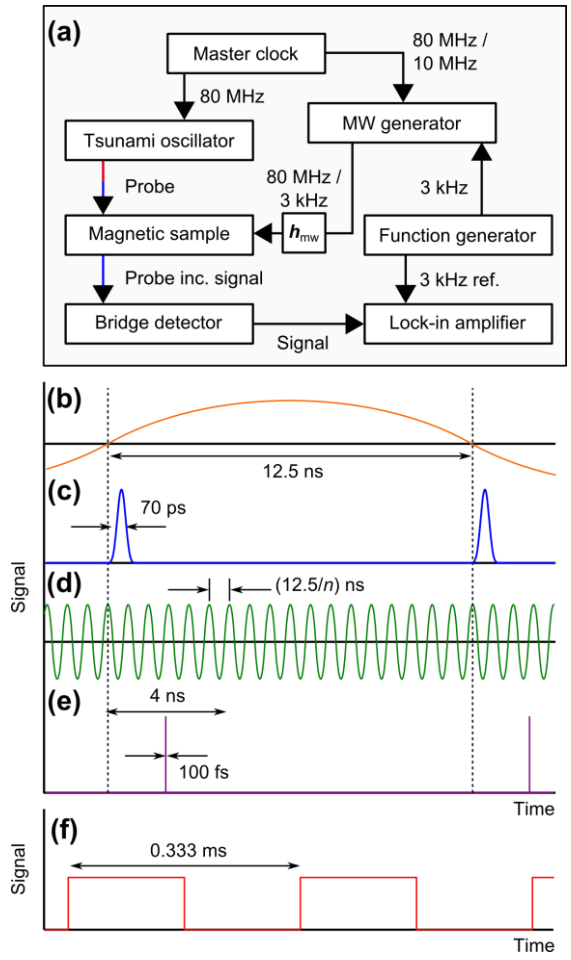

Fig. 3.3 **(a)** A schematic of the electrical circuitry underpinning the TRSKM system. **(b)-(f)** The relative timings between the electronic and optical signals interacting in the TRSKM system. Panel (b) shows the 80 MHz signal from the master clock, which is used to synchronize the timing of the pump and probe. Panels (c) and (d) show the electrical currents (pulsed and harmonic respectively) driven across the coplanar waveguide, used to pump magnetization dynamics. Panel (e) shows the optical pulse, which is used to probe the magnetization dynamics across an adjustable time of 4 ns. Panel (f) shows the rectangular electrical signal, used to modulate the pump at a frequency of 3 kHz.

[*****] Signal Recovery DSP Lock-In Amplifier, Model 7265.

3.3.2 Coplanar waveguide

The pumping field used within the TRSKM system was delivered by a coplanar waveguide. A schematic of the coplanar waveguide is given in Fig. 3.4. The coplanar waveguide consists of a printed circuit board (PCB), which is geometrically divided into three sections. On the left and right sides of the PCB, the regions are grounded (ground), and in the center, the region is electrically active (signal). The signal and ground lines were separated by air gaps of width 250 μm, and the width of the signal line was 500 μm. For the TRSKM measurements discussed in this thesis, the magnetic sample was always mounted on a glass cover slip, of thickness 0.17 mm. The electrical current, of either pulsed or harmonic temporal character, was delivered to the signal line via SubMiniature version A (SMA) connectors of fixed impedance 50 Ω. The static bias field was delivered by the quadrupole magnet (discussed in Section 3.3.1).

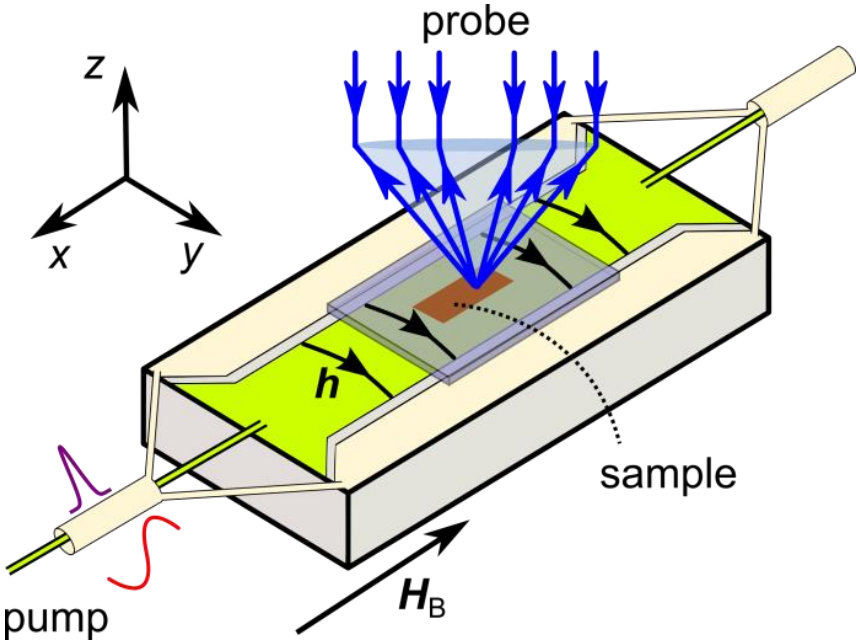

Fig. 3.4 A sketch of the coplanar waveguide, upon which the magnetic sample was mounted. The magnetic sample was uniformly biased by the static field $\boldsymbol{H}_B$, pumped by a microwave field $\boldsymbol{h}$, and the focused optical probe was scanned across the sample surface in order to measure the dynamic out-of-plane component of magnetization via the magneto-optical Kerr effect.

3.3.3 Character of the pumping field

The pump magnetic field generated by the signal line of the CPW was regularly changed, depending on the type of measurement that was being performed. The first type of pump field employed to excite magnetization dynamics had pulsed temporal character, consisting of a train of pulses, each with a full-duration half-maximum (FDHM) of 70 ps. This train was synchronized with the Tsunami oscillator, so the repetition rate was similarly 80 MHz. The FDHM of 70 ps leads to an excitation which dramatically decreases in strength at frequencies above 10 GHz. The second type of pump field had harmonic temporal profile, which was again synchronized with the Tsunami oscillator. The microwave generator used was capable of delivering continuous-wave excitations up to 20 GHz. To achieve synchronization with the Tsunami oscillator, the frequency of the continuous-wave excitation needed to be an integer multiple of 80 MHz.

Due to the sample usually being mounted on a glass substrate, and therefore being separated from the CPW by a distance of about 0.17 mm, the magnetic field generated by the current across the signal line had significant spatial nonuniformity. Assuming the distribution of current across the cross-section of the signal line is uniform, the spatial distribution of the in-plane (h_y) and out-of-plane (h_z) components of the field generated by a current-carrying strip (of width $2w$ and thickness $2s_m$, conducting a current I) is[130]

$$h_y(y,z) = -\frac{I}{8\pi w s_m}\cdot\left[\begin{array}{l}(w-y)\left[\begin{array}{c}\frac{1}{2}\ln\left(\frac{(s_m-z)^2+(w-y)^2}{(-s_m-z)^2+(w-y)^2}\right)\\ +\frac{s_m-z}{w-y}\tan^{-1}\left(\frac{w-y}{s_m-z}\right)-\frac{-s_m-z}{w-y}\tan^{-1}\left(\frac{w-y}{-s_m-z}\right)\end{array}\right]\\ -(-w-y)\left[\begin{array}{c}\frac{1}{2}\ln\left(\frac{(s_m-z)^2+(-w-y)^2}{(-s_m-z)^2+(-w-y)^2}\right)\\ +\frac{s_m-z}{-w-y}\tan^{-1}\left(\frac{-w-y}{s_m-z}\right)-\frac{-s_m-z}{-w-y}\tan^{-1}\left(\frac{-w-y}{-s_m-z}\right)\end{array}\right]\end{array}\right] \tag{3.16}$$

$$h_z(y,z) = \frac{I}{8\pi w s_m}\cdot\left[\begin{array}{l}(s_m-z)\left[\begin{array}{c}\frac{1}{2}\ln\left(\frac{(s_m-z)^2+(w-y)^2}{(s_m-z)^2+(-w-y)^2}\right)\\ +\frac{w-y}{s_m-z}\tan^{-1}\left(\frac{s_m-z}{w-y}\right)-\frac{-w-y}{s_m-z}\tan^{-1}\left(\frac{s_m-z}{-w-y}\right)\end{array}\right]\\ -(-s_m-z)\left[\begin{array}{c}\frac{1}{2}\ln\left(\frac{(-s_m-z)^2+(w-y)^2}{(-s_m-z)^2+(-w-y)^2}\right)\\ +\frac{w-y}{-s_m-z}\tan^{-1}\left(\frac{-s_m-z}{w-y}\right)-\frac{-w-y}{-s_m-z}\tan^{-1}\left(\frac{-s_m-z}{-w-y}\right)\end{array}\right]\end{array}\right] \tag{3.17}$$

as defined for the co-ordinate system shown in the inset of Fig. 3.5. One can therefore use Eqs. 3.16 – 3.17 to model the magnetic field generated by the CPW system (which was assumed to have an impedance of 50 Ω, and power of 22 dBm), at a distance of 170 μm above the signal line.

The field profiles presented in Fig. 3.5 are characteristic of the magnetic field generated by a microstrip - due to the symmetry of the microstrip, h_y (h_z) is symmetric (antisymmetric). Because there is significant distance between the PCB and the magnetic sample, h_y and h_x are relatively non-uniform. However, since the samples investigated typically spanned micron length-scales, the exciting field was assumed to be spatially uniform. Furthermore, the sample was always positioned at (or close to) the center of the signal line, and so it was reasonable to assume there was negligible out-of-plane excitation of the sample.

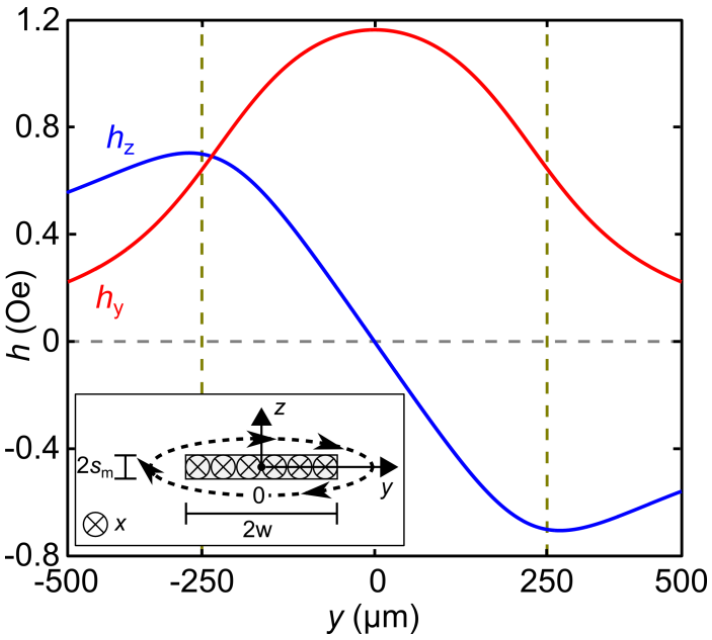

Fig. 3.5 The spatial distributions of the in-plane (blue line h_z) and out-of-plane (red line h_y) magnetic field generated by a microstrip mimicking the signal line of the CPW, as calculated using Eqs. 3.14 - 3.15. The fields were calculated for a 500 μm-wide microstrip carrying a current of 210 mA, at a height z = 170 μm above the signal line. Inset: the geometry of the system described by Eqs. 3.16 - 3.17.

3.4 Time-resolved optically-pumped scanning optical microscopy (TROPSOM)

In this section, I will discuss the TROPSOM system, which was first assembled by Dr. Toby Davison, Dr. Yat-Yin Au, and Prof. Volodymyr Kruglyak. Since I have substantially modified the experimental setup from its first design, I will discuss both the implementation and alignment of the TROPSOM system.

3.4.1 Time-resolved optically-pumped scanning optical microscopy system

The TROPSOM system shares the same optical bench as the TRSKM system, and the layout of the apparatus is shown in Fig. 3.6 (a). The Millenia pump, Tsunami oscillator, and the beam diagnostic equipment were unchanged from the TRSKM system. However, from this point on, significant changes to the setup were made. In TROPSOM's first design,[131-132] the 800 nm (400 nm) beam was used as the optical pump (probe). In the setup discussed in this section, the roles of the 800 nm and 400 nm beams were switched, so as the 800 nm (400 nm) acted as the optical probe (pump). The main motivation for implementing this change to the previously-constructed TROPSOM system involved the sensitivity of the detection mechanism. The responsivity of the silicon photodetectors to 800 nm and 400 nm light was 0.53 A/W and 0.14 A/W respectively -therefore, by switching the roles of the 800 nm and 400 nm beams, it was anticipated that the signal-to-noise ratio (SNR) in the detected signals would improve by a factor of about 4. Of course, the disadvantage associated with this change was that the spatial resolution of the acquired images was sacrificed by a factor of two, but this represented a trade-off for the improved SNR.

Considering first the pumping aspect of the TROPSOM setup, the path of the 400 nm beam was rerouted so that it was contained only on the left-hand side of the optical bench. A neutral density filter (NDF2) and two shortpass color filters (CF1 and CF2, both having a cutoff wavelength of 450 nm) were positioned immediately after the dichroic beamsplitter, so as to control the beam power and eliminate any remaining 800 nm light. The beam was then directed through an optical chopper, which consisted of a slotted disc capable of mechanically rotating at a well-defined frequency, therefore modulating the intensity of the pump. After passing through the optical chopper, the beam was directed across a series of coated broadband dielectric mirrors (added to easily adjust the length of the path traversed by the pump), and then sent through a polarizer (Pol). This ensured that light of well-defined linear polarization was incident on the sample. The beam then passed through a quarter wave-plate

(λ/4), which was occasionally used to convert the polarization of the pump light from linear to circular. The 400 nm pump was then focused through the sapphire substrate on the underside of the magnetic sample by an objective lens[†††††] (OL1), of numerical aperture 0.75, in order to form a diffraction-limited spot of diameter 340 nm on the surface of the sample. The objective lens had a correction collar, which nominally enabled the path of the focused beam to be corrected for the refraction through the sapphire substrate. To assist with the focusing and alignment of this pump beam, the objective lens was mounted on a motorized translation stage, capable of moving along the *x*-axis by 25 mm.

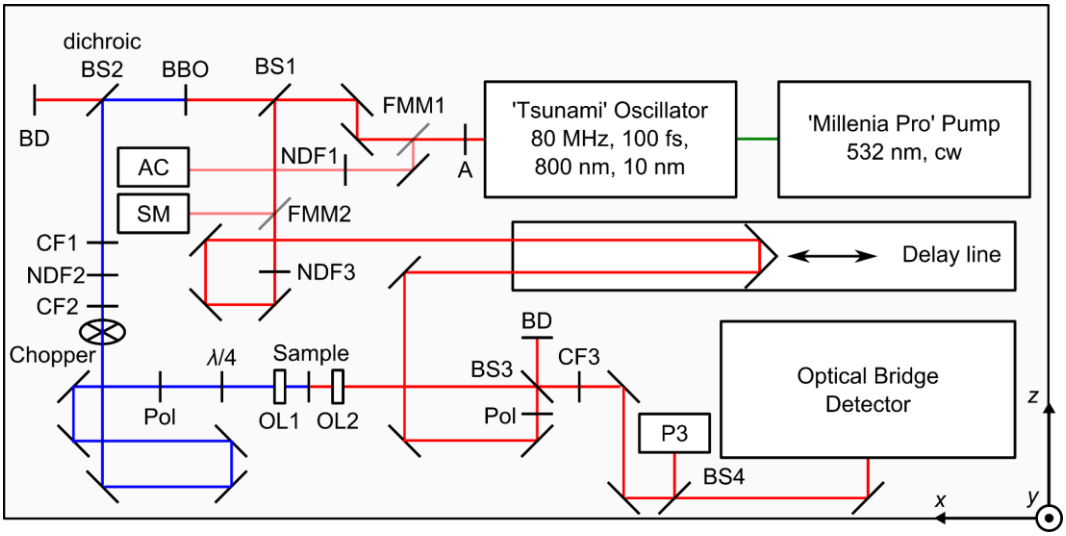

Fig. 3.6 The layout of the optical components which comprise the TROPSOM system. The abbreviations used correspond to the following: A = Aperture, FMM = Flip-mounted mirror, NDF = Neutral density filter, AC = Autocorrelator, SM = Spectrometer, BS = Beam splitter, BBO = Beta-barium-borate, BD = Beam dump, CF = colour filter, Pol = Polarizer, λ/4 = Quarter-wave plate, OL = objective lens, and P = Photodiode.

In contrast to the 400 nm pump beam, the 800 nm probe beam occupied the majority of the space across the optical bench. Prior to its arrival at the sample, it was directed across the delay line (thus giving temporal resolution), and passed through a polarizer, again to ensure vertical polarization. The beam was then split by a 70:30 non-polarizing beam splitter (BS3), which dumped 70 % of the transmitted beam, and directed the remaining 30 %

[†††††] Zeiss Objective LD Plan-Neofluar 63x/0.75 Corr Ph2

towards an objective lens[‡‡‡‡‡] (OL2) of numerical aperture 0.8. The slightly higher numerical aperture, in contrast to that used to focus the 400 nm pump beam, allowed the red probe beam to be focused to a diffraction-limited spot of diameter 637 nm on the sample surface. The objective lens used to focus the probe beam was mounted on a three-axis piezoelectric stage, and this assembly itself was mounted on a single-axis translation stage, to assist with focusing and alignment. The details of the procedures by which the pump and probe beams were focused on the sample surface is discussed in Section 3.4.2. An important point relates to the relative delay between the pump and probe beams. For the probe pulse to impinge on the sample both before and after the arrival of the pump pulse, the probe's minimum path length needed to be slightly shorter than the pump's. For the measurements discussed in this thesis, the pump's path length was fixed at about 322 cm, and the probe's minimum path length was about 289 cm. This difference allowed 1.1 ns (2.9 ns) to be recorded at negative (positive) time delay, relative to the arrival of the pump.

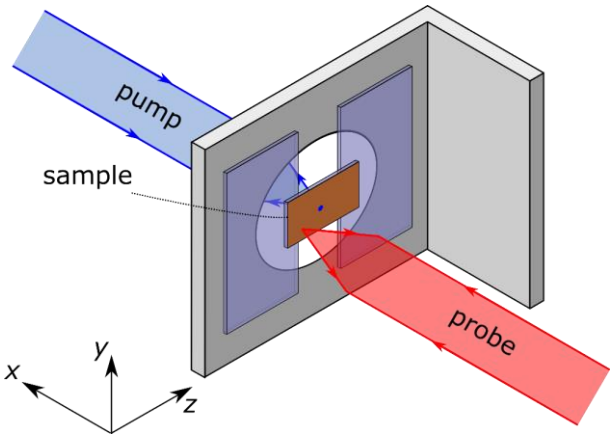

Fig. 3.7 A sketch of the sample holder, upon which the magnetic sample was mounted, and the relative orientations of the pump and probe laser beams.

Upon reflection from the sample surface, the probe was collimated by the same objective lens (OL2), and the beam thereafter was again incident on the 70:30 non-polarizing beam splitter. Now, 30% of the signal-carrying probe was dumped, and the other 70 % was filtered (using a longpass color filter, with a cutoff wavelength of 750 nm). This filter was essential in preventing any transmitted pump beam from polluting the detected signal. The filtered probe was then sampled by a 90:10 non-polarizing beam sampler, whereby 10 % of the signal was directed toward a single photodetector (labelled P3, intended to measure the

[‡‡‡‡‡] Zeiss EC Epiplan-Neofluar 50x/0.80 HD DIC M27

transient reflectivity of the sample), and the other 90 % was directed towards the same optical bridge detector as was used in the TRSKM system.

The electrical plumbing of the TROPSOM system was simpler compared to that used in the TRSKM system, due to the optical character of both the pump and probe. The mechanical chopper, used to modulate the intensity of the pump beam at a frequency of 800 Hz, was synchronized with the two lock-in amplifiers used to measure the transient reflectivity / Kerr signals. The hierarchy of the electrical circuity is presented in Fig. 3.8 (a), and the relative timings in Fig. 3.8 (b)-(e).

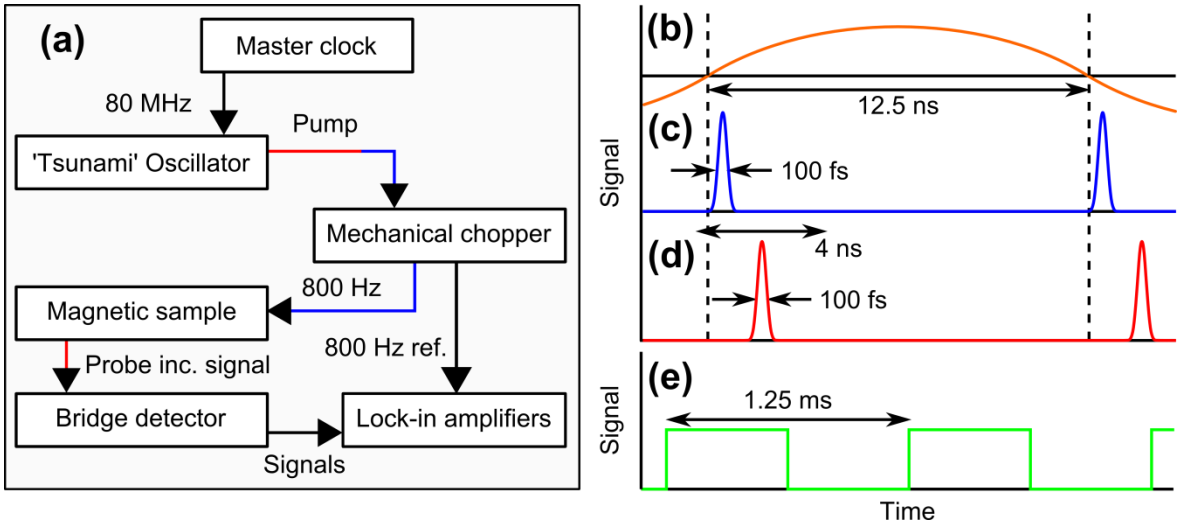

Fig. 3.8 **(a)** The circuitry which underpins the TROPSOM system. **(b)-(e)** The relative timings of the signals in the TROPSOM system. Panel (b) shows the 80 MHz signal from the master clock, which is used to synchronize the timing of the pump and probe. Panel (c) shows the 400 nm optical pulse, used to pump magnetization dynamics. Panel (d) shows the 800 nm optical pulse, which is used to probe the magnetization dynamics across an adjustable time of 4 ns. Panel (e) shows the modulation of the pump (800 Hz) introduced by the optical chopper.

3.4.2 Aligning and focusing the pump / probe beams

There were two key challenges associated with using the TROPSOM system. The first was related to the alignment of the setup. To optimally use the system, the pump and probe beams needed to be parallel to each other, and also share the same focal point in all three dimensions (prior to scanning). The second involved the maintenance of a stable

system. Due to the TROPSOM setup primarily having three independent, crucial components (the two objective lenses and the sample holder) highly sensitive to disturbances, any vibrations or fluctuations could induce non-systematic misalignment of all three components. Furthermore, since the time constant of the lock-in-amplifiers needs to be at least 500 ms to achieve a reasonable signal-to-noise ratio in the detected signals, the TROPSOM system needed to be running in a stable manner for several hours. Vibrations or fluctuations resulting in misalignments therefore posed significant problems in recording signals of good quality. As part of my redevelopment of the TROPSOM system, I have developed a protocol which addresses the challenge of static system alignment, and I will first outline this. In the subsequent section, I will then discuss the different strategies which have been used to improve system stability.

To align the TROPSOM system, the pump and probe beams needed to be aligned parallel with identical focal points. To achieve this, the pump beam was blocked, and the probe beam was first aligned so as to form a focused spot on the surface of the mounted sample (specifically, the optimum position of OL2 along the *x*-axis was determined). Subsequent optical elements were then aligned so as to direct the reflected probe beam into the two detectors. Once this was achieved (such that a well-focused reflectivity image of the sample surface could be obtained), both the magnetic sample and the color filter (CF3) were removed. Using only the optical elements prior to OL1, the path of the pump beam focused by OL1 was adjusted, so that the pump beam had similar diameter before and after passing through both objective lenses. A cartoon of this geometry is given in Fig. 3.9 (a). Again, using only the optical elements prior to OL1, the pump beam was then aligned so as to be detected by the two signal monitors of the optical bridge detector. This alignment procedure thus enabled the pump beam to be diagnosed in its spatial character, by scanning OL2. Generally, two types of optical artefacts were observed. First, coma aberration led to the appearance of the elliptical pump spot shown in Fig. 3.9 (b). This arose from the pump beam being slightly canted away from the *x*-axis. Second, clipping of the beam (shown in Fig. 3.9 (c)) arose from the beam not being centered on all the optical elements. Upon correction of these two optical artifacts, a focused pump spot as shown in Fig. 3.9 (e) was obtained. Notice that the spot does not appear to be diffraction-limited in its diameter: this is due to the two objective lenses OL1 and OL2, focusing and collimating the beam, having a slight difference in their numerical apertures. Upon defocusing the pump beam (by moving the probe lens by several microns along the optical axis), the pump spot was observed to neither significantly

distort nor shift (Fig. 3.9 (d) and Fig. 3.9 (f)), hence leading to the conclusion that the pump and probe beams were reasonably aligned across the optical bench.

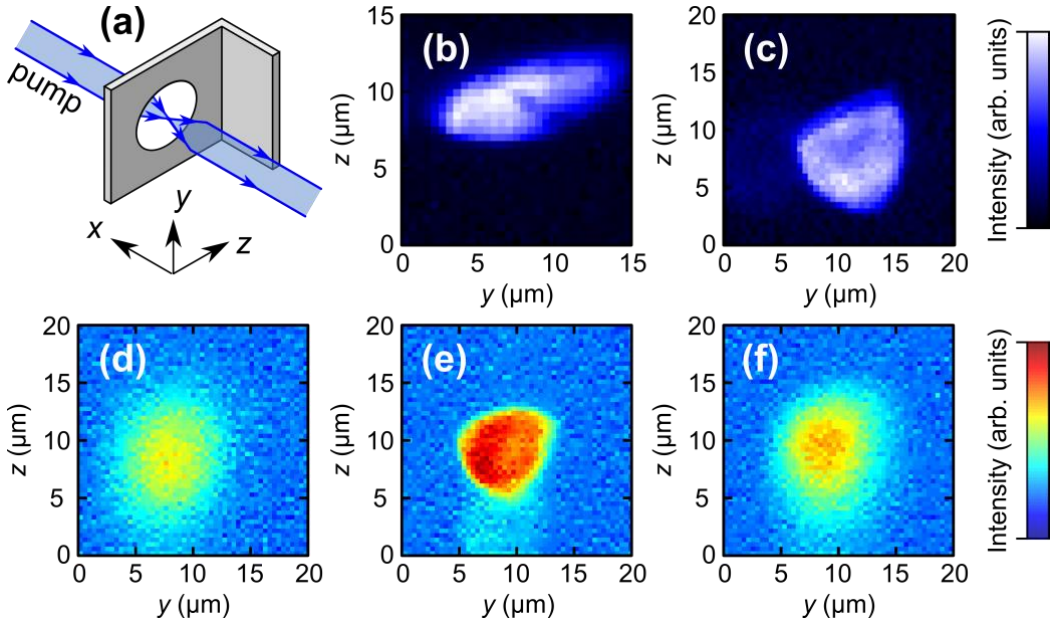

Fig. 3.9 **(a)** The geometry which enables the spatial profile and alignment of the pumping beam to be diagnosed. **(b)-(c)** Measurements of the pump spot where the optical artefacts of coma aberration and clipping have distorted the pump beam respectively. Note these images are not normalized relative to each other. **(d)-(f)** Normalized images of the correctly-aligned pump beam, recorded when the probe's objective lens was positioned at x = +13 μm, x = 0 μm and x = -7 μm respectively.

Upon correctly aligning the pump beam with respect to the probe, the sample was remounted onto the sample holder, and the color filter CF3 was reinserted. The power of the pump beam was then increased, so as to be visible upon collimation by OL2, and the position of OL1 was adjusted along the x-axis so as the diameter of the collimated beam was close to the diameter of the beam prior to it entering OL1.[§§§§§] The sample was locally ablated during this stage of the alignment, but once the suitable x-coordinate of OL1 was deduced, the power of the pump was reduced, and then the magnetic sample was moved laterally, so as to probe

[§§§§§] Throughout the work discussed in this thesis, the sample was mounted on a sapphire substrate of thickness 0.33 mm ($n_{Sapphire}$ = 1.79). This led to a conflict in that the correction collar of all objective lenses commercially available is designed for use with glass (n_{glass} = 1.5). The correction collar was therefore adjusted to (0.33×[$n_{Sapphire}$/n_{glass}]) = 0.39 mm. This seemed to be adequate in forming a focused pump spot with a diameter close to that defined by the diffraction limit.

an undamaged surface. The focus of the pump and probe beams was fine-tuned by iteratively recording the transient reflectivity signal on the surface of the sample, for varying positions of OL1 and OL2. It was assumed that the transient reflectivity signal at small but positive time-delay represented the spatial distribution of the pump spot. Images of the focused pump spot (acquired for a 20 nm-thick film of Permalloy) at varying positions of OL1 are shown in the top panels of Fig. 3.10 (a) - (d). In the bottom panels of Fig. 3.10 (a) - (d), cross-sectional slices across the images are presented, revealing quantitatively the spatial-extent of the pump spot. In Fig. 3.10 (c) in particular, the transient reflectivity signal had a cross-sectional full-width half-maximum of 1.4 μm and 1.8 μm.

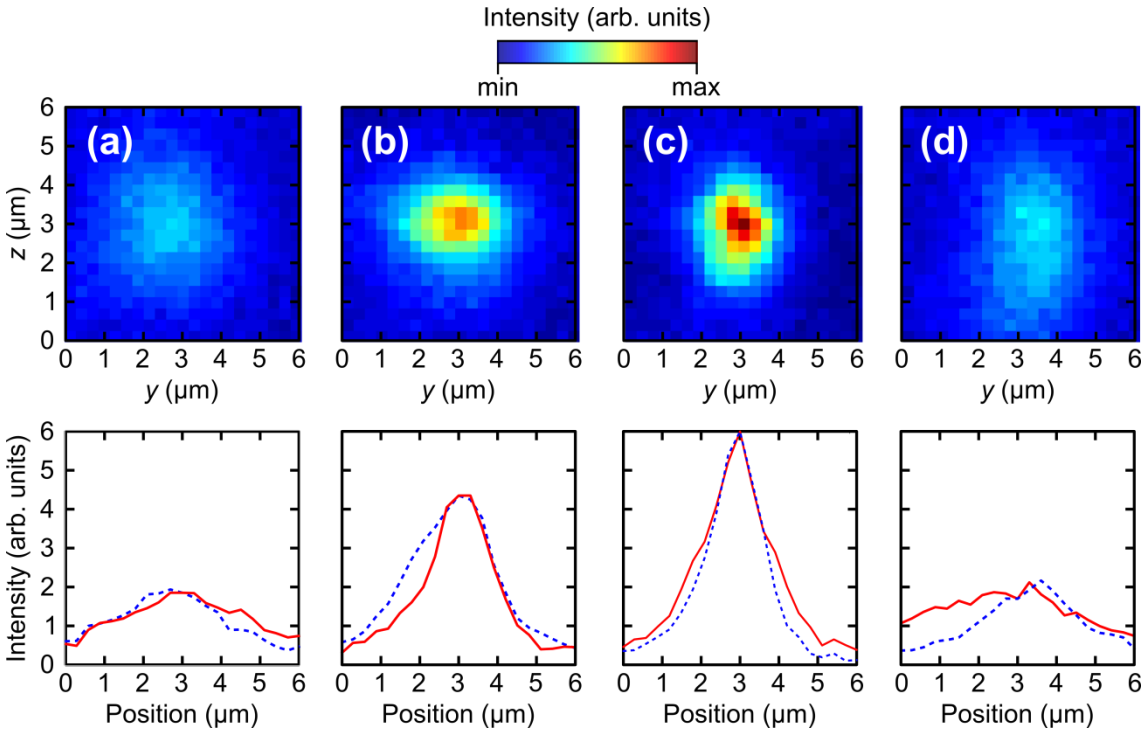

Fig. 3.10 Top panels: Spatial images of the transient reflectivity signal. Bottom panels: Cross-sectional slices taken from the top panels, either along the line y = 3 μm (red solid line) or z = 3 μm (blue dashed line). **(a) - (d)** The signals acquired with a 20 nm-thick Permalloy film, when the objective lens focusing the pump was positioned at x = +6 μm, x = +1 μm, x = 0 μm, and x = -3 μm respectively.

3.4.3 Maintaining system stability

After aligning the TROPSOM system, preliminary measurements were performed in order to gain insight into the signals that one could expect. This testing revealed a significant source of instability in the setup. Presented in the top panels of Fig. 3.11 (a)-(b) are the DC

reflectivity signal (left panel) and the dynamic Kerr signal (right panel), recorded across a uniformly-flat surface of Permalloy, far from the pump spot. Evident in both images are bands of increased / decreased signal. The images were obtained through raster-scanning the focused probe across the *y*-axis, with a time-constant of 1 s, and each pixel took 3 s to record. It must be emphasized that the bands are slightly inclined in the shown images. The images were then replotted as a function of time, as shown in the middle panels of Fig. 3.11 (a) - (b), and the previously-identified bands clearly correspond to periodic oscillations. Upon Fourier-transforming the time-varying signals, the frequency spectra shown in the lower panels of Fig. 3.11 (a) - (b) were obtained. The oscillations clearly had a characteristic frequency of 0.4 mHz.

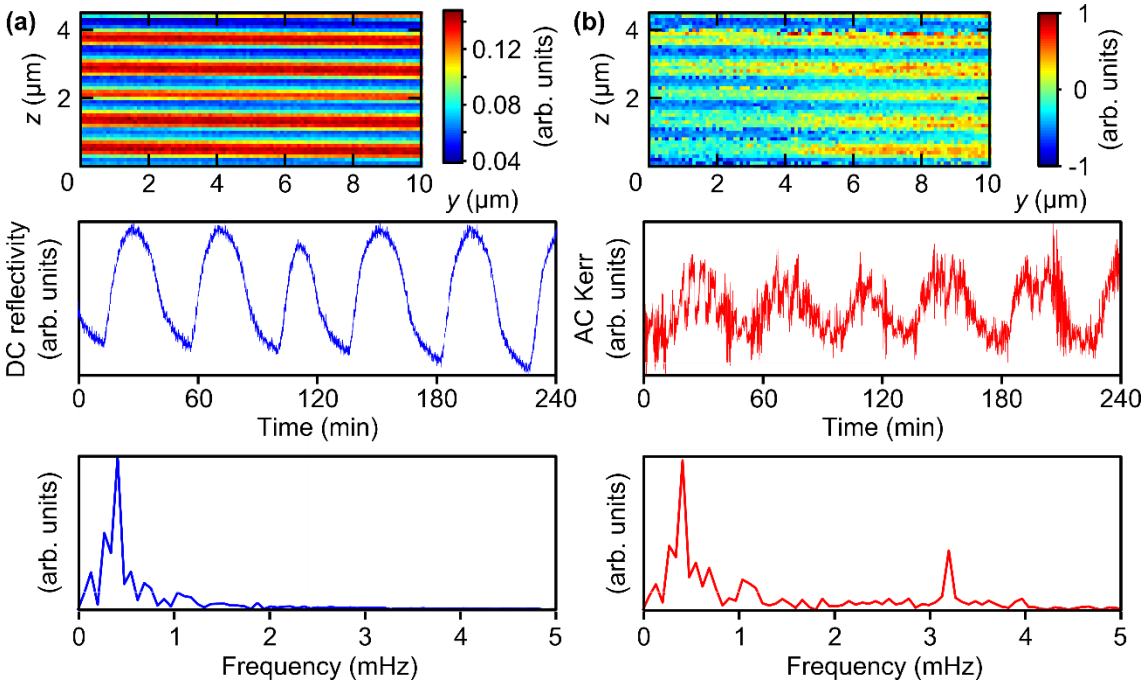

Fig. 3.11 **(a)-(b)** Top panel: Spatially-resolved DC reflectivity (left) and AC Kerr signals (right) respectively, acquired far from the pump spot on a continuous film of 20 nm-thick Permalloy. Middle panel: The spatial images as shown in the top panels, but given as a function of time. Lower panel: The Fourier transform of the signals shown in the middle panels.

The bands / oscillations observed in Fig. 3.11 are not associated with any signal induced by the pump. Rather, they must either originate from oscillations of the sample, or from fluctuations inherent to the laser generated by the Millenia pump / Tsunami oscillator system. To try to identify the source of the oscillations, the power of the laser beam was

recorded at various positions across the optical bench. The results of this testing are shown in Fig. 3.12 (a) - (c), where the top panels show the time-varying oscillation, and the lower panels show the corresponding frequency spectra. The signal shown in Fig. 3.12 (a) was recorded immediately after the color filter CF3, corresponding to the probe beam reflected by the sample. Here, the oscillations are very strong, on the order of 25% of the entire beam amplitude. The same signal was then recorded after POL2 but before BS3, corresponding to the probe beam prior to incidence on the sample. In this signal, the oscillations are still apparent, but the oscillations are on the order of about 3%. This indicated that the beam reflection led to an eight-fold reduction in the signal-to-noise ratio.

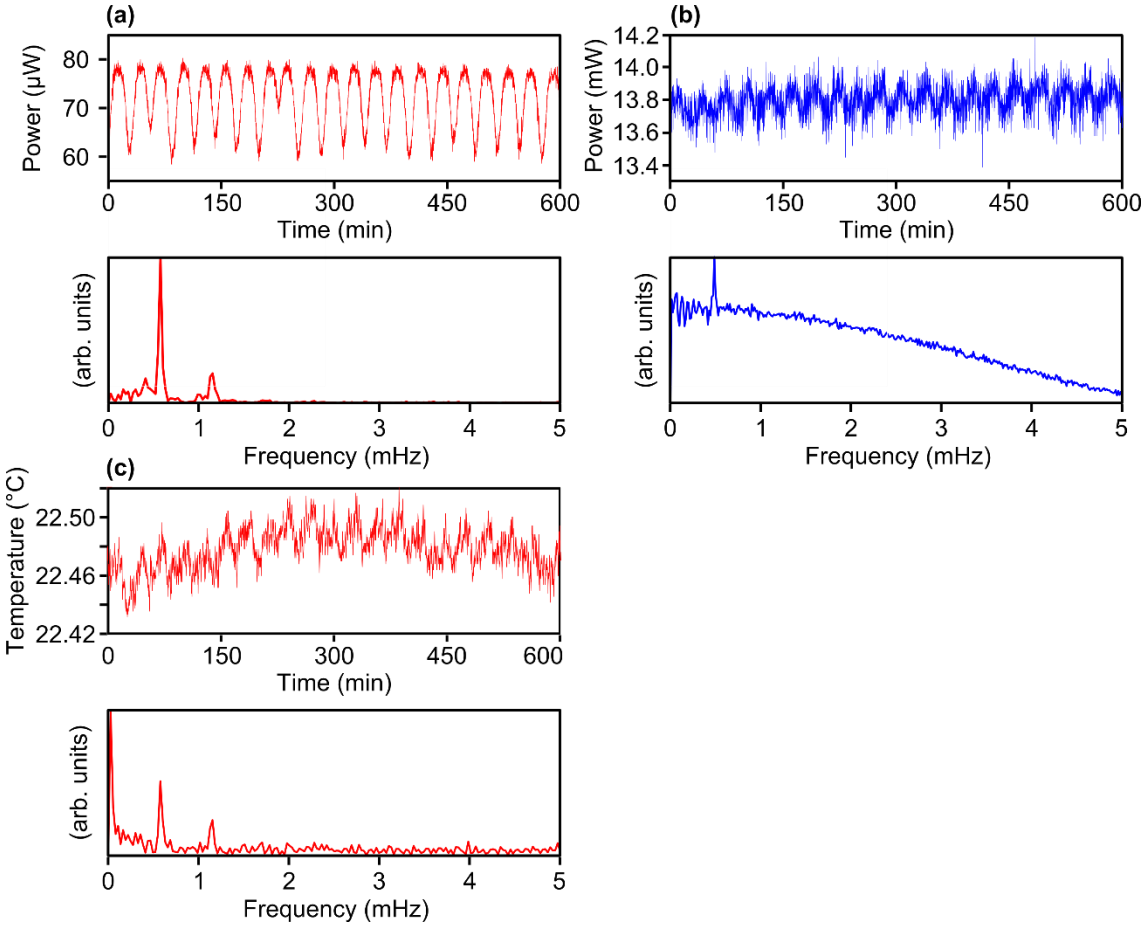

Fig. 3.12 **(a)-(b)** The power of the 800 nm beam (upper panels) recorded after and before reflection of the beam by the sample surface respectively, and the corresponding frequency spectra (lower panels). **(c)** The local temperature (upper panel), recorded at the same time as the measurement presented in (a), and the corresponding frequency spectrum (lower panel).

Along with recording the power of the laser beam, the power meter used was also capable of simultaneously recording the local temperature. Presented in Fig. 3.12 (c) is the temperature variation simultaneously recorded alongside the signal shown in Fig. 3.12 (a). Apparent are oscillations in the local temperature, with frequencies corresponding to the observed bands. The laboratory was air-conditioned in order to maintain a constant temperature of 18 °C. The fact that the local temperature across the enclosed optical bench was about 22.5 °C demonstrated that the Millenia pump, while continuously water-cooled to maintain an operating temperature of 18 °C, radiated heat which generally raised the temperature of the enclosed TRSKM / TROPSOM system.

It was therefore hypothesized that the laser diode was improperly chilled, leading to weak oscillations in the laser power. This improper chilling also generated periodic air currents across the optical bench, which caused the sample holder to similarly oscillate – this latter effect led to the eight-fold increase in the oscillations detected. Further discussion of the approaches used to minimize the impact of this noise will be given in Chapter 7.

3.5 Brillouin light scattering (BLS) microscopy

The results of Brillouin light scattering (BLS) microscopy are occasionally referred to in this thesis. These results were collected not by myself, but by Dr. Alexandr Sadovnikov and Dr. Sergey Grishin at Saratov State University in Russia. These experimental measurements were used to complement the results of micromagnetic simulations wholly performed by myself. Since I had no part in recording the experimental BLS measurements, I will only discuss (very briefly) the theory underlying BLS microscopy, and the experimental setup, so as the results referred to can be understood.

BLS microscopy[82] is underpinned by the inelastic interaction between light and spin waves. This can be understood using the particulate description of photons and magnons scattering off each other. Specifically, the energy- and momentum-conservation relations lead to the equations

$$\omega_r = \omega_i \pm \omega_{SW} \tag{3.16}$$

$$\boldsymbol{k}_r = \boldsymbol{k}_i \pm \boldsymbol{k}_{SW} \tag{3.17}$$

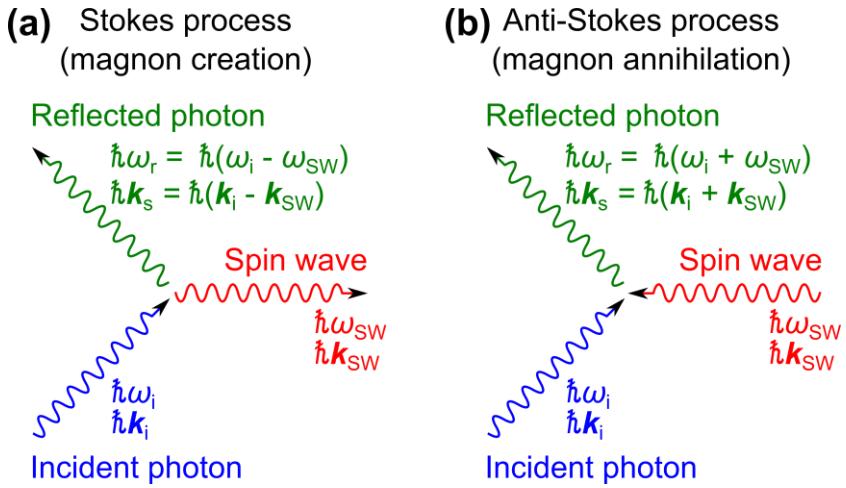

Fig. 3.13 Diagrams[82] showing **(a)** the Stokes process, and **(b)** the anti-Stokes process, by which the incident photon creates and annihilates a magnon respectively.

where ω_i, ω_r and ω_{SW} refer to the frequency of the incident light, the reflected light, and the spin wave respectively, and $\boldsymbol{k}_i$, $\boldsymbol{k}_r$ and $\boldsymbol{k}_{SW}$ refer to the in-plane wave vector of the incident light, the reflected light, and the spin wave respectively. The scattering can take on one of two forms, depending on whether the magnon is generated or annihilated (these are referred to as Stokes and Anti-Stokes processes respectively). These two mechanisms are sketched in Fig. 3.13. In the Stokes process, the incident photon creates a magnon, and so the reflected photon has a reduced energy, with the shift given by the energy of the generated magnon. In the Anti-Stokes process, the incident photon instead annihilates a magnon, thus causing the reflected photon to have an increased energy.

A schematic showing the basic setup of the Brillouin Light Scattering (BLS) microscopy system is given in Fig. 3.14.[134] A single-frequency Nd:YAG laser emits light of wavelength 532 nm / frequency 564 THz, which is focused onto the sample at close to normal incidence. The spatial resolution of the setup is governed mainly by the numerical aperture of the objective lens used to focus the laser – in the experiments discussed in this thesis, an objective lens of numerical aperture NA = 0.025 was used, yielding a spatial resolution of about 10 µm. When a spin wave (of frequency ω_{sw}) then propagates across the position of the focused laser spot, the reflected light is shifted positively in frequency ($\omega_r = \omega_i + \omega_{SW}$) via the anti-Stokes process. To detect the change in frequency, the reflected light is then directed into a multi-pass Tandem Fabry-Perot interferometer.[133] By changing the width of the etalon, one

can alter the frequency of transmission, and so the spectrum of the transmitted light therefore directly reveals the amplitude of the propagating spin wave, in a frequency-resolved manner.

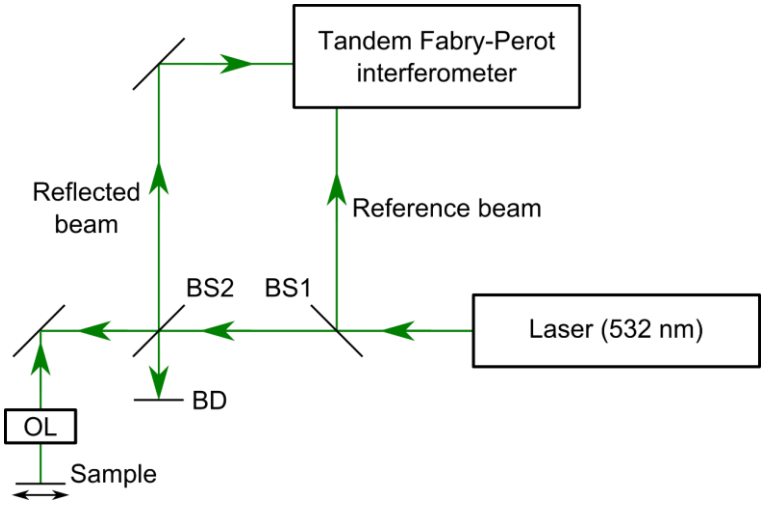

Fig. 3.14 Schematic[134] of the Brillouin Light Scattering (BLS) microscopy system. The abbreviations used correspond to the following: BS = Beam splitter, BD = Beam dump, and OL = Objective lens.

3.6 Object-Oriented Micro-Magnetic Framework (OOMMF)

The development of computational power towards the end of the twentieth century led to the idea of solving the Landau-Lifshitz-Gilbert equation numerically across a mesh of magnetization vectors, discretized in both the time- and space-domain.[48] This is the principle underpinning micromagnetic packages. Broadly speaking, micromagnetic packages can be split into two groups, depending on the method of discretization. In finite-difference time-domain (FDTD) packages, such as OOMMF[135] and MuMax3,[136] the geometry is divided into a regular lattice of cuboid cells, and both the magnetization and effective field are assumed to be uniform in each and every cell. With the finite-element method (FEM), as used in NMag[137] and FastMag[138] for example, the geometry is instead divided into a lattice of (generally nonuniform) tetrahedral elements, and $\boldsymbol{M}$ and $\boldsymbol{H}_{\text{eff}}$ are calculated at the vertices of the tetrahedral elements. This geometrical difference between the two approaches leads to tradeoffs in the computational time required and accuracy of the geometrical modelling, but should (in principle) lead to the same results. In the work discussed in this thesis, all micromagnetic calculations were performed using OOMMF.

OOMMF was first released in 1998 by Michael Donahue and Don Porter.[135] As noted earlier, OOMMF is a FDTD program, and so at the first step the LLG equation is discretized such that

$$\frac{\partial \boldsymbol{M}_{u,v,w}}{\partial t} = -\gamma_{u,v,w}\boldsymbol{M}_{u,v,w} \times \left(\boldsymbol{H}_{eff}\right)_{u,v,w} + \frac{\alpha_{u,v,w}}{\left[\left(M_s\right)_{u,v,w}\right]^2}\boldsymbol{M}_{u,v,w} \times \frac{\partial \boldsymbol{M}_{u,v,w}}{\partial t} \tag{3.18}$$

where $\boldsymbol{M}_{u,v,w}$, $\gamma_{u,v,w}$, $\left(\boldsymbol{H}_{eff}\right)_{u,v,w}$, $\alpha_{u,v,w}$, and $\left(M_s\right)_{u,v,w}$ correspond to the magnetization, the gyromagnetic ratio, the effective field, the Gilbert damping coefficient, and the saturation magnetization at the mesh site (u,v,w) respectively. The time domain similarly becomes discretized in n steps of Δt_n (the increment Δt_n is set by the specified solver), causing a point in time t_n to be described by $t_n = t_0 + n\Delta t_n$ where t_0 is the initial time. The magnetization at the point in time t_{n+1} is then numerically calculated (for all the work presented in this thesis, the Runge-Kutta-Fehlberg[139] integration method was used), along with an estimation of the error associated with the calculation. If the error is within a predefined tolerance, the calculation is considered successful, and the solver moves forward to the next point in time. If, instead, the error exceeds that allowed, Δt_n is reduced, and the entire calculation is repeated.

Since its public release, OOMMF has been re-released twice, and the versions used to derive the work presented in this thesis are versions 1.2 alpha 5 and 6. A GPU-enabled version of OOMMF is now publicly available,[140] which offers to quicken simulations by a factor as much as 32 compared to the CPU-enabled simulations. The source code of OOMMF is continuously under development by NIST, and extensions to the source code are written both by NIST and by other research groups. Consequently, OOMMF is capable of modelling a wide range of three-dimensional systems, incorporating for example periodic boundary conditions in one-[141] and two-dimensions,[142] and additional magnetic interactions (such as the Dzyaloshinsky-Moriya interaction[143]). Moreover, OOMMF is capable of calculating both linear and non-linear spin dynamics.

3.6.1 Energy terms in OOMMF

Due to OOMMF being a FDTD solver, the field terms shown in Equation 2.90 need to be similarly discretized. The following descriptions are sourced from the user manual for OOMMF.[144] The Zeeman term is the simplest of the terms, in that it is completely specified by the user

$$\left[\boldsymbol{H}_{Zeeman}\right]_{u,v,w}(u(t),v(t),w(t)). \tag{3.19}$$

The Zeeman field is simply calculated on a cell-by-cell basis, independently of the Zeeman field across other neighbouring mesh cells.

The exchange field, as discussed in Section 2.4.2, is short-range, and dominates only across the exchange length. With a user-specified exchange coefficient $A_{(u,v,w),(x,y,z)}$ mediating the exchange interaction between the cells positioned at the mesh sites (u,v,w) and (x,y,z), the exchange energy at the mesh point (u,v,w) is given by

$$\left[E_{exchange}\right]_{u,v,w} = A_{(u,v,w),(x,y,z)} \frac{\left(\frac{\boldsymbol{M}_{u,v,w}}{\left[M_S\right]_{u,v,w}}\right)\cdot\left[\left(\frac{\boldsymbol{M}_{u,v,w}}{\left[M_S\right]_{u,v,w}}\right)-\left(\frac{\boldsymbol{M}_{x,y,z}}{\left[M_S\right]_{x,y,z}}\right)\right]}{\left[\boldsymbol{r}_{u,v,w}-\boldsymbol{r}_{x,y,z}\right]^2}, \tag{3.20}$$

The exchange energy for one cell in a three-dimensional system is assumed to only be influenced by the six neighbouring cells. Thus, the 6-neighbour exchange energy is given by summing the exchange energy defined in Eq. 3.20 across all six of the neighbouring cells. While the exchange interaction is assumed to be only occurring across the nearest neighbours, it is still possible for the exchange interaction to act across several cells if the said cells fit within the exchange length l_{ex}. For Permalloy, the exchange length is about 5 nm - thus, for the exchange interaction to be modelled correctly, the cell-size should be fixed at or below 5 nm (to satisfy $\left|\boldsymbol{r}_{u,v,w}-\boldsymbol{r}_{x,y,z}\right| \le l_{ex}$).

The energy associated with the uniaxial and cubic anisotropy terms is similar in interpretation to the Zeeman energy, in that it is independent of neighbouring cells. Depending on whether the crystalline anisotropy constant $K_{u,v,w}$ is positive or negative, the vector $\hat{\boldsymbol{u}}$ corresponds to the easy or hard axis respectively. The energy characterising the uniaxial anisotropy is given by

$$\left[E_{uniaxial}\right]_{u,v,w} = K_{u,v,w}\left(1-\left[\frac{\boldsymbol{M}_{u,v,w}}{(M_S)_{u,v,w}}\cdot\hat{\boldsymbol{u}}\right]^2\right)\Bigg\} K_{u,v,w} > 0 \tag{3.21}$$

$$\left[E_{uniaxial}\right]_{u,v,w} = -K_{u,v,w}\left(\frac{\boldsymbol{M}_{u,v,w}}{(M_S)_{u,v,w}}\cdot\hat{\boldsymbol{u}}\right)^2\Bigg\} K_{u,v,w} < 0 \tag{3.22}$$

The expression for the energy endowed by cubic anisotropy is similarly

$$[E_{cubic}]_{u,v,w} = \frac{K_{u,v,w}}{(M_s)_{u,v,w}} \left[(\boldsymbol{M}_{u,v,w} \cdot \hat{\boldsymbol{u}}_1)^2 + (\boldsymbol{M}_{u,v,w} \cdot \hat{\boldsymbol{u}}_2)^2 + (\boldsymbol{M}_{u,v,w} \cdot \hat{\boldsymbol{u}}_3)^2 \right] \quad (3.23)$$

where $\hat{\boldsymbol{u}}_1$ and $\hat{\boldsymbol{u}}_2$ are the anisotropy axes specified by the user, and $\hat{\boldsymbol{u}}_3 = \hat{\boldsymbol{u}}_1 \times \hat{\boldsymbol{u}}_2$.

The demagnetizing field has non-local character, and therefore is described (at a particular point) by the superposition of the demagnetizing fields created by all other points within the sample. It can also have contributions from the stray field emanating from a second sample, separated in space from the first sample, but still within the same considered system. To calculate this field, OOMMF first computes the demagnetizing tensor. Upon assuming that the magnetization within the cell is uniform, the demagnetizing tensor of a cell (of length *a*, width *b* and depth *c*) can be calculated using the equations obtained by Amikam Aharoni.[145] The demagnetizing tensor characterising all mesh cells is therefore calculated (since the demagnetizing tensor depends only on the dimensions of the mesh cell and the geometry of the sample, the demagnetizing tensor is calculated just once, directly at the start of the simulation). Then, in the discretised reciprocal space, the Fourier transform of the demagnetizing field is calculated through[146]

$$\boldsymbol{H}'_{demag} = -4\pi \tilde{\boldsymbol{N}}' \cdot \boldsymbol{M}', \quad (3.24)$$

where the dashed superscript indicates the corresponding quantity has been Fourier transformed. By therefore taking an inverse Fourier transform of $\boldsymbol{H}'_{demag}$, OOMMF calculates the demagnetizing field in real space.

3.7 Summary

In summary, the experimental and numerical techniques used within this thesis have been discussed at length. The setups of the TRSKM and TROPSOM systems have been elaborated on extensively. These systems, used by myself, were capable of imaging magnetization dynamics in real-space / time-domain, with a spatial (temporal) resolution of about 500 nm (5 fs). An outline of the BLS microscopy system has also been provided - this experimental setup was used to image magnetization dynamics in the frequency-domain, with a spatial resolution of about 10 μm. Finally, the underlying principles of OOMMF have been discussed. The micromagnetic package outputs magnetization dynamics in real-space / time-domain, with a resolution as specified by the user. In the following chapters, the results acquired using TRSKM, TROPSOM, BLS and OOMMF will be discussed.

CHAPTER 4

EXCITING SPIN WAVES USING A GRADED MAGNONIC INDEX

4.1 Introduction

In order to successfully miniaturize magnonic technology, it is essential to have some mechanism of exciting spin waves with high wave vector. Most typically, propagating spin waves are excited through the application of a fast-varying magnetic field, delivered by a current-carrying electrical element. Depending on the size and position of the magnetic system, with respect to the current-carrying element, the exciting magnetic field can be considered (from the perspective of the magnetic system[147]) to be either spatially uniform or non-uniform. Non-uniform exciting fields are experimentally generated by positioning micron-sized electrical elements[148-152] on the surface of a larger magnetic body. The frequency of the excited monochromatic spin wave can be tuned via the frequency of the delivered microwave current. This approach can be further adapted in order to excite spin waves with fixed wave vector[153] or beam-like character,[154] merely through patterning the current-carrying elements. Inescapable ohmic losses, however, impose limits on both the line dimensions and the impedance range of such spin-wave transducers.[155] The former limitation, in particular, represents a significant challenge for the future development of miniaturized spin-wave-based devices, as transducers of width w excite a locally-uniform field of width w, and so the minimum wavelength (maximum wave vector) of any spin wave excited will be $2w$ (π/w).

Instead of therefore using non-uniform exciting fields to excite spin waves, it could be simpler to excite dynamics with spatially-uniform exciting fields. Arguably, the simplest system one can consider is a continuous, uniformly-magnetized thin film. Upon exciting the film with a uniform magnetic field, the translational symmetry of the system allows only the

fundamental spin-wave mode – ferromagnetic resonance - to be excited. To excite non-uniform dynamics, the translational symmetry of the magnetic system must be broken, via for example patterning of the film geometry. It is well-understood that, by imposing symmetrical geometrical boundaries on the film (giving rise to a stripe or square), confined spin-wave modes can be excited[51,156-157] where the spin-wave wave vector is inversely related to the distance between the film edges.

In a pair of articles published in 1964, Ernst Schlömann[24, 158] theoretically outlined how propagating spin waves could be excited using a spatially-uniform exciting magnetic field, by breaking the translational symmetry of a magnetized stripe in a particular way. Schlömann assumed the strength of the static bias field to be parabolic across the length of the magnetic stripe, highest at the stripe's edges, and lowest at the center. Via the dispersion relation characterizing exchange spin waves, one can then define an effective spin-wave wave vector

$$\left[k_{eff}(x)\right]^2 = \frac{\left[\omega/\gamma - H_B(x)\right]}{D}, \qquad (4.1)$$

with a corresponding frequency ω. Upon exciting the entire slab with a spatially-uniform microwave magnetic field, of frequency $\omega = \gamma H_B$, quasi-uniform FMR ($k_{eff} = 0$) was excited most efficiently within a well-defined region close to the stripe's edges. The region in which the magnetization was most efficiently excited then coupled with the neighboring region of magnetization (where H_B was reduced), launching spin waves with raised k_{eff} along the stripe. This is referred to as the Schlömann mechanism of spin-wave excitation.

Direct experimental verification of the Schlömann mechanism of spin-wave excitation in micron-sized samples was not presented, however, until 2011.[147] Au *et al.* considered a patterned structure - a semi-continuous film connected to a stripe - uniformly biased transversely to the stripe's length. The non-uniform internal field across the structure caused there to be two dominant modes of resonance, each spatially confined to either within the semi-continuous film or the stripe. The structure was then excited by a spatially-uniform harmonic magnetic field, tuned in frequency so as to continuously excite the mode of resonance in the semi-continuous film, and spin waves (with a wavelength about 36 μm) were observed propagating along the stripe away from the semi-continuous film. The efficiency of the coupling between the magnetic field and the dominant mode of resonance within the semi-

continuous film was further investigated,[159] and it was shown that that this mechanism of excitation is rather narrow in frequency.

In the first two sections of this chapter, I will discuss the results of BLS microscopy and micromagnetic calculations, which reveal how the Schlömann mechanism can be exploited to provide a source of propagating spin waves. Through patterning of the magnetic thin film, the internal / effective field can be raised in specific regions of magnetization (giving rise to a graded magnonic index), therefore enabling spin waves with zero effective wave vector to be excited in these targeted regions. Spin waves, either in the form of caustic beams or regular plane-like waves, are then observed propagating across the magnetic sample. In the third and final section of this chapter, I will then discuss a hybrid numerical / analytical model that allows the local frequency of resonance to be determined more accurately. This model, in principle, could take into account all contributions that can be calculated within standard micromagnetic packages. These results demonstrate that the Schlomann mechanism of spin-wave excitation can be effectively and efficiently used to generate spin waves across a broad range of frequencies, and with highly-tunable spatial character.

4.2 Sample details and experimental / numerical results

The sample under investigation is schematically shown in Fig. 4.1 (a). A (2×8) mm^2 film of Yttrium-Iron-Garnet (YIG), 10 μm thick, was grown on a substrate of Gadolinium-Gallium-Garnet[******] (GGG) using liquid-phase epitaxy. This process[160] involves the GGG substrate (of thickness 500 μm) being dipped into a molten solution of PbO / B_20_3, which is supersatured with the components Y_2O_3 / Fe_2O_3. The melt is then rotated, which leads to crystal growth. While liquid-phase epitaxy enables YIG of very high quality to be grown, its biggest disadvantage lies in the thickness of the produced defect-free film, which is on the order of several micrometres. Some progress has been recently reported in overcoming this restrictrion,[161] using (for example) the technique of pulsed laser deposition to fabricate YIG films with a thickness as small as 10 nm.[162]

A single circular antidot, of diameter 100 μm, was laser scribed at the center of the YIG film, and the patterned film was then incorporated within the BLS microscopy system. The YIG / GGG bilayer was laid face-down above a 250 μm-wide microstrip, positioned so

[******] GGG has a cubic crystalline structure, with a lattice constant of 1.2383 nm, whereas YIG (a body-centred cubic crystal) has a lattice constant of 1.2376 nm. This very small lattice mismatch (7×10^{-5} nm) therefore renders GGG an ideal substrate for defect-free YIG.

the antidot was centered relative to the microstrip. The entire system was then uniformly biased by an in-plane field H_B = 500 Oe applied parallel to the microstrip. Due to both the relative width of the microstrip compared to the antidot's diameter, and the close proximity of the microstrip to the YIG film, the microwave magnetic field produced by the microstrip antenna was judged to be reasonably uniform in strength and orientation in the vicinity of the antidot.

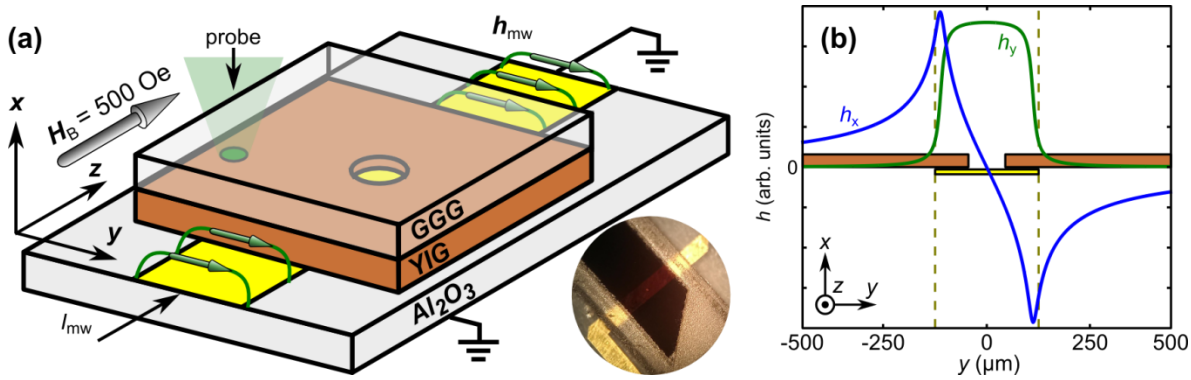

Fig. 4.1 **(a)** The studied sample is schematically shown. Inset: a photograph of the system, courtesy of Dr. Alexandr Sadovnikov. **(b)** The in-plane and out-of-plane distributions of the magnetic field (h_y and h_x respectively) generated by the 250 μm-wide microstrip antennae, 10 μm above the microstrip, as calculated using Eqs. 3.16 – 3.17.

4.2.1 Characterization of the ground magnetic state

To understand the ground-state distributions of the internal field and magnetization across the antidot system, a thin film of size (2000 × 2000 × 9.99) μm^3 was modelled using OOMMF. The gyromagnetic ratio and saturation magnetization of YIG were assumed to be $\gamma/2\pi$ = 2.80 MHz / Oe and M_S = 140 G respectively. Meshing cells of size (2 × 2 × 3.33) μm^3 were adopted, and the antidot - positioned at the center of the square sample - was modelled as a 9.99 μm-thick cylinder, of diameter 100 μm and zero saturation magnetization. The exchange interaction was completely neglected,[††††††] and to suppress effects associated with the outer edges of the simulated sample (for example, edge-induced magnetization canting and demagnetization), two-dimensional periodic boundary conditions[142] were implemented

[††††††] In YIG, the exchange length is about 15 nm. Since the dimensions of the YIG sample are so much larger than this, however, it was assumed reasonable to neglect the exchange interaction entirely.

across its plane. In principle, this generated a regular array of widely-spaced antidots, but since the spacing between neighboring antidots was 19 times higher than the antidot diameter, the influence of inter-antidot coupling on the static behavior was assumed to be negligible.

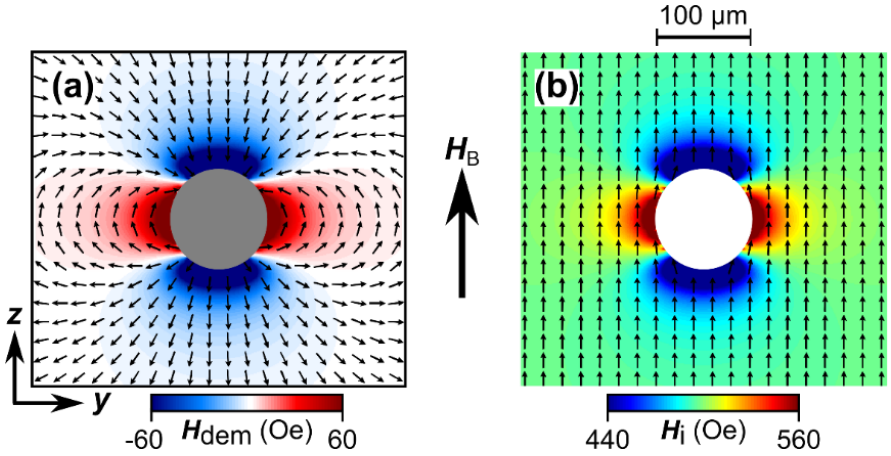

Fig. 4.2 **(a)-(b)** The calculated distributions of the demagnetizing and internal field respectively, in the immediate vicinity of the antidot. The vectors show the local orientation (normalized and averaged over 10 × 10 mesh cells) of the demagnetizing field / magnetization, and the color scale represents the projection of the demagnetizing / internal field onto the static magnetization.

For the static micromagnetic simulation[163] of the aforementioned YIG system, the YIG system was initially magnetized uniformly along the *z*-axis. The Gilbert damping coefficient was assumed to be 0.5,‡‡‡‡‡‡ and a spatially-uniform bias magnetic field H_B = 2000 Oe was applied along the *z*-axis. This field was then reduced incrementally, in stages of 50 Oe, until H_B = 500 Oe, (each stage was considered complete when the maximum rate of precession *dM/dt* across all meshing cells was below 1 °/ns). Once the ground magnetic state was calculated with H_B = 500 Oe, the magnetization was further relaxed so as $(dM/dt)_{max}$ < 0.01 °/ns. The static spatial distributions of the projections of the demagnetizing and internal field onto the magnetization are shown in Figs. 4.2 (a) - (b) respectively. Immediately above and below the antidot, magnetic poles have clearly formed, arising from the demagnetizing field opposing the bias. Expectedly, this reduces the internal field in these two regions. The demagnetizing field, however, must generally form a closed loop so as to avoid the formation

‡‡‡‡‡‡ Here, the system was relaxed by artificially increasing the damping coefficient. There is also the so-called method of 'steepest descent', where the magnetization is not allowed to precess, but rather forced to evolve toward static equilibrium along the quickest path. Both methods, in principle, generate the same micromagnetic ground state.

of magnetic monopoles, and so the demagnetizing field aligned parallel to the applied bias field across the regions left and right of the antidot. Thus, the local internal field in these two regions experience an increase in strength, relative to the internal field far from the antidot.

The uniform frequency of FMR of a continuous film, magnetized in-plane, is given by Eq. 2.103, and is a function of the gyromagnetic ratio, internal field and saturation magnetization. As discussed in Section 3.6, FDTD simulations are underpinned by the assumption of uniform effective field and magnetization within each and every mesh cell, and so one can crudely use Eq. 2.103 to calculate the distribution of the local FMR frequency associated with each mesh cell.[164-165] This distribution, corresponding to the studied YIG sample, is presented in Fig. 4.3 (a). Interpreted in this way, the local frequency of FMR represents the frequency of FMR in a continuous thin film magnetized uniformly and experiencing the same internal field as experienced by the mesh cell. Physically, the local frequency of FMR is the limiting value of the spin-wave frequency as $k_{eff} \to 0$. This approximation therefore enables qualitative understanding of the quasi-uniform modes of resonance confined above and below the antidot, which have been observed and studied extensively before.[166-168] On the left and right-hand sides of the antidot, in contrast, the local frequency of FMR was raised, compared to the local frequency of FMR belonging to the otherwise-continuous film (across the continuous film, f_{FMR} = 2.98 GHz). This non-uniform

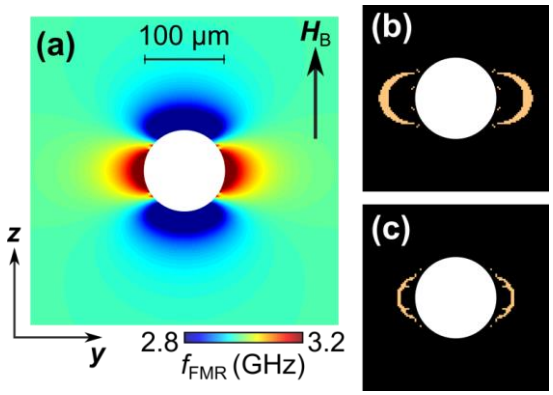

Fig. 4.3 **(a)** The distribution of the local frequency of FMR, calculated according to Eq. 2.103 in the immediate vicinity of the antidot. **(b)-(c)** Binary images, where the bright regions of magnetization have local frequencies of resonance approximately equal to 3.1 GHz and 3.2 GHz respectively.

internal field led to the formation of ring-shaped regions of magnetization with a correspondingly higher frequency of resonance, as shown for example in Fig. 4.3 (b) - (c). These were plotted within the ranges 3.05 GHz < f_{FMR} < 3.15 GHz and 3.15 GHz < f_{FMR} < 3.25 GHz respectively.

4.2.2 Characterization of the dynamic magnetization

The micromagnetic results presented in Fig. 4.3 suggest that regions of magnetization with a raised frequency of resonance existed on the left- and right-hand sides of the antidot, originating from the alignment of the demagnetizing field with the bias field. To validate this inference experimentally, the BLS microscopy setup shown in Fig. 4.1 (a) was used. The probing laser beam, of 532 nm wavelength, was focused through the GGG substrate to form a spot of diameter 20 μm on the upper surface of the YIG film, and then positioned either on the right-hand side of the antidot, or at a distance far from the antidot. The frequency of the temporally-harmonic microwave current driven across the microstrip was increased in well-defined steps, and at each individual frequency of excitation, the intensity of the inelastically-scattered light was measured. This generated the frequency spectra presented in Fig. 4.4 (a)-(b), measured with frequency steps of 10 MHz and 2.5 MHz respectively. These spectra not only evidence the graded variation of the local frequency of resonance (the signal recorded

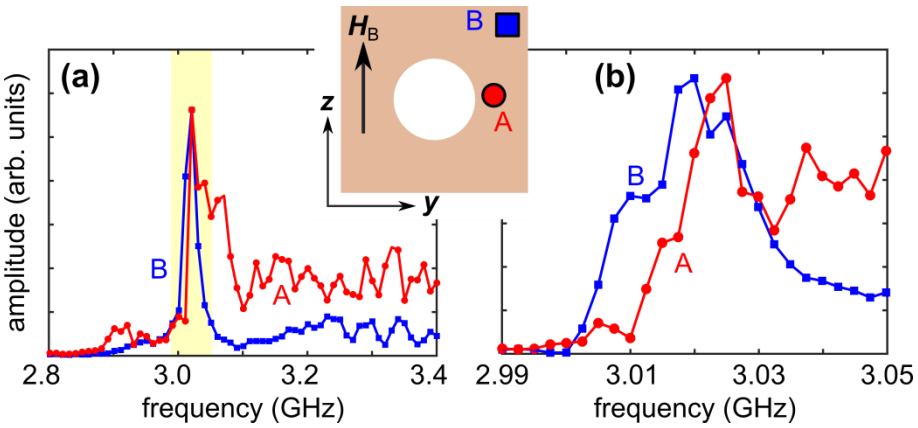

Fig. 4.4 Inset: A cartoon of the experimental geometry. **(a)** The efficiency of excitation measured with the probe focused at point A (red circles) and at point B (blue squares), with a frequency resolution of 10 MHz. **(b)** The excitation signals obtained in the same fashion as in (a), except with a frequency resolution of 2.5 MHz.

close to the antidot is consistently raised in intensity higher frequencies), but also reveal an offset in frequency of 5 MHz between the maximum responses measured at points A and B. This latter observation in particular provides convincing experimental evidence of the local frequency of resonance (and by extension the graded magnonic index), immediately on the right-hand side of the antidot, being raised.

The non-uniform distribution of the internal field – and the corresponding distribution of the local frequency of resonance - suggested that the direct resonant excitation of the half-rings of magnetization (in which the internal field was raised) would lead to the excitation of propagating spin waves, via the Schlömann mechanism. BLS imaging was therefore performed, whereupon the microstrip was loaded with 500 ns microwave current bursts, at a repetition rate of 500 kHz and with an average power of 1.25 dBm. The results of the BLS microscopy are presented with a logarithmic color scale in the upper panels of Fig. 4.5, where panels (a) - (c) show the images acquired when the frequency of excitation was 3.1 GHz, 3.2 GHz and 3.3 GHz respectively.

The results shown in the upper panels of Fig. 4.5 (a) - (c) clearly show the excitation of spin-wave caustic beams on the right side of the antidot. These waves originated from the finite size of the excited region of magnetization[169] - such a source excites spin waves with a broad range of k_z values, and k_y values related by the isofrequency curves shown in the lower panels of Fig. 4.5. The isofrequency curves presented in the lower panels of Fig. 4.5 (a) - (c) were calculated using Eq. 2.130 with the frequencies 3.1 GHz, 3.2 GHz and 3.3 GHz respectively, with the system parameters M_s = 140 G, H_B = 500 Oe, and s = 10 μm. As was discussed in Section 2.5.6, the isofrequency curves characterizing MSSWs are approximately straight, and so the group velocities associated with the wide range of allowed wave vector solutions are approximately collinear. This leads to the beaming of the spin-wave amplitude. In addition to the spin-wave caustic beams, it should also be noted that there are distinct "extinction lines" on the left side of the antidot.[151]

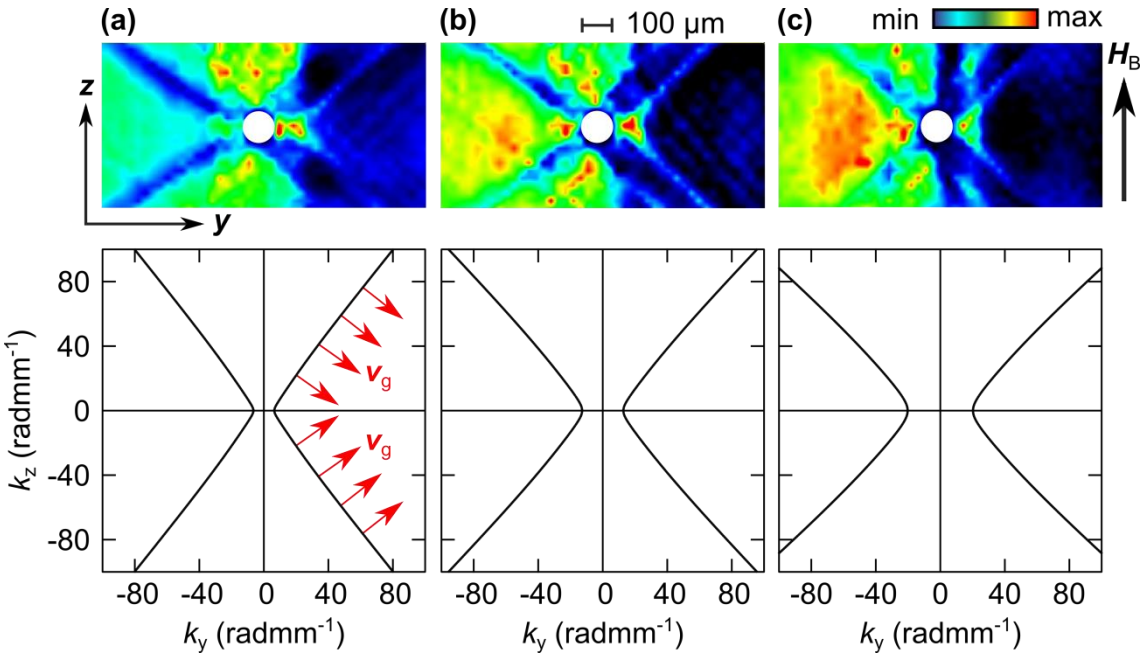

Fig. 4.5 **(a)-(c)** Upper panels: Amplitude-resolved BLS images, acquired at the excitation frequencies 3.1 GHz, 3.2 GHz and 3.3 GHz respectively, where H_B = 500 Oe throughout. Lower panels: Isofrequency curves corresponding to the images shown in the upper panels, calculated using Eq. 2.130 for M_s = 140 G and s = 10 µm. Exemplary group velocity vectors are indicated by the red arrows.

To visualize the orientation of the spin-wave wavefronts (the acquired BLS images only reveal the direction of the energy flow), dynamic micromagnetic simulations were performed. The system used previously for the static micromagnetic simulations did not lend itself well to such dynamic calculations, as the excited spin waves were anticipated to propagate across the boundaries of the (2 × 2) mm^2 supercell. The system was therefore modified, so as to comprise a thin film of size (8 × 8 × 0.01) mm^3, meshed with cells of size (4 × 4 × 10) µm^3. The antidot was again modelled as a cylinder of diameter 100 µm and zero saturation magnetization, and two-dimensional periodic boundary conditions were again used to eliminate geometrical boundary effects. The same strategy as described earlier was used to relax the magnetization with an external bias field H_B = 500 Oe.

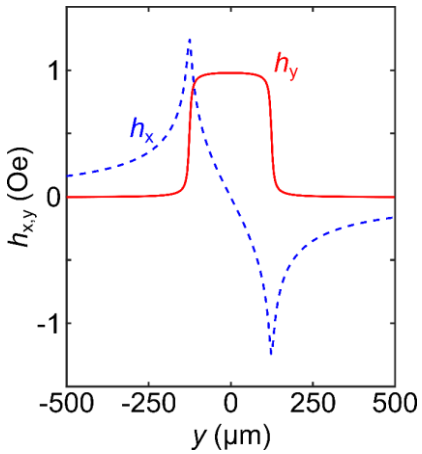

Fig. 4.6 The spatial distributions of the in-plane h_y (red solid line) and out-of-plane h_x (blue dashed line) components of the magnetic field generated at a distance of 10 μm above the microstrip, as described by Eqs. 4.2 – 4.3.

The spatial distributions of the exciting field generated by the microstrip are reasonably given by Eqs. 3.14 – 3.15. However, this form was cumbersome to define as an input within OOMMF, and so the Karlqvist equations[170] (originally derived to describe the magnetic fields generated by an inductive read / write head) were used instead as an approximation, where the equations are of the form

$$h_{kq,y}(x,y) = \frac{1}{\pi}\cdot\left[\tan^{-1}\left(\frac{w+2y}{2x}\right)+\tan^{-1}\left(\frac{w-2y}{2x}\right)\right], \tag{4.2}$$

$$h_{kq,x}(x,y) = \frac{1}{2\pi}\cdot\ln\left(\frac{[w-2y]^2+4x^2}{[w+2y]^2+4x^2}\right). \tag{4.3}$$

The spatial distributions described by Eqs. 4.2 - 4.3 are presented in Fig. 4.6, and approximate well the distributions presented in Fig. 4.1 (b). The time dependence of the exciting magnetic field was defined as being harmonic, having the form

$$h_t(t) = h_0 \sin(2\pi f\cdot t), \tag{4.4}$$

where h_0 = 1 Oe and f = 3.1 GHz, 3.2 GHz or 3.3 GHz.

Dynamic micromagnetic simulations were then performed, using the exciting magnetic field described by Eqs. 4.2 – 4.4. The calculated magnetization $\boldsymbol{M}(y,z,t)$ was recorded in time steps of $1/8f$, so as to reveal the spatially-resolved magnetization at 8

equidistant points across one period of the exciting field, for a total of 18 ns.[§§§§§§] The static out-of-plane component of magnetization $M_{0,x}(y,z)$ was then subtracted from $M_x(y,z,t)$, yielding the dynamic component $m_x(y,z,t)$. Presented in the middle panels of Fig. 4.7 are snapshots of m_x, taken about 18 ns after the excitation was initially applied, where the distributions shown in panels (a)-(c) were acquired with f = 3.1 GHz, 3.2 GHz or 3.3 GHz respectively. Shown in the top panels of Fig. 4.7 are the results obtained using BLS, reproduced from Fig. 4.5, provided here so as to enable straightforward comparison (note the simulated snapshots are zoomed out by a factor of about 3, relative to the experimentally-acquired images). These results are in good agreement, and confirm that spin-wave caustics were indeed being excited on the right-hand side of the antidot (due to the wavefronts being canted in the micromagnetic images). Moreover, plane MSSWs were observed propagating on the left-hand side of the antidot, arising because of the non-uniform spatial profile of the exciting field. Further micromagnetic simulations showed that these uni-directional MSSWs could be switched to propagate on the right-hand side of the antidot by either reversing the polarity of the static magnetization, or by positioning the microstrip above the YIG sample (but the direction of propagation did not depend on the chirality of the driving magnetic field).

To deduce the origin of the experimentally-observed extinction lines, the micromagnetic simulations were performed again, except with the antidot "filled in" so that a continuous film was being modelled. For these latter simulations, the dynamic out-of-plane component $m_{x,\,film}(y,z,t)$ was again deduced (in response to the same excitation fields), and then the quantity

$$\delta m_x = m_x(y,z,t) - m_{x,\,film}(y,z,t) \qquad (4.5)$$

was calculated, in order to "subtract" the MSSWs. The spatial distribution of δm_x are presented in the lower panels of Fig. 4.7, again where the results shown in panels (a) - (c) were acquired when f = 3.1 GHz, 3.2 GHz and 3.3 GHz respectively. These clearly show that spin-wave caustics were excited symmetrically about the antidot, while interference of the plane spin waves and spin-wave caustic beams led to the experimentally-observed extinction lines on the left side of the antidot.

[§§§§§§] The magnetization dynamics was observed to be broadly periodic after about 5 ns.

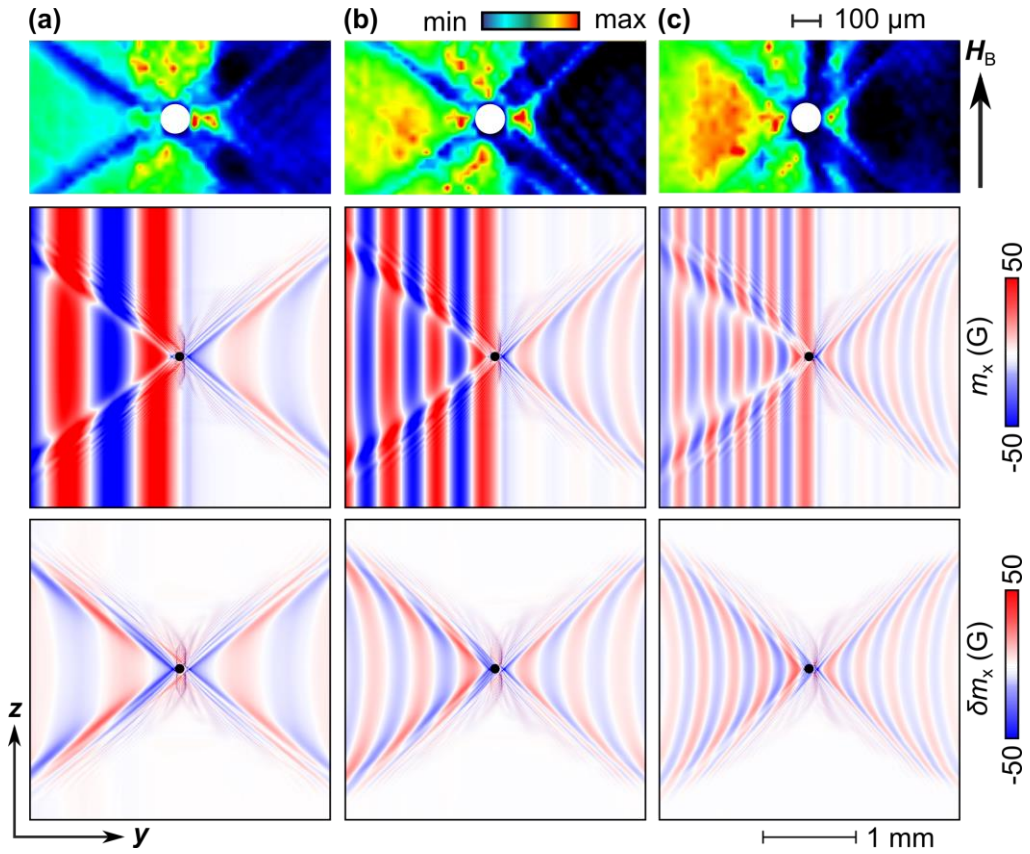

Fig. 4.7 The stimulated magnetization dynamics across the YIG sample is shown for the excitation frequencies of **(a)** 3.10 GHz, **(b)** 3.20 GHz, and **(c)** 3.30 GHz. The upper panels correspond to the experimentally-acquired images (reproduced from Fig. 4.5), the middle panels show the numerically-calculated dynamic out-of-plane component of magnetization m_x, while the lower panels show δm_x as calculated using Eq. 4.5. Note the images in the middle and lower rows have been zoomed out by a factor of about 3, compared to the images shown in the top row.

4.3 Micromagnetic modelling of miniaturized systems

The magnetization dynamics discussed in section 4.2 were wholly dominated by the dipolar interaction, so much so that the exchange interaction was neglected completely in the micromagnetic calculations. For the results discussed in section 4.2 to be useful technologically, however, it would be necessary to significantly reduce the dimensions of the system. Further micromagnetic simulations were therefore performed in order to identify how the mechanism of spin-wave excitation evolves upon down-scaling.

4.3.1 Exciting spin waves within miniaturized antidot systems

The first system studied consisted of an antidot of diameter 200 nm, embedded within a thin film of Permalloy spanning (6 × 6) μm^2. The thickness of the film (s) was set to either 40 nm, 20 nm, 6 nm or 2 nm, and the system was meshed with cells of size (5 × 5 × s) nm^2. Two-dimensional periodic boundary conditions[142] were used to approximate the continuous film. The exchange stiffness A_{ex}, magnetization of saturation M_s, gyromagnetic ratio $\gamma/2\pi$ and Gilbert damping coefficient α were set to 1.3 μerg / cm, 800 G, 2.80 MHz / Oe and 0.008 respectively.[171-174] In an identical approach as was discussed in Section 4.2, the ground-state magnetic configuration of the film was calculated when the film was subjected to a bias field H_B = 500 Oe applied parallel to the z-axis, taking into account the magnetic hysteresis. A spatially-uniform exciting magnetic field, identical to that described by Eq. 4.4, was applied along the y-axis. The amplitude and frequency of the excitation was 1.75 Oe and 9 GHz respectively, and the magnetization was sampled at time steps $1/8f$, for a total of 18 ns.

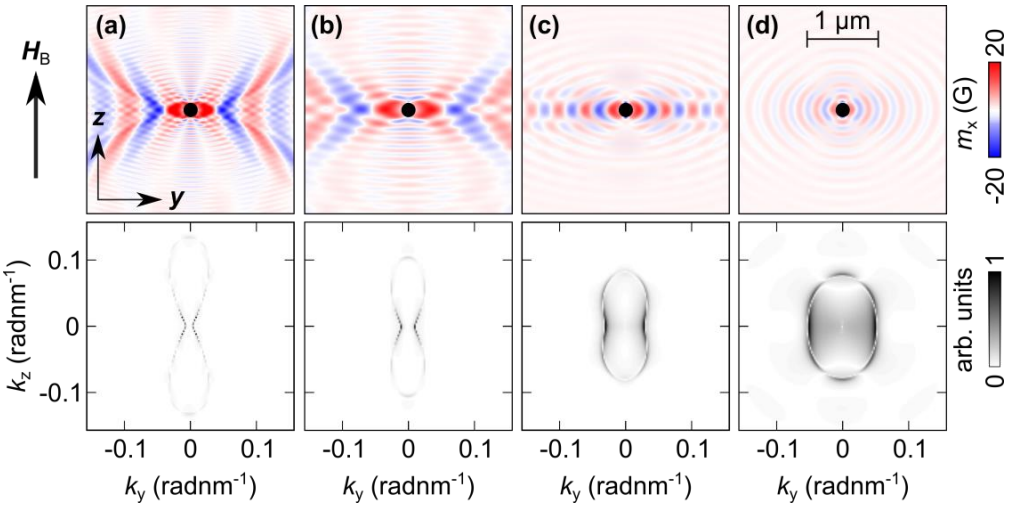

Fig. 4.8 Upper panels: Snapshots of the dynamic out-of-plane component of magnetization across the Permalloy film, taken 4 ns after the initial application of the exciting field, at identical points across the phase of the excitation field. Lower panels: The distributions of the spin-wave amplitude mapped in reciprocal space. **(a)-(d)** The spin-wave propagation is shown in films of thickness 40 nm, 20 nm, 6 nm and 2 nm respectively, where the embedded antidot had a diameter of 200 nm. The Permalloy throughout was continuously excited at 9 GHz, and uniformly biased by H_B = 500 Oe.

Presented in the upper panels of Fig 4.8 (a) - (d) are snapshots of the dynamic out-of-plane component of magnetization, across Permalloy films of thickness 40 nm, 20 nm, 6 nm, and 2 nm respectively, acquired 18 ns after the initial application of the exciting magnetic field. For the thickest films studied (Fig. 4.8 (a) - (b)), the excited spin waves still had caustic character, qualitatively similar in distribution to those presented for YIG in Fig 4.7. As the film thickness was then reduced, the caustic beams reduced in angular divergence, gradually becoming more plane-like, as shown in Fig. 4.8 (c) - (d).

To confirm that the exchange interaction was indeed responsible for the change in character of the excited spin waves, the propagating spin waves were mapped in reciprocal space. Presented in the lower panels of Fig 4.8 (a)-(d) are the spatial distributions of the spin-wave amplitude $S_{A,2D}$, calculated using

$$S_{A,2D} = \left| FFT\left(m_{x,t}(y,z) + i \cdot m_{x,t+2}(y,z)\right) \right|, \tag{4.6}$$

where $m_{x,t}$ and $m_{x,t+2}$ correspond to the dynamic out-of-plane components of magnetization sampled at time steps 90° out of phase with respect to the exciting magnetic field. The spin-wave amplitude was universally strongest at $k_y = k_z = 0$.[*******] This dc contribution was therefore subtracted, and the remaining distribution of the spin-wave amplitude was then normalized. The maps presented in the lower panels of Fig. 4.8 are all characteristic of the isofrequency curves characterising dipole-exchange spin waves, which were discussed in Section 2.5.6. Furthermore, the spin-wave amplitude was throughout concentrated close to the line $k_z = 0$. As the film thickness decreased, the isofrequency curves became increasingly isotropic, reflecting the increasing dominance of the exchange interaction in mediating the propagation of the excited spin waves.

4.3.2 Exciting spin waves within a miniaturized semi-infinite film

By making the antidot elliptical in shape, the magnetic poles above and below the antidot could be moved closer together or further away from each other. This would significantly influence the strength and distribution of the positive static demagnetizing field. Completely neglected so far, however, is the contribution to the spin-wave excitation from the

[*******] Further micromagnetic simulations, performed by Dr. Fedor Mushenok, have shown that the spin-wave amplitude at $k_y = k_z = 0$ (the "dc contribution") could be naturally removed either by convolving the sinusoidal excitation with a function of the form $exp(-1/[f.t])$, or by merely waiting long enough for the driven excitation to become completely periodic.

dynamic demagnetizing field. A magnetic stripe – the limiting case of an elliptical dot, with its major axis extended toward infinity - was therefore modelled. Biased longitudinally, the stripe had zero static dynamic demagnetizing field, but it is well understood[51] that, at the edge of the stripe, there is strong dynamic demagnetizing field. This refers to the demagnetizing field generated by the dynamic precession of the magnetization. In an infinitely-extending magnetic body, biased along the *z*-axis, the magnetization will trace a wholly circular trajectory. If now the medium is severely confined along the *y*-axis, the magnetization, upon tipping towards the *y*-axis, will instantaneously generate a demagnetizing field parallel to the *y*-axis. Consequently, the magnetization will instead trace an elliptical trajectory, in order to minimize the strength of the dynamically-induced stray field. The dynamic demagnetizing field has been used before to derive boundary conditions for longitudinally-magnetized stripes.[107] Here, instead, the possibility of exciting propagating spin waves using the dynamic demagnetizing field was investigated.

The Permalloy stripe - of length 100 nm, width 20 μm, and thickness 40 nm – was assumed to represent a semi-infinite magnetic film. The in-plane cell-size was (5×5) nm^2, and the stripe was assumed to be one-cell thick. One-dimensional periodic boundary conditions[141] were applied along the length of the stripe, which was also longitudinally biased by $H_B = 500$ Oe. Since the bias field was applied exactly parallel to the edge, the distribution of the static demagnetizing field was uniformly zero. A spatially-uniform continuous-wave magnetic field was then applied along the *y*-axis, with a frequency of 14 GHz, and the magnetization was sampled every 8.93 ps. Presented in Fig. 4.9 (a) are snapshots of the dynamic out-of-plane component of magnetization close to the left edge of the stripe, taken 18 ns after the exciting field was first applied, and arranged in sequential time steps. Two points can be noted here. First, the background of the waveguide is observed to resonate. Second, and more significantly, spin waves can be observed propagating from the left edge of the waveguide towards the center of the waveguide, with a wavelength of 425 nm.

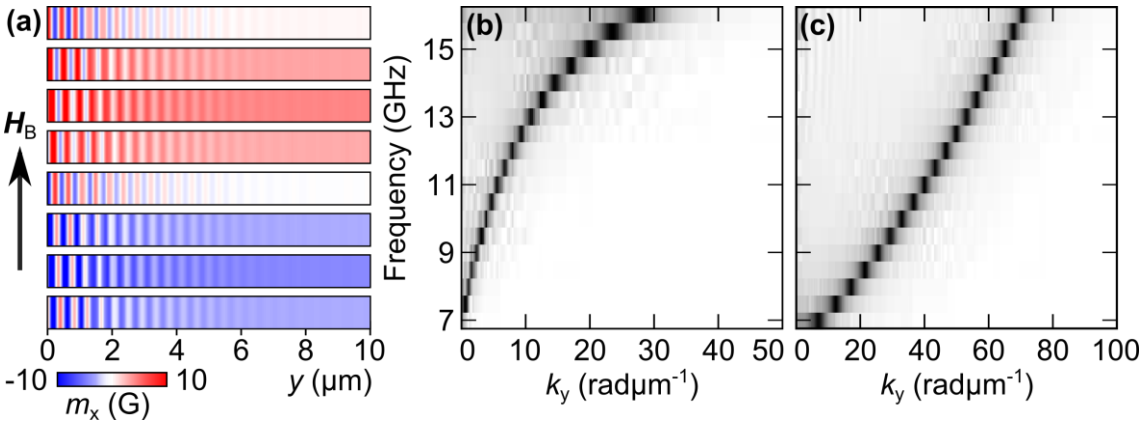

Fig. 4.9 **(a)** Top to bottom: Snapshots of the dynamic out-of-plane component of magnetization across the 40 nm-thick Permalloy film, taken 18 ns after the initial application of the exciting field (of frequency 14.0 GHz), given in sequential time steps of 8.93 ps. **(b)-(c)** Dispersion of the excited spin-waves excited in the Permalloy stripe of thickness 40 nm and 2 nm respectively. These were calculated using continuous-wave excitation, where the spectra corresponding to each frequency has been normalized.

To map the dispersive character of the excited spin waves, a continuous-wave approach (as put forward by Van de Wiele *et al.*[175]) was therefore adopted, whereby the dynamic continuous-wave micromagnetic simulations were repeated with stepped frequencies of excitation. To automate the running of these series of simulations, a MatLab script was used to generate a series of dynamic ".mif" files, where the frequency of the excitation f (and the corresponding sampling time $1/8f$) was adjusted from 7 GHz to 16 GHz, in discrete steps of 0.5 GHz. The MatLab script also generated a sequence of batch files, which were used to call OOMMF via the command line and also start the dynamic simulation. Upon completion of the said simulation, MatLab was then called, and a further script was used to calculate the one-dimensional Fourier transform across the width of the stripe (using Eq. 4.5). This procedure was then repeated sequentially for every frequency step, enabling the dispersion profile shown in Fig. 4.9 (b) to be constructed. Note that, again, the contribution at $k_y = 0$ was zeroed. This dispersion profile confirms that MSSWs were being excited close to the edge of the 40 nm-thick stripe, which was anticipated due to the thickness of the stripe being ~8 times larger than the exchange length. The dispersion corresponding to the spin waves excited across a 2 nm-thick stripe was also calculated in the same fashion, and is presented in Fig. 4.9 (c). Here, in stark contrast, the dispersion is of quadratic form, revealing that the propagating

spin waves were dominated by the exchange interaction. These results demonstrate the efficiency with which spin waves can be excited using the dynamic demagnetizing field, and furthermore the possibility to excite spin waves with a very wide range of frequencies and wavelengths.

4.4 Hybrid analytical / numerical model of the local susceptibility

The definition of the local FMR frequency used so far crudely involves the Kittel equation, taking into account only the internal magnetic field and the out-of-plane dynamic demagnetization. So, a quantitative model was developed to calculate more precisely the local frequency of resonance.

4.4.1 Analytical generalization of the Polder susceptibility

In Section 2.5.2 (specifically, Eqs. 2.98 - 2.99), the demagnetizing tensor was used to split both the static and dynamic effective fields into their constituent parts. Traditionally, the effective field in Eq. 2.97 is considered to be composed of only the static Zeeman $\boldsymbol{H}_B$ and demagnetizing $\boldsymbol{H}_{demag} = -4\pi\overleftrightarrow{N}\boldsymbol{M}$ fields. Instead, here the demagnetizing tensor is recast as the effective demagnetizing tensor $\overleftrightarrow{N}^{eff}$, which characterizes the response of the magnetization to all the contributing magnetic fields (except the Zeeman field)

$$\begin{aligned}\boldsymbol{H}_{eff} &= \boldsymbol{H}_B - 4\pi\overleftrightarrow{N}^{eff}\boldsymbol{M} \\ &= \boldsymbol{H}_B - 4\pi\begin{pmatrix} N_{xx}^{\ eff} & N_{xy}^{\ eff} & N_{xz}^{\ eff} \\ N_{yx}^{\ eff} & N_{yy}^{\ eff} & N_{yz}^{\ eff} \\ N_{zx}^{\ eff} & N_{zy}^{\ eff} & N_{zz}^{\ eff} \end{pmatrix}\boldsymbol{M}\end{aligned} \tag{4.7}$$

Following the derivation already outlined in Section 2.5.2, it is assumed that the bias field is applied along the *z*-axis. The effective field can now be split into its static and dynamic contributions

$$\begin{aligned}\boldsymbol{H}_{0,eff} + \boldsymbol{h}_{eff} &= \boldsymbol{H}_{0,B} + \boldsymbol{h}_B - 4\pi\overleftrightarrow{N}^{eff}\left(\boldsymbol{M}_0 + \boldsymbol{m}\right) \\ \boldsymbol{H}_{0,eff} &= \boldsymbol{H}_{0,B} - 4\pi\overleftrightarrow{N}^{eff}\boldsymbol{M}_0 \\ \boldsymbol{h}_{eff} &= \boldsymbol{h}_B - 4\pi\overleftrightarrow{N}^{eff}\boldsymbol{m}\end{aligned} \tag{4.8}$$

Substitution of Eqs. 4.8 into Eq. 2.97 yields

$$i\omega\boldsymbol{m} = -\gamma\boldsymbol{M}_0 \times \boldsymbol{h}_B + 4\pi\gamma\boldsymbol{M}_0 \times \overleftrightarrow{N}^{eff}\boldsymbol{m} - \gamma\boldsymbol{m} \times \boldsymbol{H}_{0,B} + 4\pi\gamma\boldsymbol{m} \times \overleftrightarrow{N}^{eff}\boldsymbol{M}_0 . \tag{4.9}$$

If the oscillations are assumed to be free, Eq 4.9 reduces to a more complete form of the Kittel equation (a more detailed derivation is supplied in Appendix 1)

$$\omega_0 = \gamma\sqrt{\left(H_{0,B} + 4\pi\left(N_{xx}{}^{eff} - N_{zz}{}^{eff}\right)M_S\right)\left(H_{0,B} + 4\pi\left(N_{yy}{}^{eff} - N_{zz}{}^{eff}\right)M_S\right) - \left(4\pi M_S\right)^2 N_{xy}{}^{eff} N_{yx}{}^{eff}} . \tag{4.10}$$

If instead the oscillations are forced i.e. $h_B \neq 0$, the LLG equation (Eq. 4.9) leads to the system of equations

$$\begin{aligned} i\omega m_x + 4\pi\gamma M_S\left(N_{yx}{}^{eff} m_x + N_{yy}{}^{eff} m_y\right) + \gamma m_y\left(H_{0,B} - 4\pi N_{zz}{}^{eff} M_S\right) + i\alpha\omega m_y &= \gamma M_S h_{B,y} \\ i\omega m_y - 4\pi\gamma M_S\left(N_{xx}{}^{eff} m_x + N_{xy}{}^{eff} m_y\right) - \gamma m_x\left(H_{0,B} - 4\pi N_{zz}{}^{eff} M_S\right) - i\alpha\omega m_x &= -\gamma M_S h_{B,x} \\ -4\pi N_{yz}{}^{eff} m_x + 4\pi N_{xz}{}^{eff} m_y &= 0 \end{aligned} \tag{4.11}$$

Solving this set of inhomogeneous equations leads, in the linear approximation, to the effective susceptibility tensor

$$\begin{pmatrix} m_x \\ m_y \end{pmatrix} = \begin{pmatrix} \chi_{xx}{}^{eff} & \chi_{xy}{}^{eff} \\ \chi_{yx}{}^{eff} & \chi_{yy}{}^{eff} \end{pmatrix} \begin{pmatrix} h_{B,x} \\ h_{B,y} \end{pmatrix} \tag{4.12}$$

where

$$\begin{pmatrix} m_x \\ m_y \end{pmatrix} = \begin{pmatrix} \dfrac{\gamma M_S\left[\omega_H + 4\pi\gamma M_S N_{yy}{}^{eff} + i\alpha\omega\right]}{\left(-\omega^2 + 2i\alpha\omega_1\omega + \omega_0{}^2\right)} & \dfrac{\gamma M_S\left(i\omega - 4\pi\gamma M_S N_{xy}{}^{eff}\right)}{\left(-\omega^2 + 2i\alpha\omega_1\omega + \omega_0{}^2\right)} \\ \dfrac{-\gamma M_S\left(i\omega + 4\pi\gamma M_S N_{yx}{}^{eff}\right)}{\left(-\omega^2 + 2i\alpha\omega_1\omega + \omega_0{}^2\right)} & \dfrac{\gamma M_S\left[\omega_H + 4\pi\gamma M_S N_{xx}{}^{eff} + i\alpha\omega\right]}{\left(-\omega^2 + 2i\alpha\omega_1\omega + \omega_0{}^2\right)} \end{pmatrix} \begin{pmatrix} h_{B,x} \\ h_{B,y} \end{pmatrix} \tag{4.13}$$

$$\omega_1 = \omega_H + \frac{1}{2}\gamma M_S\left(N_{xx}{}^{*} + N_{yy}{}^{*} + N_{yx}{}^{*} - N_{xy}{}^{*}\right), \tag{4.14}$$

$$\omega_H = \gamma\left(H_{0,B} - 4\pi N_{zz}{}^{eff} M_S\right). \tag{4.15}$$

The elements of the effective susceptibility tensor are, to first order, therefore of the form

$$\chi_{xx,yy}{}^{eff} = \frac{\begin{array}{c}\gamma M_S\left(\omega_0{}^2 - \omega^2\right)\left(\omega_H + 4\pi\gamma M_S N_{yy,xx}{}^{eff}\right) + 2\gamma M_S\alpha^2\omega_1\omega^2 \\ -i\left\{-\alpha\omega\gamma M_S\left[\omega_0{}^2 - \omega^2\right] + 2\alpha\omega\omega_1\gamma M_S\left(\omega_H + 4\pi\gamma M_S N_{yy,xx}{}^{eff}\right)\right\}\end{array}}{\left[\left(\omega_0{}^2 - \omega^2\right)^2 + \left(2\alpha\omega_1\omega\right)^2\right]} \tag{4.16}$$

$$\chi_{xy,yx}^{\ eff} = \frac{\begin{matrix} -4\pi(\gamma M_S)^2 N_{xy,yx}^{\ eff}\left(\omega_0^{\ 2}-\omega^2\right) \pm 2\gamma M_S \alpha\omega_1\omega^2 \\ -i\left\{+\omega\gamma M_S\left(\omega_0^{\ 2}-\omega^2\right) - 2(4\pi)(\gamma M_S)^2 \alpha\omega_1\omega N_{xy,yx}^{\ eff}\right\} \end{matrix}}{\left[\left(\omega_0^{\ 2}-\omega^2\right)^2 + (2\alpha\omega_1\omega)^2\right]} \qquad (4.17)$$

4.4.2 Numerical calculation of the effective demagnetizing tensor

The elements of the effective susceptibility tensor defined in Eq. 4.12 requires the calculation of the 5 elements of the effective demagnetizing tensor $\overleftrightarrow{N}^{eff}$. Analytically, it is generally impossible to calculate the spatial distribution of the elements of $\overleftrightarrow{N}^{eff}$ - micromagnetic calculations are therefore used to obtain numerical solutions. The co-ordinate system used in all OOMMF calculations (unless otherwise stated) discussed in this thesis is shown in Fig. 4.10 (a). The thin film is assumed to extend in the *x*-*y* plane, have thickness along the *z*-axis, and is globally biased along the *y*-axis. As a result of some competing magnetic interactions, the spatially-varying magnetization is given by a distribution of vectors with non-zero projections on all three axes.

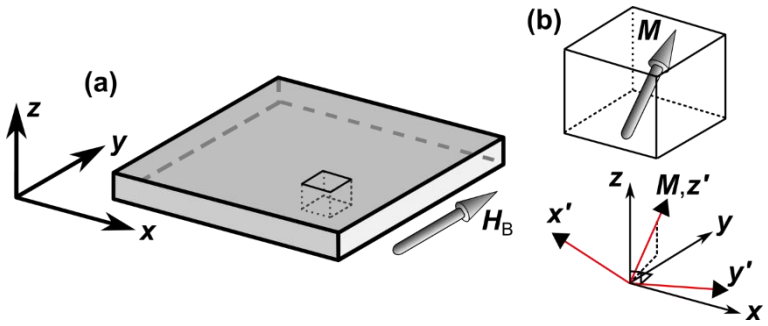

Fig. 4.10 **(a)** The co-ordinate system typically adopted in OOMMF. **(b)** An example magnetization vector characteristic of a mesh-cell (top panel), and the transformed co-ordinate system (bottom panel) as defined by Eqs. 4.18 - 4.20.

Eqs. 4.9 - 4.17, however, were derived with a different co-ordinate system where the static magnetization was assumed to be parallel to the spatially-varying *z*-axis. To reconcile this difference, a co-ordinate transform was therefore applied to all magnetization vectors computed using OOMMF, so that the transformed *z*-axis (*z´*) was aligned parallel to the magnetization.

$$\hat{\boldsymbol{z}}' = \frac{1}{M_s}\left(M_x\hat{\boldsymbol{x}} + M_y\hat{\boldsymbol{y}} + M_z\hat{\boldsymbol{z}}\right). \tag{4.18}$$

By definition, the *x´*-*y´* plane is orthogonal to *z´*, but the precise orientation of the *x´*-*y´* axes is ambiguous. Since the magnetization is most frequently lying within the plane of the film, the newly transformed *y*-axis (*y´*) is defined as being orthogonal to the newly transformed *z´*-axis, but within the plane of the thin film. Thus the *y´*-axis is given by

$$\hat{\boldsymbol{y}}' = \begin{vmatrix} \hat{\boldsymbol{x}} & \hat{\boldsymbol{y}} & \hat{\boldsymbol{z}} \\ M_x & M_y & M_z \\ 0 & 0 & 1 \end{vmatrix} = \frac{1}{\sqrt{\left(M_x{}^2 + M_y{}^2\right)}}\left(M_y\hat{\boldsymbol{x}} - M_x\hat{\boldsymbol{y}}\right). \tag{4.19}$$

The newly transformed *x*-axis (*x´*) is then simply given by the cross-product of the *y´*-*z´* axes.

$$\begin{aligned} \hat{\boldsymbol{x}}' &= \frac{1}{M_s\sqrt{\left(M_x{}^2 + M_y{}^2\right)}}\begin{vmatrix} \hat{\boldsymbol{x}} & \hat{\boldsymbol{y}} & \hat{\boldsymbol{z}} \\ M_y & -M_x & 0 \\ M_x & M_y & M_z \end{vmatrix} \\ &= -\frac{M_xM_z}{M_s\sqrt{\left(M_x{}^2 + M_y{}^2\right)}}\hat{\boldsymbol{x}} - \frac{M_yM_z}{M_s\sqrt{\left(M_x{}^2 + M_y{}^2\right)}}\hat{\boldsymbol{y}} + \frac{\sqrt{\left(M_x{}^2 + M_y{}^2\right)}}{M_s}\hat{\boldsymbol{z}} \end{aligned} \tag{4.20}$$

An example of this co-ordinate transform is shown in Fig. 4.10 (b).

Using OOMMF, the ground-state magnetization was calculated, and then exported and manipulated, so that the magnetization was slightly "deflected" along either the *x´*-axis or *y´*-axis. This was implemented by tipping the magnetization by $M_s/1000$ along the respective transformed axes, so that the new magnetic ground states are given by

$$\boldsymbol{M}_{ip} = \left[M_x + \frac{M_sM_y}{1000\sqrt{\left(M_x{}^2 + M_y{}^2\right)}}\right]\hat{\boldsymbol{x}} + \left[M_y - \frac{M_sM_x}{1000\sqrt{\left(M_x{}^2 + M_y{}^2\right)}}\right]\hat{\boldsymbol{y}} + M_z\hat{\boldsymbol{z}} \tag{4.21}$$

$$\boldsymbol{M}_{oop} = \left[M_x - \frac{M_xM_z}{1000\sqrt{\left(M_x{}^2 + M_y{}^2\right)}}\right]\hat{\boldsymbol{x}} + \left[M_y - \frac{M_yM_z}{1000\sqrt{\left(M_x{}^2 + M_y{}^2\right)}}\right]\hat{\boldsymbol{y}} + \left[M_z + \frac{\sqrt{\left(M_x{}^2 + M_y{}^2\right)}}{1000}\right]\hat{\boldsymbol{z}} \tag{4.22}$$

where the subscripts "ip" and "oop" refer to whether the deflection was applied in or out of the plane of the film respectively. The magnetization distributions defined by Eqs. 4.21 -4.22 were then loaded into OOMMF separately as new ground-state magnetic configuration, for the same magnetic system as considered before. As already discussed in Section 3.6.1, prior

to running any micromagnetic simulation, OOMMF calculates the demagnetizing tensor characterizing the sample. The effective field generated as a response to the applied deviation of the magnetization was therefore calculated. The precise manner in which the magnetization was "deflected" (always locally orthogonal to the direction of the static magnetization) leads to the system of equations

$$\begin{pmatrix} h'_{eff,oop,x} - h'_{Zeeman,oop,x} \\ h'_{eff,oop,y} - h'_{Zeeman,oop,y} \end{pmatrix} = \begin{pmatrix} N_{xx}^{\ eff} & N_{xy}^{\ eff} \\ N_{yx}^{\ eff} & N_{yy}^{\ eff} \end{pmatrix} \begin{pmatrix} m'_x \\ 0 \end{pmatrix} \& \begin{pmatrix} h'_{eff,ip,x} - h'_{Zeeman,ip,x} \\ h'_{eff,ip,y} - h'_{Zeeman,ip,y} \end{pmatrix} = \begin{pmatrix} N_{xx}^{\ eff} & N_{xy}^{\ eff} \\ N_{yx}^{\ eff} & N_{yy}^{\ eff} \end{pmatrix} \begin{pmatrix} 0 \\ m'_y \end{pmatrix} \quad (4.23)$$

where the dynamic effective / Zeeman fields and dynamic magnetization are projected onto the appropriate transformed axes via

$$h'_{ip,x} = \boldsymbol{h}_{ip} \cdot \hat{\boldsymbol{x}}' = -\frac{h_{ip,x} M_x M_z}{M_s \sqrt{\left(M_x^{\ 2} + M_y^{\ 2}\right)}} - \frac{h_{ip,y} M_y M_z}{M_s \sqrt{\left(M_x^{\ 2} + M_y^{\ 2}\right)}} + \frac{h_{ip,z} \sqrt{\left(M_x^{\ 2} + M_y^{\ 2}\right)}}{M_s} \quad (4.24)$$

$$h'_{ip,y} = \boldsymbol{h}_{ip} \cdot \hat{\boldsymbol{y}}' = -\frac{h_{ip,x} M_y}{\sqrt{\left(M_x^{\ 2} + M_y^{\ 2}\right)}} + \frac{h_{ip,y} M_x}{\sqrt{\left(M_x^{\ 2} + M_y^{\ 2}\right)}} \quad (4.25)$$

$$h'_{oop,x} = \boldsymbol{h}_{oop} \cdot \hat{\boldsymbol{x}}' = -\frac{h_{oop,x} M_x M_z}{M_s \sqrt{\left(M_x^{\ 2} + M_y^{\ 2}\right)}} - \frac{h_{oop,y} M_y M_z}{M_s \sqrt{\left(M_x^{\ 2} + M_y^{\ 2}\right)}} + \frac{h_{oop,z} \sqrt{\left(M_x^{\ 2} + M_y^{\ 2}\right)}}{M_s} \quad (4.26)$$

$$h'_{oop,y} = \boldsymbol{h}_{oop} \cdot \hat{\boldsymbol{y}}' = -\frac{h_{oop,x} M_y}{\sqrt{\left(M_x^{\ 2} + M_y^{\ 2}\right)}} + \frac{h_{oop,y} M_x}{\sqrt{\left(M_x^{\ 2} + M_y^{\ 2}\right)}} \quad (4.27)$$

$$m'_x = m_x \cdot \hat{\boldsymbol{x}}' = -\frac{m_x M_x M_z}{M_s \sqrt{\left(M_x^{\ 2} + M_y^{\ 2}\right)}} - \frac{m_y M_y M_z}{M_s \sqrt{\left(M_x^{\ 2} + M_y^{\ 2}\right)}} + \frac{m_z \sqrt{\left(M_x^{\ 2} + M_y^{\ 2}\right)}}{M_s} \quad (4.28)$$

$$m'_y = m_y \cdot \hat{\boldsymbol{y}}' = -\frac{m_x M_y}{\sqrt{\left(M_x^{\ 2} + M_y^{\ 2}\right)}} + \frac{m_y M_x}{\sqrt{\left(M_x^{\ 2} + M_y^{\ 2}\right)}} \quad (4.29)$$

The elements of the effective demagnetizing tensor are then given by

$$N_{xx}^{\ eff} = \frac{-\left(h'_{eff,oop,x} - h'_{Zeeman,oop,x}\right)}{m'_x} \quad (4.30)$$

$$N_{yx}^{\ eff} = \frac{-\left(h'_{eff,oop,y} - h'_{Zeeman,oop,y}\right)}{m'_x} \quad (4.31)$$

$$N_{xy}^{\ eff} = \frac{-\left(h'_{eff,ip,x} - h'_{Zeeman,ip,x}\right)}{m'_y} \tag{4.32}$$

$$N_{yy}^{\ eff} = \frac{-\left(h'_{eff,ip,y} - h'_{Zeeman,ip,y}\right)}{m'_y} \tag{4.33}$$

and the tensor component $N_{zz}^{\ eff}$ is merely found using the ground state magnetization and effective field

$$N_{zz}^{\ eff} = \frac{-\left(H_{eff,x} - H_{Zeeman,x}\right)\cdot M_x - \left(H_{eff,y} - H_{Zeeman,y}\right)\cdot M_y - \left(H_{eff,z} - H_{Zeeman,z}\right)\cdot M_z}{{M_s}^2}. \tag{4.34}$$

These quantities are then fed into Eqs. 4.13 - 4.14 to obtain the spatial distributions of $\chi_{xx,xy,yx,yy}^{\ eff}$.

4.4.3 Local frequency of resonance across a miniaturized antidot system

To test the utility of the model discussed in Section 4.4.2, the model was applied to explain the results presented in Sections 4.3.1 - 4.3.2. The local frequency of resonance was calculated for the results presented in Fig. 4.8 (c) involving the 6 nm-thick Permalloy film in which a circular antidot was embedded. Presented in Fig. 4.11 (a) is the distribution of the effective field (projected onto the magnetization) in the vicinity of the 6 nm-thick antidot. It was anticipated, and indeed observed, that the magnetization was aligned almost completely within the plane of the film (the maximum out-of-plane component of magnetization was measured as being 10 mG), due to both the in-plane application of the bias field, and the thinness of the film itself. In Fig. 4.11 (b) - (f), the spatially-resolved effective demagnetizing tensor elements are presented.

To understand the distribution of the effective demagnetizing tensor elements, it is useful to first understand the general properties of the demagnetizing tensor characterizing a magnetized cuboid, in the macrospin approximation.[145] For a thin film extending to infinity in the *y*-*z* plane, and of finite thickness along the *x*-axis, the demagnetizing factor in the *x*-direction is unity, and all other demagnetizing factors are zero. If now the thin film is confined in the *y*-*z* plane, the demagnetizing factor in the *x*-direction reduces below unity, and the other demagnetizing factors adjust so that the trace of the demagnetizing tensor is unity. As the confinement increases, N_{xx} decreases. For a sample of size (1 × 1000 × 1000) nm^3, for

example, N_{xx} = 0.995, whereas when the sample spans (1 × 100 × 100) nm^3, N_{xx} = 0.966.[176] When the sample is confined so as to form a cube, N_{xx} = 1/3.

The out-of-plane responsive tensor element N_{xx}^{eff}, presented in Fig. 4.11 (b), is radially symmetric about the antidot. Upon deflecting the magnetization normal to the plane of the sample, the induced demagnetizing field was wholly out-of-plane far from the antidot, and so the effective demagnetizing tensor element far from the antidot was approximately 1. Close to the antidot however, the geometrical edge causes N_{xx}^{eff} to decrease, independently of the magnetization's in-plane orientation. Hence the radially-symmetric reduction in N_{xx}^{eff} is to be expected.

The next two elements calculated, N_{xy}^{eff} and N_{yx}^{eff}, were both very close to zero (with absolute values smaller than 6×10^{-5}) - indeed, it could be argued that they merely correspond to numerical error, due to their small size. The distribution of N_{yy}^{eff}, shown in Fig. 4.11 (c), has significant non-zero value immediately on the left and right-hand sides of the antidot. Here, the magnetization is strongly pinned to the antidot (due to the alignment of the magnetization with the geometrical boundary), leading to a spatial profile of N_{yy}^{eff} reminiscent of the quasi-concentric rings discussed earlier in Fig. 4.3 (b) - (c). Last but not least, the distribution of N_{zz}^{eff} (shown in Fig. 4.11 (d)) is strongly similar to the distribution of the static effective field shown in Fig. 4.11 (a), as would be anticipated. The trace of the demagnetizing tensor is traditionally always 1, but such a condition is not generally satisfied by Eqs. 4.29 - 4.33, due to the inclusion of interactions other than that associated with the demagnetization.

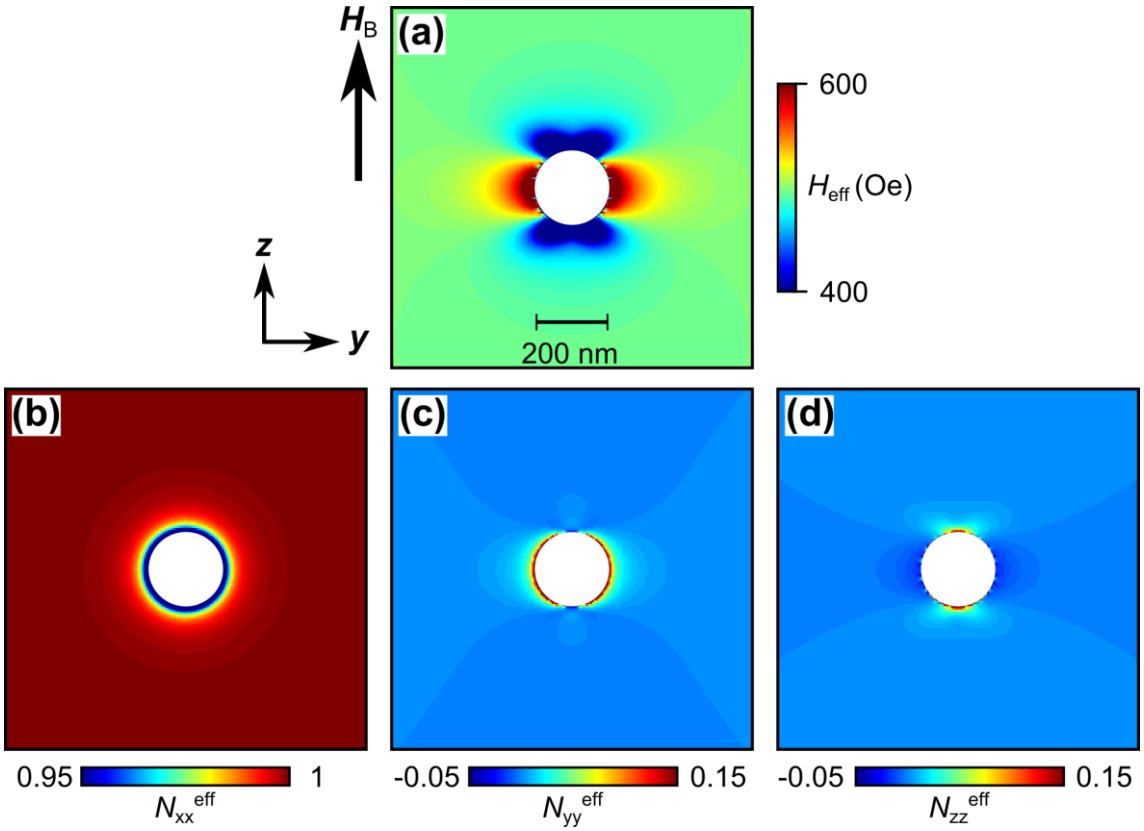

Fig. 4.11 **(a)** The calculated projection of the effective field onto the static magnetization, in the immediate vicinity of the Permalloy antidot (6 nm thick). **(b)-(d)** The distributions of N_{xx}^{eff}, N_{yy}^{eff} and N_{zz}^{eff} respectively, calculated using Eqs. 4.30 - 4.34.

Using the spatial distributions of the elements belonging to the effective demagnetizing tensor, the distribution of the local frequency of resonance (Eq. 4.10) was calculated, and this is presented in Fig. 4.12 (a). This distribution is qualitatively similar to that shown in Fig. 4.3 (a). The effective susceptibility elements were then calculated using Eqs. 4.14 - 4.15 – shown in Fig. 4.12 (b) is the spatial distribution of the absolute value of χ_{xy}^{eff} calculated with f = 9 GHz. The distributions of $\left|\chi_{xx}^{eff}\right|$, $\left|\chi_{xy}^{eff}\right|$, $\left|\chi_{yx}^{eff}\right|$ and $\left|\chi_{yy}^{eff}\right|$ were all proportional to each other. The region of magnetization boasting the maximum value of $\left|\chi_{xy}^{eff}\right|$ is most efficiently excited by the spatially-uniform driving magnetic field of frequency 9 GHz. Plotted in Fig. 4.12 (c) is the variation of $\left|\chi_{xy}^{eff}\right|$ along the equator of the antidot – by inspecting this, it can be deduced that (along the equator of the antidot) the magnetization 25 nm away from the antidot is most efficiently excited at resonance.

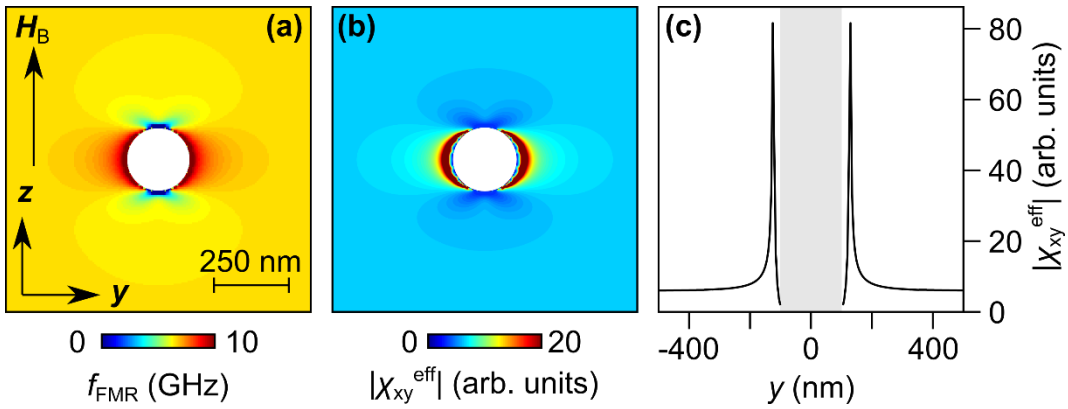

Fig. 4.12 **(a)** The distribution of the local frequency of resonance, calculated using Eq. 4.10. **(b)** The spatial variation of $|\chi_{xy}^{eff}|$ across the 1 μm^2 region in the vicinity of the antidot, calculated for the frequency f = 9 GHz using Eq. 4.15. **(c)** Cross-sectional profile of $|\chi_{xy}^{eff}|$ across the equator of the antidot. The grey section corresponds to the width of the antidot.

4.4.4 Local frequency of resonance across a longitudinally-biased semi-infinite film

The model discussed in Sections 4.4.2 - 4.4.3 should also be capable of determining the local frequency of resonance across a longitudinally-magnetized stripe (hence explaining the results discussed in Section 3.4.2). The analysis discussed in Section 4.4.3 was therefore repeated, but for the Permalloy stripe system (of thickness 40 nm) discussed in Section 4.3.2.

Presented in Fig. 4.13 (a) - (b) is the distribution of the local frequency of resonance across the first 2.5 μm and 1 μm from the edge of the stripe respectively, calculated using Eq. 4.10. As can be seen, the local frequency of resonance is highest at the edge of the stripe (y = 0), and rapidly decreases as y increases. Using this profile, the local frequency of resonance of 9 GHz was identified as belonging to magnetization at a distance y = 120 nm from the edge of the semi-infinite film.

The spatial distribution of the susceptibility component χ_{yy}^{eff} is presented in Fig. 4.14 (c), calculated using Eq. 4.14 with an excitation frequency of 9 GHz. The imaginary part is maximized at y = 120 nm, and the real part is approximately zero at y = 120 nm. This calculation clearly confirms that the dynamic demagnetizing field was indeed responsible for the excitation of spin waves observed in Fig. 4.10.

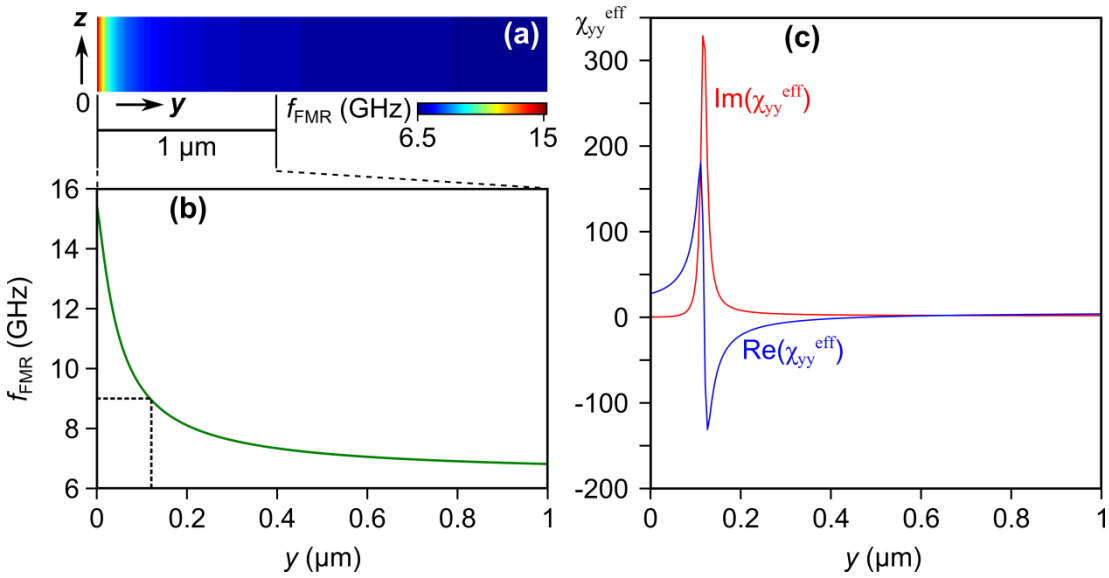

Fig. 4.13 **(a)-(b)** The distribution of the local frequency of resonance across the first 2.5 μm and 1 μm from the edge of the stripe respectively. **(c)** The distributions of the real (blue line) and imaginary (red line) parts of the effective susceptibility tensor χ_{yy}^{eff}, calculated at the frequency of 9 GHz, using Eq. 4.14.

4.5 Summary

In summary, the method of exciting spin waves (with finite wave vector) using global exciting fields has been discussed. By tuning the frequency of the global excitation, specifically-targeted regions of magnetization, with a graded magnonic index, can be efficiently excited, leading to the generation of propagating spin waves. The spin waves can manifest in the form of spin-wave caustic beams (when the dipolar interaction dominates), or more regular plane waves (when instead the exchange interaction dominates). A hybrid numerical / analytical model has been developed in order to enable the identification of the coordinates of different regions of magnetization, within a non-uniformly magnetized medium, which most efficiently couple to the exciting magnetic field. This model can predict not only the influence of the static demagnetizing and Zeeman fields on the frequency of resonance, but can also incorporate the impact of the exchange field and the geometry of the system. In principle, the model can also take into account all other magnetic interactions that can be suitably included within micromagnetic simulations.

Going beyond the basic mechanism outlined by Schlömann back in 1964, the work discussed in this chapter has successfully demonstrated that magnetic non-uniformities can be used to excite spin waves, in conjunction with a spatially-uniform temporally-harmonic microwave field. At the time of writing, the most popular scheme of spin-wave emission involves micron-sized electrical circuitry – the nonuniformity of the exciting field allows spin waves with finite wave vector to be generated. This scheme does not lend itself to miniaturization, however. Instead, using the nonuniformities of magnetization and effective field - i.e. the graded magnonic index - naturally associated with micro- and nano-magnetic structures, one can successfully reduce the spin-wave wavelength towards the nanometric scale (in Fig. 4.9, for example, a spin-wave wavelength of 90 nm was obtained). In order to extend this work, it is necessary to explore how a wide variety of magnetization configurations (such as domain walls, magnetic vorticies etc) influence the distribution of $f_{FMR}(\mathbf{r})$. Then, one can go about constructing and designing suitable spin-wave emitters.

CHAPTER 5

STEERING SPIN WAVES USING A GRADED MAGNONIC INDEX

5.1 Introduction

Classically, the trajectory of propagating waves can be understood using the principles of geometrical optics.[177-178] This approach can be traced back to Fermat's Principle, and is underpinned by four axioms – namely, that wave propagation is both rectilinear and reversible, and obeys both the law of reflection and Snell's Law. The lattermost law is essential for understanding how waves refract across the interface between two dissimilar media. Snell's Law states that the angles of incidence θ_1 and refraction θ_2 for light traversing an interface between two media (of refractive index n_1 and n_2 respectively) are connected via

$$n_1 \sin\theta_1 = n_2 \sin\theta_2 . \tag{5.1}$$

Snell's Law is generally a consequence of electromagnetic boundary conditions – specifically, that the component of $\boldsymbol{E}$ parallel to the translationally-invariant interface should be conserved. Analogous forms of Snell's Law, describing the propagation of other types of waves (e.g. phonons[179] and acoustic waves[180] etc.) can also be derived. For the case of spin waves, Snell's Law has been successfully adapted[181-186] to describe the reflection and refraction of exchange and dipole-exchange spin waves across a well-defined sharp interface, where the two ferromagnetic films on the opposite sides of the interface differ in either their magnetization orientation or effective field strength.

In an extensive series of articles,[66, 187-190] Anatoly Vashkovskii and Edwin Lock theoretically studied the reflection and refraction of dipolar spin-wave beams across distinct boundaries, through considering not Snell's Law, but rather by ray tracing across isofrequency curves. Specifically, the isofrequency curves characterizing the two coupled

ferromagnetic films were constructed, and by assuming the tangential wave vector component was conserved, the trajectory of a wave traversing the interface was calculated. As a consequence of the anisotropy of the dipolar spin-wave dispersion, a wealth of counter-intuitive effects, such as total non-reflection and negative refraction, were predicted (the former was recently experimentally observed by Geniusz *et al*).[191]

In optics, the propagation of electromagnetic waves across media with smoothly-varying refractive index is studied under the umbrella fields of graded-index optics and transformation optics.[192] By tailoring the spatial distribution of the refractive index, it is possible to realize exotic electromagnetic functionalities, such as invisibility cloaking,[193] optical black holes[194] and "superlensing".[195] Inspired by such demonstrations, research is now being devoted to mapping the concepts of transformation optics onto magnonics. It has already been noticed that, by modifying the ground state magnetization distributions across patterned structures, spin waves can be continuously steered around bends.[56,196] Moreover, by directing spin waves through regions in which the internal field smoothly varies, the wave vector can be increased,[197] or an "interface-mode" can be generated.[198] Finally, Elyasi *et al.* have theoretically demonstrated[199] the possibility of magnonic cloaking, whereby non-magnetic obstacles do not affect the wave fronts of passing spin waves.

In this chapter, I will discuss experimental and numerical results which demonstrate that continuously-varying magnetic parameters can be used to smoothly steer propagating spin waves across a T-junction of waveguides. Throughout, spin waves are excited using the Schlömann mechanism (which was studied previously in Chapter 4). In the first section of this chapter, I will discuss the results of TRSKM imaging, which reveal that when the T-junction is biased symmetrically, symmetrical propagation of the excited spin waves is observed across both "arms" of the T-junction. When the T-junction is instead biased obliquely, spin-wave propagation is instead observed along one arm only. In the second section, I then discuss the results of OOMMF simulations, which are used to both corroborate and (partially) understand some of the experimentally-observed features. In the third section, I will discuss extensive calculations involving the micromagnetic results, which demonstrate that the experimentally-observed behavior emerges as a natural consequence of spin waves traversing continuously-varying distributions of the internal field and magnetization – these distributions are responsible for steering the spin waves in particular ways. This

interpretation is considered to be part of the theme of research termed "graded-index magnonics", due to it being inspired by the principles of graded-index optics.

5.2 Sample details and experimental measurements

The magnetic sample studied in this chapter is a Permalloy microstructure geometrically patterned to form an 'H'-shape. The microstructure was fabricated by Dr. Sergei Chertapolav using a combination of magnetron sputtering and electron beam

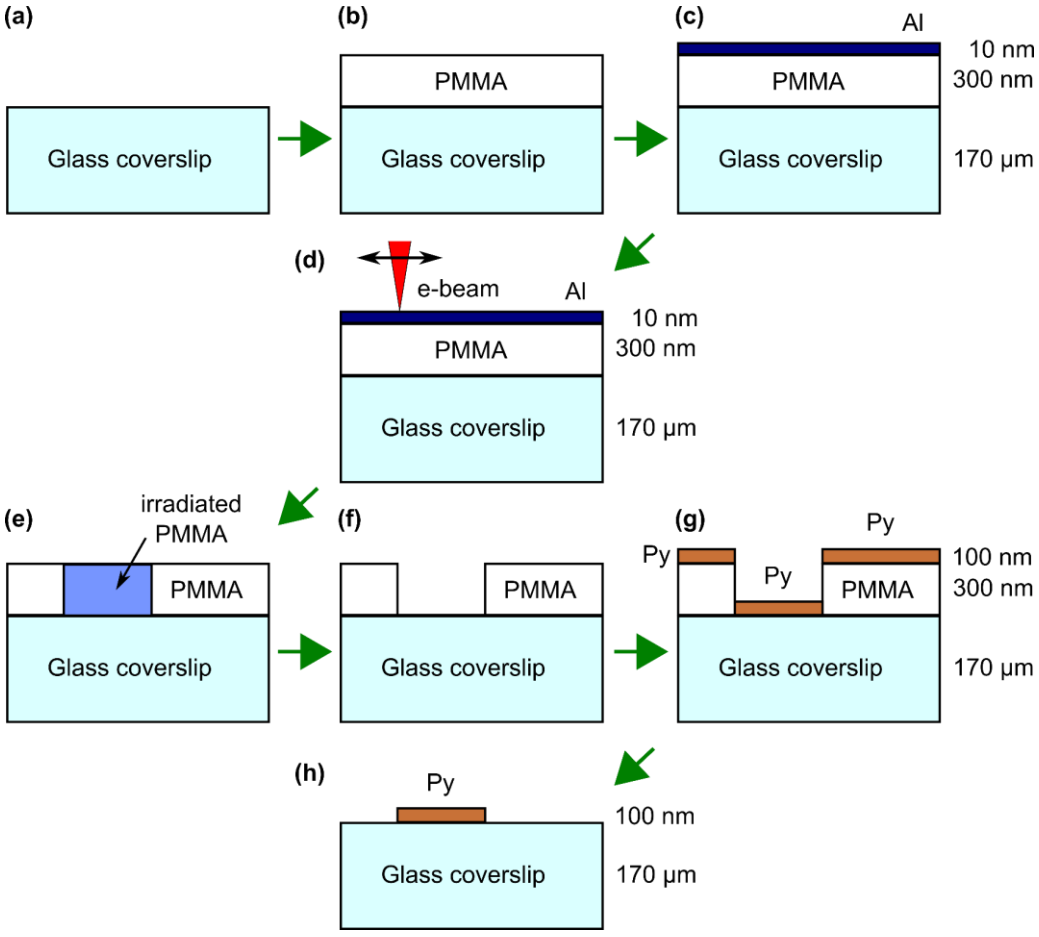

Fig. 5.1 A schematic of the procedure used to fabricate the studied Permalloy microstructure. **(a)-(c)** A 300 nm-thick layer of PMMA - Poly(methyl methacrylate) – was deposited on a glass coverslip, and capped by a thin layer of Aluminium. **(d)-(f)** Electron-beam lithography was used to pattern the PMMA into a mask. **(g)-(h)** A thin layer of Permalloy was sputtered across the entire sample, and the PMMA film was then removed using acetone, leaving behind the Permalloy microstructure mounted on the glass substrate.

lithography. A schematic of the fabrication process is shown in Fig. 5.1. In the first stage, a thin layer of PMMA (poly(methyl methacrylate)) was deposited on a glass coverslip. In order to remove any charges induced through the electron beam lithography, a further layer of Aluminium was deposited on the PMMA using thermal vacuum deposition. Electron beam lithography was then used to geometrically irradiate the PMMA , and the irradiated PMMA was then removed using 2-Propanol, 4-Methyl-2-Pentanon, and Ethyl Methyl Ketone. Permalloy was then deposited across the entire structure, using a calibrated rate of film deposition (3.33 Å /s) to control the final film thickness. The PMMA layer was then removed using acetone, leaving behind the Permalloy microstructure mounted directly on the glass substrate. An optical photograph of the five fabricated microstructures is given in Fig. 5.2. The microstructures had a uniform thickness of 100 nm, a fixed waveguide width of 5 μm, and were nominally identical, differing only in their relative orientation (by angles of 15°).

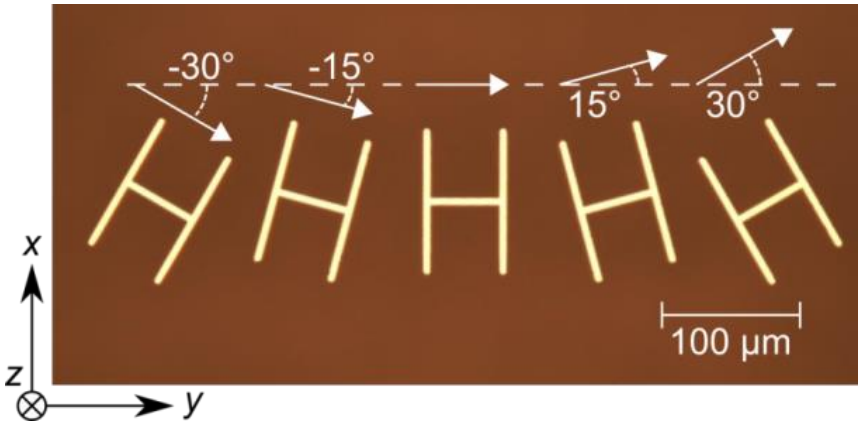

Fig. 5.2 An optical photograph of the magnetic samples under investigation. The five Permalloy 'H'-shaped microstructures were nominally identical, differing only in their relative orientation as indicated.

The microstructures shown in Fig. 5.2 were, in the first stage, positioned above the 500 μm-wide signal line of the CPW discussed in Section 3.3.2, and affixed to the said waveguide using Kapton tape. The mounted structure was then inserted within the TRSKM system for further study, and uniformly magnetized along the *y*-axis by a bias field H_B = 729 Oe. This bias field - the maximum that can be delivered using the electromagnet integrated within the TRSKM system - was applied in order to reasonably saturate the magnetization of the microstructures. This bias magnetic field was then reduced incrementally so as H_B = 500 Oe. Upon focusing the probing laser beam onto the surface of the microstructures, the pulsing

current as described in Section 3.3.3 was applied across the signal line of the CPW. The time-varying signals shown in the left panels of Fig. 5.2 (a) were then recorded, where the upper red (lower blue) signals were acquired when the probing laser beam was focused on the center of the leg (arm) of the T-junction. These time-varying signals were all obtained with a time-step of 3.33 ps, and a lock-in time-constant / sensitivity / gain of 1 s / 10 μV / 20 dB. The time-varying signal has been nulled (during post-processing) prior to the arrival of the pumping field, and due to the oscillations decaying mostly within the remaining 3.203 ns, a rectangular window function was used to compute the Fourier Transform of the signals. These frequency spectra are presented in the right panel of Fig 5.2 (a). The dominant modes of resonance can be clearly identified, where the frequency of the dominant mode in the leg of the T-junction (8.25 GHz) exceeds that of the arm (5.75 GHz).

Presented in Fig. 5.3 (b) - (k) are the time-varying signals, and their corresponding Fourier Transforms, presented in order of increasing angle α of the bias magnetic field relative to the leg of the T-junction. While these are shown sequentially, they were acquired in different order. Specifically, after measuring the response of the system when $\alpha = 0°$, the laser probe was moved to the other two neighboring microstructures, hence allowing the signals for $\alpha = 15°$ and $\alpha = 30°$ to be collected. The sample was then completely removed from the TRSKM system, physically rotated above the coplanar waveguide (e.g. by 22.5°), and reinstalled back within the TRSKM system. In this fashion, time-varying signals for three different values of α were recorded, until the entire data set shown in Fig. 5.2 was collected. To evaluate the frequency of resonance / full-width half-maximum, the frequency spectra were fitted with a Lorentzian distribution (this is discussed more fully in Appendix 2).

The dependence of the frequency of the dominant mode of resonance on the orientation of the bias field – summarized in Fig. 5.3 (l) - can be understood as a consequence of the static demagnetizing field.[200] When the bias field was aligned parallel to the length of the considered geometrical element, the static demagnetizing field was approximately zero, therefore causing the internal field (and by extension the frequency of the dominant mode) to be maximized. If instead the bias field was orthogonal to the waveguide's long axis, the static demagnetizing field was maximized in strength, causing the internal field / frequency of the dominant mode of resonance to be reduced. At intermediate angles of the bias field relative to the waveguide's length, the frequencies of the two dominant modes approach each other, until they overlap when $\alpha = 45°$.

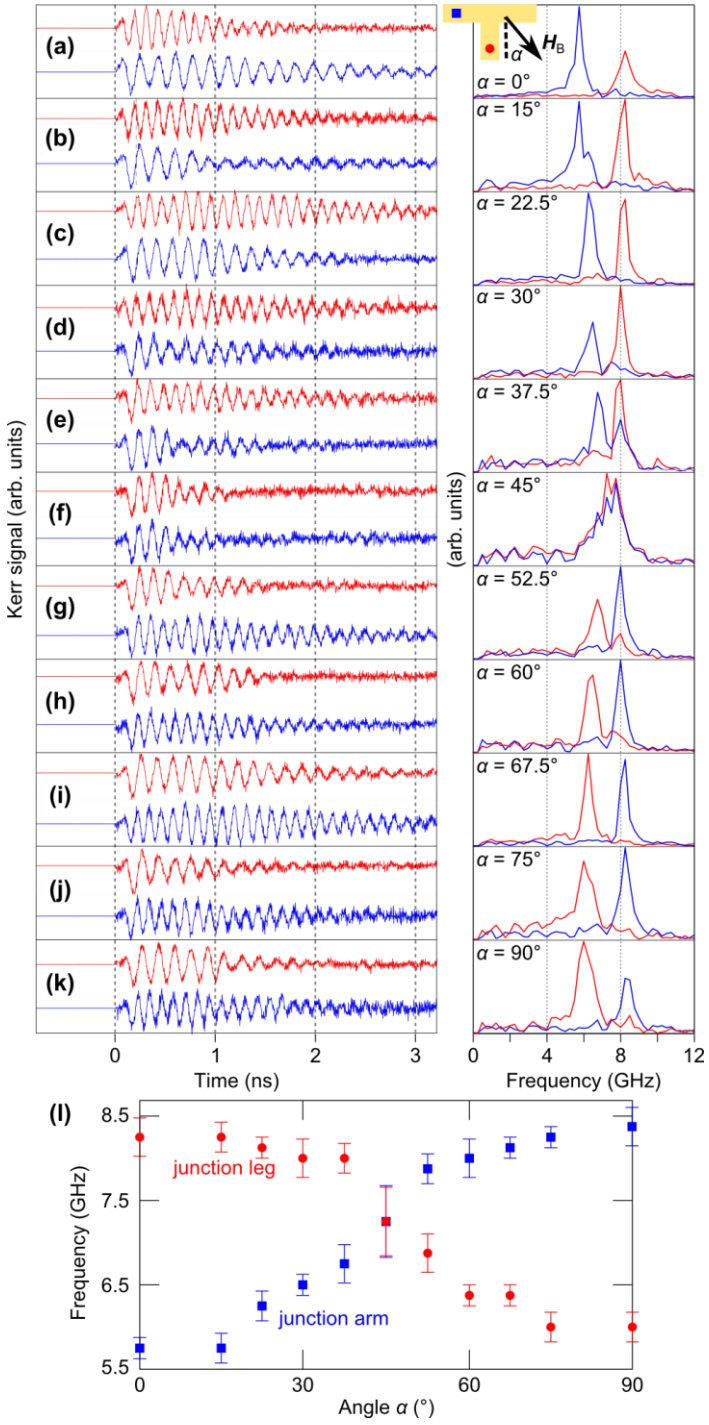

Fig. 5.3 **(a) - (k)** Left panel: time-varying Kerr signals, acquired when the probing laser was focused on the "leg" (red line) / "arm" (blue line) of the Permalloy T-junction. Right panel: the Fourier transform of the time-varying signals. Panels (a) to (k) show the signals and spectra recorded with the bias field orientation as indicated (H_B = 500 Oe throughout). **(l)** The dependence of the frequency of the dominant mode of resonance on the orientation of H_B.[3]

After acquiring the results presented in Fig. 5.3, the previously-pulsed temporal aspect of the driving magnetic field was switched to continuous-wave form. As already outlined in Section 3.3.3, the continuous-wave excitation was harmonic, with a frequency defined as a multiple of 80 MHz. In order to excite spin waves of finite wave vector using the Schlömann mechanism, the frequency of excitation was selected so as to correspond closest to the higher frequency of the two dominant modes. For example, when the bias magnetic field was applied parallel to the leg of the T-junction ($\alpha = 0°$), the frequency of the dominant mode in the leg was 8.25 GHz, and so the frequency of the harmonic excitation was set to 8.24 GHz. For all the experimentally-acquired images presented henceforth, the H-shaped Permalloy microstructure was initially magnetized by a reasonably-saturating field $H_B = 729$ Oe which was then reduced incrementally such that $H_B = 500$ Oe. Subsequently, the signal generator was used to apply a sinusoidal current of 45 mA across the coplanar waveguide, generating an exciting magnetic field across the sample. With the signal generator synchronized to the laser's ouput, time-resolved images of the dynamic out-of-plane component of magnetization across the surface of the sample were then acquired stroboscopically. The images were always recorded with a time-step of $T/8$ seconds, where T was the period of the harmonic exciting field, and the lock-in-amplifier's time-constant / sensitivity / gain was always set to 2 s / 50 μV / 20 dB.

Due to the measured TRSKM images needing both a high resolution and a large spatial extent, the TRSKM images presented in this chapter were acquired over a relatively long period of time. Typically, space-resolved steps of (200 × 200) nm^2 were used to acquire an image spanning (28 × 8) μm^2. Since the signal at each pixel took 7 s to measure, the time needed for a single image to be recorded was around 11 hours. During this time, the TRSKM system had to remain stable in all respects, which represented the key challenge associated with acquiring the presented data. To reduce the impact of mechanical drift and temperature-variation, the images presented in this chapter were all acquired at night and / or over weekends (when the shared laboratory was unoccupied, and the otherwise-cyclic central heating of the building was switched off). Some in-plane mechanical drift - whilst minimized - was still anticipated and indeed observed, so the imaging was frequently performed across a spatial extent larger than that strictly required. Furthermore, the reflectivity of the imaged sample was checked and refocused after every individual image of a series was acquired, so as to reduce the impact of mechanical drift in the out-of-plane direction.

Presented in Fig 5.4 are the reflectivity and Kerr images recorded across the T-junction when H_B = 500 Oe and α = 0°. These images were obtained with an exciting continuous-wave magnetic field of frequency 8.24 GHz, and are arranged sequentially from panels (a) - (h) in increasing time steps of 15.2 ps. The left panel corresponds to the reflectivity (the intensity of reflected light measured by one photodiode in the optical bridge detector). In the middle panel, the entire raw Kerr image is presented. In the right panel, the reflectivity signal has been used as a mask, to remove the Kerr signal not originating from the surface of the Permalloy microstructure. No Kerr images were calibrated to the cone angle of precession.

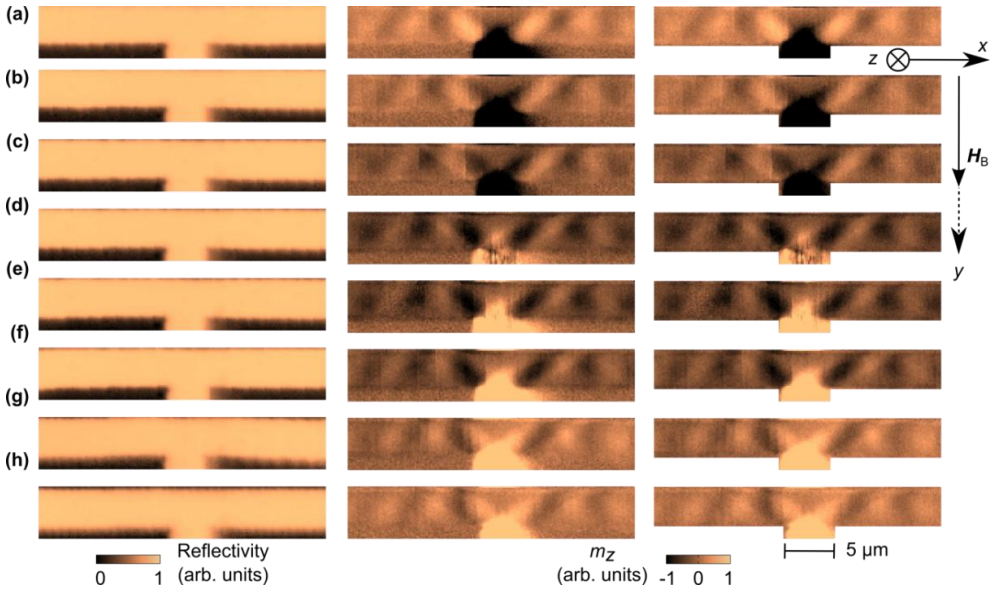

Fig. 5.4 Left panel: reflectivity signal of the imaged microstructure. Middle panel: the raw Kerr image of the out-of-plane dynamic component of magnetization within the T-junction, when pumped continuously at 8.24 GHz. Right panel: the Kerr image as shown in the middle panel, but cropped according to the reflectivity to show only the Kerr signal arising from the sample surface. **(a)-(h)** The sequence of TRSKM images, taken in increments of 15.2 ps, where the bias field H_B = 500 Oe was applied parallel to the leg of the T-junction (so α = 0°).

Resonance was successfully excited in the leg of the T-junction, as evidenced by the sign of the Kerr signal changing every half-period. Furthermore, spin waves are observed propagating along both arms of the T-junction. The excited spin waves are approximately

equal in amplitude, identical in phase, and have their wavefronts inclined at an angle. This suggests the propagation of spin-wave caustic beams.

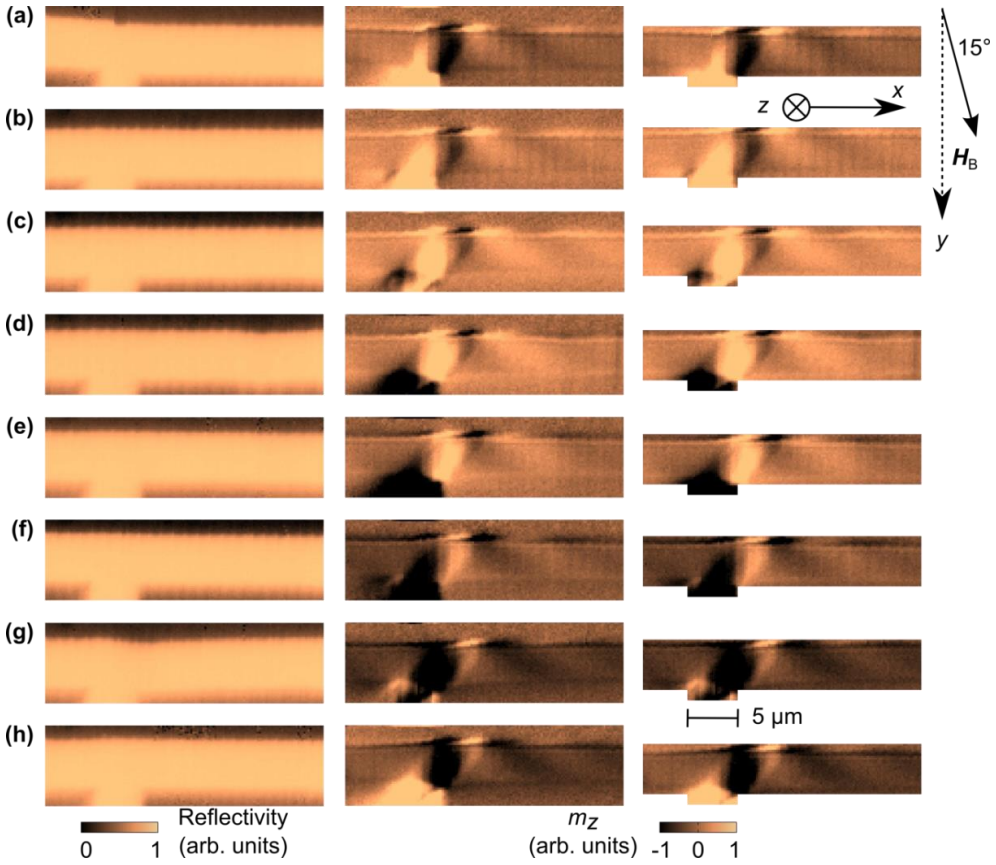

Fig. 5.5 Left panel: reflectivity signal of the imaged microstructure. Middle panel: the raw Kerr image of the out-of-plane dynamic component of magnetization within the T-junction, when pumped continuously at 8.24 GHz. Right panel: the Kerr image as shown in the middle panel, but cropped according to the reflectivity to show only the Kerr signal originating from the sample surface. **(a)-(h)** The sequence of TRSKM images, taken in increments of 15.2 ps, where the bias field H_B = 500 Oe was applied at an angle α = +15° to the leg of the T-junction.

Upon rotating the bias field by ±15° relative to the leg of the T-junction, the frequencies of the dominant precessional modes within the leg and arm of the T-junction were observed in Fig 5.3 to not vary (some slight variation was anticipated, but the resolution associated with the pulsed TRSKM measurements made any such change unobservable). The frequency of excitation was therefore kept at 8.24 GHz, and the piezo-electric stage upon

which the samples were mounted was moved, so as to bring a neighboring (rotated) microstructure within the field of view of the probing lens. This, in effect, rotated the bias magnetic field relative to the microstructure. The corresponding reflectivity images, Kerr images, and Kerr images normalized to the reflectivity (identical in fashion to those presented in Fig. 5.4) are presented in Figs 5.5 and 5.6, where the bias field was rotated relative to the T-junction's leg by α = +15° and α = -15° respectively.

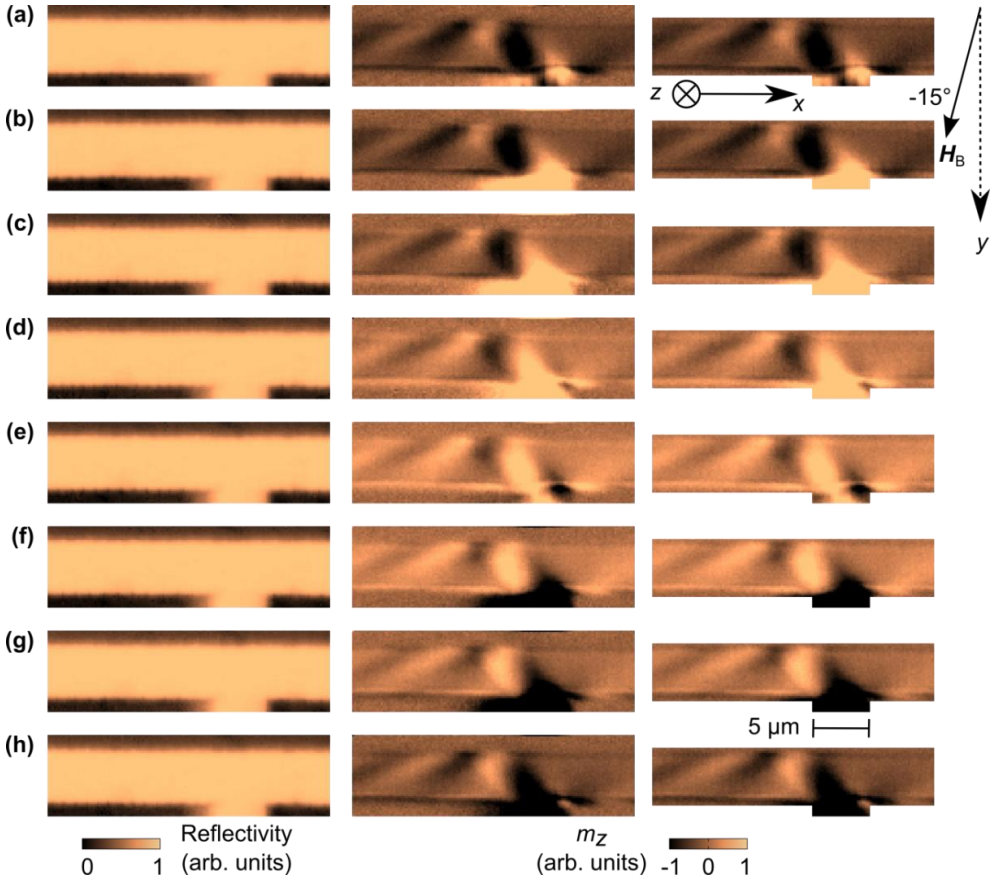

Fig. 5.6 Left panel: reflectivity signal of the imaged microstructure. Middle panel: the raw Kerr image of the out-of-plane dynamic component of magnetization within the T-junction, when pumped continuously at 8.24 GHz. Right panel: the Kerr image as shown in the middle panel, but cropped according to the reflectivity to show only the Kerr signal arising from the sample surface. **(a)-(h)** The sequence of TRSKM images, taken in increments of 15.2 ps, where the bias field H_B = 500 Oe was applied at an angle α = -15° to the leg of the T-junction.

The TRSKM images presented in Figs. 5.5 and 5.6 share some similarities. In both sets of images, the symmetry of the spin-wave excitation and propagation has been broken, whereby a single spin wave is observed to propagate along the right (left) arm when α = +15° (α = -15°). The relative angle of the wave fronts appears to rotate across the waveguide. Across the other waveguide, in contrast, spin-wave propagation is absent. Significant amplitude of precession is also observed along a distinct "stripe", localized along the upper (lower) edge of the arm when α = +15° (α = -15°).

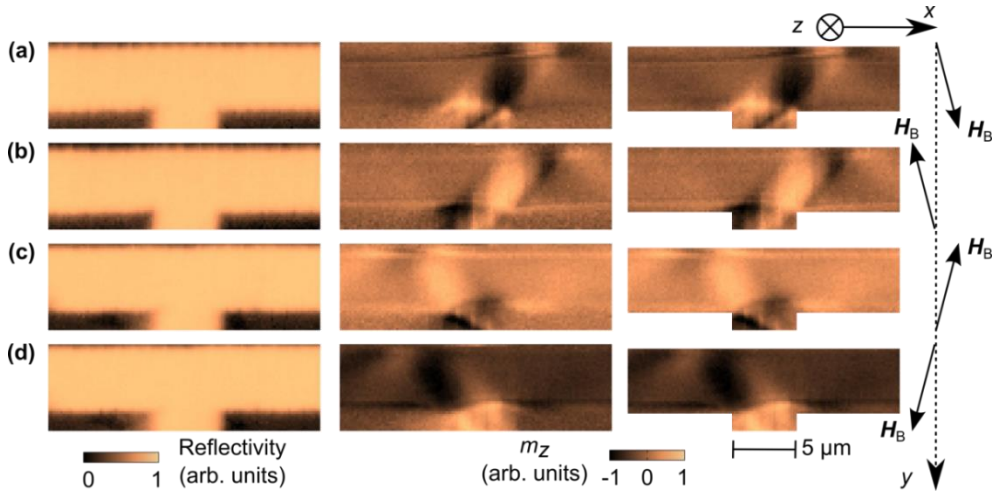

Fig. 5.7 Left panel: reflectivity signal of the imaged microstructure. Middle panel: the raw Kerr image of the T-junction, when pumped continuously at 8.24 GHz. Right panel: the Kerr image as shown in the middle panel, but cropped according to the reflectivity to show only the Kerr signal originating from the sample surface. **(a)-(d)** TRSKM images acquired with the bias magnetic field H_B = 500 Oe applied at an angle α = +15°, α = -165°, α = +165° and α = -15° relative to the leg of the T-junction. The snapshots were obtained with a relative phase difference of either 0° or 180°, with respect to the exciting field.

The experimentally-acquired images suffer due to the viewing window not being symmetrical relative to the leg of the T-junction. For example, in Fig. 5.5, 14 μm of the arm is imaged on the left-hand side of the leg, but only 5 μm of the arm is imaged on the right. This was done deliberately, in order to reduce the (already substantial) time required for the measurements. Compensatory images, with equal and symmetrical extension of the arms across the viewing window, were therefore acquired to verify the absence of spin-wave

propagation. Furthermore, the bias field was reversed in polarity, in order to check the symmetry of the observed spin-wave features. These measurements are presented collectively in Fig. 5.7 (a) - (d), acquired with a phase difference of either 0° or 180° with respect to the phase of the exciting field. These images reveal that the observed spin-wave beam propagated along one waveguide consistently, regardless of the polarity of the canted bias field. Moreover, the absence of the spin-wave beam across the other waveguide is certainly more pronounced.

5.3 Micromagnetic modelling

The experimentally-acquired results discussed in Section 5.2 were restricted by limitations associated with the TRSKM system. The probing laser beam had a finite penetration depth of about 20 nm,[201] and so the experimental results only show the magnetization dynamics excited across the upper surface of the sample. Moreover, the finite diameter of the probe spot on the surface of the sample also resulted in the detected signal being averaged across the spot-size.††††††† To therefore overcome these restrictions, and furthermore to quantitatively study the spin-wave propagation, micromagnetic calculations were performed. The geometry modelled within the micromagnetic simulations was designed to mimic the sample described in Section 5.2 - specifically, the H-shaped structure was enclosed within a cuboid of size (40 × 40 × 0.1) μm^3, and discretized into a mesh of cells of size (100 × 100 × 10) nm^3. The exchange interaction was wholly neglected – the justification for this approximation will be discussed shortly. The gyromagnetic ratio $\gamma/2\pi$ and saturation magnetization M_s of Permalloy was assumed to be 2.8 MHz / Oe and 800 G respectively. At the first step of the micromagnetic calculations, the structure was uniformly magnetized along the vector $0.01\hat{x} + \hat{y}$. The slight tilt of the magnetization was imposed so as to avoid the unrealistic micromagnetic "flower" state,[202] which is energetically unstable at finite temperatures. The bias magnetic field H_B, aligned similarly along the vector $0.01\hat{x} + \hat{y}$, was reduced incrementally from 2000 Oe to 500 Oe, in stages of 100 Oe. The Gilbert damping coefficient was inflated to 0.5 for this micromagnetic calculation, in order to reduce the computational time required. Each stage of the micromagnetic relaxation was considered complete when the maximum rate of magnetization precession across the entire system

††††††† The laser beam had a Gaussian cross-section, and so the acquired signal strictly represents the convolution of the measured Kerr rotation with the nominally diffraction-limited probing spot.

decreased below 0.01 °/ns. Using this approach, the ground-state magnetization corresponding to H_B = 500 Oe was calculated.

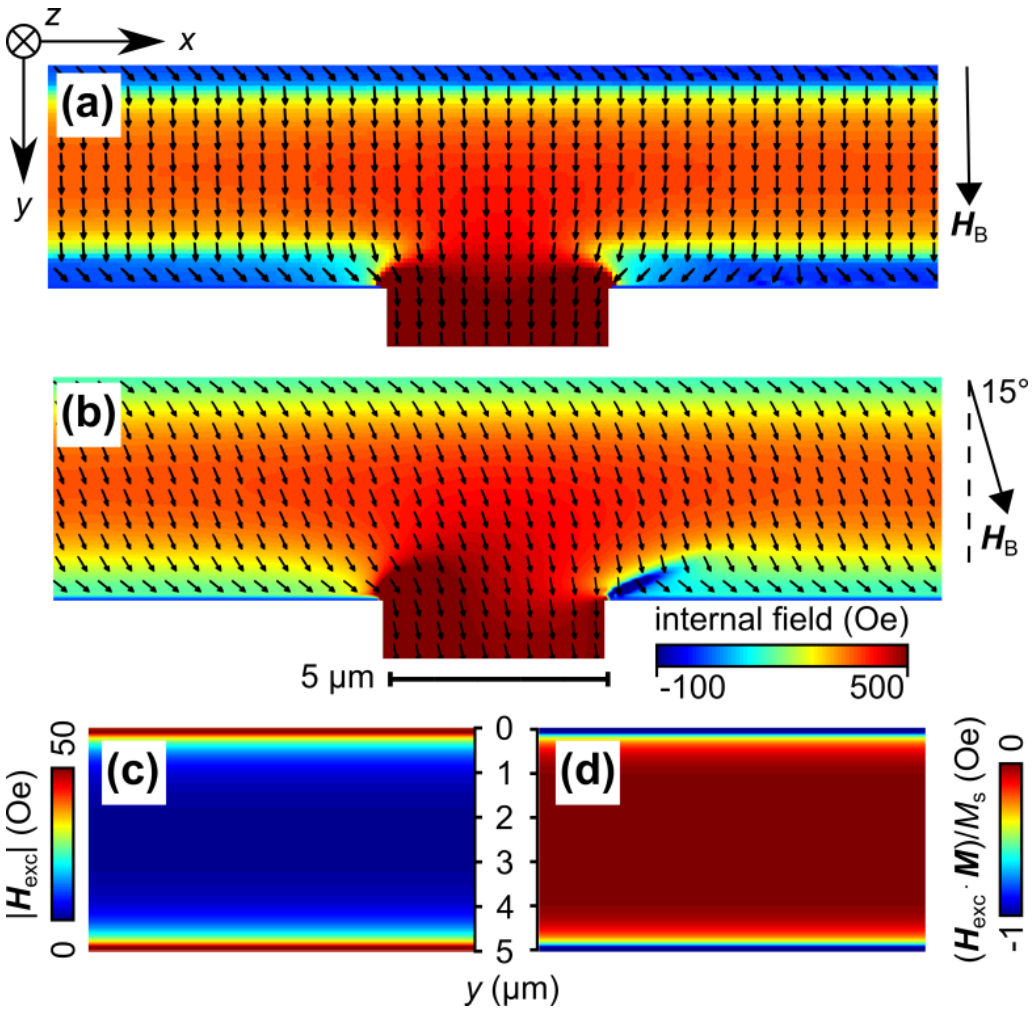

Fig. 5.8 **(a)-(b)** The calculated distributions of the static magnetization (arrows) and the projection of the internal magnetic field onto the magnetization (color scale) are shown when the magnetic field H_B = 500 Oe was applied at α = 0° and α = +15° to the leg of the T-junction respectively. Each arrow represents the average of (5 × 5) mesh cells, where the mesh-cells were of size (100 × 100 × 10) nm^3. **(c)-(d)** The calculated distribution of the magnitude of the exchange field, and the projection of the exchange field onto the magnetization respectively. These were calculated across a 5 μm wide / 100 nm thick waveguide subjected by a bias magnetic field H_B = 500 Oe applied at α = +15°. The meshing cells were of size (5 × 5 × 5) nm^3.

As part of the micromagnetic calculation of the static magnetization configuration, the distribution of the Zeeman and demagnetizing fields were calculated. The Zeeman field, due to the uniformity of the external bias, was uniformly 500 Oe and aligned with the vector $0.01\hat{\boldsymbol{x}} + \hat{\boldsymbol{y}}$. In contrast, the static demagnetizing field was strongly non-uniform across the transversely-magnetized waveguide, due to the formation of fictitious magnetic charges at the waveguide's geometrical edges. The demagnetizing field was strongest at the edges of the waveguide, and weakest at the center. As a result, the projection of the internal field onto the magnetization was strongly non-uniform across the transversely-biased arm of the T-junction, as shown in Fig. 5.7 (a). The orientation of the magnetization was similarly non-uniform: across the center of the arm, the magnetization was crudely parallel to the bias field (i.e. transverse to the waveguide), but close to the edges, the magnetization was strongly canted, as it was seeking to align with the edges of the waveguide. Similar character of the projected internal field and magnetization was observed when α = +15°, as is presented in Fig. 5.7 (b). The ground-state magnetic configurations for α = ±15° were calculated in an identical manner as for α = 0°, except for the rotation of the bias magnetic field.

To incorporate the exchange interaction correctly, it is necessary for the meshing cell-size to be equal to or less than the exchange length – for Permalloy, this is about 5 nm. However, if such a cell-size was adopted, more than one billion cells would have been required to model the considered (40 × 40 × 0.1) μm^3 system - this is beyond the capability of even GPU-enabled micromagnetic packages, such as MuMax3.[136] To therefore model such gargantuan systems, one is forced to adopt a cell-size greater than the exchange length, which invalidates any calculations involving the exchange interaction. The exchange interaction was therefore neglected for these calculations. On a physical level, this approximation can be justified to some extent, as the physical length-scales being studied are far in excess of the exchange length. To ultimately evaluate whether this approximation was reasonable, the exchange field was calculated across a simpler (and smaller) magnetic system. A waveguide of size (15 × 5000 × 100) nm^3 was modelled, using a mesh cell of size (5 × 5 × 5) nm^3 and with one-dimensional periodic boundary conditions[141] applied along the *x*-axis. The ground state magnetization of this waveguide, when subjected to a bias magnetic field H_B = 500 Oe applied at 15° to the waveguide's short axis, was calculated, with the exchange interaction included (the exchange constant A_{ex} of Permalloy was assumed to be 1.3 μerg / cm).

Presented in Fig. 5.8 (c) is the absolute value of the calculated exchange field across the width of the waveguide. The exchange field was uniformly below 15 Oe within the central 4 μm of the waveguide's width, but grew substantially to about 50 Oe within a distance of 100 nm from the waveguide edges. This calculation could be (naively) interpreted as showing the exchange field is significant. When projected onto the static magnetization, however, the exchange field was only on the order of 1 Oe across almost the entire waveguide, as shown in Fig. 5.7 (d). This indicated that the demagnetizing and Zeeman fields completely dominate the magnetic system – close to the edges of the waveguide, the exchange field did indeed become stronger, but it was still dwarfed by the demagnetizing and Zeeman fields - and so the exchange interaction was judged as having negligible influence within the magnetic system.

The experimental signals acquired using TRSKM all represent dynamic quantities, and so to effectively corroborate the experimental measurements, dynamic simulations were performed. As was done with the experimental measurements, the dynamic micromagnetic simulations were classified into two categories, depending on whether the spatially-uniform exciting magnetic field had pulsed or harmonic temporal profile. For the pulsed excitation, the temporal profile of the exciting magnetic field was designed to mimic the pulsed field used within the TRSKM system. Specifically, the pulse had the form

$$h_{pulsed}(t) = h_0 \exp\left(-\frac{(t-t_0)^2}{2t_w{}^2}\right), \tag{5.2}$$

with time-resolved field steps given by

$$\Delta h = -h_0 \cdot \frac{(t-t_0)}{t_w{}^2} \exp\left(-\frac{(t-t_0)^2}{2t_w{}^2}\right). \tag{5.3}$$

The amplitude h_0, time delay t_0, and the full-duration half-maximum (t_w) of the pulsed field were set to 0.1 Oe, 500 ps, and 25 ps respectively. This exciting field was applied uniformly along the *z*-axis, the Gilbert damping coefficient of Permalloy was set to 0.008 (as is characteristic of Permalloy), and the magnetization state was recorded in time steps of 10 ps, for a duration of 10.24 ns.

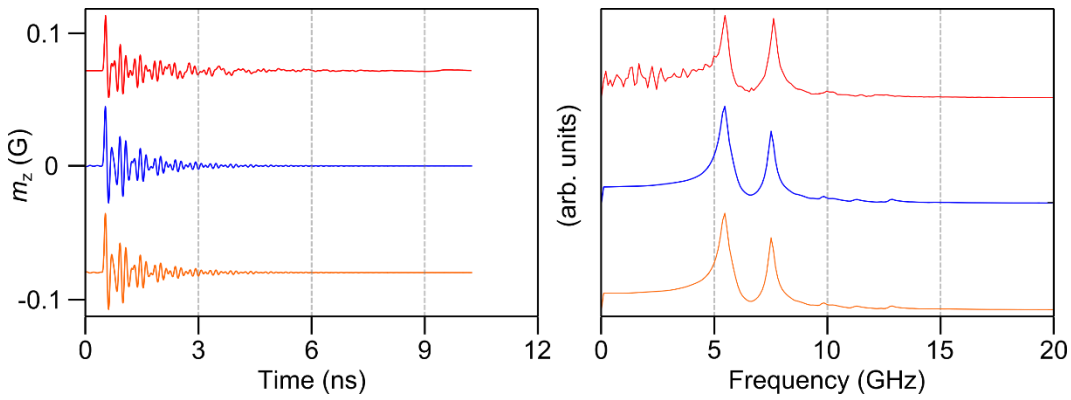

Fig. 5.9 The spatially-averaged out-of-plane component of magnetization (left panel) and the corresponding Fourier transform (right panel), presented from top to bottom where α = 0° (red), α = +15° (blue) and α = -15° (orange) respectively.

The spatially-averaged response of the magnetization to the pulsed excitation, and the corresponding Fourier transform, is presented in the left and right panels of Fig. 5.9 respectively. The signals and spectra in panels (a) - (c) correspond to the systems in which α = 0°, α = +15° and α = -15° respectively. Evident throughout are two maxima, corresponding to the dominant modes of resonance within the arm and leg of the T-junction. Specifically, the frequencies of the dominant modes when α = 0° was 5.47 GHz and 7.62 GHz, and when α = ±15°, 5.47 GHz and 7.52 GHz. Experimentally, however, the frequencies of the dominant modes were around 7.50 GHz and 8.25 GHz respectively. This difference was attributed to the assumed system parameters used to characterize the Permalloy in the micromagnetic calculations. Permalloy typically has a saturation magnetization quoted in the literature as ranging from 700 G to 860 G.[196,203] Furthermore, the gyromagnetic ratio of Permalloy is known to differ from the gyromagnetic ratio of a free electron by around 5%.[203] These potential sources of error could reasonably explain the discrepancy between the numerically-calculated and experimentally-measured frequencies of resonance.

In the next set of micromagnetic calculations, the magnetic system was uniformly excited using a continuous-wave excitation

$$\boldsymbol{h}_{cw}(t) = h_0 \sin(2\pi f \cdot t)\hat{\boldsymbol{z}}\,. \tag{5.4}$$

The amplitude h_0 was 1.75 Oe and the frequency f was set to the frequency of the higher of the two dominant modes shown in Fig. 5.8 (f = 7.62 GHz when α = 0°, and f = 7.52 GHz when α = ±15°). The magnetization was then recorded at eight equidistant points across the period of the exciting field (so $\Delta t = \frac{1}{8f}$), and the static magnetization was subtracted from each magnetization state in order to obtain dynamic results. It was observed that the

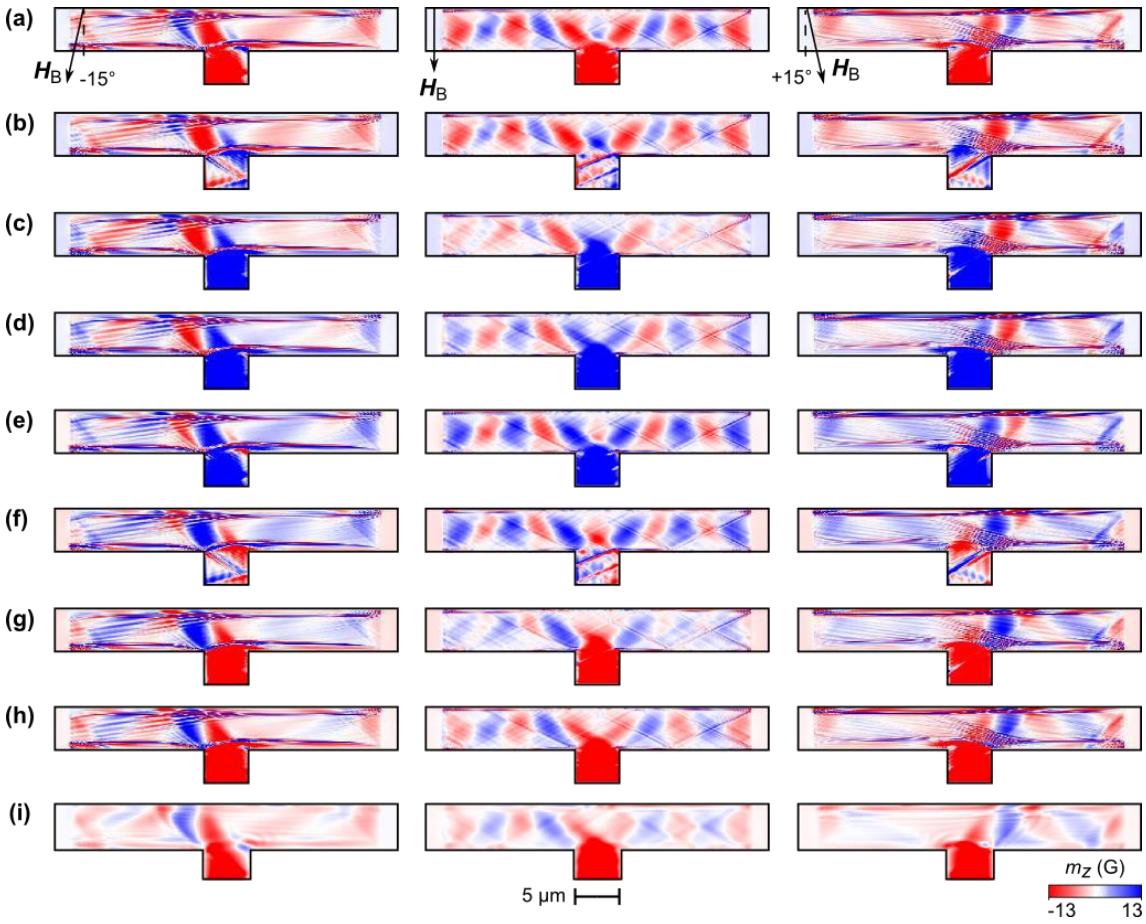

Fig. 5.10 **(a)-(h)** Snapshots of the raw dynamic out-of-plane component of magnetization across the T-junction, which was biased by H_B = 500 Oe applied at the angle α = -15° (left column), α = 0° (middle column) and α = +15° (right column) relative to the leg of the T-junction. The snapshots in the left, middle and right panels are sequentially arranged from top to bottom in increasing time steps of 16.6 ps, 16.4 ps and 16.6 ps respectively. **(i)** The same snapshots as shown in (h), except the raw snapshots have been convolved with a Gaussian smoothing kernel.

precession of magnetization was wholly periodic after about 2 ns after the exciting field was applied. The images presented in the left, middle and right panels of Fig. 5.9 are the time-resolved raw snapshots of the dynamic out-of-plane components of magnetization, when the microstructure was biased at an angle α = -15°, α = 0° and α = +15° respectively. Despite the mismatch in the frequencies of resonance, there is qualitatively good agreement between the images obtained experimentally and numerically. This agreement is further augmented by smoothing the images shown in Fig. 5.10 (a) - (h), as shown in the example presented in Fig. 5.10 (i). Here, a Gaussian kernel with one standard deviation of 3 cells has been convolved with the raw images, providing a resolution more comparable to that associated with the TRSKM images.

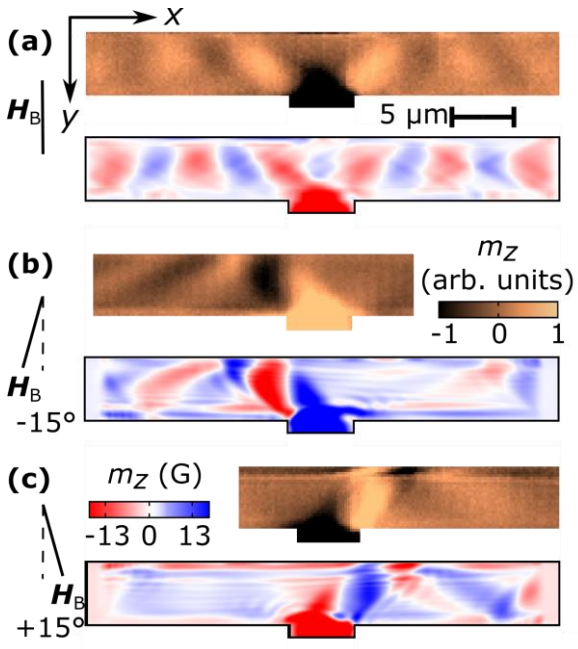

Fig. 5.11 Snapshots of spin waves propagating in the arms of the Permalloy T-junction.[3] The bias magnetic field $\boldsymbol{H}_B$ = 500 Oe is applied **(a)** and at angles of **(b)** α = −15° and **(c)** α = +15° relative to the leg of the junction. In each case, the top (blue-white-red colour scale) and bottom (black-yellow colour scale) panels show results of the TRSKM imaging and micromagnetic simulations, respectively. The frequency of the cw pump was 8.24 GHz for experiments, while for simulations it was 7.62 GHz in (a) and 7.52 GHz in (b) and (c).

Presented in Fig. 5.11 are comparable side-by-side snapshots of the spin-wave propagation, acquired experimentally (black-yellow colour scale) and numerically (red-white-blue colour scale). Qualitatively, these images show very good agreement. When the bias magnetic field is applied parallel to the T-junction's leg, spin-wave propagation is observed across both arms, with similar canting of the wavefronts. Similarly, when the bias magnetic field is canted in either direction, only one spin-wave beam is observed. Again, the orientation of the spin-wave wavefronts agree remarkably well. Also apparent is a concentration of spin-wave amplitude at the lower-right (lower-left) corner of the T-junction when $\alpha = -15°$ ($\alpha = +15°$). Beyond these features, there is also a horizontal "stripe" of amplitude close to the lower (upper) edge of the horizontal waveguide, when $\alpha = -15°$ ($\alpha = +15°$). The only disagreement between the snapshots lies in the frequency of excitation (corresponding to about 0.75 GHz), as already discussed.

The strong agreement between the experimentally-acquired images and the micromagnetic results indicated that the micromagnetic simulations could be used to successfully infer the depth-dependent magnetization dynamics. Shown in Fig. 5.12 (a) - (b) are smoothed snapshots of the dynamic out-of-plane component of magnetization across the top and bottom surfaces of the sample respectively, when $\alpha = +15°$. The excited spin wave

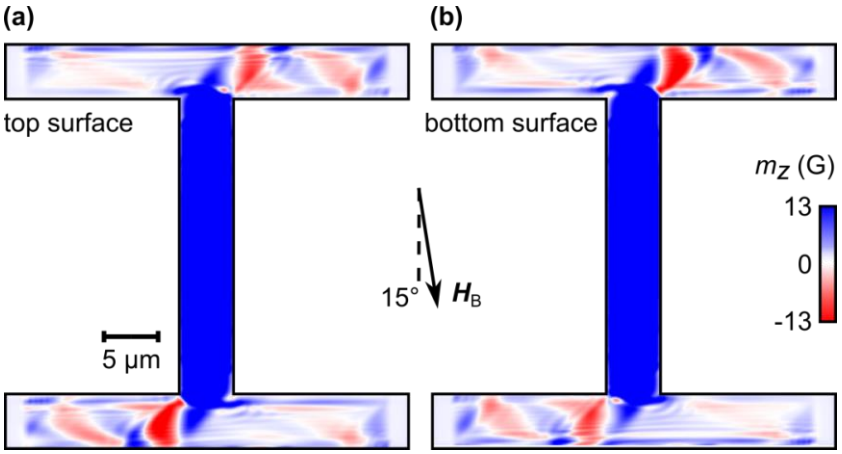

Fig. 5.12 **(a)-(b)** The images of the out-of-plane component of the dynamic magnetization, convolved with a Gaussian kernel, across the top and bottom surfaces of the Permalloy structure respectively, when the microstructure was continuously pumped at 7.52 GHz.[3]

propagating along the arm clearly has depth-resolved character, due to the spin-wave amplitude being lower (higher) on the top (bottom) surface of the magnetic structure.[204] This therefore confirmed that magnetostatic surface spin waves were being excited across the microstructure, rather than backward-volume magnetostatic spin waves.

Another interpretative question that was explored using micromagnetic simulations related to the character of the excited spin waves. The rotated orientation of the wavefronts observed in Figs. 5.4 - 5.7 suggested that the excited spin waves were caustic beams. However, caustic beams are typically observed[97, 169] to be tightly-focused, with a narrow angular aperture, which contrasts with the 5 μm wide beam observed in Figs 5.4 – 5.7. To therefore provide ultimate evidence that the spin waves were caustic beams, the micromagnetic simulations for the system (in which $\alpha = +15°$) was repeated, except the width of the T-junction's leg was reduced to 1 μm. After relaxing the magnetization across microstructure, the spatially-averaged response of the out-of-plane component of magnetization to a pulsed magnetic field was Fourier transformed to obtain a characteristic frequency spectrum, shown respectively in Fig. 5.13 (a) - (b). The frequency of the dominant mode in the arm remained unchanged from before, but the dominant mode in the leg shifted significantly to the higher frequency of 10.3 GHz. Such a change was anticipated, due to the transverse wave vector of the dominant confined mode in the leg being significantly increased. Sequential snapshots of the dynamic out-of-plane component of magnetization of the microstructure, obtained after globally and harmonically exciting the system at a frequency of 10.3 GHz, are presented in Fig. 5.13 from top to bottom (in time steps of 24.3 ps). The reduced width of the leg caused the excited spin wave to have a substantially reduced angular width, hence confirming that the Schlömann mechanism used here was exciting spin-wave caustic beams at the aperture of the T-junction's leg. Specifically, due to the finite width of the leg, the continuously-excited resonance at the interface of the leg-arm junction represented a 5 μm wide source of spin waves. The finite width of this source leads to the excitation of spin waves with a broad range of transverse wave-vector components, hence forming the spin-wave caustic beams.

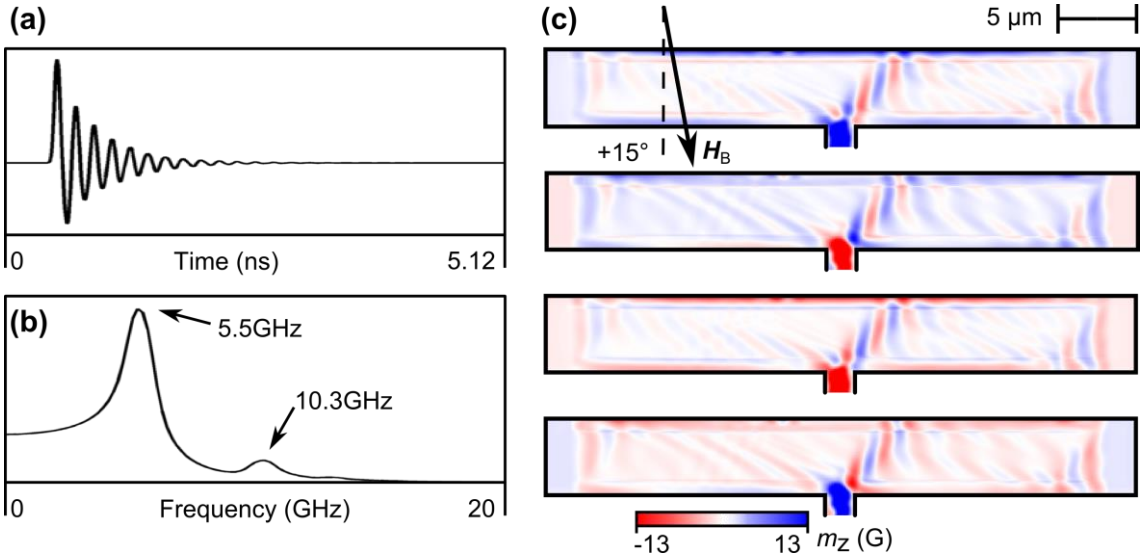

Fig. 5.13 **(a)** The space-averaged temporal response of the Permalloy T-junction to excitation by a uniform pulsed magnetic field is shown for a bias magnetic field of 500 Oe oriented at 15° to the leg. **(b)** The FFT spectrum of the signal in (a) is shown. The peaks at 5.5 GHz and 10.3 GHz correspond to the quasi-uniform modes of resonance confined within the arms and the leg of the T-junction respectively. **(c)** The images of the out-of-plane component of the dynamic magnetization within the T-junction, when continuously pumped at 10.3 GHz, are shown for four moments in time-increments of 24.3 ps.[3]

5.4 Hybrid numerical / analytical model of the spin-wave trajectories

The experimental and numerical results discussed in Sections 5.2 and 5.3 agree remarkably well in demonstrating the spin-wave switching functionality of the T-junction (where the control mechanism was the rotation of the global bias magnetic field). Furthermore, the micromagnetic calculations revealed that spin-wave caustic beams (with MSSW dispersive character) were being excited by the continuous pumping of the dominant mode within the leg of the T-junction. When the bias magnetic field was applied parallel to the leg of the T-junction (α = 0°), the spin-wave beams can be understood as merely undergoing continuous reflection from the edges of the waveguide.‡‡‡‡‡‡‡ There still remained, however, a key question involving the behavior of the excited spin waves when α =

‡‡‡‡‡‡‡ More precisely, the spin-wave beams were reflected from the channels of non-uniform field close to the geometrical edges of the arms.

±15°. The spin-wave excitation was asymmetric, whereby a spin wave propagated along one arm of the T-junction, but no propagation was observed along the other. This was in stark contrast to the effect observed in a similarly-patterned YIG structure.[150]

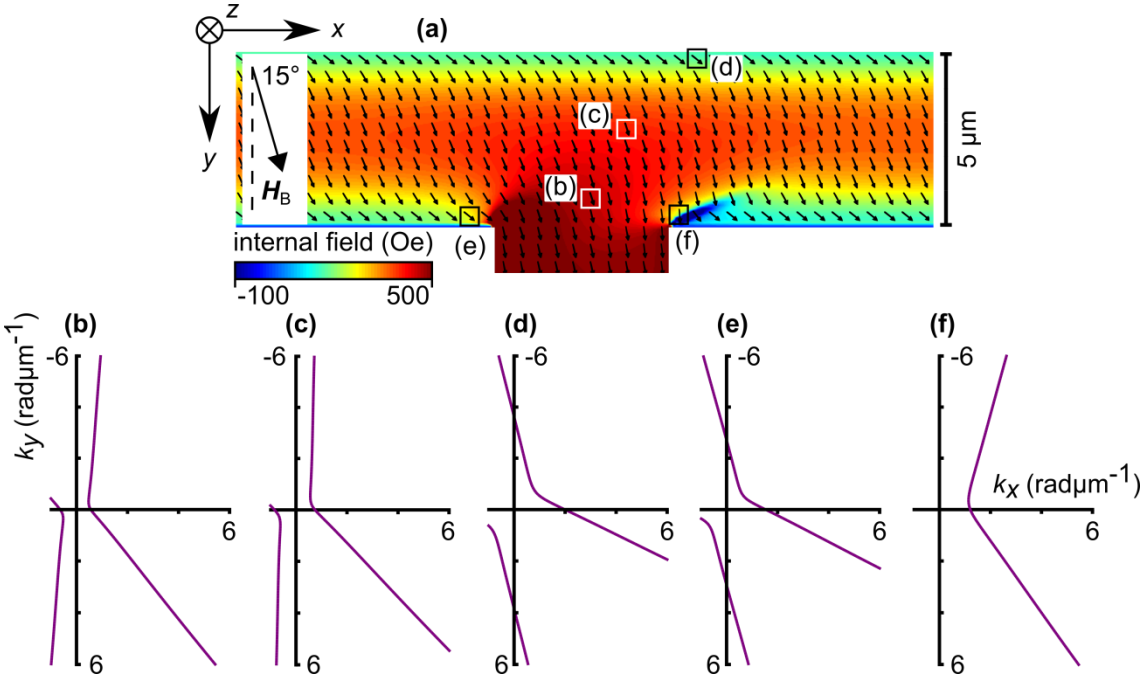

Fig. 5.14 **(a)** The projection of the internal field onto the ground state magnetization and the local orientation of the magnetization across the T-junction, reproduced from Fig. 5.7 (b). **(b)-(f)** The isofrequency curves belonging to the points labelled in panel (a). These were all calculated for magnetostatic spin waves of frequency 7.52 GHz propagating in a Permalloy film of thickness 100 nm, in which the internal field H_i and orientation of magnetization θ was (b) H_i = 441 Oe, θ = 17°, (c) H_i = 386 Oe, θ = 21°, (d) H_i = 210 Oe, θ = 39°, (e) H_i = 303 Oe, θ = 39°, and (f) H_i = 180 Oe, θ = 10°.

Upon exciting the Permalloy microstructure at the frequency of 7.52 GHz, the energy of the pumping magnetic field, via the Schlömann mechanism, was most efficiently transferred to the magnetization within the leg of the T-junction. This resonantly-excited magnetization then emitted a spin-wave caustic beam from the leg-arm interface, propagating to the right when α = +15°. This beam then traversed the non-uniform internal field / magnetization across the arms of the T-junction. Across each mesh cell, the magnetization and effective field was assumed to be uniform - this fact was exploited, in Chapter 4, to calculate the spatially-varying frequency of resonance. This idea can be extended further in order to calculate the spin-wave dispersion at each and every mesh cell. Presented in Fig.

5.14 (b) - (f) are the isofrequency curves characterizing the dispersion of plane spin waves (of frequency 7.52 GHz) propagating in a 100 nm-thick continuous film of Permalloy, across various mesh cells as indicated in Fig. 5.14 (a).

The trajectory of the spin-wave caustic beam can therefore be understood using the continuously-varying isofrequency curves across the geometry of the T-junction. As the spin wave propagates from one region of magnetization / internal field to another, the longitudinal wave vector component adiabatically adjusts in order to satisfy the local dispersion. In contrast, the wave vector component parallel to the long axis of the arms (across which the film was translationally invariant) was assumed to be conserved. To identify the transverse wave vector component, a Fourier transform was applied along two slices across the T-junction, as shown in the inset of Fig. 5.15. To acquire such spectra, the spin-wave amplitude

$$S_{A,1D} = \left| FFT\left[m_{z,t}(x) + i \cdot m_{z,t+2}(x) \right] \right|, \qquad (5.5)$$

was calculated. The spin-wave amplitude spectra, across the interface of the arm-leg junction and the center of the arm, are presented in Fig. 5.15 (a) - (b) respectively. Significant asymmetry towards positive k_x in both power distributions was evident, and notably the maximum in the spectrum acquired across the center of the arm was k_x = +0.94 radμm^{-1}.

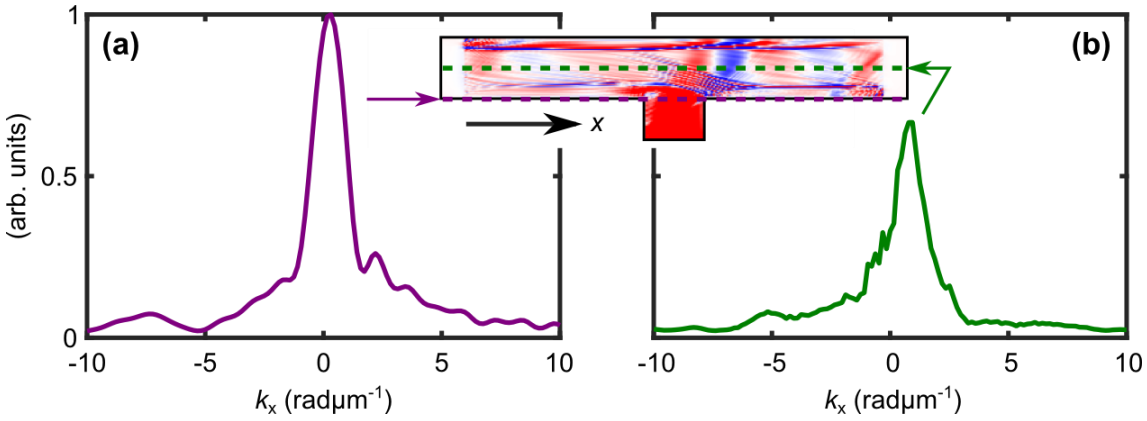

Fig. 5.15 **(a)-(b)** The Fourier transform of the dynamic out-of-plane component of magnetization, taken across a slice positioned across the opening of the leg and 2.5 μm from the upper edge of the arm of the T-junction respectively, as indicated in the inset. The spectrum in (b) has been amplified by a factor of 5.

In order to map the trajectory of the propagating spin-wave beam, the isofrequency curves for each mesh cell within the entire T-junction were numerically constructed. Then, with the transverse wave vector component being fixed at k_x = +0.94 radμm^{-1}, both longitudinal wave vector components k_y were calculated for each and every mesh cell. The gradient of the dispersion at the calculated wave vector points were also numerically evaluated. Conditional tests were then applied to distinguish which wave vector components yielded group velocities with positive and negative projections along the *y*-axis. The wave vector solution with a group velocity component pointing upwards from the leg of the T-junction was then classified as being "incident", and the other wave vector solution was classified as "reflected." In such a fashion, maps of the spin-wave group velocity and wave vector (both incident and reflected) were constructed, as presented in the left columns of Fig. 5.16 (a) - (d). By overlaying all four maps, the net trajectory of the spin wave, presented in Fig. 5.16 (e), was obtained.

The maps presented in Fig. 5.16 require significant exposition. Initially, the spin-wave caustic beam is directed from the leg-arm aperture obliquely towards the upper edge of the right arm. Since the magnetization and internal field are reasonably uniform across this region, the spin-wave path consists of a straight line. Then, as the spin wave approaches the upper geometrical edge of the arm, the internal field reduces, and further the magnetization significantly rotates. This leads to a spin-wave mirage effect - the spin wave smoothly curves towards the normal of the waveguide's edge - consistent with that discussed by Gruszecki *et al.*[205-206] Across this entire path traced by the spin wave, significant distributed scattering of the spin wave from the nonuniformity of the field / magnetization occurs - the strength of this scattering depends on the size of the nonuniformity being traversed.

Across the lower right corner of the T-junction, there are no vectors apparent at all (Fig. 5.16 (a) - (d)). This feature arises due to the internal field being too weak in this region. As a result, the isofrequency curves were pushed so far from the origin that there was no intersection between the said curves and the line k_x = +0.94 radμm^{-1}. This gives rise to a wave-vector-specific region of magnetization, across which the spin wave is (in principle) forbidden from traversing.

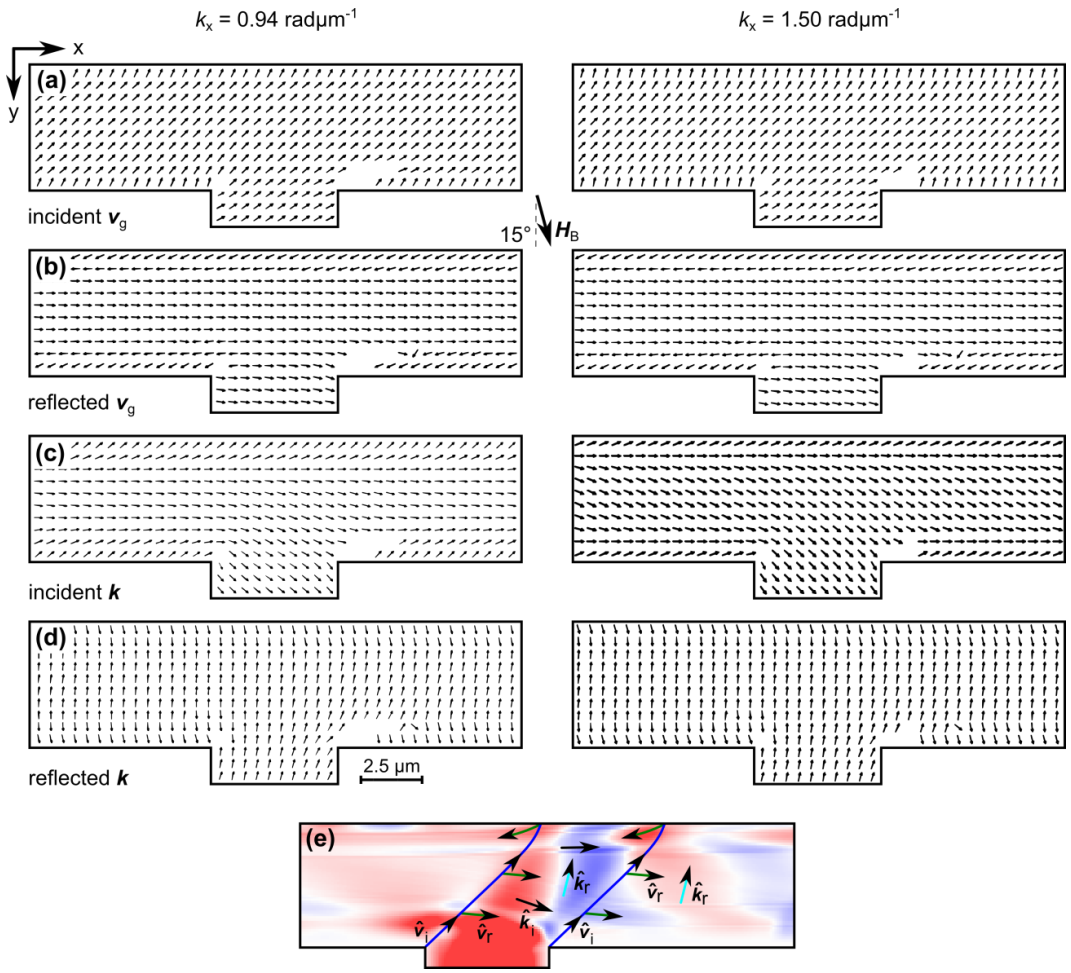

Fig. 5.16 **(a)-(b)** Vector maps of the spatial variation of the group velocity across the Permalloy T-junction are shown for the incident and scattered spin waves respectively. **(c)-(d)** Vector maps of the spatial variation of the wave vector across the Permalloy T-junction are shown for the incident and scattered spin waves respectively. The maps presented in the left and right panels of (a) - (d) were calculated with the horizontal projection of the wave vector k_x = +0.94 μm^{-1} and k_x = +1.5 μm^{-1} respectively, and each unit vector in all the maps represents an average over 5 x 5 computational cells. **(e)** The trajectory of the propagating incident and reflected spin wave (index "i" and index "r" respectively). The blue (green) arrows indicate the direction of the incident (reflected) group velocity, and the black (cyan) arrows indicate the direction of the incident (reflected) wave vector. The calculated trajectory overlays a smoothed numerically-calculated snapshot of the spin-wave propagation, as presented earlier in Fig. 5.9.

The linearity of the isofrequency curves, which was responsible for the formation of self-focused spin-wave caustic beams, also leads to robust tolerance of the propagation trajectory to variation in k_x. Presented in the right column of Fig. 5.16 (a) - (d) are maps of the incident and reflected group velocities / wave vectors calculated with $k_x = +1.50$ radμm^{-1}. The maps are, in the main, identical to those calculated with $k_x = +0.94$ radμm^{-1}. The only significant difference lies in the spatial extent of the wave vector-specific forbidden region of magnetization: since here k_x is larger, the "forbidden" region of propagation is smaller.

Within the central 4 μm across the width of the arm, the orientation of the magnetization was reasonably uniform. Thus, according to the isofrequency curves, the reflected group velocity was crudely parallel to the waveguide. At 1 μm from the upper edge of the waveguide, however, the magnetization experienced substantial rotation. Consequently, the reflected group velocity actually pointed towards the left waveguide. To understand this behavior, maps of the group velocity for the incident and reflected spin wave are presented in Fig. 5.17 (b) - (c) respectively, close to the upper geometrical edge of the T-junction (as indicated in Fig. 5.17 (a)). Here, the vectors correspond to each mesh cell. Presented in Fig. 5.17 (d) - (h) are constructions of the isofrequency curves belonging to the mesh cells indicated in Fig. 5.17 (a) - (b). As the spin wave traverses the isofrequency curves shown in Fig. 5.17 (d) - (h), the smooth rotation of the magnetization / smooth reduction in the internal field leads to the smooth bending of the incident spin wave towards the normal of the waveguide's edge. As the spin wave then reflects (so moving from panel (h) to (d)), the isofrequency curves have rotated so much that the reflected group velocity emerges from the opposite isofrequency curve. This leads to the phenomenon of "anomalous reflection", whereby the incident and reflected group velocities are pointing up and to the right, and down and to the left respectively. As the spin wave then reflects back towards the center of the waveguide, the rotation of isofrequency curve causes the group velocity to become increasingly parallel to the waveguide's edge (note that k_y, in this situation, is tending towards infinity). This is, of course, an unstable trajectory, as k_y cannot increase indefinitely. Instead, it is therefore supposed that the spin-wave is reflected back upon itself when k_y becomes intolerably large. In this fashion therefore, the spin wave is essentially trapped within this region of magnetization.

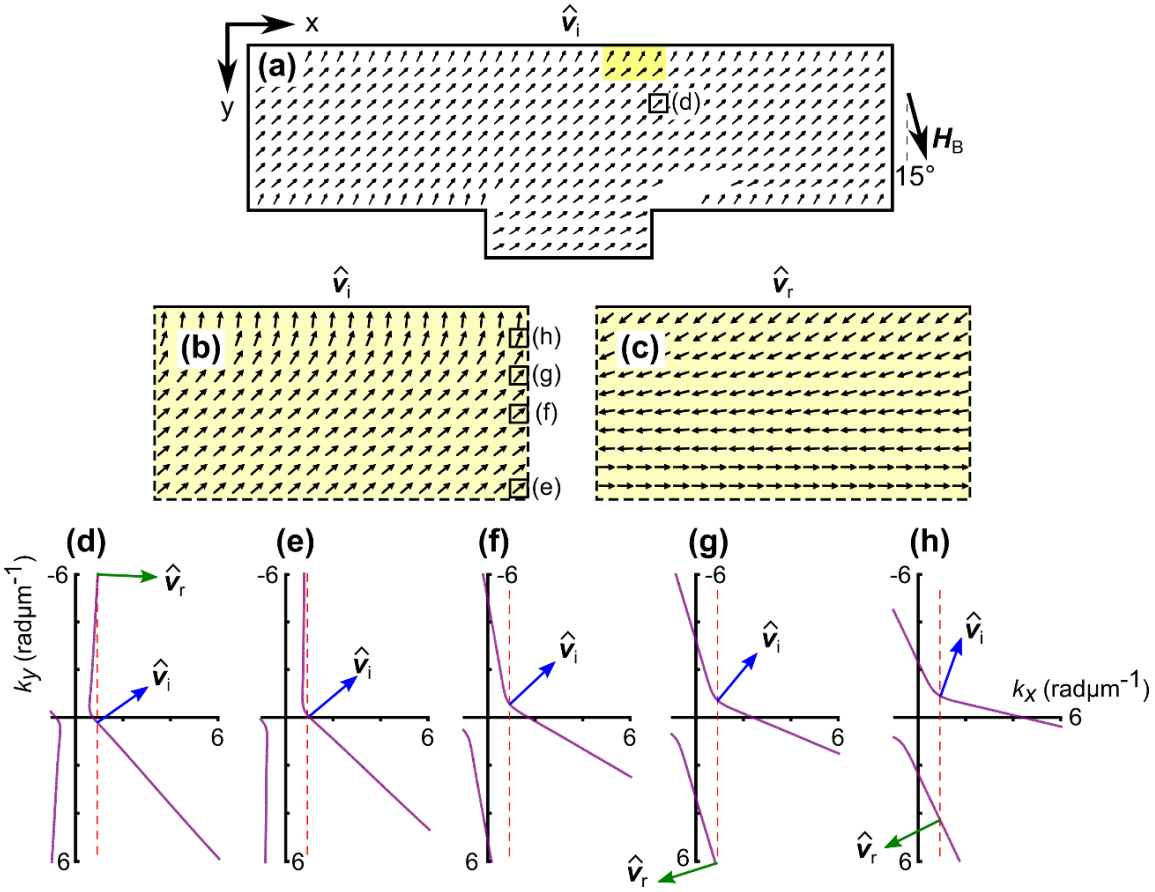

Fig. 5.17 **(a)** The vector map of the spatial variation of the incident group velocity across the Permalloy T-junction, reproduced from Fig. 5.14 (a), where the vectors represent the average of 5 × 5 mesh cells. **(b)-(c)** The vector maps of the spatial variation of the group velocity across the Permalloy T-junction are shown for the incident and scattered spin waves respectively, in the (2 × 1) μm^2 region indicated in (a). The vectors correspond to each mesh cell. The maps presented in (a)-(c) were calculated with the horizontal projection of the wave vector k_x = +0.94 radμm^{-1}. **(d)-(h)** Constructions of the isofrequency curves (purple) corresponding to the mesh cells indicated in (a)-(b). The red dashed line corresponds to k_x = +0.94 radμm^{-1}, and the blue and green unit vectors show the orientation of the incident (subscript "i") and reflected (subscript "r") spin waves with k_x = +0.94 radμm^{-1}.

The maps presented in Fig. 5.16 - 5.17 enable the visualization of the spin-wave trajectory, providing a powerful tool for understanding how spin waves propagate across a non-uniform magnetic landscape. To attempt to understand why no spin-wave beam was observed propagating across the left arm, the above analysis was repeated, but with k_x equal to -1.0 radμm^{-1}. Presented in Fig. 5.18 (a) is a zoomed image of the ground-state magnetization across the lower left corner of the T-junction. The isofrequency curves belonging to the pixels indicated in Fig. 5.18 (a) are presented in Fig. 5.18 (b) - (d). Initially, the spin-wave caustic beam propagates toward the left, as shown in Fig. 5.18 (d). However, the spin wave encounters the region of strongly canted magnetization localized at the edge of the transversely-magnetized arm, and is smoothly refracted towards the lower edge of the arm, as is apparent in Fig. 5.18 (e). Upon reflection, the spin wave experiences "anomalous reflection", as shown in Fig. 5.18 (b) - (c), and is then directed back towards the right arm.

The blank pixels immediately next to the lower left corner of the T-junction correspond to regions in which the projection of the internal field onto the magnetization is significantly high. A translationally-invariant uniformly-magnetized film of Permalloy, of thickness 100 nm, experiences FMR at a frequency of 7.52 GHz when the internal field across the Permalloy film is about 672 Oe. At fields above this, the spin wave is instead of backward-volume type. The internal field in the lower left corner of the T-junction therefore represents a barrier for any propagating spin waves, as the isofrequency curves transform to a single point (at $k_x = k_y = 0$) when $H_i = 672$ Oe. When the projected internal field therefore equaled or exceeded 672 Oe across the T-junction, no wave vector solutions were permitted in the corresponding calculations of the spin-wave trajectory.

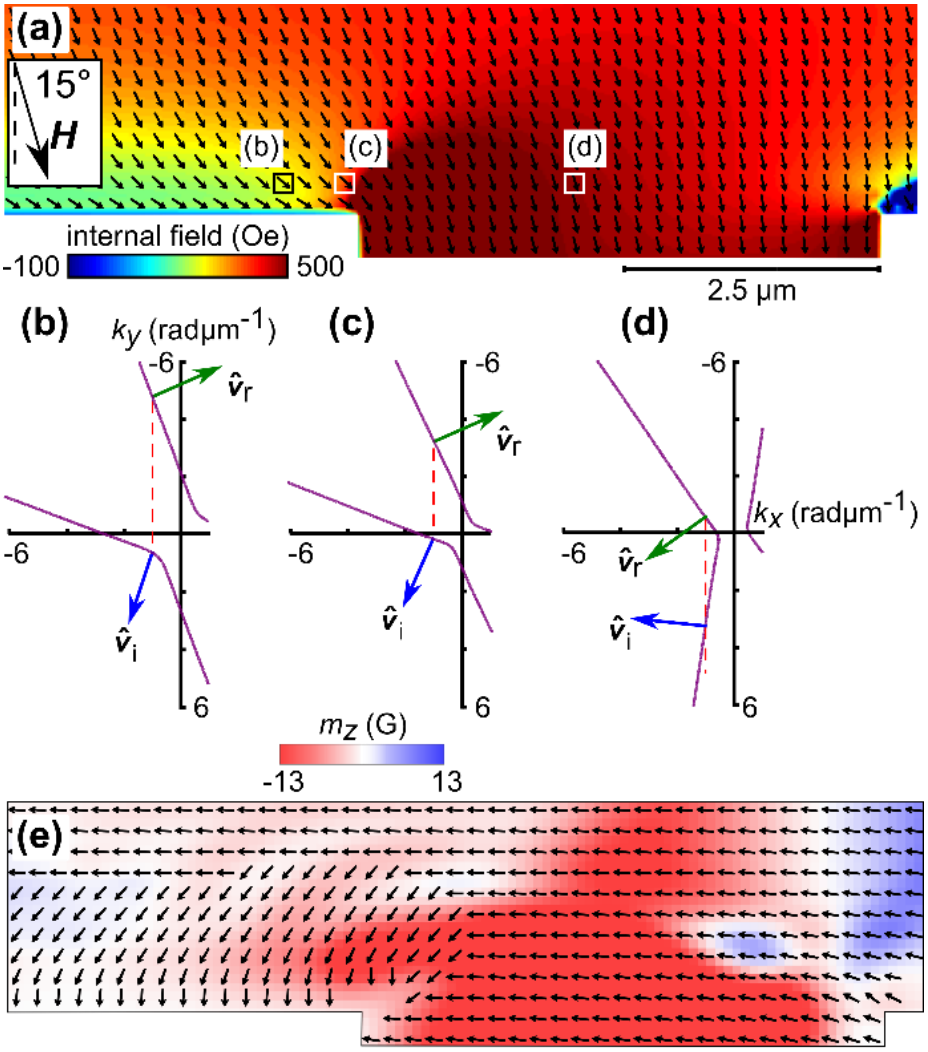

Fig. 5.18 **(a)** The ground-state magnetization across the lower left corner of the T-junction, reproduced from Fig. 5.7 (b). The vectors represent the average of 2 ×2 computational cells. **(b)-(d)** Constructions of the isofrequency curves (purple) corresponding to the mesh cells indicated in (a). The red dashed line corresponds to k_x = -1.0 radμm^{-1}, and the blue and green unit vectors show the orientation of the incident (subscript "i") and reflected (subscript "r") spin waves with k_x = -1.0 radμm^{-1}. **(e)** The vector map of the spatial variation of the incident group velocity across the lower-left corner of the Permalloy T-junction, calculated with k_x = -1.0 radμm^{-1}. The vectors represent the average of (2 × 2) computational cells.[3]

5.5 Summary

In summary, the excitation and propagation of spin waves across a T-junction of Permalloy waveguides has been extensively imaged using both TRSKM and OOMMF. Spin waves of finite wave vector were excited at the leg-arm interface of the T-junction via the Schlömann mechanism. When the T-junction was biased symmetrically, the spin waves propagated symmetrically across both arms of the T-junction. Upon rotating the bias magnetic field by as little as 15°, however, strongly asymmetrical propagation was observed, whereby the spin waves propagated across one arm, but were absent in the other. To explain this behavior, a hybrid analytical-numerical model has been constructed, which takes into account the continuous variation of the internal field and magnetization (i.e. the graded magnonic index) across a magnetic landscape. This enables the propagation path – consisting of both reflection and refraction - of a spin wave to be traced. This model explains the absence of the spin wave as a result of strongly localized reflection from the channel of non-uniformity localized at the edge of the transversely-biased arms. The model developed is quite general, and can in principle be used to predict and explain the propagation paths of spin waves across any arbitrary (but stable) magnetic configuration.

In the context of contemporary research devoted to understanding and controlling the steering of spin waves, the work discussed in this chapter was the first to show that nonuniformities across both the magnetization and effective field distributions could continuously steer spin waves. Substantial research, since the 1990s, has already explored the process of spin-wave refraction across a distinct interface.[181-186] Going beyond this, the spin-wave "mirage" effect was numerically demonstrated in 2015 by Gruszecki *et al.*,[205-206] arising solely from a nonuniform distribution of the effective field strength. The results discussed in this chapter (in particular, the hybrid analytical/numerical model used to map the spin-wave propagation) is, in principle, capable of explaining all the previously-discussed results. It is important to emphasize that the model is general indeed, since any non-uniformity will influence the magnetization or effective field (or both), which can therefore be accounted for. This work was also the first comprehensive demonstration of how the principles of "graded-index magnonics" could be used to realize technological applications - in this case, the demultiplexing of spin waves.

CHAPTER 6

LATERAL CONFINEMENT AND DISPERSIVE CONVERSION OF PROPAGATING SPIN WAVES

6.1 Introduction

In order to advance the development of all-magnonic circuitry, it is necessary for researchers to construct both the necessary circuit elements, and the means by which to connect them. Due in part to the current ubiquity of electronics, the design of magnonic technology is frequently inspired by their electrical counterparts. In recent years, for example, researchers have proposed how one could realize a wide range of magnonic devices including transistors,[207] logic gates[208] and filters.[209] These all suffer, however, either from their macroscopic dimension, or because they are still yet to be demonstrated experimentally. The main challenge ahead, in the future development of magnonic technology, certainly lies in the experimental demonstration of truly miniaturized functional devices.

Along with the construction of individual circuit elements, it is also imperative to consider how these components could be joined to form a circuit. In electrical circuits, wires are used for this purpose. To steer propagating spin waves around magnonic printed circuit boards, it may therefore be desirable to use waveguides in a similar fashion. Magnonic waveguides have the added advantage of being robustly non-volatile (when magnetized along their long axis), due to shape anisotropy. In order to successfully miniaturize magnonic chips down towards the nanoscale[163] one needs to preserve space, and so it will be essential to steer spin waves across twisted magnonic waveguides. Extensive research has therefore been devoted in recent years towards understanding how spin waves propagate across bends and skews. This theme of research comes directly within the remit of graded-index magnonics, since the bending of magnonic waveguides directly leads to the curvature of the static magnetization and / or the spatial variation of the spin-wave group velocity. A significant step forward in this research direction was made by Dvornik *et al*.[163] In their work, Dvornik

et al numerically studied the propagation of dipole-exchange spin waves along longitudinally-magnetized waveguides, and demonstrated that spin waves (of a certain frequency) retained their uniform spatial profile when navigating a U-bend. The spin waves therefore appeared to exhibit a group velocity that adapted with the curvature of the waveguide, and no significant losses were evident.[210] This research was built upon by Xing *et al*,[211] who revealed that, when directing dipole-exchange spin waves with different frequencies across a smooth bend, one can actually achieve multimode propagation, whereby the output spin wave is a superposition of width-modes with different antinode numbers.

Width-modes are also capable of propagating along transversely-magnetized waveguides, and so some researchers have begun to study how these spin waves are affected when the system symmetry is broken. Clausen *et al*[109] imaged the propagation of magnetostatic spin waves across a skewed waveguide. It was revealed that the broken symmetry of the waveguide led to multimode propagation past the skew, where the even and odd width-modes interfered to give rise to a "snake-like" propagation path.

In an unstructured magnetic film, MSSWs and BVMSWs exist in distinct frequency regimes, and so there is no possibility in converting spin waves between the two types. In waveguides however, as already discussed in Chapter 2.6.7, the dispersions of laterally-confined MSSWs and BVMSWs shift towards lower and higher frequencies respectively, allowing spin waves to be converted between the two dispersive types. This overlap was exploited by Brächer *et al*,[212] who generated laterally-confined propagating BVMSWs via the interference of counter-propagating confined MSSWs across a T-junction of Permalloy waveguides. Depending on the relative phase / frequency of the counter-propagating MSSW modes, the mode number of the outputted BVMSW width-mode was controlled.

In this chapter, the work reported by Brächer *et al*[212] is extensively discussed and generalized for the case of dielectric waveguides, albeit with reversed functionality. Specifically, Brächer *et al* discussed the possibility of combining spin waves, whereas I discuss here the splitting of spin waves. This is perceived as being a first step in the design of parallel magnonic circuitry, enabling multiple spin-wave devices to possibly operate in tandem. In the first section of this chapter, waveguides formed of YIG will be experimentally and numerically characterized. Depending on the orientation of the bias field, the spin-wave dispersion was observed to be modified, in agreement with the literature already discussed. In the second section, spin-wave propagation across a T-junction of waveguides is imaged. It is

clearly observed that the laterally-confined spin waves reciprocally convert in dispersive type, when navigating the structure.

6.2 Characterization of spin-wave propagation across a waveguide

In this section, I will discuss the experimental and numerical characterization of the dynamic magnetization within waveguides. All the experimental measurements presented in this chapter were performed by Dr. Alexandr Sadovnikov and Dr. Sergey Grishin, and all the numerical results were obtained by myself.

6.2.1 Experimental measurements

The sample under investigation is schematically shown in Fig. 6.1 (a). In the first series of investigations, a single waveguide, of thickness s = 7.7 μm and width w = 3 mm or 0.5 mm, was fabricated by laser scribing a continuous film of YIG, which was itself epitaxially grown on a substrate of GGG (using the same procedures as discussed in Section 4.2). Two microstrip antennas, of width 30 μm, were positioned on either ends of the waveguide: across the input antenna, current pulses were delivered so as to excite spin waves, and the efficiency of spin wave propagation was measured across the output antenna using a vector-network-analyser. The bias magnetic field was applied either parallel or orthogonal to the long axis of the waveguide, hence leading to a geometry supporting the propagation of MSSWs or BVMSWs, as shown in the upper and lower schematics of Fig. 6.1 (a) respectively.

The transmission spectra, characterizing the spin-wave propagation across the 3 mm-wide and 0.5 mm-wide waveguides, are presented in Fig. 6.1 (b) - (c) respectively. In the 3 mm-wide waveguide, there was a common cut-off frequency between the two spectral types, coinciding with the frequency of FMR f_{FMR} = 5.345 GHz. No overlap in the transmission spectra was observed, and so the 3 mm-wide waveguide was judged as approximating well a continuous film of YIG. In contrast, the transmission spectra for the 0.5 mm-wide waveguide showed an overlap of 114 MHz - the upper cut-off frequency for the BVMSW spectra still coincided with f_{FMR}, but the MSSW band's lower cut-off frequency was shifted to 5.231 GHz.

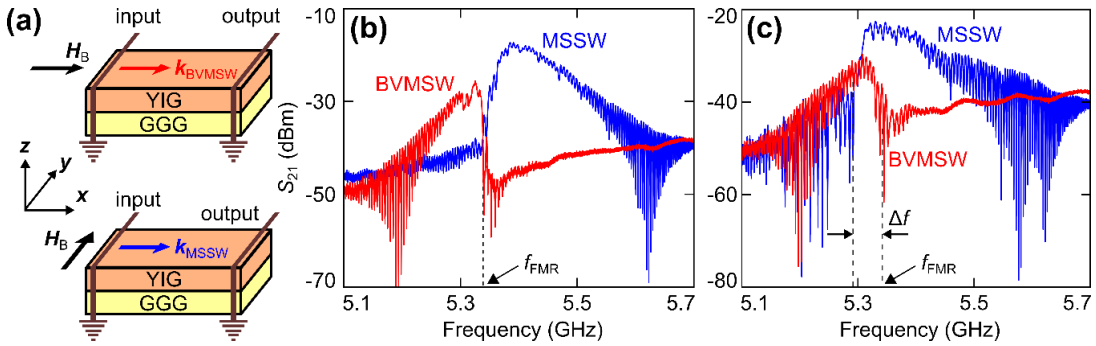

Fig. 6.1 **(a)** Schematics of the ferromagnetic waveguides studied, in the configurations which support the propagation of BVMSWs (top) and MSSWs (bottom). **(b)-(c)** Transmission characteristics S_{21} of the waveguides, with width w = 3 mm and 0.5 mm respectively, measured in the MSSW (blue line) and BVMSW (red line) configurations.[5]

6.2.2 Micromagnetic modelling

To explore the origin of the experimentally-observed overlap in frequency of transmission, extensive micromagnetic simulations were performed. The waveguide was modelled as a cuboid of size (600 × w × 0.0077) mm^3, meshed with cells of size (10 × 0.05 × 7.7) μm^3, and assumed to have the same magnetic parameters as used to model the YIG discussed in Section 4.2 (specifically, M_s = 140 G). One-dimensional periodic boundary conditions[141] were applied along the long axis of the waveguide (consistently aligned parallel to the x-axis), and the exchange interaction was neglected completely, due to the dimensions of the sample being so far in excess of the exchange length. The micromagnetic methodology was the same as was used before – to obtain the ground magnetic state, the waveguides were saturated along either the long- or short-axis of the waveguide, and the bias magnetic field was then reduced so as H_B = 1225 Oe. Presented in Fig. 6.2 (a) are the internal field profiles across the width of the waveguide. In the BVMSW configuration, the static demagnetizing field across the waveguide was uniformly zero, as anticipated, and so the static internal field was identical to the bias magnetic field applied along the waveguide. In contrast, the static demagnetizing field was significantly non-uniform in the MSSW configuration. With the waveguide having a width of 3 mm, the demagnetizing field was strongly localized to the edges of the waveguide,[104] and in the center of the waveguide, H_i = 1222 Oe. Upon reducing the width of the waveguide to 0.5 mm, the non-uniformity of the demagnetizing field was less localized, and the internal field was H_i = 1208 Oe at the center of the waveguide. This

calculated field difference (ΔH_i = 17 Oe) corresponds to a difference Δf_{FMR} = 39 MHz, when describing the frequency of FMR in a continuous film.

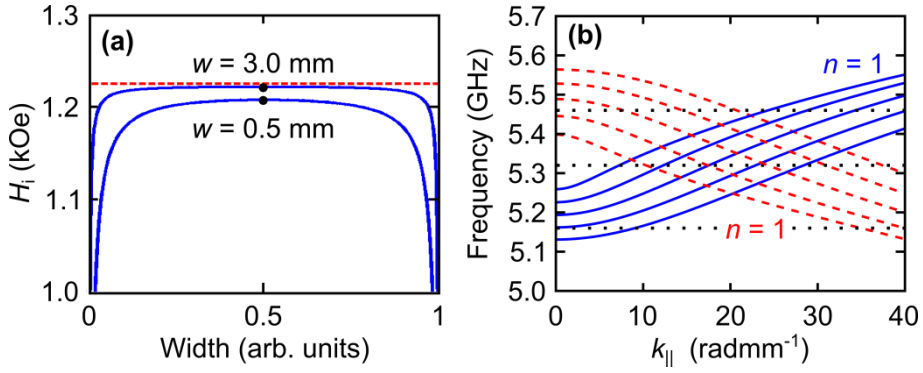

Fig. 6.2 **(a)** The projection of the internal field onto the magnetization across the width of the waveguide, in the MSSW (solid-blue line) and BVMSW (dashed-red line) configurations. **(b)** Analytically-calculated dispersion curves for the longitudinal wave vector $k_{||}$ of the spin-wave width modes. The curves are in order of increasing integer values of n, ranging between n = 1 and n = 5 for both geometries.[5]

The experimentally-measured overlap in frequency between the MSSW and BVMSW spectra in the 0.5 mm-wide waveguide was Δf = 114 MHz, but the difference in the internal field accounted for only Δf_{FMR} = 39 MHz. To therefore account for the still significant difference, the influence of lateral confinement on the dispersion of the propagating spin waves needs to be considered. In the simplest form, the confinement of the propagating spin wave can be expressed via the quantization of the transverse wave vector given by Eq. 2.142. If the magnetization at the geometrical edges of the waveguide is completely unpinned, one is assuming $w_{eff} \to \infty$. For a longitudinally-magnetized waveguide considered in the dipolar limit, Guslienko *et al* calculated the effective width to more precisely have the form[107]

$$w_{eff} = w \cdot \frac{\pi}{\pi - p \cdot \left[1 - 2\ln(p)\right]} \tag{6.2}$$

where $p = s/w$ is the waveguide's aspect ratio. For the YIG waveguide in the BVMSW configuration studied in this section, therefore, w_{eff} = 0.525 mm. By therefore setting k_y = (5.98n) radmm^{-1} in Eqs. 2.136 – 2.141, the longitudinal wavevector $k_z = k_{||}$ can be calculated to form the red dashed dispersive branches shown in Fig. 6.2 (b). Upon introducing lateral

confinement, the branches of the backward-volume dispersion shift towards higher frequencies as n increases, as anticipated. In the MSSW configuration, the effective width is more difficult to quantify, due to the non-uniformity of the static internal field. In lieu of any analytical description, the effective width for the BVMSW geometry was assumed, and this leads (by setting $k_z = (5.98n)$ radmm^{-1} in Eqs. 2.135 – 2.140) to the blue dispersive branches shown in Fig. 6.2 (b). As n increases, the branches shift towards lower frequencies. By therefore taking into account the effects of lateral confinement, in addition to the reduction of the internal field in the MSSW configuration, the calculated frequency overlap of the fundamental spin-wave modes was Δf = 139 MHz, which is substantially closer to the experimentally-measured overlap of Δf = 114 MHz.

To identify the source of the remaining difference between the experimentally-observed and analytically-calculated spectral overlap, dynamic micromagnetic simulations were performed with the intention of numerically calculating the spin-wave dispersion. The geometry of the considered waveguide was adapted so as to span a cuboid of size (16.384 × 0.5 × 0.0077) mm^3 with a cell-size of (1 × 20 × 7.7) μm^3.[§§§§§§§] One-dimensional periodic boundary conditions[141] were again applied along the length of the waveguide, and the exchange interaction was neglected completely. The ground-state magnetization characteristic of the waveguide was calculated using the same approach as discussed earlier, and the Gilbert damping coefficient was set to 1×10^{-4} in the subsequent dynamic micromagnetic calculations.

To excite the dynamics in the experimental system, a current-carrying microstrip was employed - in the micromagnetic simulations, therefore, it was necessary to model the spatial and temporal distribution of the field generated by the microstrip, tuned so as to locally excite broadband spin waves. In Chapter 5, the pulsed excitation used in the experimental setup had Gaussian character in the time-domain, and so the micromagnetic model similarly used a Gaussian exciting field. Here, in contrast, no such imitation was required. The temporal profile of the exciting field was therefore selected to be of cardinal sine (or 'sinc') form

$$h_p(t) = h_0 \cdot \frac{\sin(\omega_c \cdot [t - t_0])}{\omega_c \cdot [t - t_0]} \tag{6.3}$$

[§§§§§§§] The waveguide was deliberately meshed by 2^{14} cells in order to maximise the computational efficiency of the applied fast Fourier transform, and the length of the waveguide was selected so as to give a wave vector resolution 0.38 radmm^{-1} in reciprocal space.

where the amplitude h_0, the time delay t_0 of excitation, and the angular cut-off frequency ω_c (where $\omega_c = 2\pi f_c$) were user-defined. The typical time-varying profile of this function is shown in Fig. 6.3 (a). The sinc function is unique in that its Fourier transform produces a rectangular function in the frequency domain, as shown in Fig. 6.3 (b). In principle, therefore, an excitation with temporal form given by the sinc function is capable of exciting all frequencies below f_c with equal distribution of power.

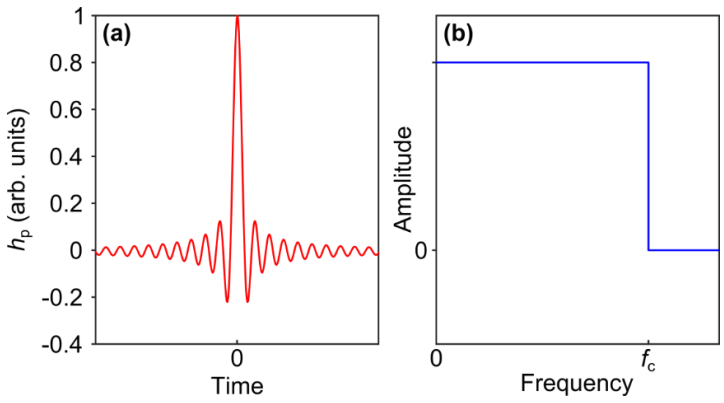

Fig. 6.3 **(a)** The ideal time-varying profile of the 'sinc' function, described by Eq 6.3. Note the time-window has been cropped here, but realistically the oscillations converge to zero at infinitely positive and negative time. **(b)** The Fourier transform of the function shown in (a).

The discretization associated with numerical methods, however, leads to the challenge of how to optimize the discretized sinc function in order to achieve fair broadband excitation. As the BLS measurements were performed with excitation frequencies of about 5 GHz, the cut-off frequency f_c was set to 9 GHz. The amplitude h_0 of the excitation was 10 Oe, and the magnetization was recorded in time steps Δt = 50 ps, which allowed signals with a frequency of up to 10 GHz to be detected. The total duration of the micromagnetic simulation was 300 ns, which provided a frequency resolution of 3.33 MHz. The pulse was offset in time by t_0 = 2 ns. These parameters gave rise to the time-varying signal and corresponding frequency response presented in Fig. 6.4 (a) - (b) respectively, which approximated well the characteristics of the ideal sinc function. The spatial distribution of the exciting field was assumed to be given by the Karlqvist equations (Eqs. 4.2 – 4.3), with the spatial profiles shown in Fig. 6.4 (c). Since the microstrip was positioned directly on top of the YIG waveguide, the in-plane component of the exciting field approximated well a rectangular function, with a width of 30 μm.

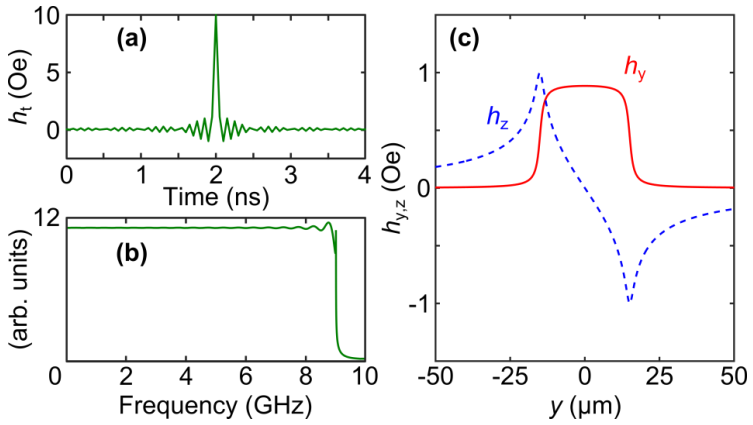

Fig. 6.4 **(a)** The temporal aspect of the excitation described by Eq. 6.3, where h_0 = 10 Oe, f_c = 9 GHz, and t_0 = 2 ns. The time is discretized in steps Δt = 50 ps, and the total duration of the excitation is 300 ns (note only the first 4 ns of the excitation are shown). **(b)** The Fourier transform of the function shown in (a). **(c)** The spatial distributions of the in-plane h_y (red solid line) and out-of-plane h_z (blue dashed line) components of the magnetic field, as described by Eqs 4.2 – 4.3.

Upon completion of the dynamic micromagnetic simulation, the data files (saved in binary format so as to reduce the size of the files) occupied around 56 GB of memory, which proved impossible to load into MatLab collectively and entirely. To handle the memory problems associated with such large data, the out-of-plane component of magnetization across the entire waveguide was loaded into MatLab one time-step at a time. For each time-step, the out-of-plane component of static magnetization was subtracted (therefore yielding the dynamic out-of-plane component of magnetization), and then a fast-Fourier transform was applied immediately across the length of the waveguide. All the k_x bins corresponding to negative values and in excess of 500 radmm^{-1} were then discarded. After iterating this process across all time-steps, the fast-Fourier transform was then applied along the time-dimension, generating a two-dimensional matrix of data contained within a file of size 1.5 GB. The magnitude of the twice Fourier transformed data was then calculated, and the calculated dispersion along the center of the waveguide was extracted. This calculated dispersion is presented in Fig. 6.5 (a) - (b) for the geometries in which the bias magnetic field was aligned parallel and orthogonal to the waveguide's long axis respectively. Note the dispersion profiles are shown in a logarithmic scale, in order to improve the visibility of the higher-order modes.

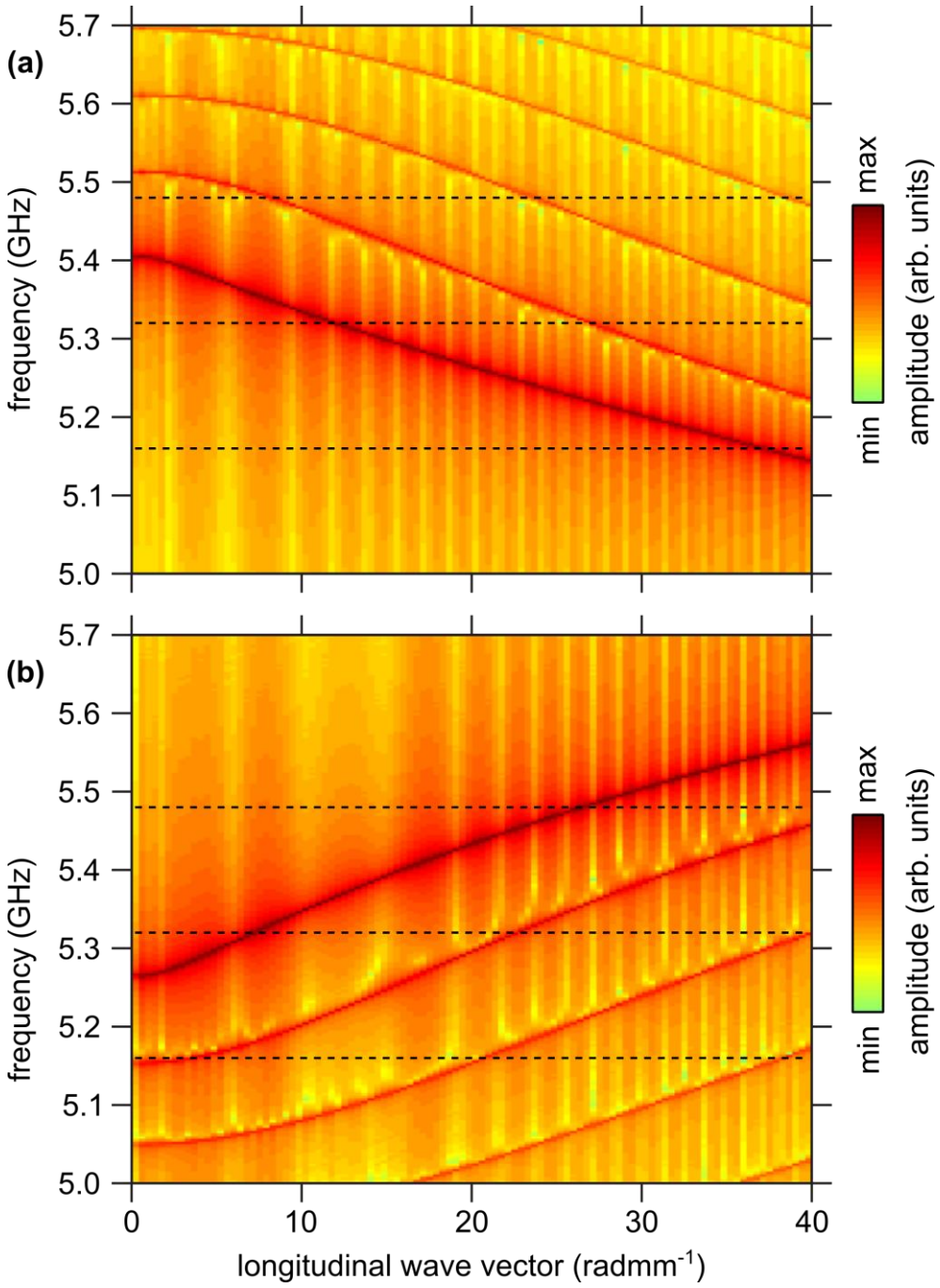

Fig. 6.5 **(a)-(b)** The dispersion curves corresponding to backward-volume magnetostatic spin waves and magnetostatic surface spin waves respectively, propagating in a 0.5 mm-wide YIG waveguide, calculated from the results of micromagnetic simulations.

The most intensive branches in Fig. 6.5 (a) - (b) agreed well with the analytically-calculated branches corresponding to the fundamental modes presented in Fig. 6.2 (b). The higher-order modes, however, did not agree so well with the branches calculated analytically

– the discrepancy was attributed to the discretization across the width of the waveguide (the discretization of the waveguide-width into 25 cells was anticipated as leading to similar discretization, and by extension inaccuracies, in the computation of the transverse profile of the spin-wave width-mode). The frequency overlap between the fundamental width-modes calculated numerically was Δf = 133 MHz, which successfully validated the analytically-calculated overlap of Δf = 139 MHz (the small remaining difference was readily explained by inescapable differences between the experiment and micromagnetic model, such as the precise value of M_s).

6.3 Dispersive conversion of laterally-confined spin waves

The overlap observed in both the transmission spectra and the dispersion profiles belonging to the BVMSW and MSSW configurations suggested the possibility of conversion between the two spin-wave types. To investigate this, a T-junction of YIG waveguides was therefore constructed, as shown in Fig. 6.6 (a). The waveguides were nominally identical to those discussed in Section 6.2.1. The microstrip antenna was positioned about 3 mm away from the leg-arm junction, and then loaded with current pulses. Amplitude-resolved BLS images were then recorded at the excitation frequencies of 5.16 GHz, 5.32 GHz and 5.48 GHz (indicated in Fig. 6.2 (b) by dotted lines), with the bias field H_B = 1225 Oe aligned either parallel or orthogonal to the leg of the T-junction. The experimental images obtained are presented in Fig. 6.6 (b) – (e), plotted in a logarithmic scale. At the frequency 5.32 GHz, which lies within the dispersion overlap between the fundamental MSSW and BVMSW width-modes, spin-wave propagation across the entire network of waveguides was clearly observed, whereby the spin wave traced a snake-like propagation path across the arms of the T-junction. At the frequencies outside of the dispersion overlap, however, the propagation was only observed across the leg of the T-junction.

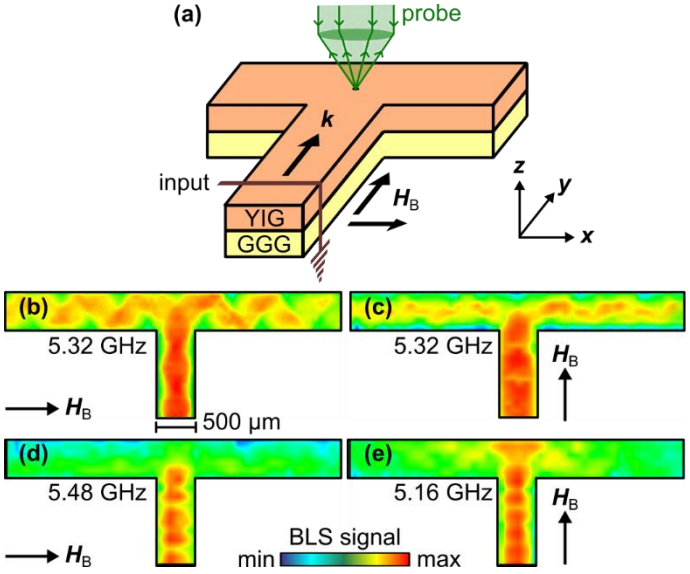

Fig. 6.6 **(a)** A schematic of the beam-splitter geometry **(b)-(e)** Amplitude-resolved BLS maps, acquired with the frequency and bias orientation indicated, where H_B = 1225 Oe throughout.

To complement the results acquired experimentally, and furthermore to understand the observed mode conversion quantitatively, the BLS measurements were modelled using micromagnetic simulations. The beam-splitter was enclosed within a cuboid of size (6.5 × 2.5 × 0.0077) mm^3 with meshing cells of size (10 × 10 × 1.54) μm^3. The beam-splitter had a fixed waveguide width of 0.5 mm, and the arms of the beam splitter were capped by a block 4-cells long, in which the Gilbert damping coefficient – otherwise 1×10^{-4} (characteristic of YIG) - was inflated to 0.5. This was introduced so as to reduce the strength of reflections. The geometry was initially biased by a global uniform bias field of H_B = 2000 Oe, and reduced to H_B = 1225 Oe, to obtain the ground magnetic state. Spin waves were then excited at the base of the leg, by a magnetic field with a spatial profile as described by the Karlqvist equations (Eqs. 4.2 – 4.3). The modelled microstrip was positioned at the base of the leg of the T-junction. The time-varying profile corresponded to the sine cardinal function (Eq. 6.3), where t_0 = 4 ns, f_c = 9 GHz and h_0 = 5 Oe. The magnetization was then recorded every 50 ps, for a total of 1 μs. This dynamic simulation generated a total micromagnetic data set of size 36 GB.

To obtain micromagnetic results directly comparable to those acquired through amplitude-resolved BLS microscopy, it was necessary to transform the real-time dynamic

micromagnetic data into the frequency domain. For each time step, therefore, the static magnetization was subtracted, yielding the dynamic out-of-plane component of magnetization. A fast Fourier transform was then applied in the time-domain for each and every mesh cell, and then the spatially-resolved amplitude was calculated. This generated maps of the spin-wave amplitude, which are presented in Fig. 6.7, at frequencies between 5.16 GHz and 5.48 GHz. At all the frequencies of excitation, the spin-wave propagation is observed across both the leg and the arms of the T-junction.

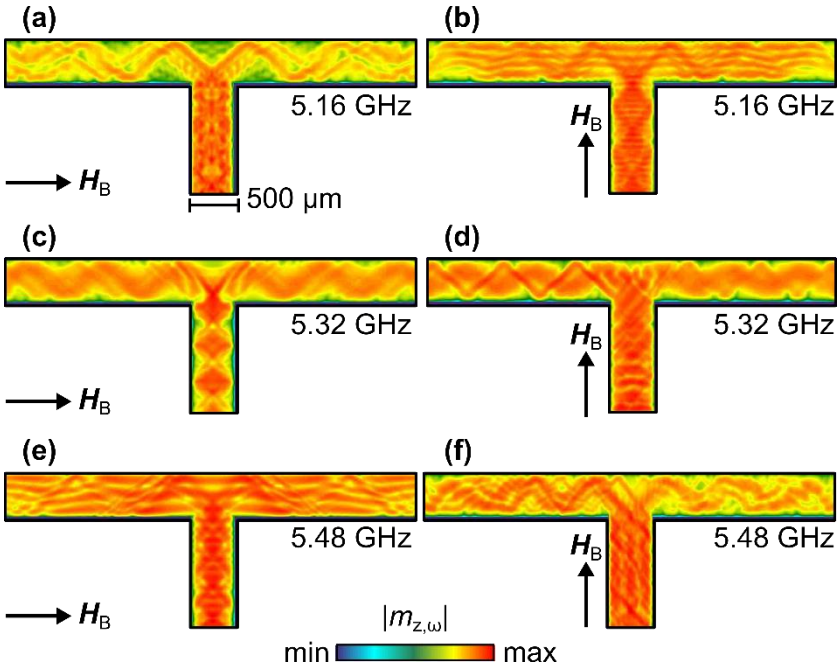

Fig. 6.7 **(a)-(f)** Calculated maps of the spin-wave propagation, with the bias field orientation and frequency indicated. These images were acquired using a pulsed exciting field (given by Eq. 6.3) and post-processed so as to be comparable with the experimentally-acquired amplitude-resolved BLS results shown in Fig. 6.6.

To reveal the phase information of the propagating spin waves, allowing the mode numbers of the confined spin waves to be identified more clearly, the dynamic micromagnetic simulations were repeated, but with a continuous-wave temporal profile as given by Eq. 4.4. This excitation (of strength h_0 = 1.75 Oe) was applied continuously for 3000 time steps, where each time step was of duration $T/8$ (T is the period of the exciting field). Presented in Fig. 6.8 are snapshots of the dynamic magnetization, where the frequency of the harmonic excitation was 5.16 GHz, 5.32 GHz and 5.16 GHz. At the frequency 5.32 GHz, the spin wave

propagating along the leg is composed of odd width-modes: in both the MSSW and BVMSW configurations (panels (c) and (d) respectively), the spin wave converts to both the n = 1 and n = 2 modes, which interfere to generate the snake-like propagation path observed across the arms. At the frequency 5.16 GHz in the BVMSW and MSSW geometries, the width-mode within the leg is of the order n = 1 and n = 5 respectively. This single mode then converts into multiple modes, of opposite dispersive type, across the arms of the junction. At the frequency 5.48 GHz, similar (but opposite) behavior is observed.

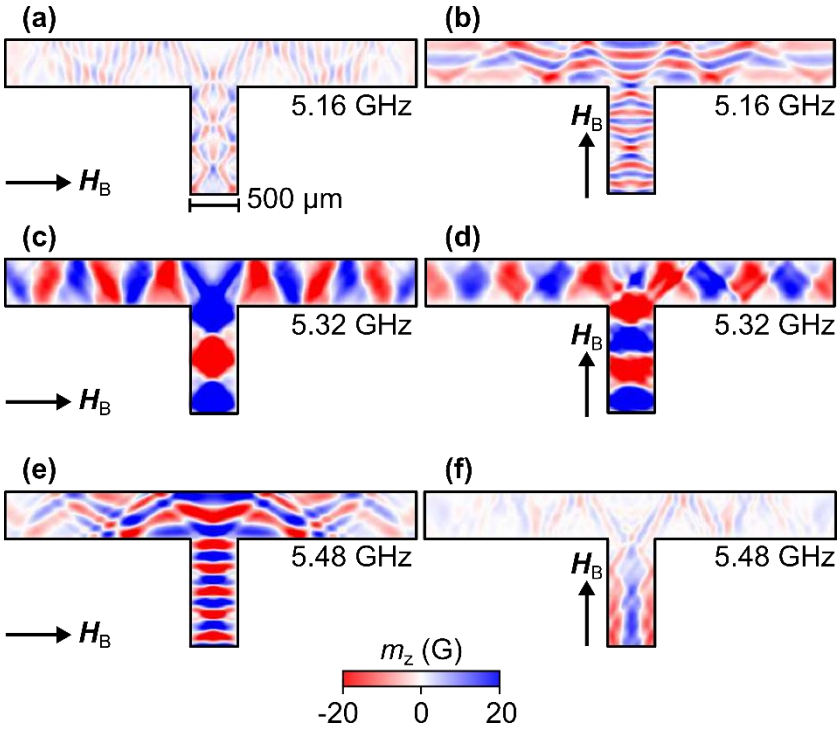

Fig. 6.8 **(a)-(f)** Simulated snapshots of the dynamic out-of-plane component of magnetization, with the frequency of excitation and bias field orientation indicated (H_B = 1225 Oe throughout). All the snapshots were acquired at the same point across the phase of the continuous-wave excitation, at about 700 ns after the excitation was applied.

6.4 Summary

In summary, the conversion of magnetostatic spin waves from magnetostatic-surface to backward-volume dispersion (and vice versa) has been successfully demonstrated. In continuous magnetic media, the magnetostatic spin waves lie in different frequency regimes, and share a common cut-off frequency corresponding to the frequency of ferromagnetic

resonance. In waveguides in contrast, due to the inescapable consequences of their lateral width, there is dispersive overlap between laterally-confined propagating MSSWs and BVMSWs. By therefore connecting two waveguides to form a T-junction structure, spin-wave propagation across the network of waveguides was successfully realized, through the conversion of the spin-wave dispersive types. The mode numbers of the excited spin waves in the leg of the T-junction were all odd (dictated by the uniformity of the excitation across the waveguide's width), whereas in the arms of the T-junction, a superposition of even and odd spin-wave modes were observed. This behavior can be predicted and explained through comparing the frequency of excitation with the appropriate dispersion profiles of the laterally-confined propagating spin waves.

The results discussed in this chapter are important for the design of parallel magnonic circuitry. In electronics, the splitting of an electrical current is straightforward (the only prerequisite is that the circuit is complete). In wave-based devices, however, where the waves have anisotropic dispersion, the splitting of such waves across a junction is more nuanced. With regards to the magnonic beam-splitter discussed in this chapter, the beam-splitting was controlled via the spin-wave frequency. It would therefore be useful to investigate how the beam-splitting could be alternatively controlled, perhaps through rotation of the bias magnetic field[1], or passing an electrical current across either arm of the T-junction.[213] It should also be noted that the spin waves investigated were wholly dominated by the dipolar interaction. Upon downscaling, therefore, the process of beam-splitting may be rendered simpler, since the exchange interaction is isotropic. Micromagnetic investigations therefore need to be performed to investigate how the splitting evolves on the nanometer scale.

CHAPTER 7

SPATIOTEMPORAL IMAGING OF THE LASER-INDUCED DYNAMICS ACROSS MAGNETIC FILMS

7.1 Introduction

The excitation of magnetization dynamics, within the research field of magnonics, is most conventionally achieved through the use of a fast-varying magnetic field delivered by a microstrip / coplanar waveguide. Indeed, this means of stimulation underpinned the experimental results presented and discussed in Chapters 4 – 6. This approach, however, does not lend itself well to either miniaturization or high-frequency operation, due to the radiation / leakage of energy by the current-carrying element. The task of down-scaling spin-wave sources could possibly be circumvented using the Schlömann mechanism, as extensively discussed in Chapter 4. There is no possible way, however, to overcome the GHz frequency barrier while still using electrical currents.

Instead of therefore using electrical currents to excite magnetization dynamics, researchers are now searching for alternative faster means by which to pump magnetic systems. One attractive option involves the use of optical pulses: commercially-available laser diodes are able to deliver pulses with duration on the order of tens of femtoseconds. Indeed, some research groups have demonstrated that optical pulses with duration approaching attoseconds can even be achieved.[214-215] Such ultrafast stimuli enable the phenomena of demagnetization, spin-reorientation, and even magnetic-restructuring to be realizable on sub-picosecond timescales, opening up the possibility of storing, retrieving and processing data at incredibly fast speeds.[216]

The means through which optical pulses stimulate magnetization dynamics can take one of two pathways, depending on whether the excitation is thermal or non-thermal.[216] The thermal pathway is underpinned by the Bloch equation (Eq. 2.63). Since the magnetization of

a ferromagnetic body is temperature-dependent, the thermal load delivered by an ultrafast pulse will reduce the magnetization length - this transient reduction, in turn, generates a transient demagnetizing field, which can lead to the excitation of propagating spin waves.[132,217-220] Since the magnetization is one of the two key ingredients of the magnonic index, one could interpret this mechanism as belonging to the field of graded-index magnonics. Indeed, some recent studies have already advanced this idea by using thermally-defined magnetic landscapes to support confined spin-wave modes[221] or to influence the character of propagating spin waves.[222] It must be emphasized, however, that the results discussed in this chapter do not clearly extend this theme of research.

This thermal pathway, in addition, can also excite propagating magnetoelastic waves via the magnetoelastic coupling[223-225] between magnons and phonons. Specifically, the optical pulse can deliver a pressure- or shear-induced stress to the lattice, which in turn causes the magnetization to precess. It should be noted that this phenomena can only occur when the magnetostriction of the magnetic system is sufficiently high, and the dispersions of the supported magnons and phonons are close. Magnetoelastic waves have already been observed[226-227] propagating along garnet films, excited by optical pulses. Intriguingly, the pressure strain excited longitudinal magnetoelastic waves with dipolar symmetry, whereas the shear strain excited transverse waves with quadrupolar symmetry – this difference enables one to identify whether shear- or stress-strains dominate the excitation mechanism. Such knowledge is invaluable for the future design of spin-wave sources involving piezoelectric components.

The non-thermal pathway is even more complex, involving a broad range of polarization-dependent effects. For example, Hansteen *et al.*[228-229] used linearly-polarized light to modify the magnetocrystalline anisotropy of garnet films – this transient modification led to measurable spin precession. The inverse Faraday[230-231] and inverse Cotton-Mouton[232-233] effects also involve the generation and / or modification of magnetization using circularly-polarized and linearly-polarized light respectively. Overall, the non-thermal mechanism involves the generation of local magnetic fields – again, this brings the non-thermal optical stimulation of magnetization dynamics within the jurisdiction of graded-index magnonics. This pathway strongly depends on the polarization of the optical pulse, whereas the thermal pathway is entirely independent of this feature (this difference allows one to identify, in a practical experiment, which of the two mechanisms is dominating). It should be noted,

however, that it is impossible to completely remove the thermal contribution from any such optical pump.

From the viewpoint of technological application, the optical excitation of magnetization dynamics via thermal loading is (at first glance) rather unattractive – the reputation frequency of the excitation is hampered by the cooling of the substance, and moreover such heating limits the conceivable recording density. However, since the thermal load is impossible to remove from optical excitations, it is important for magnonic engineers to understand and anticipate the possible effects generated by thermal effects. It should also be noted that heat-assisted magnetic recording (HAMR)[234] exploits the transient demagnetization induced by thermal loads in order to reduce the magnetic bias field needed to reorient magnetic bits. It is not inconceivable, therefore, that thermal loads could eventually be used to excite and control spin waves.

In this chapter, I present and discuss the results of TROPSOM measurements performed on films of Permalloy, of thickness 20 nm and 50 nm. Both samples were fabricated using magnetron sputtering. The experimental development of the stroboscopic TROPSOM system used at the University of Exeter is still in its infancy, and for the first time, measurements were performed with pump and probe beams of wavelength 400 nm and 800 nm respectively. Two types of experiments were performed. The first involved time-resolved measurements, by which the probe spot was fixed and focused at a certain position. The second involved time-resolved spatial imaging, whereby the focused probe was raster-scanned across the surface of the sample. As discussed in Chapter 3, both the transient reflectivity and magneto-optical Kerr signals were recorded. In the first and second sections of this chapter, the experimental measurements of 20 nm- and 50 nm-thick films of Permalloy are respectively presented and discussed. Since many data sets were acquired using TROPSOM, there is a strong need to programmatically apply post-processing and surface fitting to the recorded measurements. The post-processing procedures are therefore discussed in depth. Unfortunately, the measurements presented here are not, at the present time, underpinned by self-consistent theoretical understanding – I therefore conclude this chapter by briefly discussing the measurements as a whole, and speculating as to how the signals arose.

7.2 Measurements of a 20 nm-thick film of Permalloy

The first sample investigated using the TROPSOM system consisted of a continuous film of Permalloy, of thickness 20 nm, mounted on a 330 μm-thick substrate of Sapphire (the sample spanned an area of 1 cm^2). The Permalloy film was magnetized in-plane throughout by an alnico horseshoe magnet, which was measured as delivering a bias magnetic field H_B = 145 Oe across the sample.

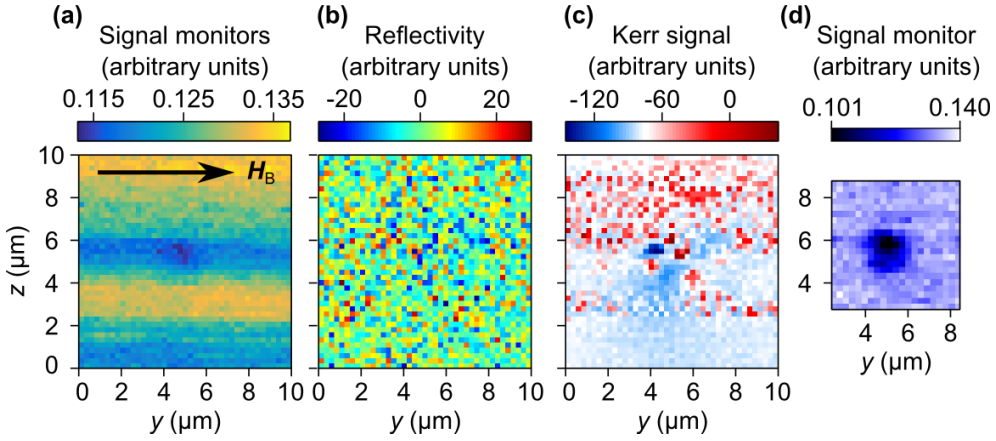

Fig. 7.1 **(a)-(c)** dc reflectivity, transient reflectivity and Kerr signals respectively, acquired with a pixel acquisition time of 4 s. These measurements were performed about 24 hours after the pump beam, of power 2.00 mW, was focused at the same point on the surface of the 20 nm-thick Permalloy film. **(d)** dc reflectivity signal acquired with a pixel acquisition time of 10 ms, recorded immediately after the signals presented in (a) - (c) were recorded.

The first point to note is that the Permalloy film appeared to be very sensitive to the pump beam. The pump power needed to be low enough to avoid ablating the film, but high enough to induce a measurable signal. Extensive testing was therefore performed to identify an optimum pump power. It was found that a pump power below 2.00 mW (corresponding to a pulse of 25 pJ, and a fluence of 28 mJ / cm^2) rendered the reflectivity signal too weak to reliably measure above the noise threshold. The 2.00 mW pump, however, gradually burned a hole in the sample, which was visible after 24 hours of exposure to the pump. This is shown in Fig. 7.1. All the measurements across the 20 nm-thick film of Permalloy were therefore performed across the space of about 18 hours, and the sample was then moved laterally by a small distance. Testing revealed that a probe with power as high as 20 mW did not

immediately damage the sample. The probe was therefore fixed as having a power of 2.00 mW (corresponding to a fluence of 7 mJ / cm^2).

A second important point relates to the banding observed in the Kerr channel, as was discussed in Chapter 3 - these bands were attributed to a steady oscillation of the laser power outputted by the laser system. These bands were often rather significant in amplitude, capable of obscuring useful signal. Some effort was therefore expended in order to find the optimum parameters with which images could be acquired. As already discussed in Section 3.4.3, the laser power fluctuation had a characteristic frequency of 0.4 mHz (corresponding to a period of ~40 minutes). All the images needed to span an area of (10 × 10) μm^2 – such a viewing panel was expected to be sufficient for observing the picosecond dynamics excited by a focused pump spot of size ~1 μm. The lock-in amplifier's time constant of 0.5 s was adequate in achieving reasonable signal-to-noise ratio in the detected signal. All images were therefor recorded with a spatial step of 0.25 μm, and the signal at each pixel was afforded a settling time of 1.5 s. This set of parameters led to the images needing about 40 minutes each to record, which allowed the image to be recorded within one period of the laser's power oscillation.

The first type of signal acquired in this investigation was of time-varying character. Specifically, an image was recorded, at a small but positive time delay, to reveal any features of interest. The probe was then fixed at a certain point on the sample surface, and the retroreflector was then moved in order to yield a time-resolved trace. Generally, the reflectivity and Kerr signals returned by the two-phase lock-in-amplifiers were complex. Dr. Fedor Mushenok therefore wrote a MatLab program which served to rotate the signal into one channel, as outlined in Fig. 7.2. Presented in Fig. 7.2 (a) is a typical raw Kerr signal, output from a lock-in amplifier. The rise and fall of the signal can be observed in both output channels. This data was then replotted in a phase-plane, as shown in Fig. 7.2 (b). By then rotating all the signal points about the origin, the signal occupied one output channel only, as is apparent in Fig. 7.2 (c). Upon replotting the signal channels as a function of time, therefore, the signal has been almost entirely shifted into one channel (Fig. 7.2 (d)). This procedure was used to post-process all time-varying signals presented in this chapter.

The second type of signal recorded in this investigation consisted of transient reflectivity and Kerr images. Again, the images output from the lock-in amplifiers were

complex, and so a procedure very similar to that outlined in Fig. 7.2 was also applied, so that the recorded images occupied one output channel only.

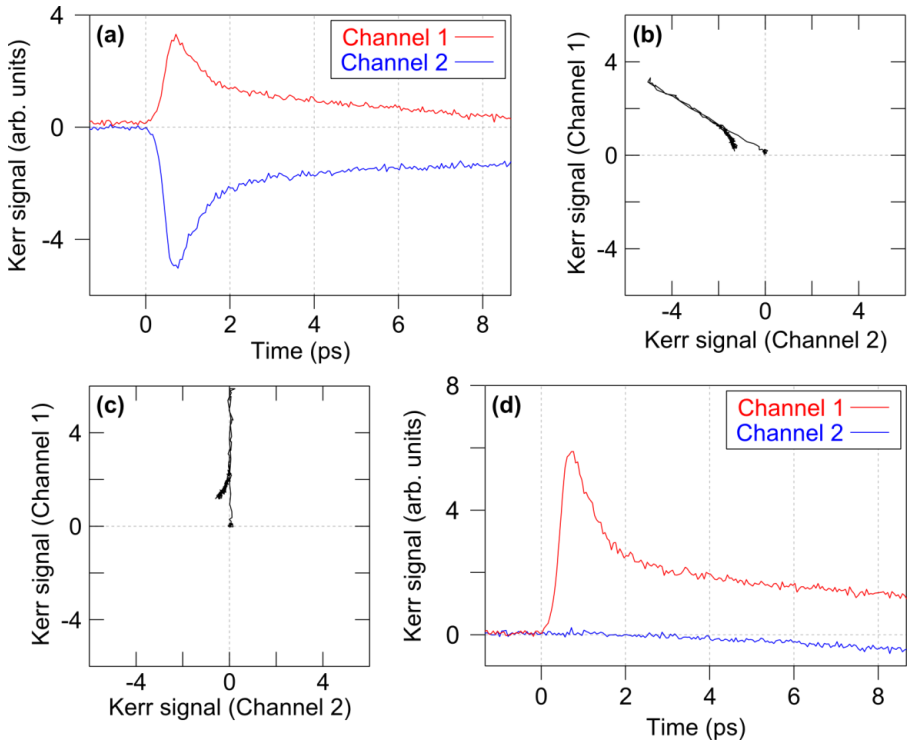

Fig. 7.2 **(a)** Typical Kerr signal acquired using lock-in-detection. **(b)** The same signal as shown in (a), except plotted within a phase-plane. **(c)** The signal shown in (b), rotated about the origin so that the signal occupies one channel only. **(d)** The signal shown in (c) is converted back to being a dependence on time.

Initially, a sequence of time-varying signals was recorded in order to identify the time-scales of interest. To identify the location of the probed regions, the images presented in Fig. 7.3 (a) were recorded at a positive time delay of 667 fs, where the left and right panels correspond to the transient reflectivity and Kerr signals respectively. The reflectivity signal consisted of a single "spot", generally attributed to the spatial distribution of the transient "temperature" increase in the sample. In contrast, the Kerr signal always had a quadrupolar spatial distribution, with the poles having alternating sign. The probe was therefore fixed either at the center of the reflectivity spot, or at the lower left lobe of the quadrupolar Kerr pattern. Time-varying reflectivity (left panel) and Kerr (right panel) signals across different time-scales were then acquired, as presented in Fig. 7.3 (b) - (f) and Fig 7.3 (g) - (k) respectively.

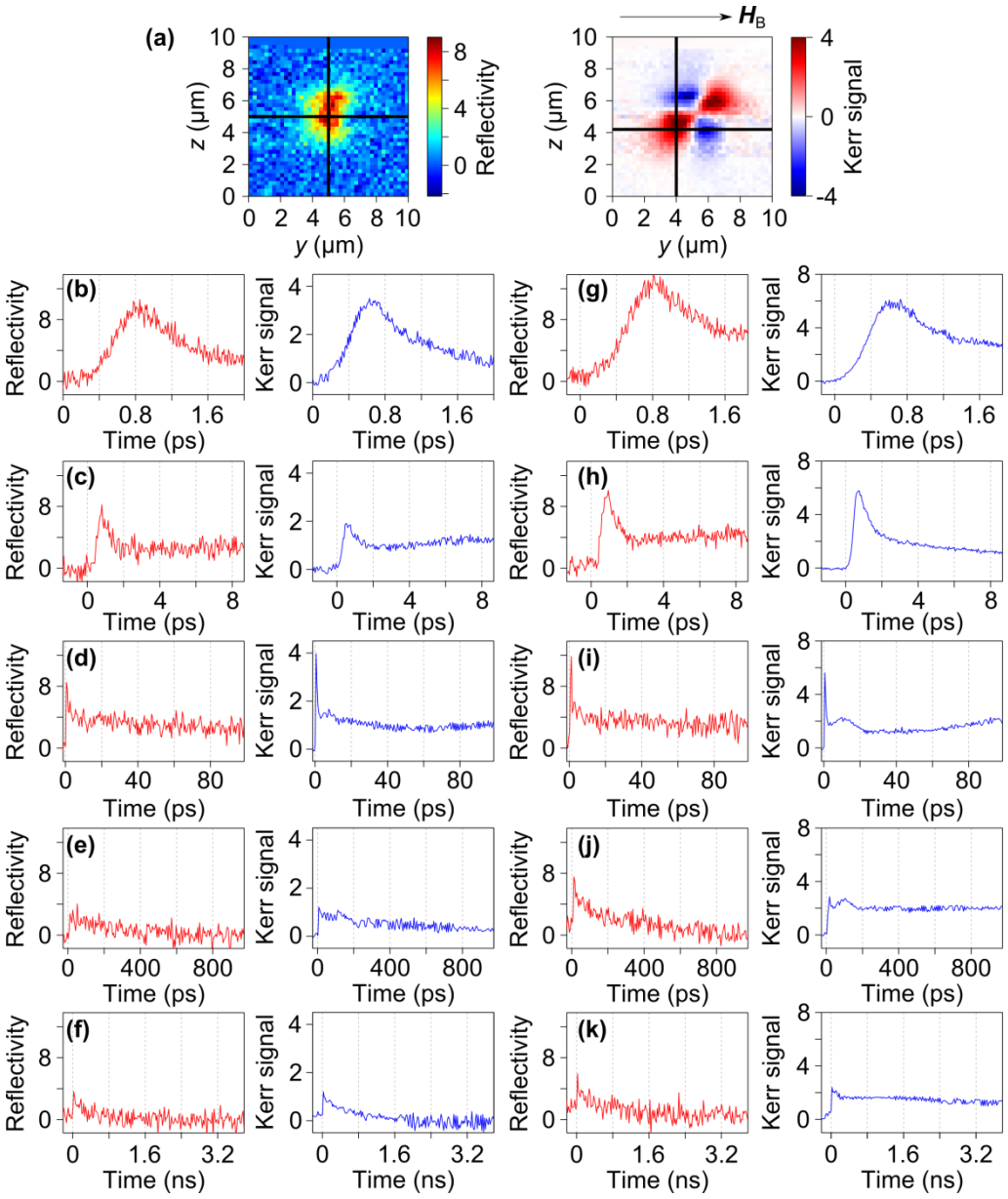

Fig. 7.3 **(a)** Typical reflectivity and Kerr images shown in the left and right panels respectively, acquired 667 fs after initial excitation of the 20 nm thick Permalloy film by the laser pulse. The film was uniformly biased along the *z*-axis by H_B = 145 Oe. **(b)-(k)** Time-resolved reflectivity and Kerr signals (presented in the left and right panels respectively) acquired across time scales of 2 ps, 10 ps, 100 ps, 1 ns and 4 ns as indicated. The signals shown in panels (b) - (f) and (g) - (k) were recorded at the positions (5.0 μm, 5.0 μm) and (4.0 μm, 4.2 μm) respectively, as indicated by the crosshairs in (a). All the images / spectra shown are given in arbitrary (but comparable) units.

The time-resolved spectra boast several features of interest. At negative time delay, no signal was detected in both the transient reflectivity and Kerr channels. At zero-time delay, the signal in the Kerr channel recorded at the center of the reflectivity spot began to rise, and reached its maximum within 650 fs. The simultaneously-recorded reflectivity signal lagged behind the Kerr signal by about 150 fs. Both the reflectivity and Kerr signals then decayed at different rates, reaching zero within about 750 ps and 2 ns respectively. The signal recorded at the lower left lobe of the quadrupolar Kerr image broadly followed the same trends. The reflectivity signal again lagged behind the Kerr signal, and decayed within about 750 ps. The Kerr signal, in contrast, appeared to be non-zero 3.8 ns after the arrival of the pulse, but had decayed entirely within 12.5 ns (since there is no accumulated signal). A slight oscillation of the Kerr signal was apparent in Fig. 7.3 (i) and (j), but there was no change in the sign of the signal.

Subsequent to the recording of the time-varying signals, transient reflectivity and Kerr imaging was performed. As already noted, the transient reflectivity and Kerr images were consistently monopolar and quadrupolar respectively. Once the raw images were therefore recorded, the output was shifted into one signal channel, and then fitted to a distribution as described by Eqs. 7.1 – 7.2

$$f_{monopolar}(y,z) = ay + bz + c + \frac{Amp}{\sqrt{2\pi\sigma^2}} e^{-\frac{(y-y_0)^2+(z-z_0)^2}{2\sigma^2}}, \tag{7.1}$$

$$f_{quadrupolar}(y,z) = ay + bz + c + \frac{Amp}{\sqrt{2\pi\sigma^2}} e^{-\frac{(y-y_0)^2+(z-z_0)^2}{2\sigma^2}} \cdot \sin\left(2\tan^{-1}\left[\frac{z-z_0}{y-y_0}\right] - \phi\right). \tag{7.2}$$

The first three coefficients (*a*, *b* and *c*) in Eqs. 7.1 – 7.2 represent the equation of a plane. This was incorporated in order to represent the possible linear variation in the "background" of the recorded image, originating (primarily) from the laser's systematic fluctuation in power. The second term represents a normalized Gaussian, with an amplitude *Amp* and standard deviation σ, centered at the position (y_0,z_0). The laser beam nominally had a Gaussian spatial profile, and so the generally monopolar reflectivity signal was assumed to be described by a Gaussian function. The amplitude and standard deviation of the fitted Gaussian surface enabled the strength and spatial extent of the acquired signal to be evaluated. The final term in Eq. 7.2 represents a quadrupolar distribution, where the 4 poles of alternating sign are rotated by an angle ϕ.

Presented in Fig. 7.4 is an example of the procedure used to apply the fitting across the same image as shown in Fig. 7.3 (a), where the upper and lower panels show the reflectivity and Kerr signals respectively. The MatLab program used to undertake this procedure was written by myself. Shown in Fig. 7.4 (a) is the raw reflectivity and Kerr signal. To use the surface-fitting program, the user inputs whether the signal is monopolar or quadrupolar in distribution, and then selects a reasonable "guess" of the coefficients z_0 and y_0, using the interactive crosshairs shown. The program then fitted the distribution given by either Eq. 7.1 or Eq. 7.2, using the optimality criterion of least absolute residuals.******** The 95% confidence intervals, associated with all eight fitting parameters, were also calculated. Images of the raw data, the fitted monopolar / quadrupolar signal, and the raw data with the plane background subtracted (presented in Fig. 7.4 (a) – (c) respectively) were then saved, along with the fitted coefficients / confidence intervals. The signal shown in panel (c) is henceforth referred to as "background-corrected".

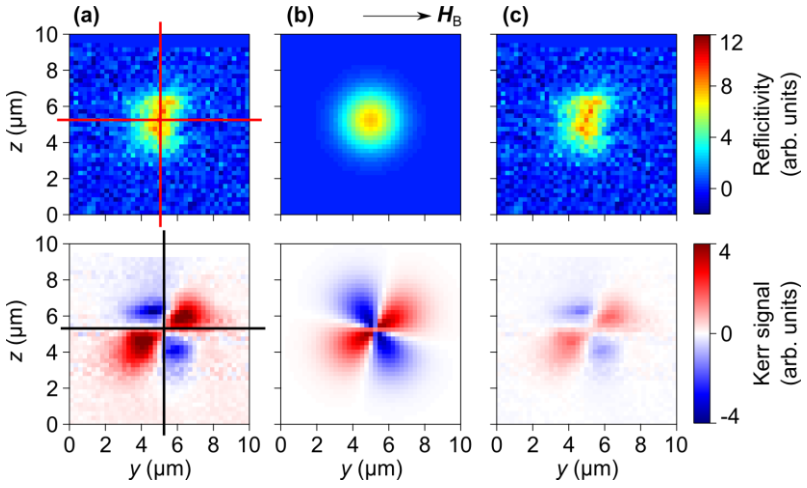

Fig. 7.4 The transient reflectivity and Kerr signals are shown in the top and bottom panels respectively. **(a)** Typical total raw signal. Overlaid is a crosshair, positioned by the user to "guess" the center of the pattern. **(b)** The fitted monopolar / quadrupolar distribution as described by Eq. 7.1 / 7.2, with zero background. **(c)** The same transient reflectivity / Kerr signal as shown in (a), except the fitted plane background has been subtracted.

******** For historical reasons, the optimality criterion of least squares is more popularly used to fit functions to recorded signals. However, it was found during testing that the above criterion generated surfaces that significantly depended on the initial values for z_0 and y_0. The optimality criterion of least absolute residual, in contrast, proved to be less sensitive to these inputs.

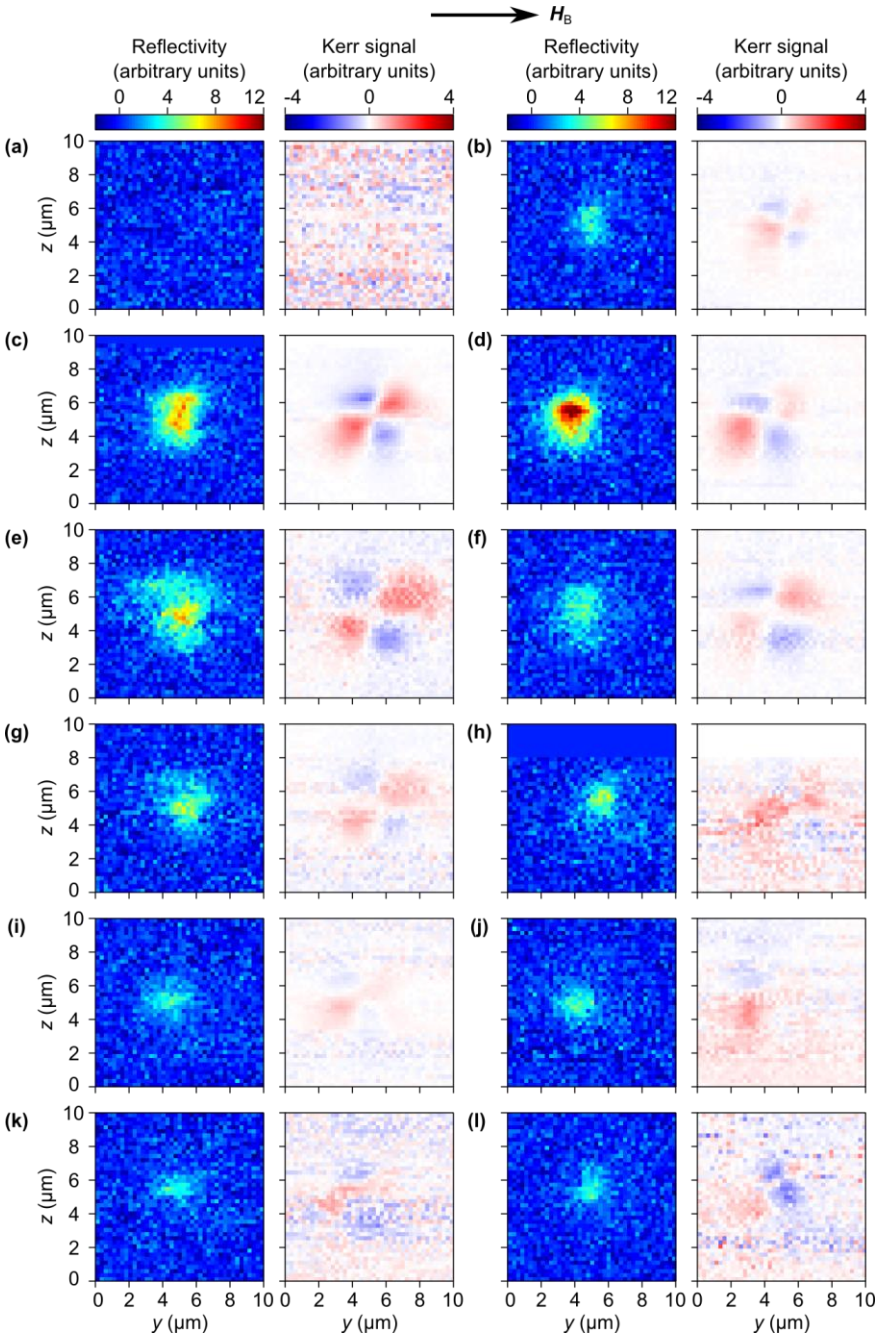

Fig. 7.5 Transient reflectivity images (left panels) and Kerr images (right panels), acquired across a 20 nm-thick Permalloy film, at time delays **(a)** -1.0 ps, **(b)** +400 fs, **(c)** +667 fs, **(d)** +800 fs, **(e)** +1.00 ps, **(f)** +1.33 ps, **(g)** +1.50 ps, **(h)** +3.00 ps, **(i)** +4.00 ps, **(j)** +8.0 ps, **(k)** +40.0 ps, and **(l)** +150.0 ps relative to the arrival of the pump pulse. All the panels are background-corrected, except for the transient reflectivity signal shown in panel (a), and the Kerr signals shown in panels (a), (h), (j), (k) and (l).

A selection of the acquired images at varying time delays is presented in Fig. 7.5. All the images presented here have undergone the fitting procedure as described in Fig. 7.4 where possible. Note that all the images acquired (raw, fitted-surface, and background-corrected) are provided in Appendix 2 for completeness. Here, the imaging confirmed that there was no signal in both the reflectivity and Kerr channels prior to the arrival of the pulse. Then, 400 fs after the nominal arrival of the pulse, a weak monopolar reflectivity / quadrupolar Kerr signal was apparent. Both the reflectivity and Kerr signals, after maximizing in strength, then decayed, and are rather faint (but still observable) at a positive time delay of +8 ps. Both signals are still, perhaps, faintly apparent and discernible at time delays of more than +100 ps.

The images presented in Fig. 7.5 do not lend themselves well to quantitative analysis, due to the prevalence of outliers and noise, and the possibility of subjective interpretation. The surface fitting, therefore, enables the monopolar and quadrupolar distributions to be studied with more rigor. Presented in Fig. 7.6 are graphs showing the temporal variation of the fitted coefficients.

The advantage of the statistics shown in Fig. 7.6 lies in the fact that they describe the entire signal, compared to the time-resolved signals presented in Fig. 7.3 (that are local in nature). The statistical results show that the amplitude of both the reflectivity and Kerr signals (as a whole) increase in strength by a factor of about 3 within one picosecond. This is consistent with the time-resolved measurements shown in Fig. 7.3. The spatial extent of the monopolar reflectivity signal increases rapidly when the pump pulse arrives, to about 1.5 μm, but then decays rapidly to a fairly constant size of 1 μm. This initial increase and subsequent decrease in spatial extent can be understood as arising from the fast delivery and dissipation of energy to and from the pumped region. The Kerr signal, in contrast, appears to only grow (while decreasing in amplitude). The statistics in Fig. 7.6 (c) - (d) show the absolute central positions of the monopolar and quadrupolar signals. While there is some small scattered mismatch, the centers do appear to coincide well – this indicates, at the very least, that both signals are consistent. Finally, the angle of the quadrupole's axis of symmetry is fairly constant across the first 1.5 ps, aligned at about -28° relative to the *y*-axis. The angle appears to then decrease by 10° in the subsequent measurements.

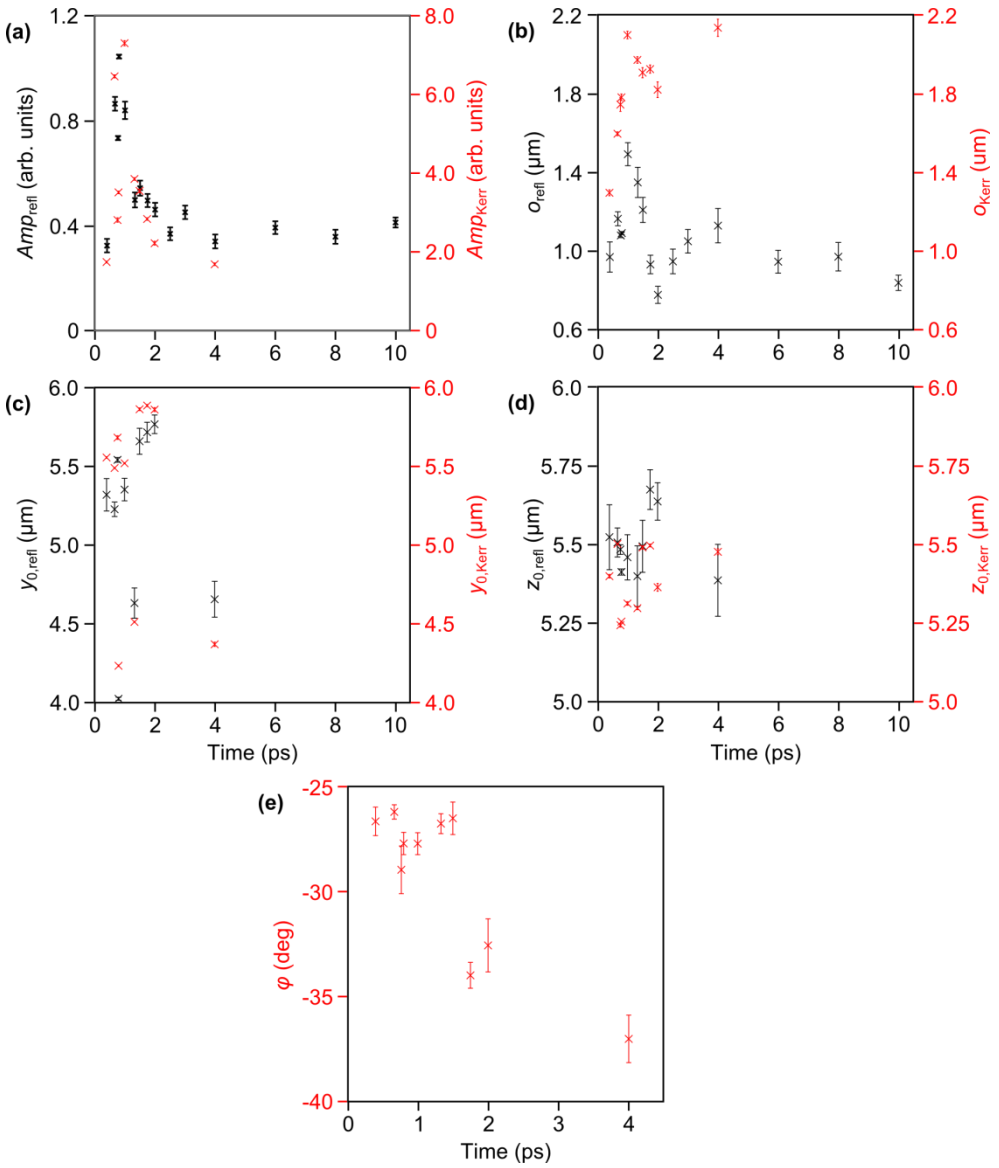

Fig. 7.6 The black and red plots show the results corresponding to the transient reflectivity and Kerr signals respectively. **(a)-(e)** The results of fitting the signals acquired across the 20 nm-thick film, showing the temporal variation of *Amp*, σ, y_0, z_0 and ϕ respectively. The error bars shown in all panels correspond to the 95% confidence limits.

The results acquired using TROPSOM should, in principle, be independent of the intensity of the probe beam. The fluctuation of the laser power, however, led to the possibility that both the pump and probe beams could vary in power across the (rather substantial) time required to acquire the images. While the pump and probe powers were checked at regular intervals (at least once a day, when the sample was moved to compensate for the effect of ablation), the signal monitor output from the reflectivity detector provided the

detected signal, but importantly with no phase-sensitive multiplication applied. This signal, therefore, was crudely used to monitor the laser power. Presented in Fig. 7.7 (a) is a typical image of the output signal monitor, acquired simultaneously with the signal shown in Fig. 7.5 (d). As can be seen, pump-induced signal is also detected in this channel, due to the strength of the 800 Hz signal. In order to therefore remove this pump-induced signal from consideration, I wrote a MatLab program which allows the user to draw a freehand line isolating the pump-induced signal (shown in Fig. 7.7 (a)). All data enclosed within this closed loop is then removed, leaving only probe-induced signal (Fig. 7.7 (b)). The mean and standard deviation of the probe-induced signal is then calculated. At first glance, the time-resolved average signal monitor (presented in Fig. 7.7 (c)) reflected the statistically-described behavior of the transient reflectivity signal. However, the typical standard deviation of the average signal was around 2 V, dwarfing the average signal monitor by a factor of 10, and so it was judged inconclusive as to whether the pump / probe varied significantly in power.

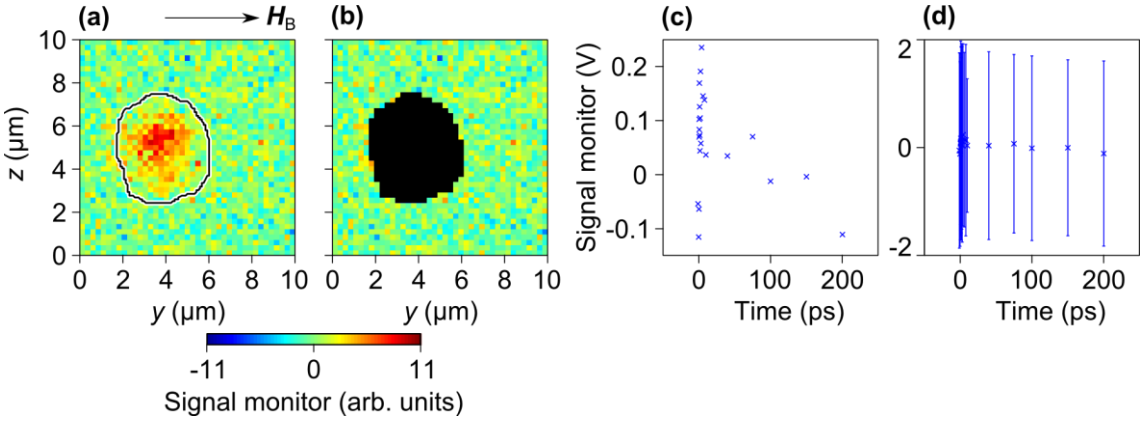

Fig. 7.7 **(a)** Typical signal monitor output acquired from the transient reflectivity detector. Overlaid is a freehand line, isolating the pump-induced signal. **(b)** Same as in (a), except the pump-induced signal has been removed. **(c)** The mean probe-induced signal monitor, as calculated from all the signal monitor images acquired. **(d)** Same as in (c), but error bars are included corresponding to the standard deviation of the average calculated probe-induced signal monitor output.

7.3 Measurements of a 50 nm thick film of Permalloy

The second film measured as part of the TROPSOM investigation was a 50 nm thick film of Permalloy, again mounted on a Sapphire substrate of thickness 330 μm. The methodology of the measurements followed the same procedures as described in Section 7.2, and all the time-varying spectra and spatially-resolved images presented here have been rotated into one output channel. In contrast with the 20 nm thick Permalloy film, the 50 nm thick Permalloy film proved to be more resistant to ablation by the pump beam - this was attributed to the larger volume over which the pump-delivered energy could dissipate into. The pump and probe powers were therefore fixed at 4.12 mW and 1.15 mW respectively (the pump pulse therefore had energy 52 pJ, and a fluence of 57 mJ / cm^2, and the probe's fluence was 4.5 mJ / cm^2).

Preliminary imaging of the transient reflectivity and Kerr signals across the 50 nm thick film was first performed, at a positive time-delay of +100 ps. These results are presented in Fig. 7.8 (a). The transient reflectivity signal was observed to be generally dipolar, where the poles had opposite sign, and the same quadrupolar Kerr signal as was observed for the 20 nm thick film was observed here too.

The time-resolved signals presented in Fig. 7.8 should be compared to the spectra corresponding to the 20 nm thick film, presented in Fig. 7.3. The rise time of the transient reflectivity / Kerr signal across the 50 nm thick film was much slower, taking about 6 ps to maximize. The reflectivity signal, again, lagged behind the Kerr signal, by about 250 fs. There was also non-zero Kerr signal at negative time delay, indicating the accumulation of heat in the vicinity of the pumped region.[221] There was also some signal in the reflectivity channel at negative time delay, but it was weak. Several oscillations in the Kerr signal could be discerned, but notably there was no change in sign.

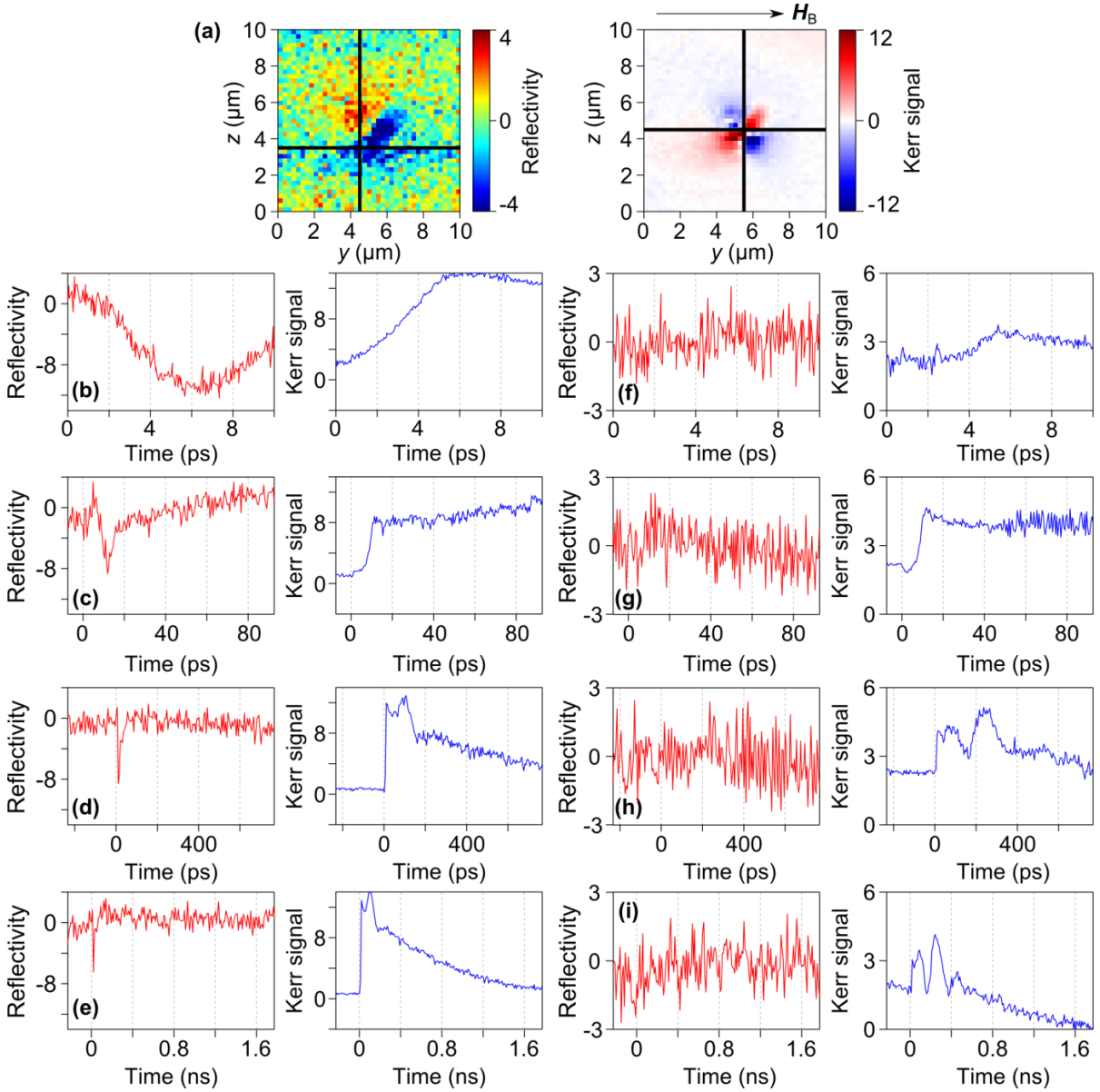

Fig. 7.8 **(a)** The characteristic reflectivity and Kerr image is shown in the left and right panel respectively, obtained about 6.67 ps after initial excitation of the 50 nm-thick Permalloy film by the laser pulse. The film was uniformly biased along the *y*-axis by H_B = 145 Oe. **(b)-(i)** Time-resolved reflectivity and Kerr signals (presented in the left and right panels respectively) acquired across time scales of 10 ps, 100 ps, 1 ns and 2 ns as indicated. The signals shown in panels (b) - (e) and (f) - (i) were obtained with the probe at the position (4.5 μm, 3.5 μm) and (5.5 μm, 4.5 μm) respectively, as indicated by the crosshairs shown in (a). All the images / spectra shown are given in arbitrary (but comparable) units.

After recording the presented time-varying signals, transient reflectivity and Kerr imaging was performed. A selection of background-corrected images is presented in Fig. 7.9, for varying time delays, and all images acquired are provided for completeness in Appendix 2. At negative time delay (-40.0 ps), it is debatable whether a faint positive reflectivity spot can be observed, but a faint quadrupolar Kerr signal is definitely present. At zero time-delay, the negative spot in the reflectivity channel appears, and both the positive and negative spots in the reflectivity signal increase in strength. The reflectivity spot of negative sign is consistently below and to the right of the spot with positive sign. The quadrupolar Kerr signal also grows in strength. After +18.0 ps, the negative spot in the reflectivity channel decays, and intermittently appears faintly from then on. At a positive time delay of +244.0 ps (Fig. 7.9 (d)), ripples can be observed close to the quadrupolar signal in the Kerr channel, propagating predominantly up and to the left, and down and to the right. These ripples propagate outwards and away from the irradiated region, beyond the field of view.

In order to quantify the analysis of the images, statistical fitting was again performed. The quadrupolar Kerr pattern was fitted using the same distribution as given in Eq. 7.2, but the transient reflectivity signal was instead fitted using a dipolar function

$$f_{dipolar}(y,z) = ay + bz + c + \frac{Amp}{\sqrt{2\pi\sigma^2}} e^{-\frac{(y-y_0)^2+(z-z_0)^2}{2\sigma^2}} \cdot \sin\left(\tan^{-1}\left[\frac{z-z_0}{y-y_0} \right] - \phi \right). \qquad (7.3)$$

The terms used in Eq. 7.3 are identical to those associated with Eq. 7.2, except ϕ is the angle of the axis of symmetry associated with the dipole. Presented in Fig. 7.10 (a) - (e) are the temporal variations of the amplitude, spatial extent, central positions and the angle of the axis of symmetry. Also shown in Fig. 7.10 (f) is the temporal variation of the signal monitor output from the reflectivity detector, where the pump-induced signal has been removed according to the procedure outlined in Fig. 7.7.

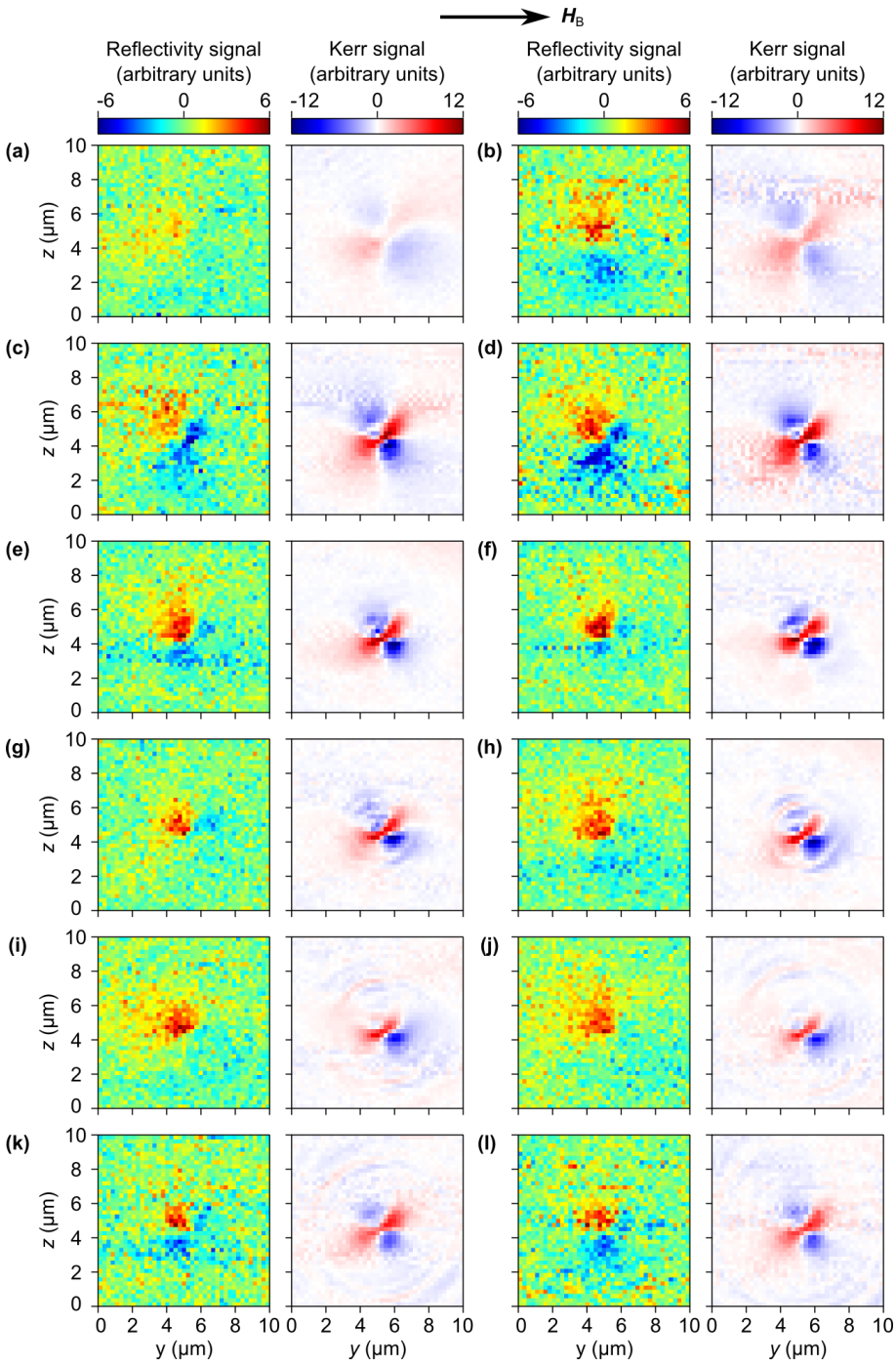

Fig. 7.9 Transient reflectivity images (left panels) and Kerr images (right panels) acquired across a 50 nm-thick Permalloy film, at time delays **(a)** -40.0 ps **(b)** 0.0 ps **(c)** +5.0 ps **(d)** +9.0 ps **(e)** +18.0 ps **(f)** +132.0 ps **(g)** +244.0 ps **(h)** +300.0 ps **(i)** +468.0 ps, **(j)** +580.0 ps, **(k)** +692.0 ps, and **(l)** +860.0 ps, relative to the arrival of the pump pulse. All the panels have had a fitted plane background subtracted, except for the transient reflectivity signals shown in panels (a), (i) and (j).

The amplitude of the detected Kerr signal across the 50 nm film is initially very weak, but non-zero. Once the pulse arrives, the Kerr signal increases rapidly in strength, and then decays (it is possible that the amplitude oscillates, but this is unclear). Spatially, the Kerr signal decreases substantially in the first 10 ps, and then appears to extend slowly outwards. The reflectivity signal, in constant, grows slightly in amplitude across the first 10 ps, but remains relatively fixed thereafter. The spatial extent of the reflectivity signal also appears to be fairly stable. Strong emphasis should be put onto the observation that the co-ordinates of the centers of the dipolar and quadrupolar patterns do not coincide. The origin of the quadrupolar Kerr pattern is consistently 0.75 μm to the right of / 0.25 μm above the origin of the dipolar reflectivity signal. This feature suggests, at least partly, that either the reflectivity or Kerr signal is artefactual in nature.

This interpretation is further supported by the statistical results shown in Fig. 7.10 (e). The orientation of the quadrupolar Kerr pattern is rather consistent (ranging within 10°), compared to the dipolar reflectivity signal. Since no system parameters were deliberately changed between the recording of the images, such variation of the dipolar reflectivity signal is difficult to explain. The signal monitor appears to show two "steps" in signal strength, but this does not appear to correlate with any of the results shown in the other panels.

At a positive time delay of about +200 ps, quasi-circular ripples were observed propagating away from the pumped region of the film. To investigate this propagation more quantitatively, a series of time-resolved signals were recorded at different positions across the film. Presented in Fig. 7.11 (a) are the reflectivity and Kerr images recorded at a positive time delay of +580 ps. Immediately after recording these snapshots, the probe beam was moved to point A (indicated in the right panel of Fig 7.11 (a)), and a time-resolved signal was recorded. The time-resolved reflectivity signal away from the pump spot was uniformly zero, and so is not shown here. The Kerr signal recorded at point A is shown on the left at the top of Fig. 7.11 (b), and a clear oscillatory packet is present.

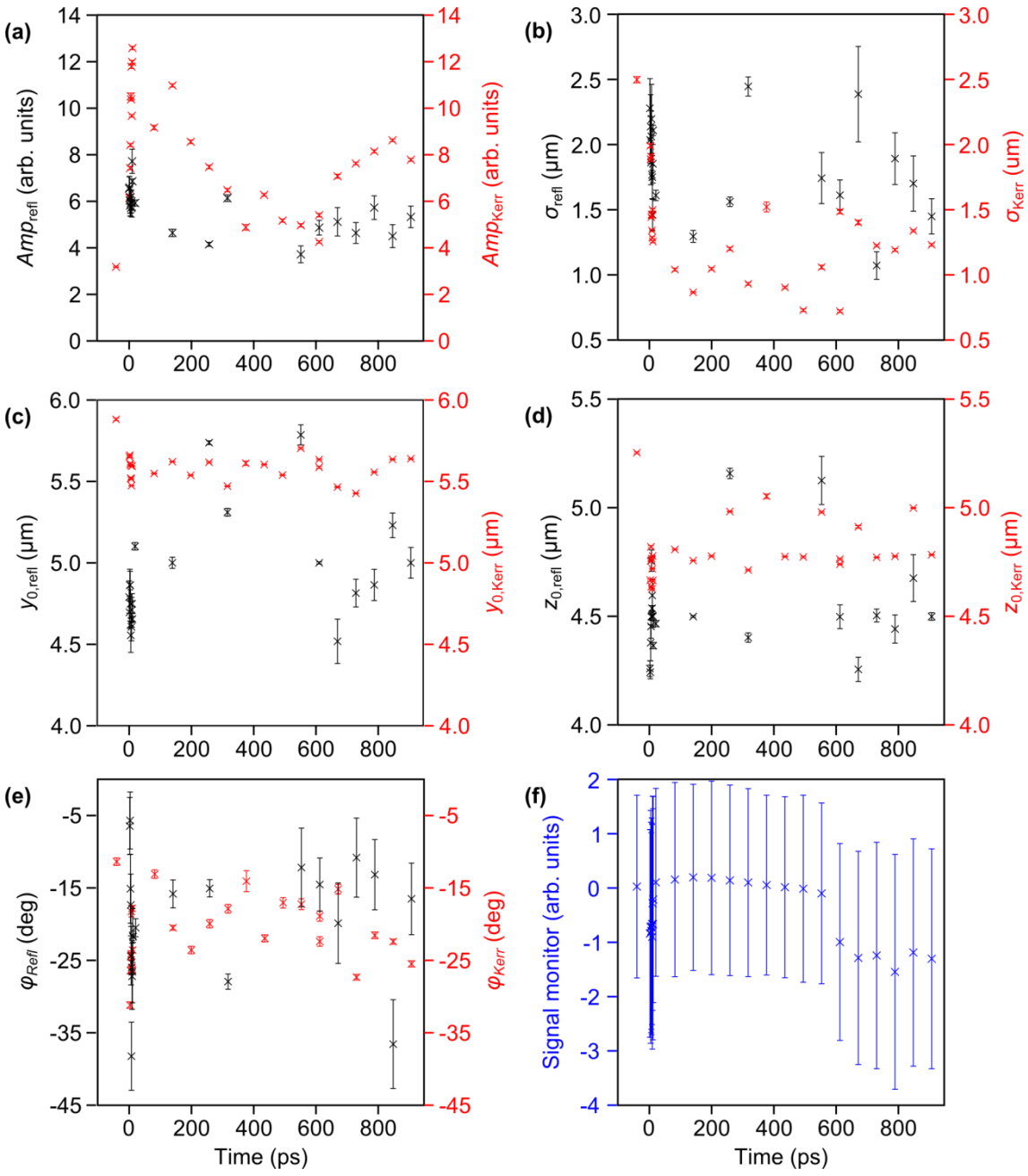

Fig. 7.10 **(a)-(e)** The results of fitting the signals acquired across the 50 nm-thick film, showing *Amp*, σ, x_0, y_0 and ϕ respectively. The black and red points show the results corresponding to the transient reflectivity and Kerr signals respectively, and the error bars correspond to the 95% confidence limits.. **(f)** The average "background" signal obtained from the signal monitor, extracted using the procedure as outlined in Fig. 7.7, but for the 50 nm-thick film. The error bars correspond to the standard deviation of the said "background" signal.

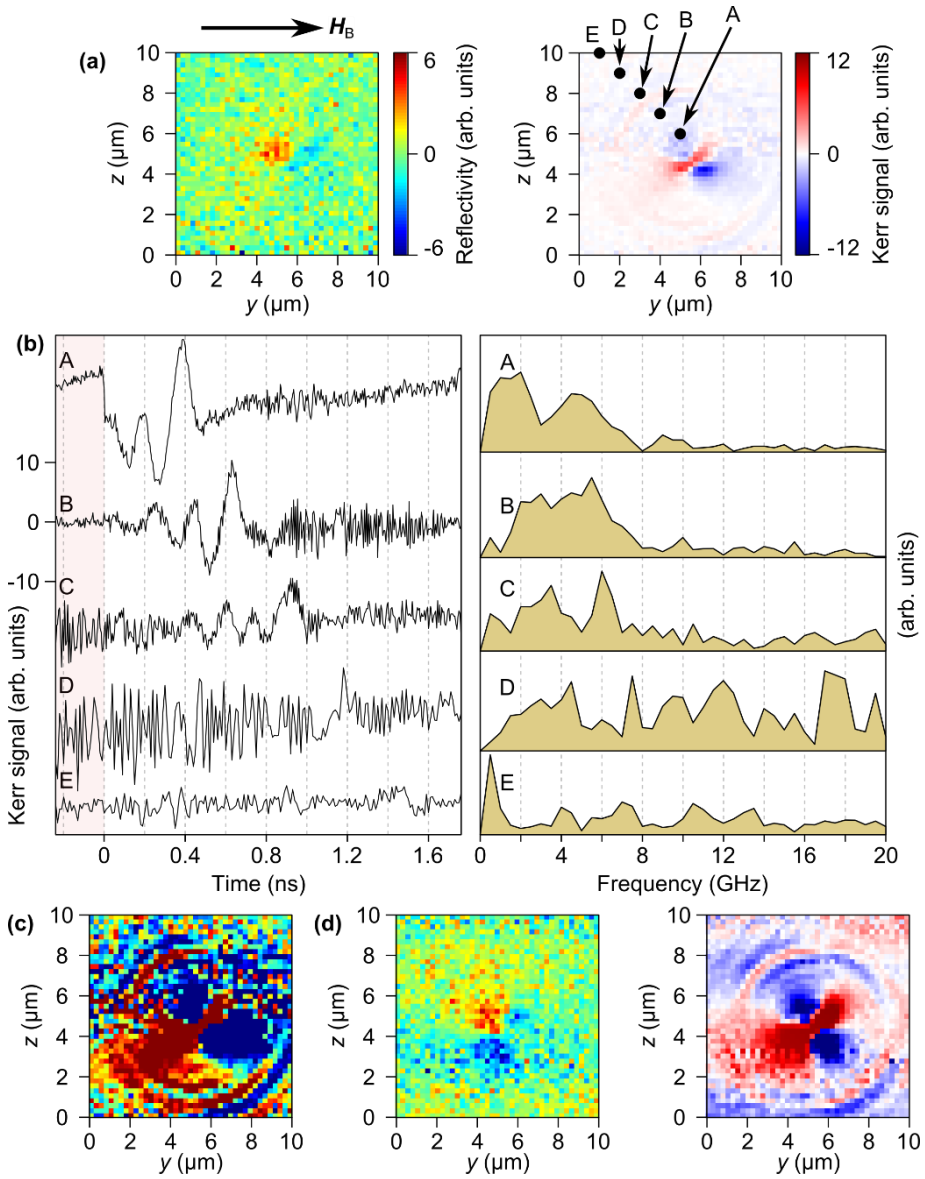

Fig. 7.11 **(a)** Transient reflectivity (left panel) and the Kerr (right panel) signals acquired at a positive time delay of +580 ps, across a 50 nm-thick Permalloy film. **(b)** Time-resolved Kerr signals acquired with the probe fixed at points A-E as indicated in the Kerr image shown in (a). The region shaded red indicates signal corresponding to negative time delay. **(c)** Kerr signal reproduced from Fig. 7.10 (a), but adjusted in color map / scale. **(d)** Transient reflectivity (left panel) and the Kerr (right panel) signals acquired at a positive time delay of +580 ps, obtained about 4 hours after the images shown in (a) were recorded, but with the sensitivity of the reflectivity and Kerr detectors reduced by a factor of 2.5 and 10 respectively.

The motion of the packet of oscillations was then recorded at points B to E, spatially separated by steps of 1.4 μm. The Kerr signals recorded at these points are given on the left side of Fig. 7.11 (b) as indicated, and the packet is clearly observed at positions B and C. By comparing the times at which the peak of the packet was recorded, the ripple was calculated as having a speed of 3.8 km / s. This is on the same order of the velocities of surface acoustic waves which propagate across Nickel films,[235] and so one could reasonably infer that the ripple is of (at least partially) surface acoustic character.

The frequency spectra of the oscillatory Kerr signals are provided on the right-hand side of Fig. 7.11 (b).[††††††††] Since no clear oscillations are present in the Kerr signals recorded at points D and E, these frequency spectra are not considered further. In the frequency spectra calculated at points A – C, the dominant frequencies lie between 1 GHz and 6 GHz. At these frequencies, in the considered Permalloy system, the magnetostatic interaction still dominates (giving rise to spin-wave caustic beams), and so the quasi-circular ripples cannot correspond to spin waves.

Throughout the images shown in Fig. 7.9, the ripples do not appear to be perfectly circular: instead, the ripples have strongest amplitude in the upper-left and lower-right sections of the images. All the images were inspected by increasing the color contrast, to identify whether any ripples could be identified in the lower-left and upper-right sections of the images. The only images which showed any such signal with improved axial symmetry were those contained in Fig. 7.9 (i) - (j) and Fig. 7.11 (a). Presented in Fig. 7.11 (c) - (d) are reproductions of the images presented in Fig. 7.9 (j) and Fig. 7.11 (a), with altered color contrast, showing the ripples are indeed present in the upper-right and lower-left sections of the images respectively. However, these certainly are weak, and the difficulty with reproducibility (in contrast to the reproducibility of the ripples in the upper-left and lower-right sections) indicates that the ripples are not wholly isotropic.

The stationary dipolar transient reflectivity and quadrupolar Kerr signals clearly possess spatial symmetry. Across Figs. 7.8 – 7.9, the dipolar reflectivity and quadrupolar Kerr signals are both canted at about 20° to the *y*-axis. To attempt to identify the origin of this axis of symmetry, a series of system parameters were adjusted, and the results are

[††††††††] Note the Kerr signals all had linearly-varying background, which led to a strong dc response in the calculated frequency spectra. To therefore remove this artefactual contribution, a linear relationship was fitted to (and then subtracted from) the Kerr signal. The Fourier transform was then applied to this modified Kerr signal.

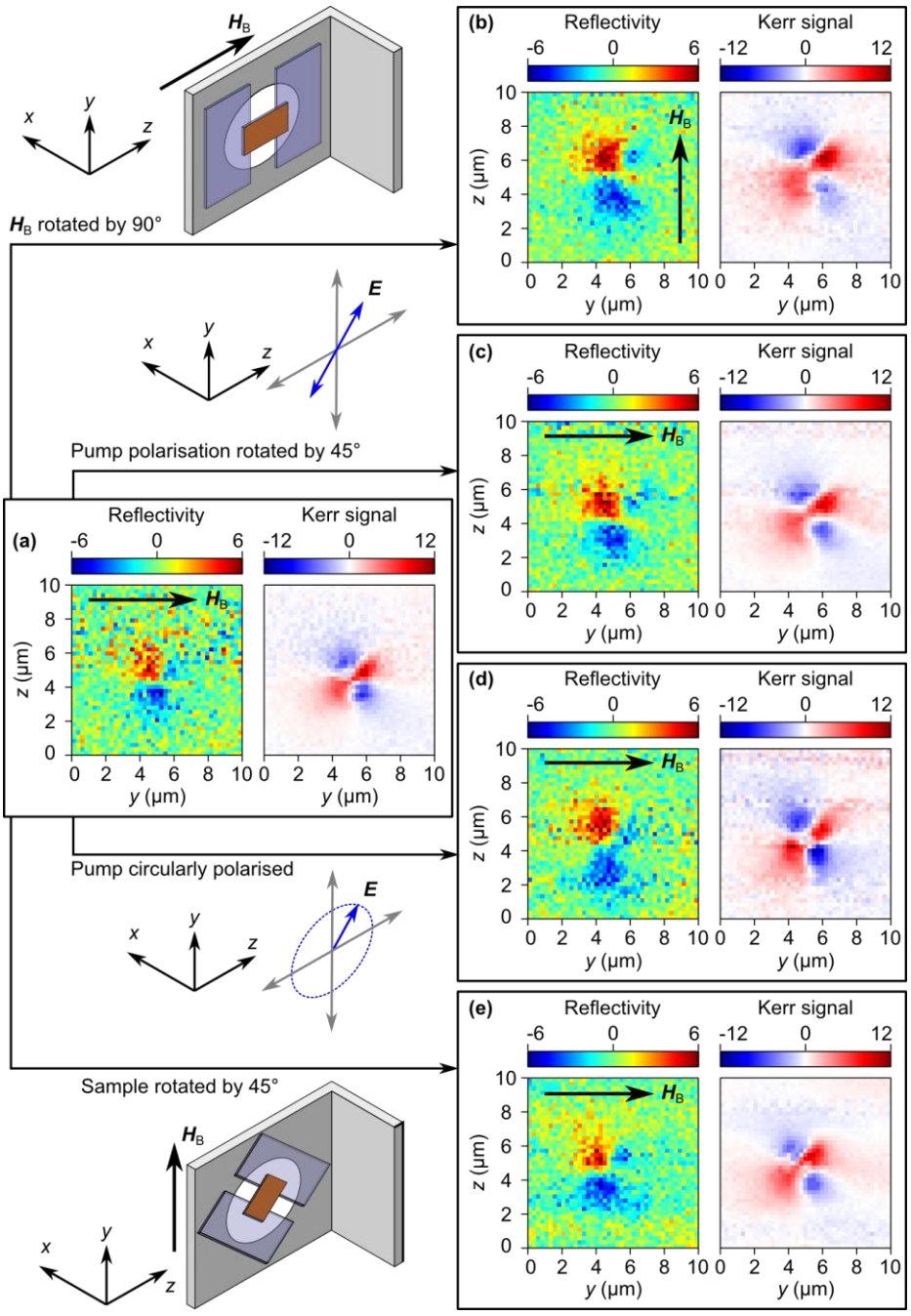

Fig. 7.12 A flowchart showing the results of measurements where system parameters were strategically adjusted. All the transient reflectivity (left panels) and Kerr (right panels) images presented were acquired at a positive time delay of 10 ps. **(a)** The signals acquired when the Permalloy film was biased by $\boldsymbol{H}_B$ = 140 Oe (applied parallel to the *y*-axis), pumped by *s*-polarised light, and mounted as shown in Fig. 3.4.2 (b). **(b)-(e)** Signals acquired upon modifying the experimental setup from that described in (a), as indicated.

presented in Fig. 7.12, where all the images were acquired at a positive time delay +10 ps. Firstly, the signals acquired and presented so far were all obtained with the bias magnetic field H_B applied along the *y*-axis. Immediately after recording the image shown in Fig. 7.12 (a), the horseshoe magnet was rotated / moved such that H_B was parallel to the *z*-axis, and the image presented in Fig. 7.12 (b) was recorded. As can be seen, the signal showed no change in its symmetry. Another possible source of symmetry laid in the properties of the pump beam. The bias magnetic field was therefore rotated back to the *z*-axis, and the pump's polarizer was rotated from the vertical by 45°, serving to rotate the pump's linear polarization. The power of the incident pump was consequently halved, so the neutral density filter was adjusted to compensate for this. The signal presented in Fig. 7.12 (c) appears to, again, show no change. The pump's polarizer was therefore rotated back to the vertical, and instead the quarter wave-plate in the path of the pump beam was rotated by 90°, causing the pump to become circularly-polarized. Again, no change was observed in the signals acquired (shown in Fig. 7.12 (d)). The final test performed concerned the sample orientation. It was hypothesized that the Permalloy / Sapphire perhaps possessed some crystallographic structure that induced significant crystalline magnetic anisotropy, or that the bias magnetic field was insufficient to magnetize the Permalloy (as H_B is admittedly not strong). The entire sample was therefore removed from the TROPSOM system, and the glass cover slips were rotated by 45°. Subsequent measurements, with linearly-polarized pump beam, revealed however that the signals (presented in Fig. 7.12 (e)) were unaffected. It should be noted also that this also revealed that the position / alignment of the pump and probe beams did not affect the signal symmetry.

7.4 Discussion

At the time of writing, only some of the results discussed in this chapter are understood. Here, therefore, I will discuss the results, and speculate about the mechanisms that could underpin the observed features.

When the TROPSOM signals were recorded, many millions of optical pulses were striking the Permalloy films (the laser's repetition frequency of 80 MHz corresponds to the arrival of 80 million pulses on the film's surface per second). Such rapid bombardment can lead to the accumulation of heat, due to the heat within the pumped spot not having enough time to dissipate away. Across the 20 nm thick film, no signal was observed prior to the

arrival of the optical pumping pulse, indicating that the pump-delivered energy had entirely dissipated away from the irradiated region within 12.5 ns. Within 650 fs and 800 fs after the arrival of the pulse, the Kerr and reflectivity signal maximized in strength.

The reflectivity signal observed across the 20 nm thick film was consistently monopolar and fairly Gaussian in distribution. This can be understood as roughly corresponding to the spatial profile of the pump spot. The stationary Kerr pattern, in contrast, was consistently quadrupolar, canted at an angle of about 28° relative to the magnetic field. The centers of the reflectivity and Kerr signals coincided consistently, suggesting that both signals were real. The Kerr signal was, however, engulfed by noise at delay times of more than 2 ps.

Across the 50 nm thick film, non-zero signal was consistently observed in both the reflectivity and Kerr channels at negative time delay. This indicated that, in the 50 nm thick film, the optically-delivered heat did not have enough time to dissipate away from the irradiated region. Again, the reflectivity signal lagged behind the Kerr signal. In the reflectivity channel, the signal observed had either monopolar or dipolar spatial character (the latter was oriented at about 22° to the bias magnetic field). This monopolar / dipolar signal did not appear to switch for any particular reason. The quadrupolar Kerr signal retained its non-stationary behavior, again canted at about 25° to the bias field. The orientation of this quadrupolar pattern neither depended on the bias magnetic field orientation, the polarization of the pump, nor the orientation of the Permalloy sample, indicating that the observed Kerr pattern was not of magnetic or photo-magnetic origin.

A highly-intriguing possibility, which could account for the observed quadrupolar features in the Kerr channel, involves the probe's polarization - throughout all the measurements discussed in this chapter, the probe was nominally *s*-polarized (aligned parallel to the *y*-axis), and no such influence of the probe on the spatiotemporal magnetization dynamics has not been reported before. The probe polarization has, however, been identified in the past as generating artefacts in magneto-optical measurements of the Kerr effect.[236-237] In 2004, Bert Koopmans *et al.* found[238] that the Kerr rotation and Kerr ellipticity did not correlate during the first 1.5 picoseconds of optical excitation, suggesting that the magneto-optical measurements did not necessarily scale with the dynamic magnetization. This was further studied by Tobias Kampfrath *et al*,[239] who argued that parasitic non-magnetic signals arising from the probe beam limit the usefulness of TRMOKE techniques when measuring

magnetization dynamics across timescales spanning the first 100 ps after optical excitation. These reports, also supported by theoretical calculations presented by Oppeneer *et al*,[240] certainly lend credence to the possibility that the quadrupolar contrast in the Kerr channel is an artefact. To investigate this possibility, one could either rotate the linear polarization of the probe, or more usefully, measure the ellipticity induced by the Kerr effect along with the transient reflectivity and Kerr rotation.[241] The integration of a vector bridge detector[242] within the TROPSOM system, allowing all three components of magnetization to be imaged, would also provide further information about the magnetization dynamics and / or optical artefacts imaged by the setup.

Beyond the field of magneto-optical microscopy, a rather novel technique of microscopy has been recently used in biological experiments. This technique – interferometric cross-polarization microscopy[243] – exploits the rotation of polarization of linearly-polarized light to image objects below the diffraction limit. The rotation of polarization arises not from magneto-optical effects, but rather from the scattering of tightly-focused light from nanometric spherical objects.[244] A signature of such scattering is a quadrupolar pattern in the measured polarization response. By rotating the polarization of the probe by 90°, the quadrupolar pattern becomes a monopolar spot. To investigate whether this is responsible for our observations, it is therefore imperative that the experiment be repeated, but the polarization of the probe be rotated, using a half-wave plate for example.‡‡‡‡‡‡‡ It would also be useful to calculate the complex point spread function[245] (the signal detected when imaging an idealized point-like object) relevant to the TROPSOM system, and compare the amplitude and phase of the point spread function to the experimentally-observed quadrupolar pattern.

In addition to the stationary quadrupolar pattern, quasi-circular propagating ripples were observed propagating in the Kerr channel. These were also observed by Au et al,[132] but in that article, the ripples (travelling with a speed of 5 km / s) were interpreted as surface-acoustic waves. It was argued, in that article, that these non-magnetic waves entered the Kerr channel due to misalignment of the optical equipment. In all the results presented in this chapter, the quasi-circular ripples were also observed wholly in the Kerr channel (with a speed of about 4 km / s). This, perhaps, suggests that the ripples are rather of magneto-elastic

‡‡‡‡‡‡‡ Rotating the polarizer usually leads to significant deflection of the laser beam, incurring realignment. In contrast, a laser beam is deflected much less by the rotation of a half-wave plate.

origin, as predicted by Shen *et al*.[227] However, Permalloy usually has small magnetostriction,[246-247] rendering this possibility unlikely – it is therefore essential that the magnetostriction of the studied Permalloy films be measured[248] to confirm or disprove this hypothesis. It is difficult to conclusively infer, from the experimental results presented here, whether the ripples have dipolar or quadrupolar character, and so no further conclusions can be drawn.

The results presented in this chapter should be compared to those presented by Au *et al.*[132] In that article, the bias magnetic field was applied almost normal to the Permalloy film, causing the magnetization to tip by several degrees out of the plane of the film. The optical pulse therefore served to immediately demagnetize the pumped region, causing the magnetization to tip further out-of-plane, and then precess. It should also be noted that Au *et al* observed a non-propagating transient dipolar pattern in the Kerr channel – the origin of this feature is still (at the time of writing) unknown. Possible candidates include the generation of a vortex-antivortex pair,[249] or some optically-induced artefact.[244] In contrast, the magnetization across all the results presented in this chapter was aligned in the plane of the film. The rapid demagnetization of the pumped region would therefore not necessarily induce much precession out of the plane of the film.

It should also be noted that propagating spin-wave caustics were not observed when the static magnetization was aligned in the plane of the film (in contrast to the observations of Au *et al*.[132] Three reasons could account for this. Firstly, the dynamic out-of-plane component of magnetization was strongly suppressed due to the in-plane anisotropy of the film (which aligned with the bias magnetic field): this could render the detected magnetic signal very weak. Secondly, in contrast to the system used by Au *et al*, the probing spot was almost doubled in diameter - consequently, the spatial resolution of the imaging was almost halved. Thirdly, the tightly-focused pump spot here was almost halved in diameter, compared to that used by Au *et al*. As a result, the angular width of the spin-wave caustic beams would halve as well.

7.6 Summary

In summary, the laser-induced spatio-temporal dynamics of two films of Permalloy, of thickness 20 nm and 50 nm (magnetized in-plane), have been studied using time-resolved optically-pumped scanning optical microscopy. Both the 400 nm pump and 800 nm probe beams were tightly focused, and both the transient reflectivity and dynamic magneto-optical polar Kerr signals were recorded. For the 20 nm thick Permalloy, subsequent to the arrival of the pump pulse, a single stationary spot was recorded in the transient reflectivity channel, and a characteristic stationary quadrupolar signal was observed in the Kerr channel. Across the 50 nm thick Permalloy film, a single stationary spot was observed in the transient reflectivity channel prior to the arrival of the pump pulse, and subsequently, a second spot (of opposite polarity) was intermittently observed, giving rise to a characteristic stationary dipolar / monopolar signal. In the Kerr channel, again a characteristic stationary quadrupolar signal, with the same symmetry as was seen across the 20 nm thick film, was observed throughout, persisting as much as 12.5 ns after the arrival of the pump pulse. About 244 ps after the pumping pulse arrived, quasi-circular wavefronts were observed emanating away from the pumped region, with a typical speed on the order of 4 km / s. The physical mechanisms underpinning the observed spatiotemporal dynamics are currently unknown. The stationary dipolar and quadrupolar signals observed in the transient reflectivity and Kerr channels respectively did not depend on the orientation of the bias magnetic field, the pump's polarization, or the sample orientation. Further TROPSOM measurements are required in order to identify whether the signal depends on the probe polarization, and extensive computational models (including magnetoelastic and polarization-dependent effects) must be developed in order to accompany and compliment the results acquired using the TROPSOM system.

CHAPTER 8

SUMMARY AND OUTLOOK

In this thesis, the results of time-resolved magneto-optical imaging experiments, micromagnetic simulations and analytical calculations have been presented. These were all performed in order to understand how spin waves can be excited or steered using the non-uniformities associated with magnetic configurations. The non-uniformity in effective field and / or magnetization has been interpreted as giving rise to a magnonic index,[4] similar in concept to the refractive index for light, or potential for a quantum-mechanical electron.

In Chapter 4, the possibility of exciting spin waves using the graded magnonic index was investigated using Brillouin light scattering microscopy,[82] micromagnetic simulations,[135] and analytical calculations. The principle of excitation relies on the Schlömann mechanism,[24] which exploits the fact that the frequency of resonance will spatially vary across a non-uniform magnetic configuration. By therefore driving the entire system at a particular frequency, the majority of magnetization vectors will not be excited efficiently, but some will be excited at resonance. This local resonance therefore acts as a spin-wave source, launching spin waves of finite wave vector into the neighboring regions of magnetization. In the first part of this chapter,[1] this mechanism of excitation was studied using a combination of Brillouin light scattering microscopy and micromagnetic simulations. The investigated magnetic system consisted of an isolated antidot embedded within an otherwise-continuous film of YIG. Upon subjecting the film to a spatially-uniform bias magnetic field, the static demagnetizing field associated with the antidot served to increase the frequency of resonance in the regions immediately adjacent to the antidot. By then driving the entire sample at a microwave frequency tuned to only resonantly excite these particular regions of the magnetization, spin-wave caustic beams[150] were observed propagating away from the antidot. These caustic beams owed their tightly-focused spatial profile to the anisotropy of the magnetostatic spin-wave dispersion.[92] In the second part of this chapter,[2] the Schlömann mechanism of spin-wave excitation was studied further using micromagnetic simulations to model spin-wave dynamics across Permalloy films of nanometer thickness. Due to the

substantially reduced thickness of the system, the spin waves excited instead had spatial character better described by the dipole-exchange dispersion formulation.[99] It was also demonstrated that the dynamic demagnetizing field on its own, substantially raised in strength close to the edge of a semi-infinite film, could also serve as a spin-wave source – this was capable of exciting plane spin waves with a tunable wavelength / frequency. In the third and final part of this chapter, a hybrid analytical / numerical model was constructed in order to map more quantitatively the spatially-varying frequency of resonance and magnetic susceptibility. These quantities enable the positions of resonance - and, by extension, the magnonic index - to be more accurately determined, and the model constructed is general enough to map the distribution of resonances across any arbitrary (but stable) magnetic configuration.

In Chapter 5, the graded magnonic index was shown to be effective in deliberately steering propagating spin waves in particular directions.[3] To demonstrate this, a T-junction of Permalloy waveguides was studied using both time-resolved scanning Kerr microscopy[147] and micromagnetic simulations. When a spatially-uniform bias magnetic field was applied parallel to the leg of the T-junction, the internal field across the leg was raised, compared to the internal field across the arms. Then, upon exciting the entire sample with a harmonic magnetic field, deliberately tuned so as to excite resonance in the leg of the T-junction, spin waves were symmetrically launched into the arms via the Schlömann mechanism. Due to the finite width of the spin-wave source (the leg-arm interface), and the anisotropy of the magnetostatic spin-wave dispersion, the excited spin waves formed spin-wave caustic beams. When the bias magnetic field was rotated by 15°, the symmetry of the spin-wave propagation was broken, in that spin waves were only observed propagating only along one arm of the T-junction. This was observed using both time-resolved scanning Kerr microscopy and micromagnetic simulations. In order to explain this feature, extensive analysis of the micromagnetic calculations was performed. The spin-wave dispersion was calculated in each and every mesh cell, and maps of the spatially-varying group and phase velocities were constructed. Using these maps, it was shown that the canting of the magnetization close to the edge of the transversely-biased waveguide was responsible for the absence of a spin-wave beam – the strong canting caused the spin-wave beam to undergo “anomalous reflection”, such that it was either refracted closer to the edge of the waveguide, or reflected wholly back upon itself.[66] The method of mapping the spatially-varying group velocity of propagating spin-wave beams, outlined in this chapter, was general indeed, and could in principle be

applied to understand and predict the propagation path of spin waves across any non-uniform magnetic landscape.

In Chapter 6, the propagation of spin-wave width modes across a T-junction of YIG waveguides was studied using Brillouin light scattering microscopy and micromagnetic simulations.[5] The graded magnonic index, in this case, arose from the spatially-varying angle between the magnetization and the spin-wave group velocity. Across an unstructured thin film, the dispersion of magnetostatic surface spin waves and backward-volume magnetostatic spin waves do not overlap at all. When spin waves are laterally confined across a waveguide, in contrast, the two dispersive bands overlap, suggesting the possibility of converting the two spin-wave types.[212] In the first section of this chapter, the propagation of spin waves across YIG waveguides was studied, and it was demonstrated that the dispersive bands did indeed overlap. Ultimate evidence of this behavior was presented via the calculation of the spin-wave dispersion using dynamic micromagnetic simulations. Due to the uniformity of the exciting field across the width of the waveguide, the spin waves that were excited had sinusoidal lateral profile, with an odd number of antinodes. In the second part of this chapter, a T-junction of YIG waveguides was studied, again using Brillouin light scattering microscopy and micromagnetic simulations, and it was demonstrated that spin waves did indeed propagate across the entire network of waveguides. Across the arms of the T-junction, the spin-wave propagation path was identified as snake-like - this pattern emerged because a mixture of even and odd width-modes was propagating.[109]

In Chapter 7, the ultrafast magnetization dynamics across Permalloy films, biased in-plane, was studied using time-resolved optically-pumped scanning optical microscopy.[132] While the graded magnonic index can, in principle, arise from both the transient length of the magnetization vector (induced by the optical pump's thermal load) and the local magnetic fields associated with the pump, no graded-index effects were definitively observed in this chapter. In this system, the pump consisted of a linearly-polarized optical pulse (of wavelength 400 nm and duration 100 fs), and the probe consisted of a similar pulse of wavelength 800 nm. Both beams were tightly focused on the surface of the sample, and both the polarization rotation and transient intensity of the probe was recorded. Two Permalloy films were studied, with a thickness of either 20 nm or 50 nm. Across the 20 nm thick film, a single spot was observed in the reflectivity channel (corresponding to the spatial distribution of the thermalized electrons / lattice), and a non-propagating quadrupolar pattern was

identified in the Kerr channel. The quadrupolar pattern in the Kerr channel was only observable for the first few picoseconds after the pumping pulse arrived. Across the 50 nm thick film, the reflectivity channel instead intermittently displayed a dipolar pattern - the origin of this feature is unknown at the time of writing. In the Kerr channel, a non-propagating four-lobed signal was again observed. In addition to these stationary patterns, quasi-circular ripples were observed propagating outwards (with a speed of about 3.8 km / s). It is unknown whether these ripples are of magneto-elastic origin.[226] The quadrupolar pattern had two characteristic axes of symmetry, which did not depend on the bias field orientation, the polarization of the pump, or the orientation of the sample. It is suspected that the probe polarization may be the origin of this pattern.[239] Substantial research is still needed in this area, in order to understand the measured results.

As a whole, the work discussed in this thesis demonstrates that non-uniformities in a magnetic configuration (i.e. a graded magnonic index) can be used to excite and steer spin waves. The experimental, numerical and analytical results discussed in Chapter 4 collectively reveal that non-uniformities in either the magnetization and / or effective field give rise to a corresponding spatially-varying frequency of resonance. By therefore subjecting the entire magnetic system to a spatially-uniform microwave field, tuned so as to excite only specific regions of magnetization at resonance, one can launch spin waves of finite wave vector into the adjacent regions of the sample. Importantly, this scheme of excitation is devoid of any limitations involving the spin-wave wavelength, allowing spin waves of any wave vector (as permitted by the magnetic film) to be generated. In Chapter 4, the non-uniformity of magnetization / effective field was delivered through patterning of the magnetic film. In Chapter 7, in contrast, spin waves (or more correctly, magnon-phonons) were excited through transient thermal modification of the magnetization, as delivered by an optical pulse. As well as demonstrating that the graded magnonic index can be used to excite spin waves, the results in Chapters 5 and 6 revealed that the said index can be used to steer spin waves, in an approach analgous to the research theme of graded-index optics. Upon encountering a region of magnetization with dissimilar magnetic parameters, a spin wave will adiabatically adjust its wave vector in order to satisfy the local dispersion. In Chapter 5, this effect was exploited to understand a variety of effects, including the spin-wave "mirage" and the "anomalous" reflection of spin waves. In particular, the latter effect was exploited to give rise to a spin-wave demultiplexer. In Chapter 6, in contrast, the graded magnonic index was exploited to realize a magnonic beam splitter – the basic building block of parallel magnonic circuitry.

For magnonics to truly complement, and perhaps rival, semiconductor technology in the field of data communication and processing, there are three significant challenges that need to be addressed. First, the damping of spin waves in metallic ferromagnetic materials needs to be reduced, in order to increase the propagation distance of spin waves, and also reduce the linewidth of spin-wave modes. The work discussed in this thesis has not addressed this challenge at all, but promising results have already been reported by some groups.[60-61] It is therefore reasonable to project that researchers in magnonics will move towards using Co-Fe alloys as a material of choice, rather than Permalloy. Second, the spin-wave wavelength needs to be reduced towards the nanometric scale. Third, an efficient and effective means by which to steer spin waves must be developed. The work discussed in this thesis goes some way towards addressing the latter two challenges. However, of course, more work needs to be done in order to truly address these obstacles.

There is a wide variety of magnetic interactions, beyond the Zeeman and demagnetizing interactions that have been predominantly studied in this thesis, that influence the spin-wave dispersion. These interactions include, but are not limited to, magnetocrystalline anisotropy, magnetostriction, exchange, DMI, magneto-elastic coupling, and superexchange. Initially, therefore, to further explore the effects of "graded-index magnonics", effort must be devoted to fully understanding how these interactions influence free and driven magnetization oscillations (giving rise to the frequency of ferromagnetic resonance and the spin-wave dispersion respectively). With this background in place, one can then design suitable magnetic configurations in order to excite spin waves using a global microwave magnetic field. In the work presented in this thesis, I have only demonstrated that the magnetic non-uniformity associated with an antidot and edge of a stripe can be used to generate spin-wave caustic beams and plane spin waves respectively. It is reasonable to project that alternative magnetic configurations, hosting (for example) vortex-antivortex pairs, domain walls and skyrmions, could be used to generate different types of spin waves. In terms of using the Schlömann mechanism to excite spin waves, the only design requirement relates to the need for a non-uniform magnetic configuration. It must be emphasized that such non-uniformity is inevitably present in micro- and nano-magnetic structures, and so the scheme of excitation will surely benefit from miniturization.

In this thesis, the spin-wave steering arising from the graded magnonic index was explained solely in terms of the demagnetizing and Zeeman fields. Upon miniaturization of

the spin-wave wavelength, however, the influence of other interactions - including exchange and DMI for example - must be also taken into account. An obvious next step would therefore be to work towards comprehensively understanding and verifying how these interactions influence the isofrequency curves (and therefore the path) of propagating spin waves. Once this understanding is gained, one can then aim to comprehensively exploit spin-wave steering for technological devices.

The spin-wave splitter discussed in this thesis was of macroscopic dimension, and composed of the dielectric YIG. To further this area of research, therefore, it is imperative that the device be miniaturized further. A similar device, composed of Permalloy on the micrometric scale, was studied by Brächer *et al*,[212] and so it is reasonable to assume that the magnonic beam-splitter will successfully operate on a similar length-scale. Moving towards nanometric dimensions, however, the isotropic exchange interaction will become more significant, and so micromagnetic simulations should be performed to identify whether the process of splitting changes substantially. In more general terms, many magnonic devices have already been demonstrated (including, for example, transistors,[207] filters,[209] and multiplexers[196]) but all these still need to be miniaturized further. In addition, these building blocks need to be joined in unison, therefore allowing the principles of "graded-index magnonics" to be utilized fully.

In the work discussed in Chapter 7, the dynamics excited by an optical pulse was not fully understood, and so it is essential that the experiment be repeated, but with varying polarization of the probe. Going beyond this, the integration of optical pulses with systems supporting spin waves provides a remarkable degree of reconfigurability. By shaping the spatial distribution of the optical pulse, it is well-known that one can generate spin waves with specific spatial profile.[220] The optical excitation of spin waves in continuous ferromagnetic / ferrimagnetic media is reasonably understood, but less attention has been paid towards the possibility of exciting propagating spin waves in (for example) more complex rare-earth orthoferrites, or using optical pulses to steer spin waves. Optical pulses could, for example, be used to excite the spin waves that are steered across magnonic devices (such as a beam-splitter). Alternatively, an optical pulse, via its thermal influence on the magnetization of a material, could instead be used to directly modify the path of propagating spin waves.[250] Such investigations necessitate a deep understanding of how the magnetoelastic interactions and transient modification of the magnetization influence the spin-wave dispersion.

APPENDIX 1

Derivation of the local frequency of resonance / effective susceptibility tensor

The derivation presented in this appendix shows, in more detail, how Eqs. 4.16 – 4.17 (discussed in Chapter 4.3) were obtained.

The linearized Landau-Lifshitz-Gilbert equation, in the presence of both damping and a driving field, is of the form

$$i\omega \boldsymbol{m} = -\gamma \boldsymbol{M}_0 \times \boldsymbol{h}_B + 4\pi\gamma \boldsymbol{M}_0 \times \overleftrightarrow{N}^{eff} \boldsymbol{m} - \gamma \boldsymbol{m} \times \boldsymbol{H}_{0B} + 4\pi\gamma \boldsymbol{m} \times \overleftrightarrow{N}^{eff} \boldsymbol{M}_0 + \frac{i\alpha\omega}{M_S} \boldsymbol{M}_0 \times \boldsymbol{m} . \qquad \text{(A1.1)}$$

This corresponds to an inhomogeneous system of equations, which can be rearranged to obtain

$$\begin{pmatrix} i\omega + 4\pi\gamma M_S N_{yx}^{\ eff} & \gamma\left(H_{z0B} + 4\pi M_S N_{yy}^{\ eff} - 4\pi N_{zz}^{\ eff} M_S\right) + i\alpha\omega \\ -\gamma\left(H_{z0B} + 4\pi M_S N_{xx}^{\ eff} - 4\pi N_{zz}^{\ eff} M_S\right) - i\alpha\omega & i\omega - 4\pi\gamma M_S N_{xy}^{\ eff} \end{pmatrix} \begin{pmatrix} m_x \\ m_y \end{pmatrix} = \begin{pmatrix} \gamma M_S h_{y,B} \\ -\gamma M_S h_{x,B} \end{pmatrix} \qquad \text{(A1.2)}$$

The determinant of the rank 2 tensor, on the left-hand side of Eq. A1.2, is given by

$$\begin{aligned} |A| = &-\omega^2 - 4\pi\gamma M_S \left(4\pi N_{xy}^{\ eff} N_{yx}^{\ eff} \gamma M_S + i\omega\left[N_{xy}^{\ eff} - N_{yx}^{\ eff}\right]\right) \\ &- \left[\gamma\left(H_{z0B} + 4\pi M_S N_{yy}^{\ eff} - 4\pi N_{zz}^{\ eff} M_S\right) + i\alpha\omega\right]\left[-\gamma\left(H_{z0B} + 4\pi M_S N_{xx}^{\ eff} - 4\pi N_{zz}^{\ eff} M_S\right) - i\alpha\omega\right], \end{aligned} \qquad \text{(A1.3)}$$

which reduces (to first order) to the form

$$|A| = -\omega^2 + 2i\alpha\omega\omega_1 + \omega_0^{\ 2}, \qquad \text{(A1.4)}$$

where

$$\omega_1 = \omega_H + \frac{1}{2}\omega_M \left(N_{xx}^{\ eff} + N_{yy}^{\ eff} + N_{yx}^{\ eff} - N_{xy}^{\ eff}\right) \qquad \text{(A1.5)}$$

$$\omega_H = \gamma H_B \qquad \text{(A1.6)}$$

$$\omega_M = 4\pi\gamma M_S \qquad \text{(A1.7)}$$

$$\omega_0 = \sqrt{\left(\omega_H + \omega_M\left[N_{xx}^{\ *} - N_{zz}^{\ *}\right]\right)\left(\omega_H + \omega_M\left[N_{yy}^{\ *} - N_{zz}^{\ *}\right]\right) - \omega_M^{\ 2} N_{xy}^{\ *} N_{yx}^{\ *}} \qquad \text{(A1.8)}$$

In the case of resonant excitation, the determinant in Eq. A1.4 is equal to zero, giving rise to the local frequency of resonance

$$\omega_{FMR} = \omega_0 + i\alpha\omega_1 . \tag{A1.9}$$

If instead the magnetization oscillations are driven ($h_B \neq 0$), Eq. A1.2 can be rearranged into the form

$$\begin{pmatrix} m_x \\ m_y \end{pmatrix} = \begin{pmatrix} \dfrac{\gamma M_S\left[\gamma\left(H_{z0B} + 4\pi M_S N_{yy}^{\ eff} - 4\pi N_{zz}^{\ eff} M_S\right) + i\alpha\omega\right]}{\left(-\omega^2 + 2i\alpha\omega_1\omega + \omega_0^{\ 2}\right)} & \dfrac{\gamma M_S\left(i\omega - 4\pi\gamma M_S N_{xy}^{\ eff}\right)}{\left(-\omega^2 + 2i\alpha\omega_1\omega + \omega_0^{\ 2}\right)} \\ \dfrac{-\gamma M_S\left(i\omega + 4\pi\gamma M_S N_{yx}^{\ eff}\right)}{\left(-\omega^2 + 2i\alpha\omega_1\omega + \omega_0^{\ 2}\right)} & \dfrac{\gamma M_S\left[\gamma\left(H_{z0B} + 4\pi M_S N_{xx}^{\ eff} - 4\pi N_{zz}^{\ eff} M_S\right) + i\alpha\omega\right]}{\left(-\omega^2 + 2i\alpha\omega_1\omega + \omega_0^{\ 2}\right)} \end{pmatrix} \begin{pmatrix} h_{x,B} \\ h_{y,B} \end{pmatrix} \tag{A1.10}$$

which simplifies to give the elements of the modified Polder susceptibility tensor shown in Eqs. 4.16 – 4.17.

APPENDIX 2

Fitting the frequency spectra characterising the biased Permalloy T-junction structure

In Chapter 5.2, magnetization dynamics across the T-junction structure was excited using a broadboand stimulus, allowing the corresponding frequency spectra to be recorded in the arm and leg of the T-junction. Here, the procedure by which the frequency spectra were fitted is outlined in detail.

To estimate the local frequency of resonance f_{FMR} and the full-width half-maximum σ, each frequency spectra $S(f)$ recorded from the leg and arm of the T-junction was fitted to a normalized Lorentzian distribution, as given by

$$S(f) = \frac{1}{\pi\sigma} \cdot \frac{S_0}{1 + \left(\dfrac{f - f_{FMR}}{\sigma}\right)^2} \tag{A2.1}$$

shere S_0 is the amplitude of the frequency spectrum. This fitting procedure was implemented for all spectra presented in Fig. 5.3, and the results are shown in Fig. A2.1 (the black circles correspond to the data points $S(f)$, and the line corresponds to the fitted Lorentzian distribution).

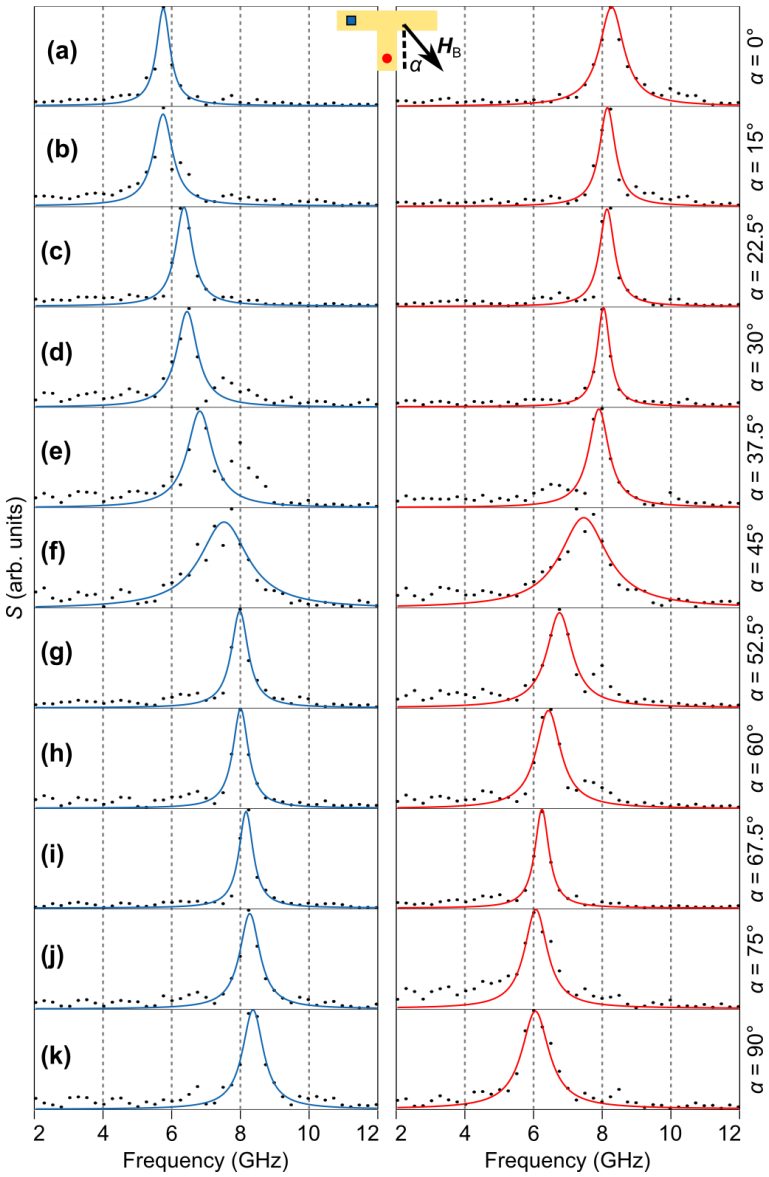

Fig. A2.1 The frequency spectra (black circles) recorded when the probing spot was positioned above the leg (left column) and arm (right column) of the T-junction. The line shown in all panels corresponds to the fitted Lorentzian function, described by Eq. A2.1. **(a)-(k)** The frequency spectra acquired with different orientation α of the bias magnetic field $\boldsymbol{H}_B$ = 500 Oe as indicated, relative to the leg of the T-junction. Note all signals and their fits have been normalized.

APPENDIX 3

Data acquired from TROPSOM measurements of a 20 nm thick Permalloy film

The figures presented in this appendix show the entire signals discussed in Chapter 7.1.

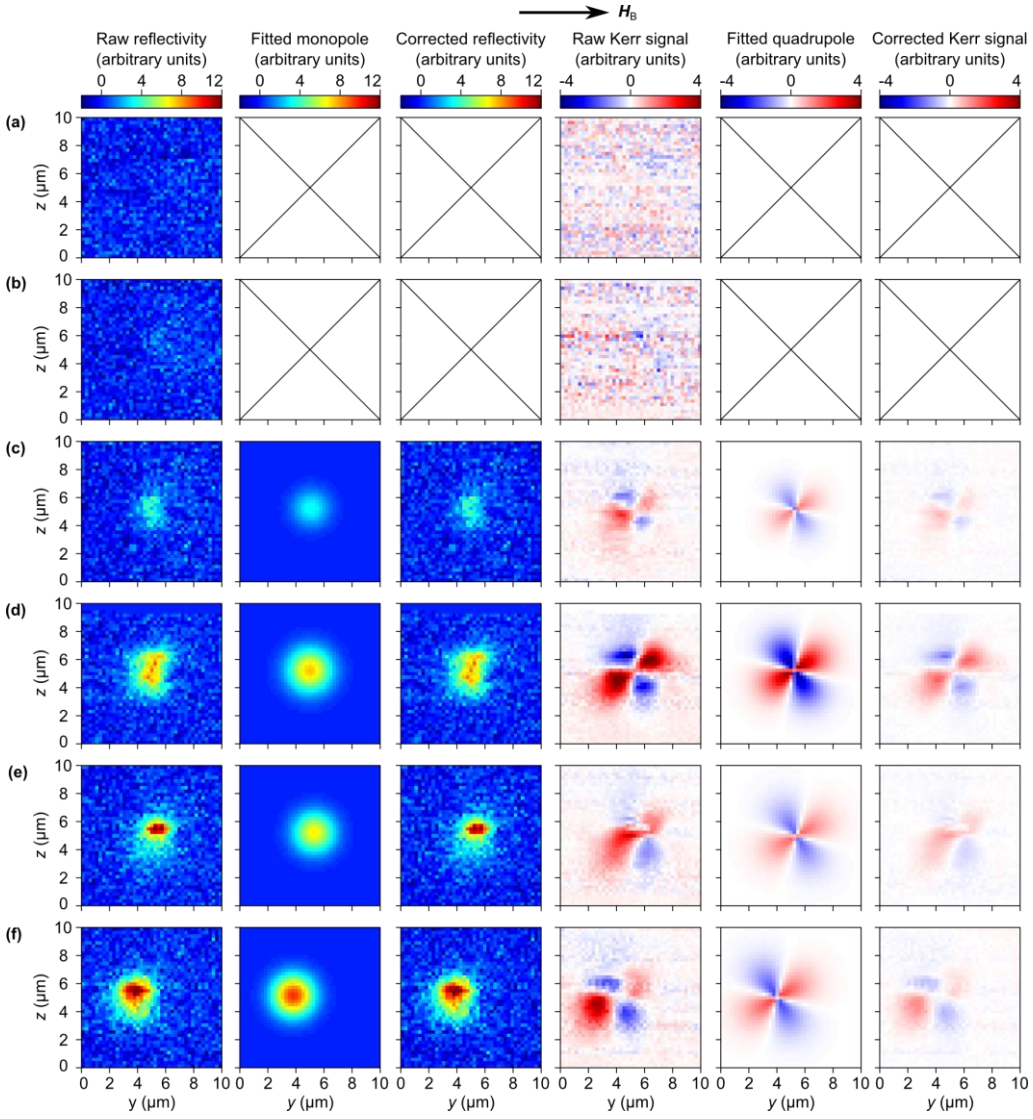

Fig. A3.1 Images acquired using the TROPSOM system for a 20 nm-thick Permalloy film, along with the corresponding surface fits, at time delays **(a)** -1.0 ps, **(b)** 0.0 ps, **(c)** 400 fs, **(d)** 667 fs, **(e)** 767 fs and **(f)** 800 fs. The reflectivity / Kerr signals were fitted using a monopolar / quadrupolar surface as defined by Eq. 7.1 / Eq. 7.2, and the "corrected" signal shows the raw signal but with a fitted plane subtracted.

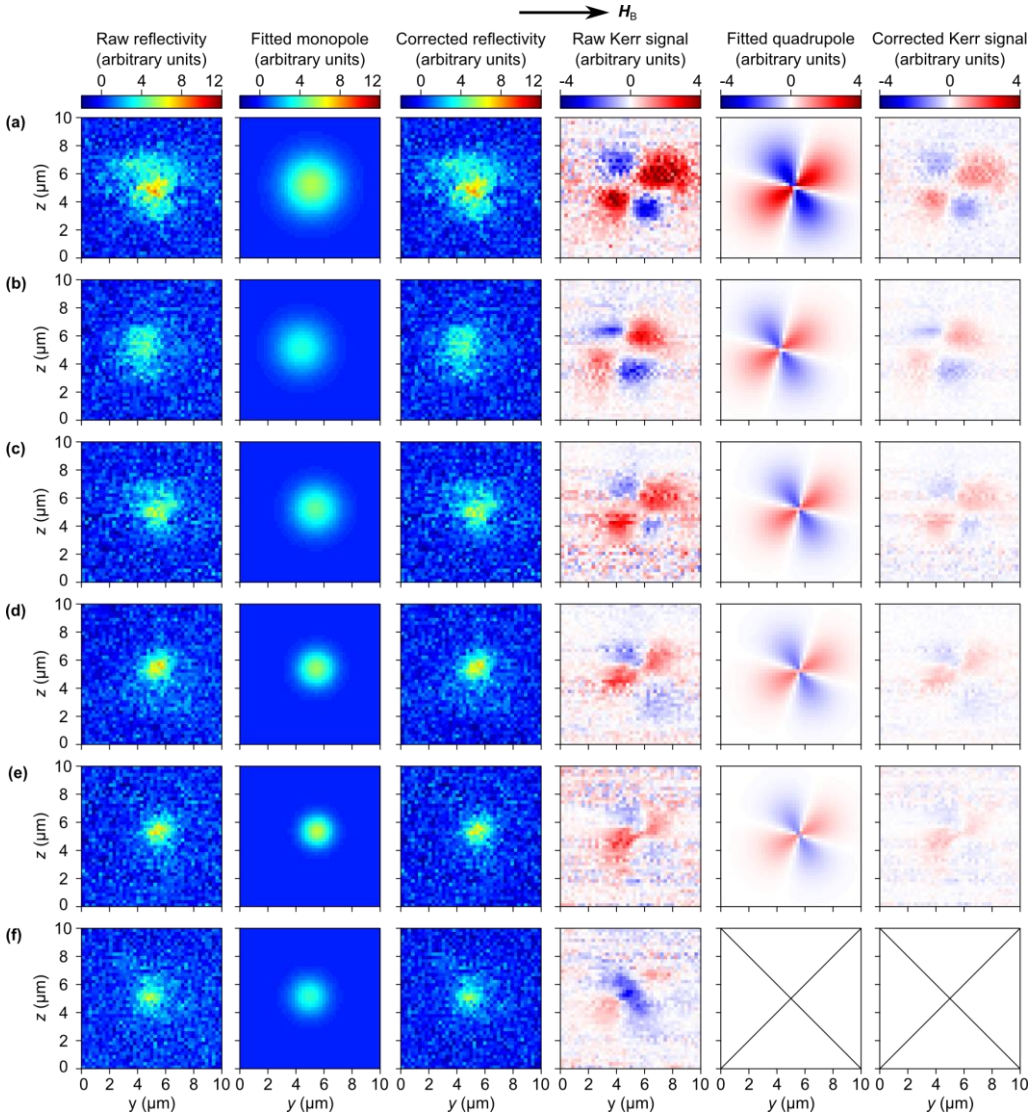

Fig. A3.2 Images acquired using the TROPSOM system for a 20 nm-thick Permalloy film, along with the corresponding surface fits, at time delays **(a)** 1.0 ps, **(b)** 1.33 ps, **(c)** 1.5 ps, **(d)** 1.75 ps, **(e)** 2.0 ps and **(f)** 2.5 ps. The reflectivity / Kerr signals were fitted using a monopolar / quadrupolar surface as defined by Eq. 7.1 / Eq. 7.2, and the "corrected" signal shows the raw signal but with a fitted plane subtracted.

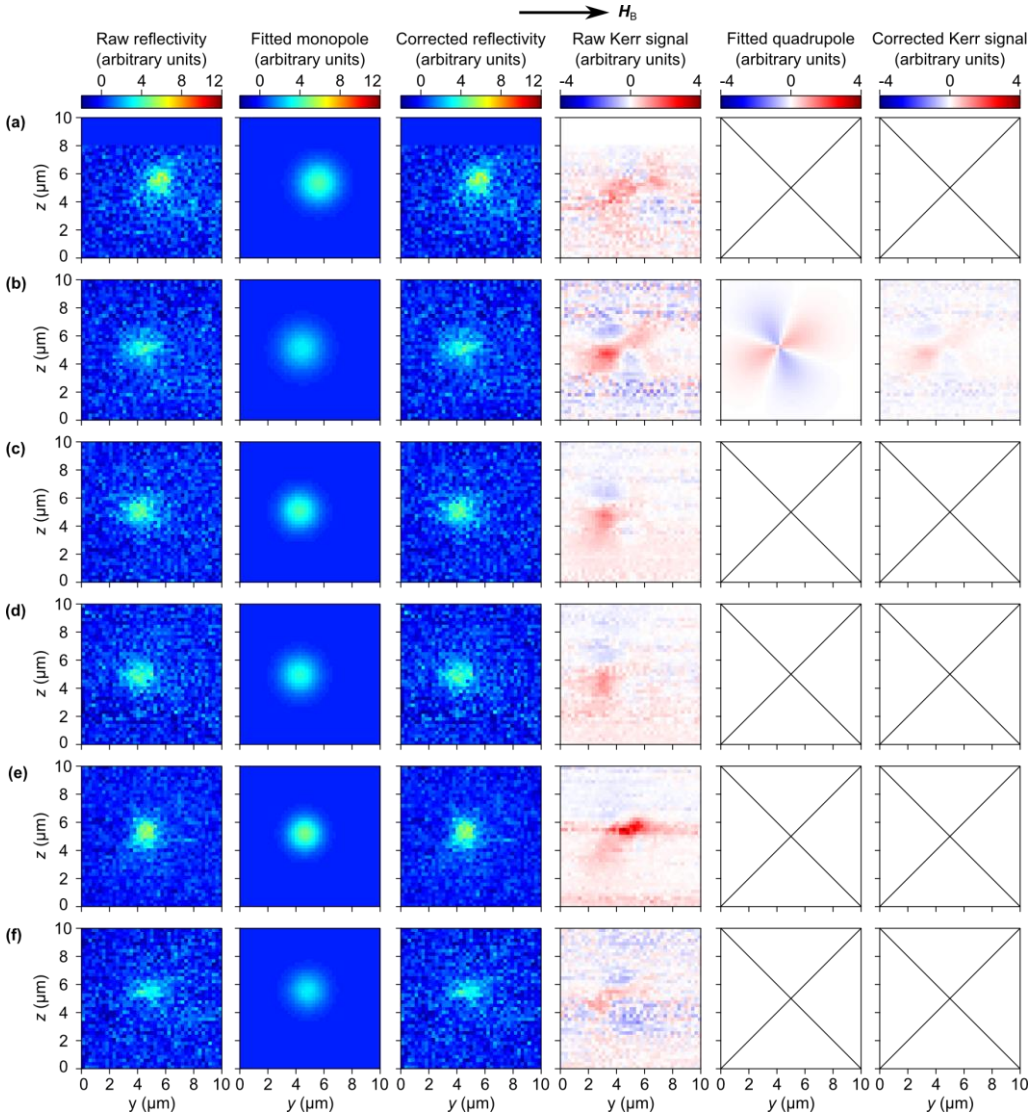

Fig. A3.3 Images acquired using the TROPSOM system for a 20 nm-thick Permalloy film, along with the corresponding surface fits, at time delays **(a)** 3.0 ps, **(b)** 4.0 ps, **(c)** 6.0 ps, **(d)** 8.0 ps, **(e)** 10.0 ps and **(f)** 40.0 ps. The reflectivity / Kerr signals were fitted using a monopolar / quadrupolar surface as defined by Eq. 7.1 / Eq. 7.2, and the "corrected" signal shows the raw signal but with a fitted plane subtracted.

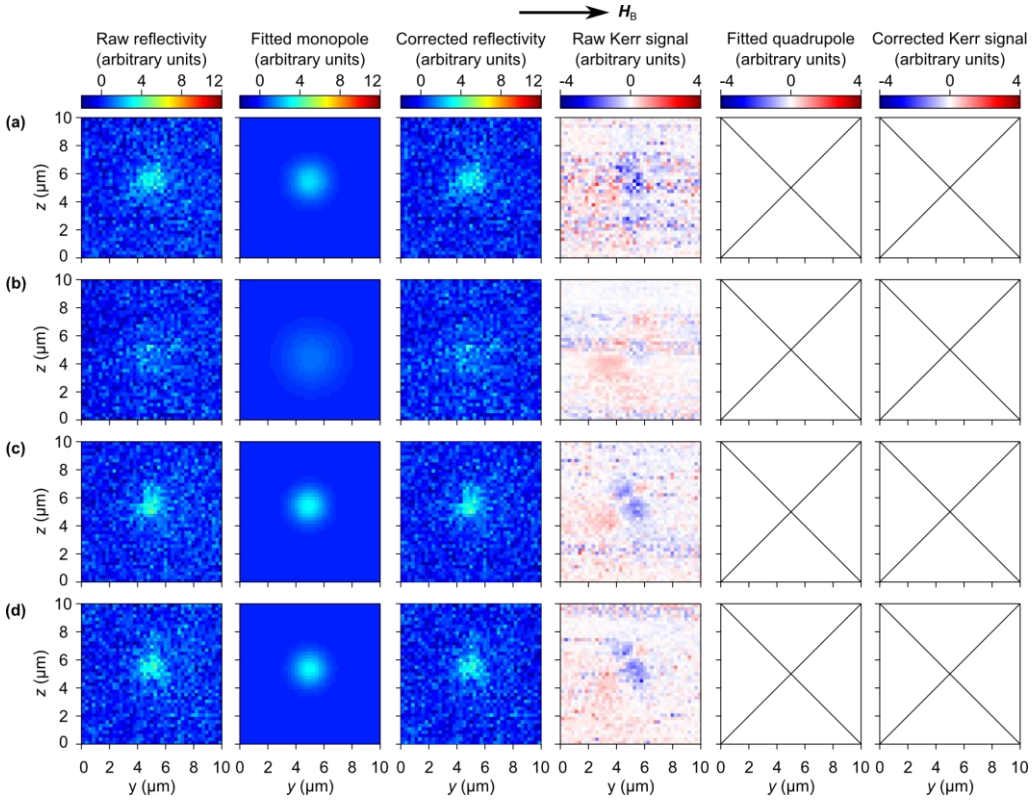

Fig. A3.4 Images acquired using the TROPSOM system for a 20 nm-thick Permalloy film, along with the corresponding surface fits, at time delays **(a)** 75.0 ps, **(b)** 100.0 ps, **(c)** 150.0 ps and **(d)** 200.0 ps. The reflectivity / Kerr signals were fitted using a monopolar / quadrupolar surface as defined by Eq. 7.1 / Eq. 7.2, and the "corrected" signal shows the raw signal but with a fitted plane subtracted.

APPENDIX 4

Data acquired from TROPSOM measurements of a 50 nm-thick Permalloy film

The figures presented in this appendix show the entire signals discussed in chapter 7.2.

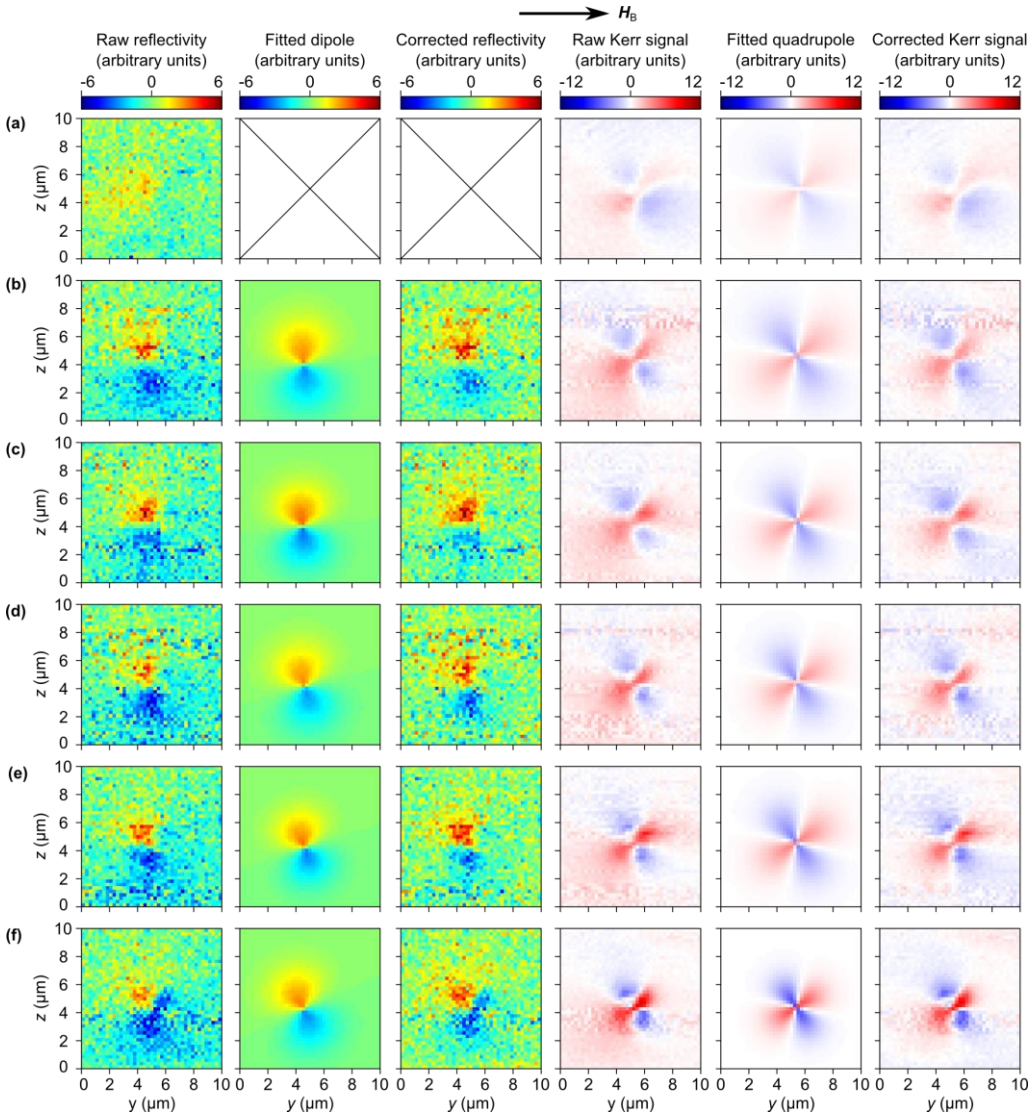

Fig. A4.1 Images acquired using the TROPSOM system for a 50 nm-thick Permalloy film, along with the corresponding surface fits, at time delays **(a)** -40.0 ps, **(b)** 0.0 ps, **(c)** 1.0 ps, **(d)** 2.0 ps, **(e)** 3.0 ps and **(f)** 4.0 ps. The reflectivity / Kerr signals were fitted using a dipolar / quadrupolar surface as defined by Eq. 7.3 / Eq. 7.2, and the "corrected" signal shows the raw signal but with a fitted plane subtracted.

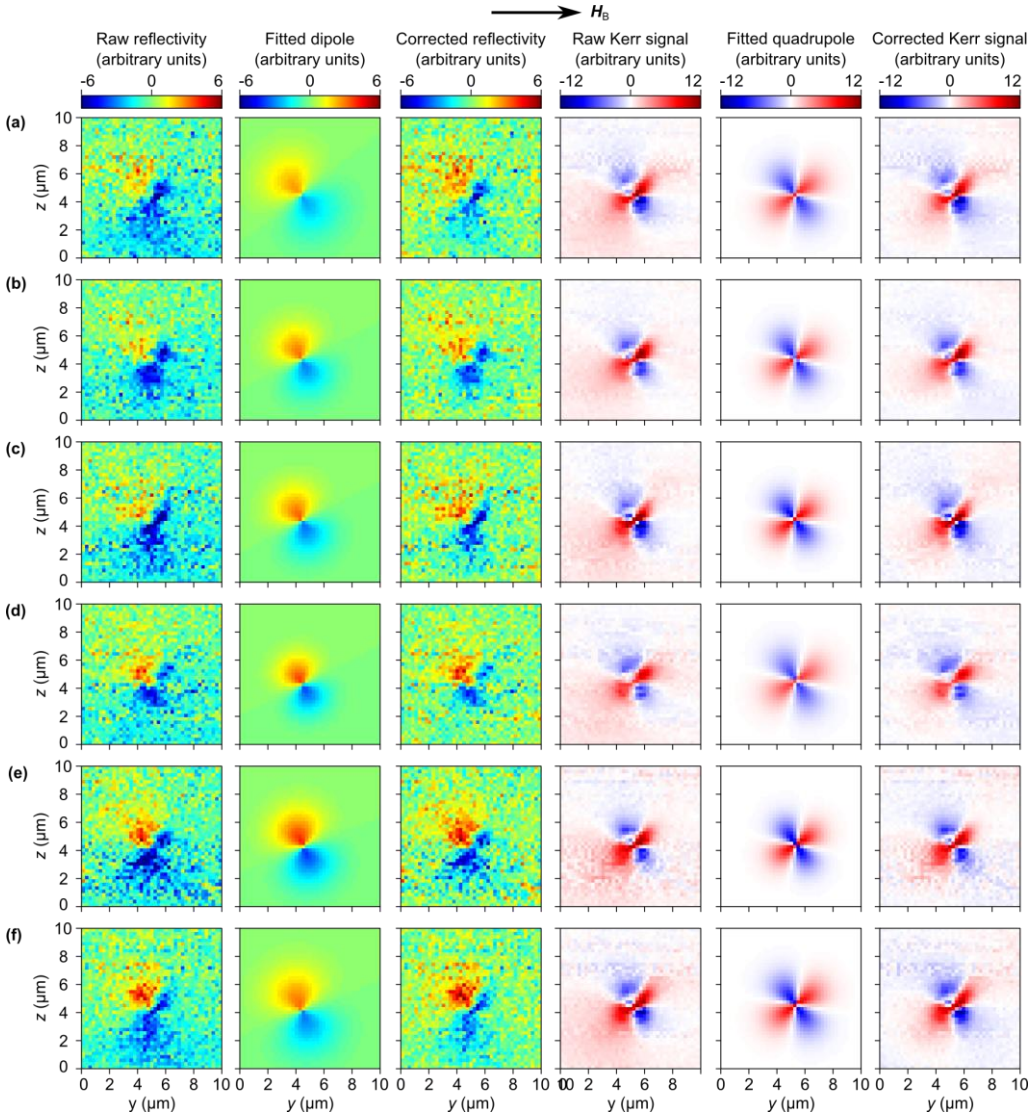

Fig. A4.2 Images acquired using the TROPSOM system for a 50 nm-thick Permalloy film, along with the corresponding surface fits, at time delays **(a)** 5.0 ps, **(b)** 6.0 ps, **(c)** 7.0 ps, **(d)** 8.0 ps, **(e)** 9.0 ps and **(f)** 10.0 ps. The reflectivity / Kerr signals were fitted using a dipolar / quadrupolar surface as defined by Eq. 7.3 / Eq. 7.2, and the "corrected" signal shows the raw signal but with a fitted plane subtracted.

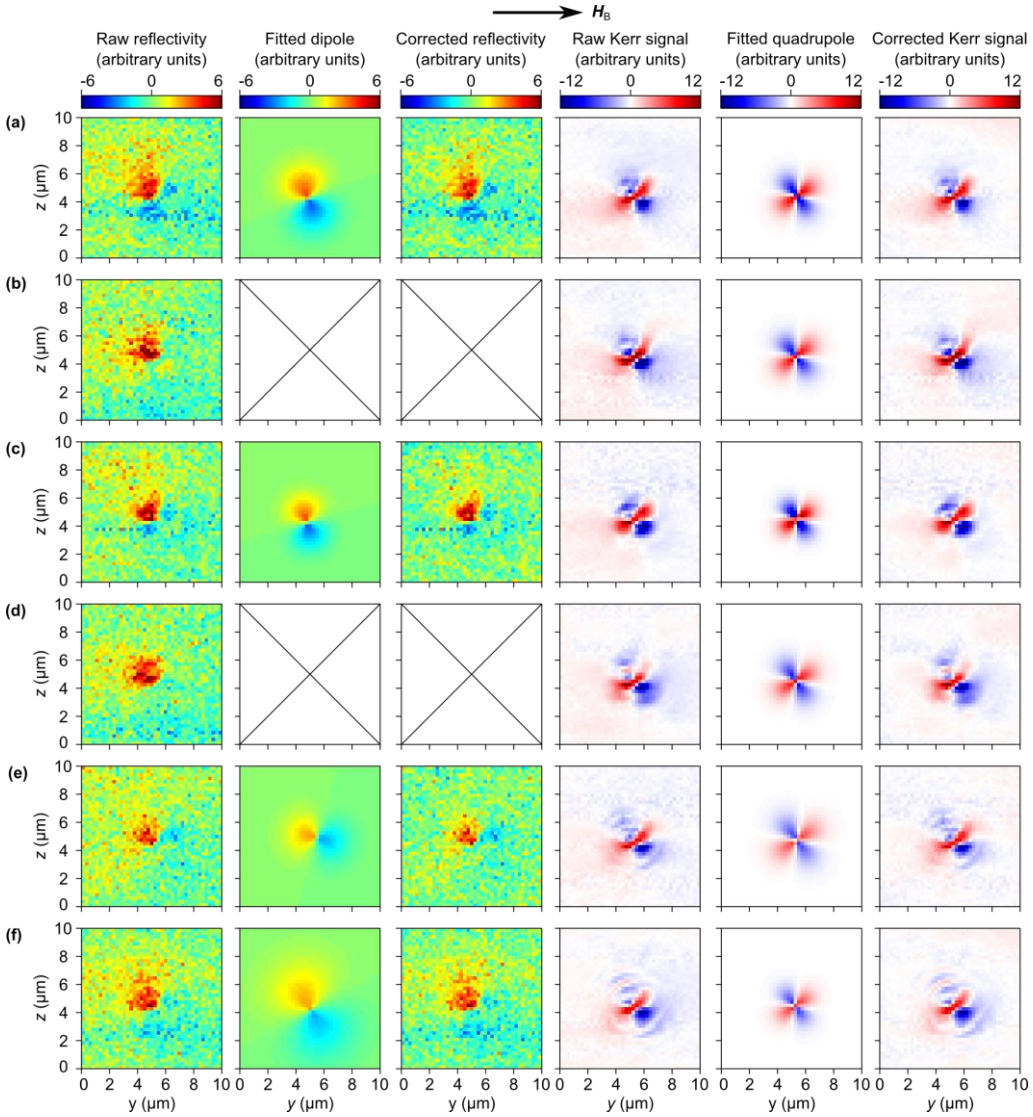

Fig. A4.3 Images acquired using the TROPSOM system for a 50 nm-thick Permalloy film, along with the corresponding surface fits, at time delays **(a)** 18.0 ps, **(b)** 76.0 ps, **(c)** 132.0 ps, **(d)** 188.0 ps, **(e)** 244.0 ps and **(f)** 300.0 ps. The reflectivity / Kerr signals were fitted using a dipolar / quadrupolar surface as defined by Eq. 7.3 / Eq. 7.2, and the "corrected" signal shows the raw signal but with a fitted plane subtracted.

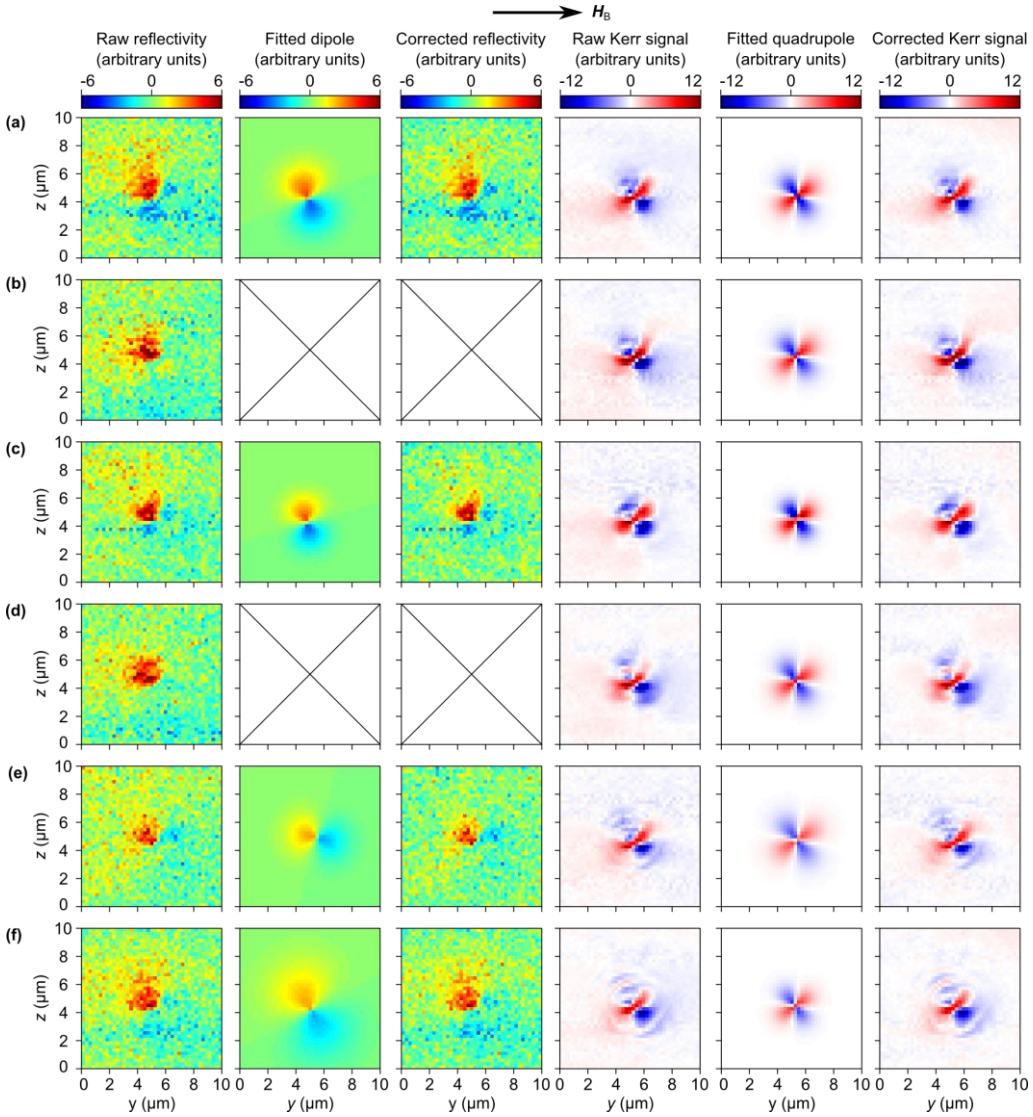

Fig. A4.4 Images acquired using the TROPSOM system for a 50 nm-thick Permalloy film, along with the corresponding surface fits, at time delays **(a)** 356.0 ps, **(b)** 412.0 ps, **(c)** 468.0 ps, **(d)** 524.0 ps, **(e)** 580.0 ps and **(f)** 636.0 ps. The reflectivity / Kerr signals were fitted using a dipolar / quadrupolar surface as defined by Eq. 7.3 / Eq. 7.2, and the "corrected" signal shows the raw signal but with a fitted plane subtracted.

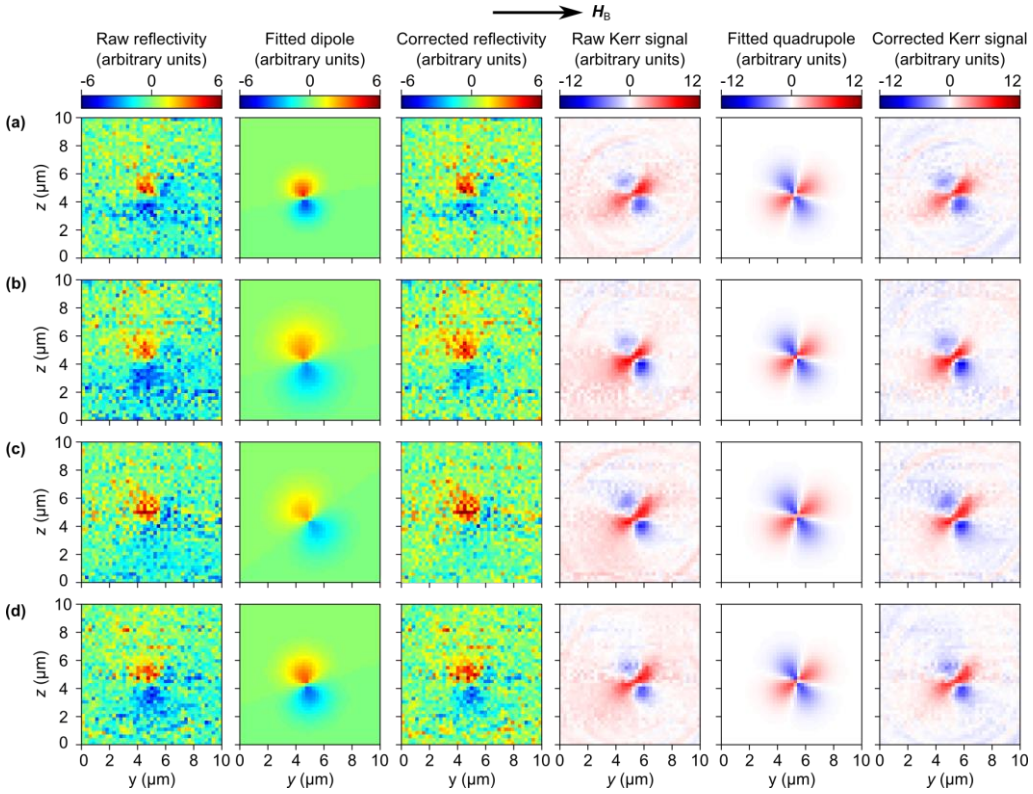

Fig. A4.5 Images acquired using the TROPSOM system for a 50 nm-thick Permalloy film, along with the corresponding surface fits, at time delays **(a)** 692.0 ps, **(b)** 748.0 ps, **(c)** 804.0 ps and **(d)** 860.0 ps. The reflectivity / Kerr signals were fitted using a dipolar / quadrupolar surface as defined by Eq. 7.3 / Eq. 7.2, and the "corrected" signal shows the raw signal but with a fitted plane subtracted.

[1] C. S. Davies, A. V. Sadovnikov, S. V. Grishin, Yu. P. Sharaevskii, S. A. Nikitov and V. V. Kruglyak, "Generation of propagating spin waves from regions of increased dynamic demagnetizing field near magnetic antidots" *Appl. Phys. Lett.* **107**, 162401 (2015).

[2] C. S. Davies and V. V. Kruglyak, "Generation of propagating spin waves from edges of magnetic nanostructures pumped by uniform microwave magnetic field" *IEEE. Trans. Magn.* **52**, 2300504 (2016).

[3] C. S. Davies, A. Francis, A. V. Sadovnikov, S. V. Chertopalov, M. T. Bryan, S. V. Grishin, D. A. Allwood, Yu. P. Sharaevskii, S. A. Nikitov and V. V. Kruglyak, "Towards graded-index magnonics: Steering spin waves across magnonic networks" *Phys Rev. B* **92**, 020408(R) (2015).

[4] C. S. Davies and V. V. Kruglyak, "Graded-index magnonics" *Low Temp. Phys.* **41**, 760 (2015).

[5] A. V. Sadovnikov, C. S. Davies, S. V. Grishin, V. V. Kruglyak, D. V. Romanenko, Yu. P. Sharaevskii and S. A. Nikitov, "Magnonic beam splitter: The building block of parallel magnonic circuitry" *Appl. Phys. Lett.* **106**, 192406 (2015).

[6] G. E. Moore, "Cramming more components onto integrated circuits" *Electronics* **38**, 8 (1965).

[7] G. E. Moore, "Progress in Digital Integrated Electronics" *IEDM Tech. Digest* 11 (1975).

[8] M. Mitchell Waldrop, "The chips are down for Moore's law" *Nature* **530**, 144 (2016).

[9] Intel Corp. "Form 10-K: Annual Report" (Intel, California, 2016).

[10] http://www.intel.com/content/www/us/en/silicon-innovations/intel-tick-tock-model-general.html, accessed 31/05/2016.

[11] http://www.itrs2.net, accessed 31/05/2016.

[12] D. Nikinov and I. Young, "Overview of beyond-CMOS devices and a uniform methodology for their benchmarking" *Proc. IEEE* **101**, 2498 (2013).

[13] S. A. Wolf, D. D. Awschalom, R. A. Buhrman, J. M. Daughton, S. Von Molnar, M. L. Roukes, A. Yu. Chtchelkanova and D. M. Treger, "Spintronics: A spin-based electronics vision for the future" *Science* **294**, 1488 (2001).

[14] S. Dutta and S. K. Pati, "Novel properties of graphene nanoribbons: a review" *J. Mater. Chem.* **20**, 8207 (2010).

[15] J.-G. Zhu and C. Park, "Magnetic Tunnel Junctions" *Mater. Today* **9**, 36 (2006).

[16] Y. V. Pershin and M. Di Ventra, "Memory effect in complex materials and nanoscale systems" *Adv. Phys.* **60**, 145 (2011).

[17] M. C. Petty, M. R. Bryce and D. Bloor, "Introduction to Molecular Electronics" (Oxford University Press, New York, 1995).

[18] V. V. Kruglyak, S. O. Demokritov and D. Grundler, "Magnonics" *J. Phys. D: Appl. Phys.* **43**, 26030 (2010).

[19] A. V. Chumak, V. I. Vasyuchka, A. A. Serga and B. Hillebrands, "Magnon spintronics" *Nat. Phys.* **11**, 3347 (2015).

[20] A. Khitun and K. L. Wang, "Non-volatile magnonic logic circuits engineering" *J. Appl. Phys.* **110**, 034306 (2011).

[21] M. Krawczyk and D. Grundler, "Review and prospects of magnonic crystals and devices with reprogrammable band structure" *J. Phys. Condens. Matter* **26**, 123202 (2014).

[22] S. Bonetti, R. Kukreja, Z. Chen, F. Macià, J. M. Hernàndez, A. Eklund, D. Backes, J. Frisch, J. Katine, G. Malm, S. Urazhdin, A. D. Kent, J. Stöhr, H. Ohldag and H. A. Dürr, "Direct observation and imaging of a spin-wave soliton with *p*-like symmetry" *Nat. Commun.* **6**, 8889 (2015).

[23] T. Sebastian, T. Brächer, P. Pirro, A. A. Serga, B. Hillebrands, T. Kubota, H. Naganuma, M. Oogane and Y. Ando, "Nonlinear Emission of Spin-Wave Caustics from an Edge Mode of a Microstructured $Co_2Mn_{0.6}Fe_{0.4}Si$ Waveguide" *Phys. Rev. Lett.* **110**, 067201 (2013).

[24] E. Schlömann, "Generation of Spin Waves in Nonuniform Magnetic Fields. I. Conversion of Electromagnetic Power into Spin-Wave Power and Vice Versa" *J. Appl. Phys.* **35**, 159 (1964).

[25] P. Langevin, "Sur la théorie du magnétisme" *Annales de Chem. et Phys.* **5**, 70 (1905).

[26] L. F. Bates, "Modern Magnetism" (Cambridge University Press, London, 1961).

[27] A.H. Morrish, "The Physical Principles of Magnetism" (John Wiley & Sons, New York, 1965).

[28] A. Aharoni, "Introduction to the Theory of Ferromagnetism" (Oxford University Press, New York, 2000).

[29] D. Jiles, "Introduction to Magnetism and Magnetic Materials" (Chapman & Hall, Suffolk, 1998).

[30] P. Weiss, "La variation du ferromagnetisme du temperature" *Compt. Rend.* **143**, 1136 (1906).

[31] H. -J. Van Leeuwen, "Problèmes de la théorie électronique du magnétisme" *J. Phys. Radium*, **2** 361 (1921).

[32] R. P. Feynman, R. B. Leighton and M. Sands, "The Feynman lectures on Physics: Vol. 2" (Addison-Wesley, Redwood City, 1965).

[33] N. Bohr, "On the Constitution of Atoms and Molecules" *Phil. Mag.* **26**, 1 (1913).

[34] A. Sommerfeld, "Zur Quantentheorie der Spektrallinien" *Annalen. Physik* **51**, 125 (1916).

[35] P. Zeeman, "On the Influence of Magnetism on the Nature of the Light emitted by a Substance" *Phil. Mag.* **43**, 226 (1897).

[36] F. Tyler, "The magnetization-temperature curves of iron, cobalt, and nickel" *Phil. Mag.* **11**, 596 (1931).

[37] W. Heitler and F. London, "Wechselwirkung neutraler Atome und homöopolare Bindung nach der Quantenmechanik" *Z. Physik* **44**, 619 (1927).

[38] W. Heisenberg, "Zur Theorie des Ferromagnetismus" *Z. Physik* **49**, 619 (1928).

[39] L. Néel, "Magnetism and the local molecular field" Nobel Lectures, Physics 1963-1970 (1970).

[40] L. F. Bates and A. Baqi, "The magnetic properties of chromium" *Proc. Phys. Soc.* **48**, 781 (1936).

[41] F. Heusler, "Über magnetische Manganlegierungen" *Veh. Dtsch. Phys. Ges.* **12**, 219 (1903).

[42] C. Felser and B. Hillebrands, "Cluster issue on Heusler compounds and devices" *J. Phys. D*: *Appl. Phys.* **42**, 080301 (2009), and the references therein.

[43] H. Bethe, "Elektronentheorie der Metalle" *Handb. d. Phys.* **24**, 595 (1933).

[44] F. Bloch, "Zur Theorie des Ferromagnetismus" *Z. Physik* **61**, 206 (1930).

[45] A. Haugh, "Theoretical Solid State Physics" (Springer, New York, 1972).

[46] H. A. Kramers, "L'interaction Entre les Atomes Magnétogènes dans un Cristal Paramagnétique" *Physica* **1**, 182 (1934).

[47] P. W. Anderson, "Antiferromagnetism. Theory of Superexchange Interaction" Phys. Rev. 79, 350 (1950).

[48] W. F. Brown, "Micromagnetics" (J. Wiley, New York, 1963).

[49] C. Kittel, "Physical Theory of Ferromagnetic Domains" *Rev. Mod. Phys.* **21**, 541 (1949).

[50] I. Dzyaloshinsky, "A Thermodynamic Theory of "Weak" Ferromagnetism of Antiferromagnetics" *J. Phys. Chem. Solids* **4**, 251 (1958).

[51] S. O. Demokritov (ed.) "Spin Wave Confinement" (Pan Stanford Publishing, Singapore, 2009).

[52] G. S. Abo, Y. K. Hong, J. Park, J. Lee, W. Lee and B. C. Choi, "Definition of Magnetic Exchange Length" *IEEE Trans. Magn.* **49**, 4937 (2013).

[53] J. C. Maxwell, "A Treatise on Electricity and Magnetism" (Clarendon Press, London, 1878).

[54] J. A. Osborn, "Demagnetizing Factors of the General Ellipsoid" *Phys. Rev.* **67**, 11 (1945).

[55] J. Crangle and G. M. Goodman, "The Magnetization of Pure Iron and Nickel" *Proc. Roy. Soc. Lond. A.* **321**, 477 (1971).

[56] K. Vogt, J. E. Pearson, T. Sebastian, S. D. Bader, B. Hillebrands, A. Hoffmann and H. Schultheiss, "Realization of a spin-wave multiplexer" *Nat. Commun.* **5**, 3727 (2014).

[57] N. Yu. Grigoryeva, D. A. Popov and B. A. Kalinikos, "Dipole-Exchange Spin Wave Spectrum in an Anisotropic Ferromagnetic Waveguide with a Rectangular Cross Section" *Phys. Solid State* **56**, 1806 (2014).

[58] R. M. Bozorth, "The Permalloy Problem" *Rev. Mod. Phys.* **25**, 42 (1953).

[59] W. Stoecklein, S. S. P. Parkin and J. C. Scott, "Ferromagnetic resonance studies of exchange-biased Permalloy thin films" *Phys. Rev. B* **38**, 6847 (1988).

[60] I. Turek, J. Kudrnovsky and V. Drchal, "Nonlocal torque operators in ab initio theory of the Gilbert damping in random ferromagnetic alloys" *Phys. Rev. B* **92**, 214407 (2015).

[61] M. A. W. Schoen, D. Thonig, M. L. Schneider, T. J. Silva, H. T. Nembach, O. Eriksson, O. Karis and J. M. Shaw, "Ultra-low damping of a metallic ferromagnet" *Nat. Phys.* **12**, 839 (2016).

[62] A. A. Serga, A. V. Chumak and B. Hillebrands, "YIG magnonics" *J. Phys. D: Appl. Phys.* **43**, 264002 (2010).

[63] V. Cherepanov, I. Kolokolov and V.S. L'vov, "The Saga of YIG, or Spectra, Thermodynamics and Relaxation of Magnons in Complex Magnets" *Phys. Rep. – Rev. Sec. Phys. Lett.* **229**, 81 (1993).

[64] S. Klingler, A. V. Chumak, T. Mewes, B. Khodadadi, C. Mewes, C. Dubs, O.Surzhenko, B. Hillebrands and A. Conca, "Measurements of the exchange stiffness of YIG films using broadband ferromagnetic resonance techniques" J. Phys. D: Appl. Phys. 48, 015001 (2015).

[65] A. G. Gurevich and G. A. Melkov, "Magnetization Oscillations and Waves" (Chemical Rubber Corp., New York, 1996).

[66] E. H. Lock, "The properties of isofrequency dependences and the laws of geometrical optics" *Phys. Usp.* **51**, 375 (2008).

[67] L. D. Landau and E. Lifshitz, "Theory of the dispersion of magnetic permeability in ferromagnetic bodies" *Phys. Z. Sowjetunion* **8**, 153 (1935).

[68] D. A. Garanin, "Fokker-Planck and Landau-Lifshitz-Bloch equations for classical ferromagnets" *Phys. Rev. B* **55**, 3050 (1997).

[69] U. Atxitia, P. Nieves, and O. Chubykalo-Fesenko, "Landau-Lifshitz-Bloch equation for ferrimagnetic materials" *Phys. Rev. B* **86**, 104414 (2012).

[70] L. D. Landau and E. M. Lifshitz, "Fluid Mechanics, Course of Theoretical Physics" Vol. **6** (Addison-Wesley, Reading, 1959).

[71] M. Bixon and R. Zwanzig, "Boltzmann-Langevin Equation and Hydrodynamic Fluctuations" *Phys. Rev.* **187**, 267 (1969).

[72] J. B. Bell, A. L. Garcia, and S. A. Williams, "Numerical Methods for the Stochastic Landau-Lifshitz Navier-Stokes Equations" *Phys. Rev. E* **76**, 016708 (2007).

[73] J. C. Slonczewski, "Current-driven excitation of magnetic multilayers" *J. Magn. Magn. Mater.* **159**, L1 (1996).

[74] J. Xiao, A. Zangwill, and M. D. Stiles, "Macrospin models of spin transfer dynamics" *Phys. Rev. B*, **72**, 014446 (2005).

[75] H. Suhl, "Theory of the magnetic damping constant" *IEEE Trans. Magn.* **34**, 1834 (1998).

[76] B. Astie and J. Degauque, "Magnetoelastic damping of iron in the presence of synchronous alternating magnetic field" *Nuovo Cimento B*, **33**, 414 (1976).

[77] S.A. Mahmoud and M.A. Semary, "Magnetomechemical damping of nickel" *Mat. Sci. Eng.* **60**, L9 (1983).

[78] V. Kambersky and C. E. Patton, "Spin-wave relaxation and phenomenological damping in ferromagnetic resonance" *Phys. Rev. B* **11**, 2668 (1975).

[79] B. Heinrich, R. Urban and G. Woltersdorf, "Magnetic relaxation in metallic films: Single and multilayer structures" *J. Appl. Phys.* **91**, 7523 (2002).

[80] R. Kikuchi, "On the Minimum of Magnetization Reversal Time" *J. Appl. Phys.* **27**, 1352 (1956).

[81] T. L. Gilbert, "A Lagrangian formulation of the gyromagnetic equation of the magnetic field" *Phys. Rev.* **100**, 1243 (1955).

[82] S. O. Demokritov, B. Hillebrands and A. N. Slavin, "Brillouin light scattering studies of confined spin waves" *Phys. Rep.* **348**, 441 (2001).

[83] J. W. Fleischer, M. Segev, N. K. Efremidis, and D. N. Christodoulides, "Observation of two-dimensional discrete solitons in optically induced nonlinear photonic lattices" *Nature* 422, 147 (2003).

[84] M. B. Jungfleisch, W. Zhang, J. Sklenar, J. Ding, W. Jiang, H. Chang, F. Y. Fradin, J. E. Pearson, J. B. Ketterson, V. Novosad, M. Wu and A. Hoffmann "Large Spin-Wave Bullet in a Ferrimagnetic Insulator Driven by the Spin Hall Effect" *Phys. Rev. Lett* **116**, 057601 (2016).

[85] G. S. Rushbrooke and P. J. Wood "On the Curie points and high temperature susceptibilities of Heisenberg model ferromagnetics" *Mol. Phys.* **1**, 257 (1958).

[86] A. T. Aldred, "Temperature dependence of the magnetization of nickel" *Phys. Rev. B* **11**, 2597 (1975).

[87] V. G. Bar'yakhtar, "Phenomenological description of relaxation processes in magnetic materials" *Sov. Phys. JETP* **60**, 863 (1984).

[88] G. V. Srotskii and L. V. Kurbatov, "Phenomenological Theory of Ferromagnetic Resonance" (Pergamon Press, Oxford, 1965).

[89] C. Kittel, "Ferromagnetic Resonance" *J. Phys. et radum* **12**, 332 (1951).

[90] B. Heinrich, K. B. Urquhart, A. S. Arrott, J. F. Cochran, K. Myrtle and S. T. Purcell "Ferromagnetic-resonance study of ultrathin bcc Fe(100) films grown epitaxially on fcc Ag(100) substrates" *Phys. Rev. Lett.* **59**, 1756 (1987).

[91] L. R. Walker, "Magnetostatic Modes in Ferromagnetic Resonance" *Phys. Rev.* **105**, 390 (1958).

[92] R. W. Damon and J. R. Eshbach, "Magnetostatic modes of a ferromagnet slab" *J. Phys. Chem. Solids* **19**, 308 (1961).

[93] R. W. Damon and J. R. Eshbach, "Surface Magnetostatic Modes and Surface Spin Waves" *Phys. Rev.* **118**, 5 (1960).

[94] M. J. Hurben and C. E. Patton, "Theory of magnetostatic waves for in-plane magnetized isotropic films" *J. Magn. Magn. Mater.* **139**, 263 (1995).

[95] F. J. Buijnsters, L. J. A. van Tilburg, A. Fasolino and M. I. Katsnelson, "Two-dimensional dispersion of magnetostatic volume spin waves" http://arxiv.org/abs/1602.01362, accessed 20/06/2016.

[96] D. D. Stancil and A. Prabhakar, "Spin Waves: Theory and Applications" (Springer, New York, 2009).

[97] T. Schneider, A. A. Serga, T. Neumann, B. Hillebrands and M. P. Kostylev, "Phase reciprocity of spin-wave excitation by a microstrip antenna" *Phys. Rev. B* **77**, 214411 (2008).

[98] V. E. Demidov, M. P. Kostylev, K. Rott, P. Krzysteczko, G. Reiss and S. O. Demokritov, "Excitation of microwaveguide modes by a stripe antenna" *Appl. Phys. Lett.* **95**, 112509 (2009).

[99] B. A. Kalinikos and A. N. Slavin, "Theory of dipole-exchange spin wave spectrum for ferromagnetic films with mixed exchange boundary conditions" *J. Phys. C* **19**, 7013 (1986).

[100] W. L. Bongianni, "Magnetostatic Propagation in a Dielectric Layered Structure" *J. Appl. Phys.* **43**, 2541 (1972).

[101] A. Barman, V. V. Kruglyak, R. J. Hicken, J. M. Rowe, A. Kundrotaite, J. Scott and M. Rahman, "Imaging the dephasing of spin wave modes in a square thin film magnetic element" *Phys. Rev. B* **69**, 174426 (2004).

[102] V. V. Kruglyak, A. Barman, R. J. Hicken, J. R. Childress and J. A. Katine, "Picosecond magnetization dynamics in nanomagnets: Crossover to nonuniform precession" *Phys. Rev. B* **71**, 220409(R) (2005).

[103] T. W. O'Keeffe and R. W. Patterson, "Magnetostatic surface-wave propagation in finite samples" *J. Appl. Phys.* **49**, 4886 (1978).

[104] J. Jorzick, S. O. Demokritov, B. Hillebrands, M. Bailleul, C. Fermon, K. Y. Guslienko, A. N. Slavin, D. V. Berkov and N. L. Gorn "Spin Wave Wells in Nonellipsoidal Micrometer Size Magnetic Elements" *Phys. Rev. Lett.* **88**, 047204 (2002).

[105] J. P. Park, P. Eames, D. M. Engebretson, J. Berezovsky and P. A. Crowell, "Spatially Resolved Dynamics of Localized Spin-Wave Modes in Ferromagnetic Wires" *Phys. Rev. Lett.* **89**, 277201 (2002).

[106] V. E. Demidov, M. P. Kostylev, K. Rott, P. Krzysteczko, G. Reiss and S. O. Demokritov, "Excitation of microwaveguide modes by a stripe antenna" *Appl. Phys. Lett.* **95**, 112509 (2009).

[107] K. Yu. Guslienko, S. O. Demokritov, B. Hillebrands and A. N. Slavin, "Effective dipolar boundary conditions for dynamic magnetization in thin magnetic stripes" *Phys. Rev. B* **66**, 132402 (2002).

[108] K. Yu. Guslienko and A. N. Slavin, "Boundary conditions for magnetization in magnetic nanoelements" *Phys. Rev. B* **72**, 014463 (2005).

[109] P. Clausen, K. Vogt, H. Schultheiss, S. Schäfer, B. Obry, G. Wolf, P. Pirro, B. Leven and B. Hillebrands, "Mode conversion by symmetry breaking of propagating spin waves" *Appl. Phys. Lett.* **99**, 162505 (2011).

[110] V. E. Demidov, S. O. Demokritov, K. Rott, P. Krzysteczko and G. Reiss, "Nano-optics with spin waves at microwave frequencies" *Appl. Phys. Lett.* **92**, 232503 (2008).

[111] A. Fresnel and F. Arago, "On the action of rays of polarized light upon each other" *Ann. Chem. Phys.* **2**, 288 (1816).

[112] E. Hecht, "Optics" (Addison-Wesley, New York, 2001).

[113] M. Faraday, "Experimental researches in electricity. Twentieth Series" *Phil. Trans. R. Soc. Lond.* **136**, 21 (1846).

[114] A. Kundt, "On the Electromagnetic Rotation of the Plane of Polarization of Light by means of Iron, Cobalt, and Nickel" *Phil. Mag.* **18**, 308 (1884).

[115] J. Kerr, "On rotation of the Plane of Polarization by reflection from the pole of a magnet" *Phil. Mag.* **3**, 321 (1877).

[116] M. I. Kaganov, I. M. Lifshitz and L. V. Tanatarov, "Relaxation between electrons and the crystalline lattice" *Sov. Phys.-JETP* **4**, 173 (1957).

[117] E. Beaurepaire, J. C. Merle, A. Daunois, and J. Y. Bigot, "Ultrafast spin dynamics in ferromagnetic nickel" *Phys. Rev. Lett.* **76**, 4250 (1996).

[118] A. K. Zvezdin and V. A. Kotov, "Modern magneto-optics and magneto-optical materials: Studies in Condensed Matter" (Taylor and Francis Group, New York, 1997).

[119] L. Onsager, "Reciprocal Relations in Irreversible Processes. I." *Phys. Rev.* **37**, 405 (1931).

[120] L. Onsager, "Reciprocal Relations in Irreversible Processes. II." *Phys. Rev.* **38**, 2265 (1931).

[121] J. Wu, J.R. Moore and R.J. Hicken, "Optical Pump-Probe Studies of the Rise and Damping of Ferromagnetic Resonance Oscillations in a Thin Fe Film" *J. Magn. Magn. Mater.* **222**, 189 (2000).

[122] S.I. Anisimov, B.L. Kapeliovich and T.L. Perel'man, "Electron emission from metal surfaces exposed to ultrashort laser pulses" *Sov. Phys. JETP* **39**, 375 (1974).

[123] T.Q. Qiu and C.L. Tien, "Heat transfer mechanisms during short-pulse laser heating of metals" *ASME J. Heat Transfer*, **115**, 835 (1993).

[124] J.K. Chen and J.E. Beraun, "Numerical study of ultrashort laser pulse interactions with metal films" *Numer. Heat Transfer A* **40**, 1 (2001).

[125] J.K. Chen, D.Y. Tzou and J.E. Beraun, "A semi-classical two-temperature model for ultrafast laser heating" *Int. J. Heat Mass Transf.* **49**, 307 (2006).

[126] V. V. Kruglyak, "Femtosecond Optical Pump-Probe Investigations of Ultrafast Electron and Spin Dynamics in Metals" (Ph.D. Thesis, University of Exeter, 2004).

[127] J. Faure, J. Mauchain, E. Papalazarou, M. Marsi, D. Boschetto, I. Timrov, N. Vast, Y. Ohtsubo, B. Arnaud and L. Perfetti "Direct observation of electron thermalization and electron-phonon coupling in photoexcited bismuth" *Phys. Rev. B* **88**, 075120 (2013).

[128] M. van Kampen, "Ultrafast spin dynamics in ferromagnetic metals" (Ph.D. Thesis, Eindhoven University of Technology, 2003).

[129] D. Rudolf "Femtosecond Spin Dynamics in Magnetic Multilayers Employing High Harmonics of Laser Radiation" (Ph.D. Thesis, Jülich Research Center, 2013).

[130] D. Chumakov, J. McCord, R. Schäfer, L. Schultz, H. Vinzelberg, R. Kaltofen, and I. Mönch "Nanosecond time-scale switching of permalloy thin film elements studied by wide-field time-resolved Kerr microscopy" *Phys. Rev. B* **71**, 014410 (2005).

[131] T. C. Davison, "Time-Resolved Imaging of Magnetisation Dynamics in Nanoscale Magnonic Structures" (Ph.D. Thesis, University of Exeter, 2012).

[132] Y. Au, M. Dvornik, T. Davison, E. Ahmad, P. S. Keatley, A. Vansteenkiste, B. Van Waeyenberge and V. V. Kruglyak "Direct Excitation of Propagating Spin Waves by Focused Ultrashort Optical Pulses" *Phys. Rev. Lett.* **110**, 097201 (2013).

[133] J. R. Sandercock and W. Wettling, "Light scattering from surface and bulk thermal magnons in iron and nickel" *J. Appl. Phys.* **50**, 7784 (1979).

[134] S. A. Nikitov, D. V. Kalyabin, I. V. Lisenkov, A. N. Slavin, Yu. N. Barabanenkov, S. A. Osokin, A. V. Sadovnikov, E. N. Beginin, M. A. Morozova, Yu. P. Sharaevsky, Yu. A.

Filimonov, Yu. V. Khivintsev, S. L. Vysotsky, V. K. Sakharov and E S Pavlov, "Magnonics: a new research in spintronics and spin wave electronics" *Phys. Usp.* **58**, 1002 (2015).

[135] M. Donahue and D. Porter, "Interagency Report NISTIR 6376" (NIST, Gaithersburg MD, 1999).

[136] A. Vansteenkiste, J. Leliaert, M. Dvornik, M. Helsen, F. Garcia-Sanchez and B. Van Waeyenberge "The design and verification of Mumax3" *AIP Advances* **4**, 107133 (2013).

[137] T. Fischbacher, M. Franchin, G. Bordignon and H. Fangohr, "A Systematic Approach to Multiphysics Extensions of Finite-Element-Based Micromagnetic Simulations: Nmag" *IEEE. Trans. Mag.* **43**, 2896 (2007).

[138] R. Chang, S. Li, M. V. Lubarda, B. Livshitz and V. Lomakin, "FastMag: Fast micromagnetic simulator for complex magnetic structures (invited)" *J. Appl. Phys.* **109**, 07D358 (2011).

[139] E. Fehlberg, "Classische Runge-Kutta Formeln vierter und niedrigerer Ordnung mit Schcrit-tweiten-Kontrolle und ihre Anvendung auf Wärmeleitungs-probleme" *Computing* **6**, 61 (1970).

[140] S. Fu, W. Cui, M. Hu, R. Chang, M. J. Donahue and V. Lomakin, "Finite-Difference Micromagnetic Solvers With the Object-Oriented Micromagnetic Framework on Graphics Processing Units" *IEEE Trans. Mag.* **52**, 7100109 (2016).

[141] K. M. Lebecki, M. J. Donahue and M. W. Gutowski, "Periodic boundary conditions for demagnetization interactions in micromagnetic simulations" *J. Phys. D.: Appl. Phys.* **41**, 175005 (2008).

[142] W. Wang, C. Mu, B. Zhang, Q. Liu, J. Wang and D. Xue "Two-dimensional periodic boundary conditions for demagnetization interactions in micromagnetics" *Comput. Mater. Sci.* **49**, 84 (2010).

[143] S. Rohart and A. Thiaville, "Skyrmion confinement in ultrathin film nanostructures in the presence of Dzyaloshinskii-Moriya interaction" *Phys. Rev. B* **88**, 184422 (2013).

[144] OOMMF manual, available at http://math.nist.gov/oommf/doc/userguide12a6/userguide/

[145] A. Aharoni, "Demagnetizing factors for rectangular ferromagnetic prisms" *J. Appl. Phys.* **83**, 3432 (1998).

[146] R. D. McMichael, M. J. Donahue, D. G. Porter and Jason Eicke, "Comparison of magnetostatic field calculation methods on two-dimensional square grids as applied to a micromagnetic standard problem" *J. Appl. Phys.* **85**, 5816 (1999).

[147] Y. Au, T. Davison, E. Ahmad, P. S. Keatley, R. J. Hicken and V. V. Kruglyak, "Excitation of propagating spin waves with global uniform microwave fields" *Appl. Phys. Lett.* **98**, 122506 (2011).

[148] A. K. Ganguly and D. C. Webb, "Microstrip excitation of magnetostatic surface waves: theory and experiment" *IEEE. Trans. Microw. Theory Tech.* **23**, 998 (1975).

[149] V. Vlaminck and M. Bailleul, "Spin-wave transduction at the submicrometer scale: Experiment and modelling" *Phys. Rev. B* **81**, 014425 (2010).

[150] T. Schneider, A. A. Serga, A. V. Chumak, C. W. Sandweg, S. Trudel, S. Wolff, M. P. Kostylev, V. S. Tiberkevich, A. N. Slavin and B. Hillebrands "Nondiffractive subwavelength wave beams in a medium with externally controlled anisotropy" *Phys. Rev. Lett.* **104**, 197203 (2010).

[151] R. Gieniusz, H. Ulrichs, V. D. Bessonov, U. Guzowska, A. I. Stognii and A. Maziewski, "Single antidot as a passive way to create caustic spin-wave beams in yttrium iron garnet films" *Appl. Phys. Lett.* **102**, 102409 (2013).

[152] P. Wessels, A. Vogel, J.-N. Tödt, M. Wieland, G. Meier and M. Drescher, "Direct observation of isolated Damon-Eshbach and backward volume spin-wave packets in ferromagnetic microstripes" *Sci. Rep.* **6**, 22117 (2016).

[153] V. Vlaminck and M. Bailleul, "Current-induced Spin-Wave Doppler Shift" *Science* **322**, 410 (2008).

[154] P. Gruszecki, M. Kasprzak, A. E. Serebryannikov, M. Krawczyk and W. Śmigaj, "Microwave excitation of spin wave beams in thin ferromagnetic films" *Sci. Rep.* **6**, 22367 (2016).

[155] S. Vasuki, D. Helena Margaret and R. Rajeswari, "Microwave Engineering" (McGraw Hill Education, New Delhi, 2015).

[156] C. Kittel, "Excitation of Spin Waves in a Ferromagnet by a Uniform rf Field," *Phys. Rev.* **110**, 1295 (1958).

[157] A. Barman, V. V. Kruglyak, R. J. Hicken, A. Kundrotaite and M. Rahman, "Anisotropy, damping, and coherence of magnetization dynamics in a 10 μm square element" *Appl. Phys. Lett.* **82**, 3065 (2003).

[158] E. Schlömann and R. I. Joseph, "Generation of Spin Waves in Nonuniform dc Magnetic Fields. II. Calculation of the Coupling Length" *J. Appl. Phys.* **35**, 167 (1964).

[159] M. Arikan, Y. Au, G. Vasile, S. Ingvarsson and V. V. Kruglyak, "Broadband injection and scattering of spin waves in lossy width-modulated magnonic crystal waveguides" *J. Phys. D.: Appl. Phys.* **46**, 135003 (2013).

[160] M. Shone, "The technology of YIG film growth" *Circ. Syst. Signal Pr.* **4**, 89 (1985).

[161] H.-U. Krebs, M. Weisheit, J. Faupel, E. Süske, T. Scharf, C. Fuhse, M. Störmer, K. Sturm, M. Seibt, H. Kijewski, D. Nelke, E. Panchenko, M. Buback, "Pulsed laser deposition (PLD) - a versatile thin film technique" *Adv. Solid State Phys.* **43**, 505 (2003).

[162] N. S. Sokolov, V. V. Fedorov, A. M. Korovin, S. M. Suturin, D. A. Baranov, S. V. Gastev, B. B. Krichevtsov, K. Yu. Maksimova, A. I. Grunin, V. E. Bursian, L. V. Lutsev and M. Tabuchi, "Thin yttrium iron garnet films grown by pulsed laser deposition: Crystal structure, static, and dynamic magnetic properties" J. Appl. Phys. 119, 023903 (2016).

[163] M. Dvornik, Y. Au and V. V. Kruglyak, "Micromagnetic simulations in magnonics" *Top. Appl. Phys.* **125**, 101 (2013).

[164] A. I. Marchenko and V. N. Krivoruchko, "Magnetic structure and resonance properties of a hexagonal lattice of antidots" *Low. Temp. Phys.* **38**, 157 (2012).

[165] V. N. Krivoruchko and A. I. Marchenko, "Spatial confinement of ferromagnetic resonances in honeycomb antidot lattices" *J. Magn. Magn. Mater.* **324**, 387 (2012).

[166] O. N. Martyanov, V. F. Yudanov, R. N. Lee, S. A. Nepijko, H. J. Elmers, R. Hertel, C. M. Schneider and G. Schönhense "Ferromagnetic resonance study of thin film antidot arrays: Experiment and micromagnetic simulations" *Phys. Rev. B* **75**, 174429 (2007).

[167] S. Neusser, B. Botters and D. Grundler, "Localization, confinement, and field-controlled propagation of spin waves in $Ni_{80}Fe_{20}$ antidot lattices" *Phys. Rev. B* **78**, 054406 (2008).

[168] B. Lenk, H. Ulrichs, F. Garbs and M. Münzenberg, "The building blocks of magnonics" *Phys. Rep.* **507**, 107 (2011), and references therein.

[169] V. Veerakumar and R. E. Camley, "Magnon focusing in thin ferromagnetic films" *Phys. Rev. B* **74**, 214401 (2006).

[170] O. Karlqvist, "Calculation of the magnetic field in the ferromagnetic layer of a magnetic drum" *Trans. Roy. Inst. Techn.* **86**, 3 (1954).

[171] R. D. McMichael and M. J. Donahue, "Head to head domain wall structures in thin magnetic stripes" *Physica B* **233**, 272 (1997).

[172] A. Hubert and R. Schäfer, "Magnetic Domains: The Analysis of Magnetic Microstructures" (Springer, Berlin, 1998).

[173] M. Dvornik, A. N. Kuchko and V. V. Kruglyak, "Micromagnetic method of s-parameter characterization of magnonic devices" *J. Appl. Phys.* **109**, 07D350 (2011).

[174] A. Baker, M. Beg, G. Ashton, M. Albert, D. Chernyshenko, W. Wang, S. Zhang, M.-A. Bisotti, M. Franchin, C. L. Hu, R. Stamps, T. Hesjedal and H. Fangohr, "Proposal of a micromagnetic standard problem for ferromagnetic resonance simulations" *J. Magn. Magn. Mater.* **421**, 428 (2017).

[175] B. Van de Wiele and F. Montoncello, "A continuous excitation approach to determine time-dependent dispersion diagrams in 2D magnonic crystals" *J. Phys. D.: Appl. Phys.* **47**, 315002 (2014).

[176] These values were obtained using the program publically available at http://www.magpar.net/static/magpar/doc/html/demagcalc.html, which was written by Rok Dittrich.

[177] E. W. Marchand, "Gradient Index Optics*"* (Academic Press, London, 1978).

[178] U. Leonhardt and T. G. Philbin, "Transformation Optics and the Geometry of Light" *Prog. Opt.* **53**, 69 (2009).

[179] G. Chen, "Thermal conductivity and ballistic-phonon transport in the cross-plane direction of superlattices" *Phys. Rev. B* **57**, 14958 (1998).

[180] D. M. F. Chapman, "Using streamlines to visualize acoustic energy flow across boundaries" *J. Acoust. Soc. Am.* **124**, 48 (2008).

[181] Yu. I. Gorobets and S. A. Reshetnyak, "Reflection and refraction of spin waves in uniaxial magnets in the geometrical-optics approximation" *Zh. Tekh. Fiz.* **68**, 60 (1998).

[182] S.-K. Kim, S. Choi, K.-S. Lee, D.-S. Han, D.-E. Jung and Y.-S. Choi "Negative refraction of dipole-exchange spin waves through a magnetic twin interface in restricted geometry" *Appl. Phys. Lett.* **92**, 212501 (2008).

[183] D.-E. Jeong, D.-S. Han, S. Choi and S.-K. Kim, "Refractive index and Snell's Law for Dipole-Exchange spin waves in restricted geometry" *SPIN* **1**, 27 (2011).

[184] Y. Sasaki and H. T. Ueda, "Reflection and Refraction Process of Spinwave in a Ferromagnet/Frustrated Ferromagnet Junction System" *J. Phys. Soc. Jpn.* **82**, 074604 (2013).

[185] K. Tanabe, R. Matsumoto, J. Ohe, S. Murakami, T. Moriyama, D. Chiba, K. Kobayashi and T. Ono "Real-time observation of Snell's law for spin waves in thin ferromagnetic films" *Appl. Phys. Expr.* **7**, 053001 (2014).

[186] J. Stigloher, M. Decker, H. S. Körner, K. Tanabe, T. Moriyama, T. Taniguchi, H. Hata, M. Madami, G. Gubbiotti, K. Kobayashi, T. Ono and C. H. Back "Snell's Law for Spin Waves" *Phys. Rev. Lett.* **117**, 037204 (2016).

[187] A. V. Vashkovskii and E. H. Lock, "Properties of backward electromagnetic waves and negative reflection in ferrite films" *Phys. Usp.* **49**, 389 (2006).

[188] A.V. Vashkovskii, A.V. Stal'makhov and D. G. Shakhanazaryan, "Formation, reflection, and refraction of magnetostatic wave beams" *Sov. Phy. J* **11**, 908 (1988).

[189] A. V. Vashkovskii and V. I. Zubkov, "Magnetostatic surface wave reflection by irregularities of various types" *J. Commun. Technol. Electronics* **48,** 131 (2003).

[190] A. V. Vashkovskii and E. H. Lock, "Negative refractive index for a surface magnetostatic wave propagating through the boundary between a ferrite and ferrite-insulator-metal media" *Physics-Uspekhi* **47,** 601 (2004).

[191] R. Gieniusz, V. D. Bessonov, U. Guzowska, A. I. Stognii and A. Maziewski, "An antidot array as an edge for total non-reflection of spin waves in yttrium iron garnet films" *Appl. Phys. Lett.* **104,** 082412 (2014).

[192] J. B. Pendry, D. Schurig and D. R. Smith, "Controlling electromagnetic fields" *Science* **312**, 1780-1782 (2006).

[193] U. Leonhardt and T. G. Philbin, "General relativity in electrical engineering" *New J. Phys* **8**, 247 (2006).

[194] E. E. Narimanov and A. V. Kildishev, "Optical black hole: Broadband omnidirectional light absorber" *Appl. Phys. Lett.* **95**, 041106 (2009).

[195] X. Zhang and Z. Liu, "Superlenses to overcome the diffraction limit" *Nat. Mat.* **7**, 435 (2008).

[196] K. Vogt, J. E. Pearson, T. Sebastian, S. D. Bader, B. Hillebrands, A. Hoffmann and H. Schultheiss, "Realization of a spin-wave multiplexer" *Nat. Commun.* **5**, 3727 (2014).

[197] V. E. Demidov, M. P. Kostylev, K. Rott, J. Münchenberger, G. Reiss and S. O. Demokritov, "Excitation of short-wavelength spin waves in magnonic waveguides" *Appl. Phys. Lett.* **99**, 082507 (2011).

[198] J.-N. Toedt, S. Mansfeld, D. Mellem, W. Hansen, D. Heitmann and S. Mendach, "Interface modes at step edges of media with anisotropic dispersion" *Phys. Rev. B* **93**, 184416 (2016).

[199] M. Elyasi, C. S. Bhatia, C.-W. Qiu and H. Yang, "Cloaking the magnons" *Phys. Rev. B* **93**, 104418 (2016).

[200] M. Pardavi-Horvath, C. A. Ross and R. D. McMichael, "Shape effects in the ferromagnetic resonance of nanosize rectangular permalloy arrays" *IEEE Trans. Magn.* **41**, 3601 (2005).

[201] R. J. Celotta, J. Unguris and D. T. Pierce, "Magnetic Interactions and Spin Transport" (*ed* A. Chtchelkanova *et al*, Springer, New York, 2003).

[202] O. Fruchart and A. Thiaville, "Magnetism in reduced dimensions" *C. R. Physique* **6**, 921 (2006).

[203] N. Yu. Grigoryeva, D. A. Popov and B. A. Kalinikos, "Dipole-Exchange Spin Wave Spectrum in an Anisotropic Ferromagnetic Waveguide with a Rectangular Cross Section" *Phys. Solid State* **56**, 1806 (2014).

[204] K. L. Wong, L. Bi, M. Bao, Q. Wen, J. P. Chatelon, Y.-T. Lin, C. A. Ross, H. Zhang and K. L. Wang "Unidirectional propagation of magnetostatic surface spin waves at a magnetic film surface" *Appl. Phys. Lett.* **105**, 232403 (2014).

[205] P. Gruszecki, J. Romero-Vivas, Yu. S. Dadoenkova, N. N. Dadoenkova, I. L. Lyubchanskii and M. Krawczyk, "Goos-Hänchen effect and bending of spin wave beams in thin magnetic films" *Appl. Phys. Lett.* **105**, 242406 (2014).

[206] P. Gruszecki, Yu. S. Dadoenkova, N. N. Dadoenkova, I. L. Lyubchanskii, J. Romero-Vivas, K. Y. Guslienko and M. Krawczyk, "Influence of magnetic surface anisotropy on spin wave reflection from the edge of ferromagnetic film" *Phys. Rev. B* **92**, 054427 (2015).

[207] A. V. Chumak, A. A. Serga and B. Hillebrands, "Magnon transistor for all-magnon data processing" *Nature Commun.* **5**, 4700 (2014).

[208] T. Schneider, A. A. Serga, B. Leven, B. Hillebrands, R. L. Stamps and M. P. Kostylev, "Realization of spin-wave logic gates" *Appl. Phys. Lett.* **92**, 022505 (2008).

[209] S.-K. Kim, K.-S. Lee and D.-S. Han, "A gigahertz-range spin-wave filter composed of width-modulated nanostrip magnonic-crystal waveguides" *Appl. Phys. Lett.* **95**, 082507 (2009).

[210] S. Bance, T. Schrefl, G. Hrkac, A. Goncharov, D. A. Allwood and J. Dean, "Micromagnetic calculation of spin wave propagation for magnetologic devices" *J. Appl. Phys.* **103**, 07E735 (2008).

[211] X. Xing, Y. Yu, S. Li and X. Hunag, "How do spin waves pass through a bend?" *Sci. Rep.* **3**, 2958 (2013).

[212] T. Brächer, P. Pirro, J. Westermann, T. Sebastian, B. Lägel, B. Van de Wiele, A. Vansteenkiste and B. Hillebrands, "Generation of propagating backward volume spin waves by phase-sensitive mode conversion in two-dimensional microstructures" *Appl. Phys. Lett.* **102**, 132411 (2013).

[213] A. A. Serga, T. Neumann, A. V. Chumak, and B. Hillebrands, "Generation of spin-wave pulse trains by current-controlled magnetic mirrors" *Appl. Pys. Lett.* **94**, 112501 (2009).

[214] E. Goulielmakis, M. Schultze, M. Hofstetter, V. S. Yakovlev, J. Gagnon, M. Uiberacker, A. L. Aquila, E. M. Gullikson, D. T. Attwood, R. Kienberger, F. Krausz and U. Kleineberg, "Single-Cycle Nonlinear Optics" *Science* **320**, 1614 (2008).

[215] M. Th. Hassan, T. T. Luu, A. Moulet, O. Raskazovskaya, P. Zhokhov, M. Garg, N. Karpowicz, A. M. Zheltikov, V. Pervak, F. Krausz and E. Goulielmakis, "Optical attosecond pulses and tracking the nonlinear response of bound electrons" *Nature* **530**, 66 (2016).

[216] A. Kirilyuk, A. V. Kimel and T. Rasing, "Ultrafast optical manipulation of magnetic order" *Rev. Mod. Phys.* **82**, 2731 (2010).

[217] M. van Kampen, C. Jozsa, J. T. Kohlhepp, P. LeClair, L. Lagae, W. J. M. de Jonge and B. Koopmans, "All-optical probe of coherent spin waves" *Phys. Rev. Lett.* **88**, 227201 (2002).

[218] B. Lenk, G. Eilers, J. Hamrle and M. Münzenberg "Spin-wave population in nickel after femtosecond laser pulse excitation" *Phys. Rev. B* **82**, 134443 (2010).

[219] B. Lenk, H. Ulrichs, F. Garbs and M. Münzenberg, "The building blocks of magnonics" *Phys. Rep.* **507**, 107 (2011).

[220] T. Satoh, Y. Terui, R. Moriya, B. A. Ivanov, K. Ando, E. Saitoh, T. Shimura and K. Kuroda, "Directional control of spin-wave emission by spatially shaped light" *Nature Photon.* **6**, 662 (2012).

[221] F. Busse, M. Mansurova, B. Lenk, M. von der Ehe and M. Münzenberg, "A scenario for magnonic spin-wave traps" *Sci. Reports* **5**, 12824 (2015).

[222] M. Vogel, A. V. Chumak, E. H. Waller, T. Langner, V. I. Vasyuchka, B. Hillebrands and G. von Freymann, "Optically reconfigurable magnetic materials" *Nature Phys.* **11**, 487 (2015).

[223] C. Kittel, "Interaction of Spin Waves and Ultrasonic Waves in Ferromagnetic Crystals" *Phys. Rev.* **110**, 836 (1958).

[224] A. I. Akhiezer, V. G. Bar'yakhtar and S. V. Peletminskii, "Coupled Magnetoelastic Waves in Ferromagnetic Media and Ferroacoustic Resonance" *Zh. Eksp. Teor. Fiz.* **35**, 228 (1958).

[225] E. Schlömann, "Generation of Phonons in High-Power Ferromagnetic Resonance Experiments" *J. Appl. Phys.* **31**, 1647 (1960).

[226] N. Ogawa, W. Koshibae, A. J. Beekman, N. Nagaosa, Masashi Kubota, M. Kawasaki and Y. Tokura, "Photodrive of magnetic bubbles via magnetoelastic waves" *Proc. Natl. Acad. Sci. USA* **112**, 8977 (2015).

[227] K. Shen and G. E. W. Bauer, "Laser-Induced Spatiotemporal Dynamics of Magnetic Films" *Phys. Rev. Lett.* **115**, 197201 (2015).

[228] F. Hansteen, A. V. Kimel, A. Kirilyuk and T. Rasing, "Femtosecond photomagnetic switching of spins in ferromagnetic garnet films" *Phys. Rev. Lett* **95**, 047402 (2005).

[229] F. Hansteen, A. V. Kimel, A. Kirilyuk and T. Rasing, "Nonthermal ultrafast optical control of the magnetization in garnet films" *Phys. Rev. B* **73**, 014421 (2006).

[230] J. P. van der Ziel, P. S. Pershan and L. D. Malmstrom, "Optically-Induced Magnetization Resulting from the Inverse Faraday Effect" *Phys. Rev. Lett.* **15**, 190 (1965).

[231] A. V. Kimel, A. Kirilyuk, P. A. Usachev, R. V. Pisarev, A. M. Balbashov and Th. Rasing, "Ultrafast non-thermal control of magnetization by instantaneous photomagnetic pulses" *Nature* **435**, 655 (2005).

[232] Y. R. Shen, "The principles of nonlinear optics" (John Wiley & Sons, New York, 2003).

[233] A. Ben-Amar Baranga, R. Battesti, M. Fouché, C. Rizzo and G. L. J. A. Rikken, "Observation of the inverse Cotton-Mouton effect" *Europhys. Lett.* **94**, 44005 (2011).

[234] M. H. Kryder, E. C. Cage, T. W. McDaniel, W. A. Challener, R. E. Rottmayer, G. Ju, Y.-T. Hsia and M. F. Erden, "Heat Assisted Magnetic Recording" *Proc. IEEE* **96**, 1810 (2008).

[235] J. Janušonis, C. L. Chang, P. H. M. van Loosdrecht and R. I. Tobey, "Frequency tunable surface magneto elastic waves" *Appl. Phys. Lett.* **106**, 181601 (2015).

[236] R. Wilks, N. D. Hughes and R. J. Hicken, "Investigation of ultrafast spin dynamics in a Ni thin film" *J. Appl. Phys.* **91**, 8670 (2002).

[237] B. Koopmans, M. van Kampen and W. J. M de Jonge, "Experimental access to femtosecond spin dynamics" *J. Phys.: Condens. Matter* **15**, S723 (2003).

[238] B. Koopmans, M. van Kampen, J. T. Kohlhepp and W. J. M. de Jonge, "Ultrafast magneto-optics in nickel: Magnetism or optics?" *Phys. Rev. Lett.* **85**, 844 (2000).

[239] T. Kampfrath, R. G. Ulbrich, F. Leuenberger, M. Munzenberg, B. Sass and W. Felsch, "Ultrafast magneto-optical response of iron thin films" *Phys. Rev. B* **65**, 104429 (2002).

[240] P. M. Oppeneer and A. Liebsch, "Ultrafast demagnetization in Ni: theory of magneto-optics for non-equilibrium electron distributions" *J. Phys.: Condens. Matter* **16**, 5519 (2004).

[241] J.-Y. Bigot, M. Vomir and E. Beaurepaire, "Coherent ultrafast magnetism induced by femtosecond laser pulses" *Nature Phys.* **5**, 515 (2009).

[242] P. S. Keatley, V. V. Kruglyak, R. J. Hicken, J. R. Childress and J. A. Katine "Acquisition of vector hysteresis loops from micro-arrays of nano-magnets" *J. Magn. Magn. Mater.* **306**, 298 (2006).

[243] T. Wilson, R. Juškaitis and P. Higdon, "The imaging of dielectric point scatterers in conventional and confocal polarisation microscopes" *Optics Communications* **141**, 298 (1997).

[244] X. Hong, E. M. P. H. van Dijk, S. R. Hall, J. B. Götte, N. F. van Hulst and H. Gersen, "Background-Free Detection of Single 5 nm Nanoparticles through Interferometric Cross-Polarization Microscopy" *Nano Lett.* **11**, 541 (2011).

[245] B. T. Miles, X. Hong and H. Gersen, "On the complex point spread function in interferometric cross-polarisation microscopy" *Opt. Express* **23**, 1232 (2015).

[246] R. M. Bozarth and J. G. Walker, "Magnetic crystal anisotropy and magnetostriction of iron-nickel alloys" *Physical Review* **89**, 624 (1953).

[247] Y. K. Kim and T. J. Silva, "Magnetostriction characteristics of ultrathin permalloy films" *Appl. Phys. Lett.* **68**, 2885 (1996).

[248] N. B. Ekreem, A. G. Olabi, T. Prescott, A. Rafferty and M. S. J. Hashmi, "An overview of magnetostriction, its use and methods to measure these properties" *J. Mat. Proc. Tech.* **191**, 96 (2007).

[249] R. Hertel, S. Gliga, M. Fähnle and C. M. Schneider, "Ultrafast Nanomagnetic Toggle Switching of Vortex Cores" *Phys. Rev. Lett.* **98**, 117201 (2007).

[250] O. Dzyapko, I. V. Borisenko, V. E. Demidov, W. Pernice, and S. O. Demokritov, "Reconfigurable heat-induced spin wave lenses" *Appl. Phys. Lett.* **109**, 232407 (2016).